MSc Thesis

Free-Space Multi-beam Optical Communication Terminal Design for Spacecraft

J.J.Spaander

Technische Universiteit Delft

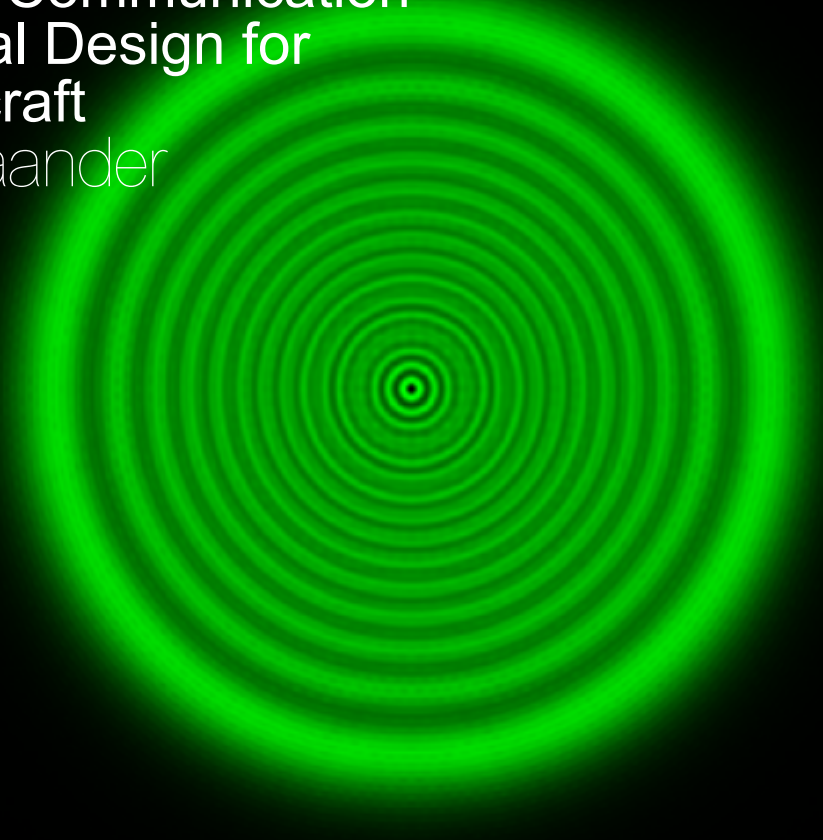

TU Delft

MSc Thesis

Free-Space Multi-beam Optical Communication Terminal Design for Spacecraft

by

J.J.Spaander

to obtain the degree of Master of Science
at the Delft University of Technology,
to be defended publicly on Tuesday April 20th, 2021 at 9:30 AM.

Student number:	4430468	
Project duration:	November, 2019 – April, 2021	
Thesis committee:	Dr. ir. J. Guo,	TU Delft, Supervisor
	Dr. ir. A. Cervone,	TU Delft, Committee Chair
	Dr. ir. D. Dirkx,	TU Delft, Examiner
	Dr. ir. R. Saathof,	TU Delft, Additional Member

This thesis is confidential and cannot be made public until April 20th, 2021.

TU Delft

Preface

Optical communication fell on my path unexpectedly half way through my Master degree while at that time my knowledge in optics didn't go any further than the lens. Soon this topic captured me with it's promise to revolutionize the way we communicate and how it can bring enormous increases in data rates. A significant part of my Master's was spent gathering information and gaining an understanding of the field of free-space optical communications, culminating into this work. Ever increasing data rates however are not the only aspect that can be improved about optical communication. Multiple beam handling or multi-beam systems will improve the diversity of potential applications. This work will discuss the design and the design process for such a multi-beam system. It can serve as a starting point for future design and research into the design of these systems and illustrate different challenges faced.

I would like to thank Dr. Jian Guo for providing me with this thesis opportunity and having the patience to guide me through it. I would like to thank my parents, Fokkelien and Adriaan Spaander, for providing me with the tools and education that has made me to who I am. I would also like to thank Johan Hettinga, my grandfather, who played a critical role in kick starting my academic Aerospace Engineering career.

J.J.Spaander
Delft, April 2021

Contents

List of Figures

List of Tables

1

Introduction and Overview

Free space optical communication is increasingly a booming industry. The promise of unprecedented data rates over long distances, using only small and low power modules, is no longer a hope kindled by faint imagination, but it is quickly becoming a reality. There have been numerous demonstrations of free space communication, both inside and outside the space industry. The prospect of small and high performance optical laser communication modules are exceedingly alluring, especially for the space industry, where mass and power consumption remain extremely expensive. There exists a substantial effort for further increasing the performance of laser communication modules through ever higher data rates. However, there can also be further performance increases by producing modules which are capable of handling multiple beams and subsequent communication links. The design of such a system is the subject of this thesis.

This chapter will provide an introduction into the work. It first discusses the background and motivation of multi-beam laser communication of this thesis. Secondly the research question is posed and explained. The resulting work is then placed in context by defining its scope and assumptions of the work and subsequent choices made in it. From this, the research methodology is explained and will make clarifying the train of thought during the design process. The report structure itself is then outlined and a short overview of its content given. Finally a short summary and conclusion will be given.

1.1. Background and Motivation

An obvious use of optical communications for terrestrial applications is the optic fiber network used for the internet. These are long distance networks which can transport data efficiently and at light speed (in glass fiber). The first generation optic fiber communications at the start of the 1980's were already capable of 45 Mbps at 800 nm. At the end of the 1990's, the fifth generation of optic fiber communications, the technology already exceeded 10 Gbps[39]. In the late 2000's, the newest generation at the time were capable of reaching 10s of Tbps. Thanks in part to better wavelengths in the near-infrared around 1550 nm, complex modulation and multiplexing over a range of frequencies is possible. The industry has also created fibers that can have through puts of 100s of Tbps, using different fiber designs[37][51].

There are however numerous drawbacks associated with fiber optical communications. First of all, these systems require large amounts of infrastructure which are static once installed, implying they are not flexible. Furthermore, the losses in the fiber propagation imply optical terminals spaced every 100 km or so are required[39]. Furthermore, it is completely unusable in space.

The use of optical wavelength for communication allows for the use of lasers, producing tight coherent beams of light. The beams limited dispersion angle allow for far lower free space propagation losses compared to conventional radio communications. Furthermore, there is no required infrastructure. Other attractive features include: private communication links, no need for frequency allocations to different users, the possibility to use optical elements, commercially available high performance hardware and so on. The applications are also interesting for terrestrial applications. RONJA in 2001 produced an open source optical communication link now also active in multiple countries[35]. The demand for free space optical communications is hence clear.

The concept and technology for space applications is also no longer a fiction either. Data speeds in

excess of 1 Gbps have been achieved. Some examples come to mind. SpaceX's Starlink uses inter-satellite laser communication to help deliver high speed internet from a large satellite network[65]. The European Data Relay System (EDRS) uses laser communication links between ground and GEO at 1.8 Gbps. It serves mainly to facilitate higher data rates and more real time data acquisition predominantly to and from ESA's Earth observation satellites[6]. Furthermore, experiments to increase data rates in communications between the ISS and ground have also resulted in NASA's Optical Communications Technology Demonstration with the Optical PAyload for Lasercomm Science (OPALS). This system was capable of a downlink of 50 Mbps[41]. In 2017, duplex communications between a LEO satellite and a ground station was realized by the Micius Coherent Laser Communication Demonstration (MCLCD). The down link had a capacity of over 5 Gbps while the up link achieved 20 Mbps but suffered from instabilities due to atmospheric turbulence[13].

Small spacecraft have also implemented laser communication in the past, thanks to small form factors and high data rates. Some examples of this include the Optical Communication and Sensor Demonstration Program (OCSD) by NASA and Nanosatellite Optical Downlink Experiment (NODE) by MIT. They should each be capable of a few 100 Mbps, illustrating that high performance for laser communications is not restricted to larger satellite platforms.

The advancements into ever higher performance and yet smaller hardware is well underway. However, for all these systems the modules can handle one link in the form of one laser beam each. Furthermore, most of them are also not duplex, implying that fast data rates are reserved for one direction. The use of laser communication satellites in large relay constellations or for multiple user applications would require multiple of the same modules. This makes scaling multi-link satellites expensive in terms of Size, Weight and Power (SWaP).

Potential benefits and applications of handling multiple links per satellite are numerous. To name a few: satellite constellations could help strengthen the global internet infrastructure, relay high speed data to multiple remote users such as aircraft and ships, increase diversity of ground stations to be less dependent on weather, allow for multiple satellites to be relayed at once optically and many more such benefits.

Being able to handle multiple beams in one module would therefore increase the utility and potential applications for high data rate optical communications satellites substantially. This is thus the motivation of this thesis and its topic. To design a duplex multi-beam laser communication system to be used for space applications, while ensuring a minimal number of components and mostly existing Commercial Off The Self (COTS) hardware. The resulting system will be more SWaP efficient per link and consequently better suited for these space applications.

1.2. Research Question

This section will state and explain the research questions. Note that these research questions where created during the literature study[56] and adjusted here. As a result of the thesis work, the main research question has been altered to be more general. In the next section the scope of the work relating to the research question will be given. From the motivation and background discussed in section 1.1, the goal of the report is hence to produce a multi-beam design to illustrate different aspects which have to be considered. The main research question and associated sub-questions are the following (note that COTS means Commercial Off The Shelf):

How can a multi-beam free-space optical communication terminal be designed using COTS technologies and components?

(a) Which technologies can be used to handle multiple beams?

(b) How do different technologies affect the performance of the terminal?

(c) What aspects of the design where the most driving?

Therefore, fundamentally the goal is to research the design and design process of a multi-beam laser communication terminal for spacecraft. The question and sub-questions require a design and a reflection on the design process to give insight. Namely into the demands for a well functioning and implementable multi-beam free-space optical communications system can be met and what the largest obstacles were when designing such a system. The question is posed in a general way but can be answered through a singular design.

To ensure that the system designed can perform at sufficient levels while simultaneously being feasible. The requirements referred to are those found in the literature study[56] and have been copied into Appendix C for reference and easy access for the reader. These requirements specify performance and design criteria which, when met, could lead to a feasible system. These requirements will be re-assessed to adjust for new insights. Furthermore, COTS components where included to ensure that the system could be feasibly constructed and did not require large technological leaps to achieve the requirements.

When the system complies with these requirements and goals, it is considered complete and the resulting question can be answered in full.

Beyond the main research questions, some additional secondary questions where created. This includes deeper questions regarding the limitations of the multi-beam system. The following questions are derived from the main question to find the more challenging aspects of the design process:

1. What are some of the practical limitations of the design?
    (a) What are the usage limitations?
    (b) Could these limitations be pushed or changed by a non-COTS custom part?
    (c) Where there any dead ends?
    (d) Why where these dead ends?
    (e) How much of the design process was affected by the facilities and other resources available?
    (f) How would a more streamlined design process look like?
    (g) Could the design process be different by use of a non-COTS custom part?

The goal of these questions is to highlight the main design but it also explores the potential improvements and alternatives. Further on in the process the scope will indicate that only one design will be made and hence some reflection on this would be interesting. For example, if the pointing accuracy is the most difficult aspect, the resulting problems and design ends associated with the pointing system would be beneficial to highlight. Other limitations might be the system response speed, the number of beams or finding high performance COTS components, to name a few examples. This will result in further recommendations for designing multi-beam terminals.

The design also has sensitivities with regards to different requirements and external factors that are important to highlight. The following question will explore this:

2. What sensitivities exist in the design?
    (a) When a sensitivity analysis on different design aspects on the performance is done, what particular aspects are most sensitive?
    (b) How crucial is the application/use case?
    (c) What aspect of the design drives the design?

Examples of sensitivities can include external factors on the system performance and design. For example, the turbulence and jitter frequencies can degrade the fiber coupling efficiency and increase the steering requirements. When these effects are exaggerated the design might stop conforming and perhaps a different approach has to be made.

Finally, the performance improvements of the multi-beam terminal over the alternatives of adding more single beam terminals should be discussed. These include the effects on SWaP and how it scales with the number of links and when the terminal becomes competitive with single beam terminals. These are important aspects for the economics and define the financial viability of different use cases.

3. Is the SWaP of each link lower than single beam terminal links?
    (a) What aspects of the design are more SWaP intensive?
    (b) What aspects of the design are less SWaP insentive?
    (c) How would non-COTS or future COTS components change the SWaP?
    (d) Why are the SWaP costs different per link?
    (e) What is the effect of use case on the SWaP?
    (f) What is the minimum number of links required before the multi-beam terminal has lower SWaP per link as a with single-beam terminals?

1.3. Scope and Assumptions

The scope of the work when applied to the research questions discussed in section 1.2, is to limit the work to one design. The main research question is posed in such a way as to allow for freedom of exploring during the design. Important aspects, such as the method by which the system controls multiple beams, are not defined. This section will make clear the exact scope of the work and the assumptions made in the design.

From the research question, the work is limited to COTS components, which are commercially available or have been created before. If there were no COTS component found which could make the system comply with the requirements, the required performance would be stated. However in the end, this was not needed. The components used should also be compatible and durable in the space environment but will not require a space track record. It will be assumed that the results of lab work and exposure to radiation which is representative or worse than the space environment will be considered adequate.

The work will also answer the main question by designing one multi-beam system and by no means provides an exhaustive look into all possible configurations. There will be trade-offs as to which components and configurations will be used. For each trade-off there will be an accompanying discussion.

An other crucial assumption will be that the electronics and computation will not be a limiting factor in the design. Hence, these will not be designed. The optics of the transceiver will be designed because of its important effects on the rest of the optical train. This is also true for the modulation or communication protocols. The data rates adhered to in this work will be the Shannon-Hartley limits, which will be higher than the practically achievable data rates.

The structure, housing and thermal control of the multi-beam terminal is very important for the accuracy of the construction and subsequent performance. However, this will also not be designed and it is assumed that it would be feasible to design it. The goal of this thesis is to design the steering systems and transceiver to make multi-beam communication possible.

Lastly, not all the requirements specified in Appendix C are relevant for this work. They where formulated in the literature study[56] to be for a general multi-beam design. The requirements will be used for the parts of the system which will be designed.

1.4. Methodology

After studying the state of the art of spacecraft optical communication, the simulation models will be made. The initial approach was to perform an experiment of the final design, which regrettably became impossible due to the Corona virus pandemic. It was hence chosen to use simulations, which are accurate enough to give a good evaluation of the design.

This might be counter intuitive to the reader, as usually the simulations are done afterwards to verify and validate the system design. At the start of the project, with the experiment being uncertain and the author's unfamiliarity with optics, extra effort was placed in understanding the physical implications of optical design and the non-linearity's associated with light propagation. This work resulted in that the simulation models where in fact built before the design of the terminal, to ensure the feasibility of the project. It turned out to be a blessing in disguise as it allowed the use of the programs during the work, which resulted in changes of different system aspects and approaches.

To examine the complex interactions of light and the steering mechanisms, optics and feedback, it was chosen to simulate it using Fresnel propagation. Light does not travel in the form of rays but instead propagates through space in the form of oscillating electro-magnetic fields. As will be explained in detail later, this property of light can influence the performance and design of the system profoundly. Due to the interaction of light with discrete steering surfaces, it has affected everything from the hardware choices to the steering algorithm. Fresnel propagation will be explained in more detail in chapter 3, however in short, it analyses the influence of each pixel of the input plane on each pixel on the output plane treating them as super imposed propagating oscillating electro-magnetic fields. The result should be a very accurate representation of the propagation of the fields. The simulation program/algorithm will be derived and adjusted from existing algorithms and theory.

It will then be verified first to work as a simulation model by comparing it with an existing simulation model, referred to as ”Transfer Function” which is a simplification of the Fresnel propagation allowing it to be expressed as a transfer matrix, and theory, such as Gaussian beams and ray tracing. These will also be explained in much more detail later. The comparison will asses different aspects of the output

fields. One of these is comparing the peak intensity, which is important for investigating optical quality and detecting individual beams for the feedback system among others. The distribution of the fields will also be assessed, to see what the spatial differences are in the output fields.

When this has been done and the differences have been found and accounted for, the simulation will be compared to some diffraction experiments. Here, diffraction patterns where created by changing the shape of a small aperture through which a laser beam was passed. The setup was then re-created in the computer and simulated. The results where then compared. The accuracy of the simulation to simulate complicated shapes will be proven and will serve to verify its accuracy in the real world.

The system design will be done in steps aligned with each stage the light passes through, starting with free space propagation and ending in the transceiver. Each aspect will be evaluated, analyzed and optimized and then placed into context of the system. This is also where the previously mentioned simulation programs are used to produce insight into the problems and where existing literature regarding these design aspects is applied. Each resulting design choice will be done with a trade-off or discussion based on the goal of the project and adherence to answering the research question. During this process, assumptions will be made and stated clearly.

The resulting design of the steering system will then be simulated to verify and validate that the system performs as expected.

1.5. Report Overview

The layout of this report was constructed in the most logical way possible, however might differ from the reader's initial intuition. For example, the modeling occurs before the system design. This was done because the models which used during the design process to gain more insight into the challenges and effects of different design aspects. However, Figure 1.1 indicates the different relations between the chapters and makes clear as to why the report structure is as chosen.

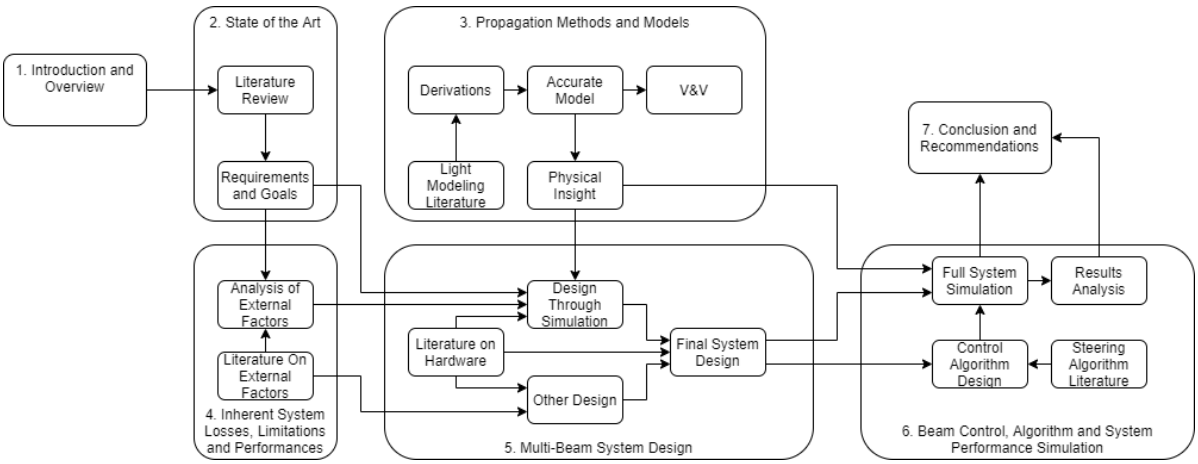

Figure 1.1: Illustrated is a high level overview of how each chapter is related.

In line with the chosen research methodology, the report was structured as shown in Figure 1.2.

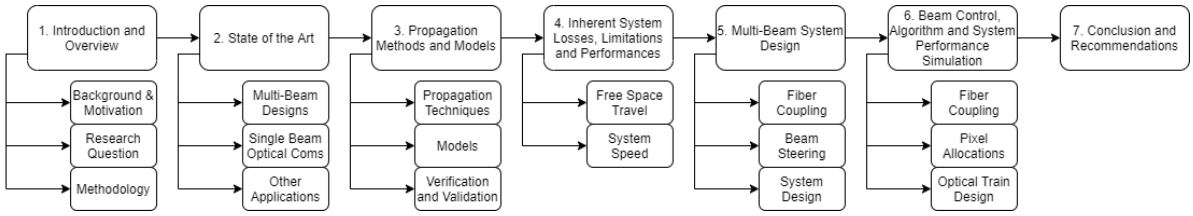

Figure 1.2: Shown is a flow block diagram of the report layout.

Considering Figure 1.1 and Figure 1.2. Following this introduction chapter will be a chapter explaining the state of the art through recent developments in free-space optical communications relevant to

this work. Here, attention will be given to both previous work and ambitions towards multi-beam communication systems will be discussed. Next to this, single beam communication systems as well as some other communication systems will also be discussed in such a way as to learn from their designs.

The modeling section will then follow after. The modeling section will lead the system design, due to some some aspects of the system design being analyzed and requiring illustration from the simulations. The models are based on Fresnel propagation and the mathematics behind the models will first be discussed. The resulting equations will be formed into an algorithm used for the models. The algorithm will be compared to existing well established theory and models to verify its accuracy. Lastly, an experiment will determine the real world accuracy of the simulation in terms of diffraction patterns and will serve as a validation.

The reasoning for deriving a unique algorithm will be discussed in more detail in the chapter itself. However in brief; the complex diffraction patterns over a short distance require more accurate simulation than might be gained from more traditional methods.

The system will then be analyzed and designed into two different chapters. First the inherent system losses, limitations and performances will be discussed. These are parameters which cannot, as of yet, be improved with COTS components and proven techniques. These are the free space travel of the signal and the resulting inherent free space losses associated with long distance communications. The second is the speed of the system which will determine its ability to counter act the effect of jitter.

The system design and the design process of the multi-beam terminal itself will be discussed. First, the design of the fiber coupling system, which primarily concerns the geometry, pointing accuracy and different design choices which can improve them. Then allocation of steering ”pixels”, the general term given to either micro mirrors or SLM pixels, to each beam and their effects on the system performance will be analyzed. It is especially this part of the design that requires further study using the models because of the complected wave interactions between discrete control surfaces and the beams.

The optical train design combines all previously discussed aspects and subsequently performs trade-offs. The results of these trade-offs are used to produce the final optical system layout. This includes the steering system feedback loop, distances and sizes between all the components and telescope design. The design of the transceiver will then be discussed by first performing a trade-off of different approaches and hardware. The system will then be integrated at the end of the optical train.

The trade-off and designs of the optical train and transceiver where performed in tandem. The design of one heavily affects the design of the other. Hence, due to limitations of the English language and the linearity of the report writing process, the trade-offs of the optical system where done knowing the transceiver design restrictions and capabilities. Subsequently, the transceiver system will be trade-off’ed and designed knowing the capabilities and design of the optical train. This might result in the reader knowing the outcome of parts of the transceiver system design before these trade-offs are done.

2

State of the Art

All research is based on the previous work done. This work is no different. This report will detail a design process and simulation of a multi-beam terminal, which has been inspired and based on previous designs in optical communications. This chapter will discuss numerous previous designs, both multi-beam and single beam, to illustrate what currently is the state of the art in the field as well as take inspiration for the design presented in this work.

Some relevant existing literature in the field of multi-beam free space optical communications will be analyzed in this chapter. It will also review existing single beam optical communications previously performed in space. Particular attention will be given to different design choices and different ways to steer beams. Hardware choices for the transceiver will also be discussed based on previous systems and existing hardware.

2.1. Multi-Beam Designs

One multi-user design of interest uses liquid lenses which can be changed in shape to steer beams, 2 of which are shown in Figure 2.1 and Figure 2.2. With 2 lenses in series, the system can deflect beams and potentially act as a steering mechanism. These lenses were also tested in a vacuum environment where it was also concluded that they perform well[18].

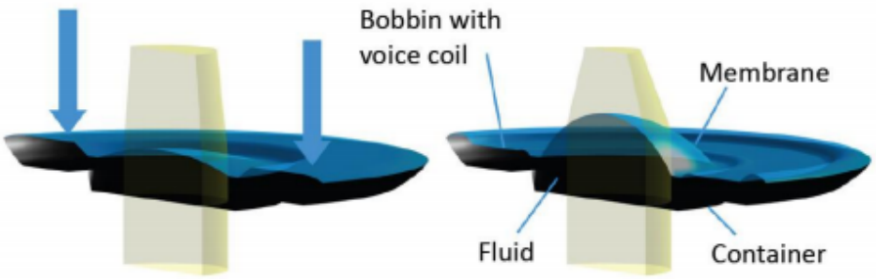

Figure 2.1: Illustration of a voice coil actuated deformable lens. Clearly visible is how fluid is pushed from the periphery containers into the center. This forms a bulge which can be adjusted and create different focal lengths. The figure was taken from the website of Optotune[42].

However, having considered this method of steering, there are some potential design hurdles which have to be overcome. The use of deformable lenses as shown in Figure 2.1 and Figure 2.2 would imply only one beam can be steered at once due to the lens shape being particular. Using a single beam implies that the terminal has to divide time between each target, effectively decreasing data rate inversely proportional to the number of targets. Lastly, the lenses are likely not perfect and will cause aberrations and distortion. The use of fiber receivers for duplex communications would be, as discussed later, hindered by the fiber coupling efficiency which decreases with distorted beams.

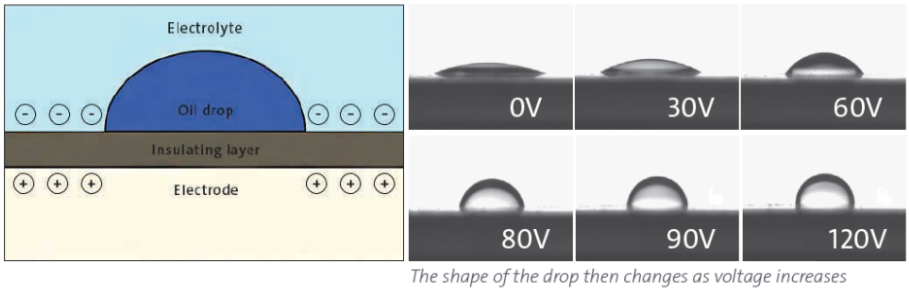

Figure 2.2: Illustration of the working and principle of an oil droplet based deformable lens. Through the application of voltage on the electrode, the shape of an oil droplet can be changed. The figure was taken from Corning[15][16].

There are substantial benefits to using these lenses for small and cube multi-user satellites this would be a very attractive option. They are compact and will allow the integration into very small systems. Furthermore, the inclusion of multiple transmitters would not always be possible or necessary. Lastly, systems which do not have to be duplex would not be benefited by better shaped lenses.

For this work, it was preferred that the system is duplex, facilitate continuous communications and not penalize the existing links by increasing the number of links. Furthermore, the terminal is not perse aimed for small satellites. The number of existing multi-beam or multi-user designs for free space optical communications that can achieve this are mostly limited to patents. Some of these will be discussed here.

The patent Multi-Beam Laser Communications System and Method by Treibes K, Enoch M, Capots L[66] is illustrated in Figure 2.3. It is a duplex system where the incoming and outgoing beams can be handled to the same target. It is hence closer to what this work seeks to achieve. The incoming and outgoing beams occupy the same path in the telescope and are distinguished by wavelength or polarization. This allows for them to be split by passive components and the use of the same telescope and fast steering mirror, increasing the number of shared components. The motion of the targets and the satellite are compensated for by the multi-element actuated stages and fast steering mirror respectively. The multi-element actuated stages follow the spots as they move to maintain signal.

There are some issues however, namely that the splitting wavelength would reduce the abilities for wavelength division multiplexing, such as those used in optic fiber communications[50]. More over, the separation of polarization would result in certain modulations not being possible. Furthermore, moving components such as those in the multi-element stages would decrease the reliability of the system over time. This should be avoided in space due to the inability to service the module after launch. The physical dimensions of the fiber ends in the multi-steering stages also imply the system might have to facilitate in handovers between different transmitters and receivers. This interrupts the communications. The transmitter and receiver components are not shared. Lastly, the spot tracker has to track both the incoming and outgoing beams.

The patent Multi-Channel Wide-Field Laser Communications Method and Apparatus by Capots L, Sigler R, Triebes S[12] provides a different take. This system is illustrated in Figure 2.4. The system is duplex, implying it can support communications in both directions. The system also uses a beam splitter to separate the incoming and outgoing signals, in this case the splitting is based on polarization. The steering is done by steering flats which received feedback from a spot tracker. The receiver fiber is integrated into the spot tracker, implying the location of the fiber is known and the spot tracker directly imaged the spot tracking on the receiver plain. This makes it inherently easier to steer the beams and saves the need of additional optical components however are not COTS. The static beams means a large amount of steering hardware is saved. Lastly, the FOV is limited by the steering flat.

Some design difficulties might have to be overcome however. First, the steering flats and the receivers are quite far apart. Due to the small fiber cross section, this makes the steering requirements very strict. Furthermore, because the incoming and outgoing beams share a path, it implies that the receiver aperture is limited by the size of the steering flat. These steering flats also show that a large part of the optical system is not shared between all beams and hence increases the number of components. The beam splitting also limits the modulation techniques. The static transmitters and receivers would also limit the number and flexibility of the possible applications.

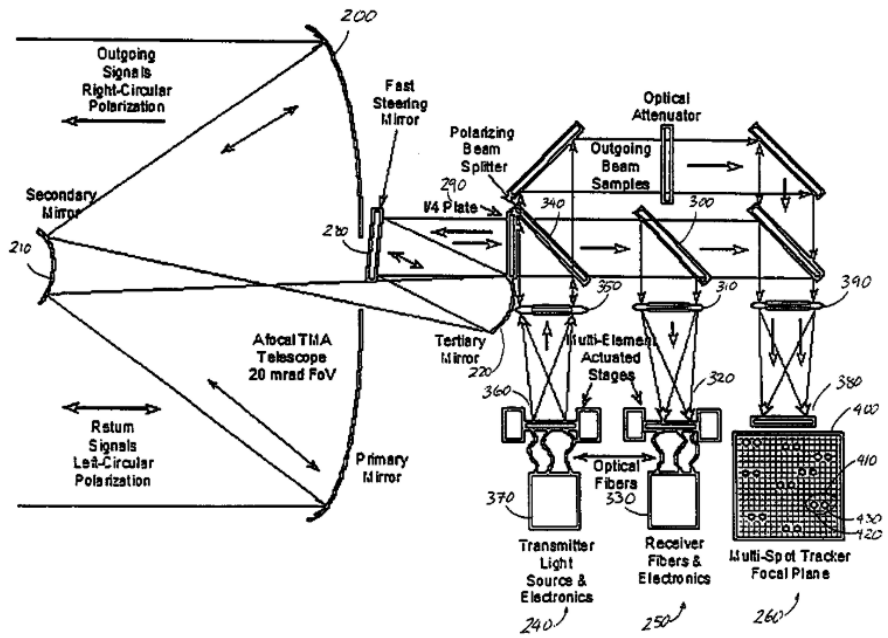

Figure 2.3: Illustrated is the patented design of a multi-beam system produced by Treibes K, Enoch M, Capots L [66]. Considering and incoming beam, it is captured by a large reflective telescope and collimated into the optical train. The optical train then uses dichroic mirrors to separate the different incoming and outgoing wavelengths. Some of the received and transmitted energy is also directed into the spot tracker through which the fast steering mirror and the locations of the transmitter and receiver optic fibers are controlled.

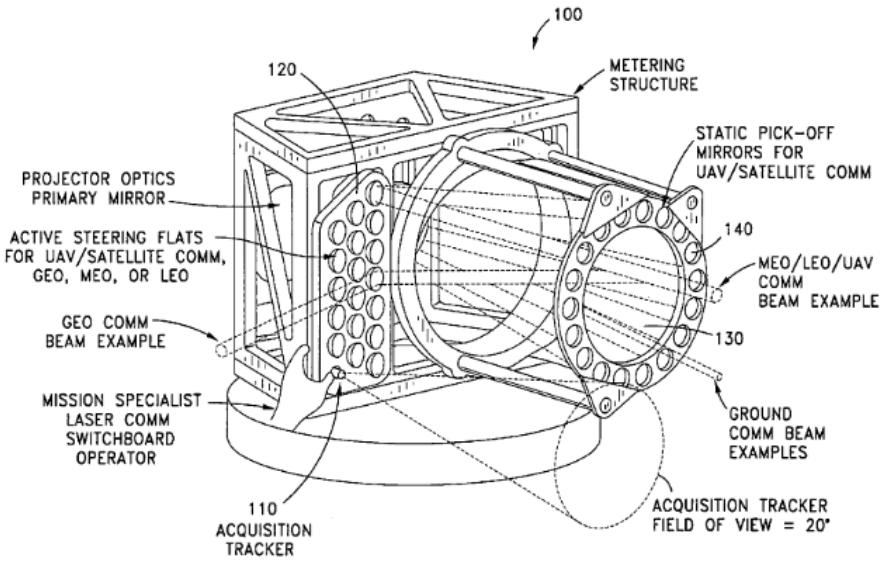

Figure 2.4: Illustrated is the patented design of a multi-beam system produced by Capots L, Sigler R, Triebes K [12]. The transmitters are on the back of the system and through a number of mirrors emit the beam to the static pick off mirrors. The mirrors then reflect it to the active steering flats which direct the beams to the targets. Static targets are directly mapped to the transmitters, implying they are pre-placed in the right location. The system hence is to be placed in geostationary orbit where these targets are not moving relative to the terminal. The non-static targets after the pick-off mirrors are directed onto the steering slats. The acquisition tracker finds the targets. Feedback is provided by a spot tracker on the receiver plane. The system is duplex where the incoming and outgoing beams follow the same path.

The patent Agile Multi-Beam Free-Space Optical Communication Apparatus by Harry Presley, Har-

ris Corporation[47], shown in Figure 2.5, does away with a steering mechanism all together. Instead, it uses arrays of both transmitters and receivers with the specific transmitters and receivers turned on based on tracking spots. This saves the need for steering mechanisms and fundamentally decreases the number of moving components. The feedback is also easier considering that all the locations of the transmitters and receivers are known. The telescope also captures the beams and maps incident angles in the FOV to linear spacing. It subsequently allows for all beams to share the telescope.

However, the beams vary their positions implying that they will not always be well aligned with the receivers. Should the receivers be fiber based, this would come at the cost of fiber coupling efficiency. Furthermore, this alignment is also a problem for the transmitters, which leads to pointing inaccuracies and losses. The wavelength selective splitter would also lead to limitations for wavelength based multiplexing.

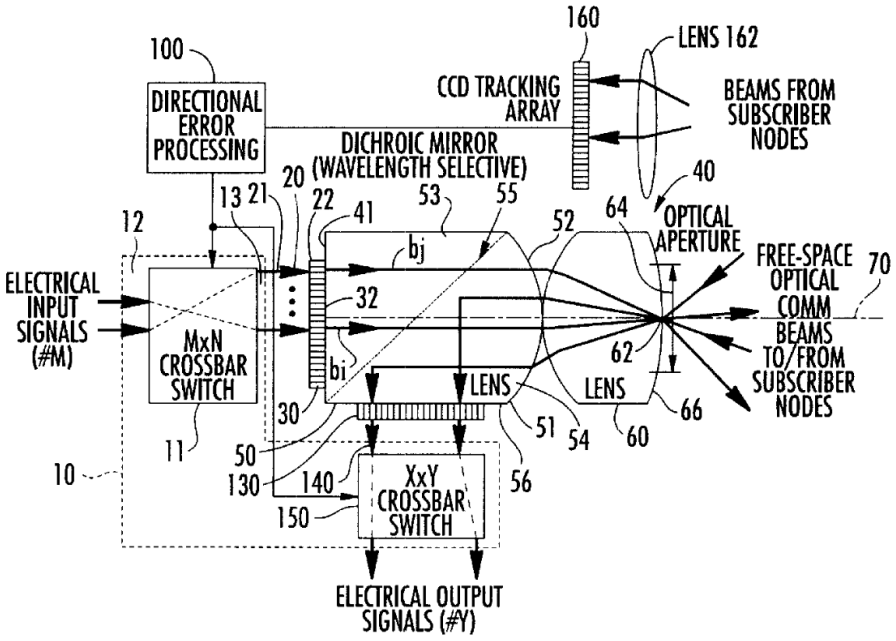

Figure 2.5: Illustrated is the patented design of a multi-beam system produced by Harry Presley, Harris Corporation[47]. The system does not have moving parts and instead has an array of receivers. The beams enter an leave a telescope where the incoming beams are mapped by incoming angle to parallel rays. The incoming beams are reflected to the receivers down by a wavelength selective dichroic mirror. The outgoing beams are sent through an unaffected wavelength out of the terminal by a transmitter in an array of transmitters. The locations and resulting directions are determined by a CCD spot tracker.

The patent Free-Space Optical Communication System with Spatial Multiplexing by Vladimir G. Sidorovich, Aleksei A. Leshev, Valery V. Ragulsky, Mikhail A. Sadovnikov, Mikhail V. Vasiliev, Vladimir P. Vasiliev[53], shown in Figure 2.6, illustrates a method of using wide FOV's. This design is also echo'ed in a later patent by the same inventors[54]. Both designs in both patents are not complete in their details compared to the previously discussed designs and are also no meant for space communications. They do show the benefit of using large FOV telescopes, in this case consisting of a single spherical optical component. The receivers are distributed radially allowing, eliminating the need for mapping angles to linear displacements and simplifying the design. The Independence of the transmitter and receivers would not have to make concessions based on polarization and wavelengths.

However, for non-static targets these designs are hard to implement. The transceivers would have to change physical location, which comes with numerous hurdles and issues. The independent steering of the transmitters also makes for more moving components due to the incoming and outgoing beams not following the same path. The feedback is also not obvious and might have to resort to open loop control.

The above systems each have good and bad aspects for the purposes of this work. As a whole, the optical paths are not completely shared between the incoming and outgoing beams and in the work here the path difference should be reduced to near zero to maximize the sharing of components. There are also numerous concessions on polarization and wavelengths so removing these would be beneficial.

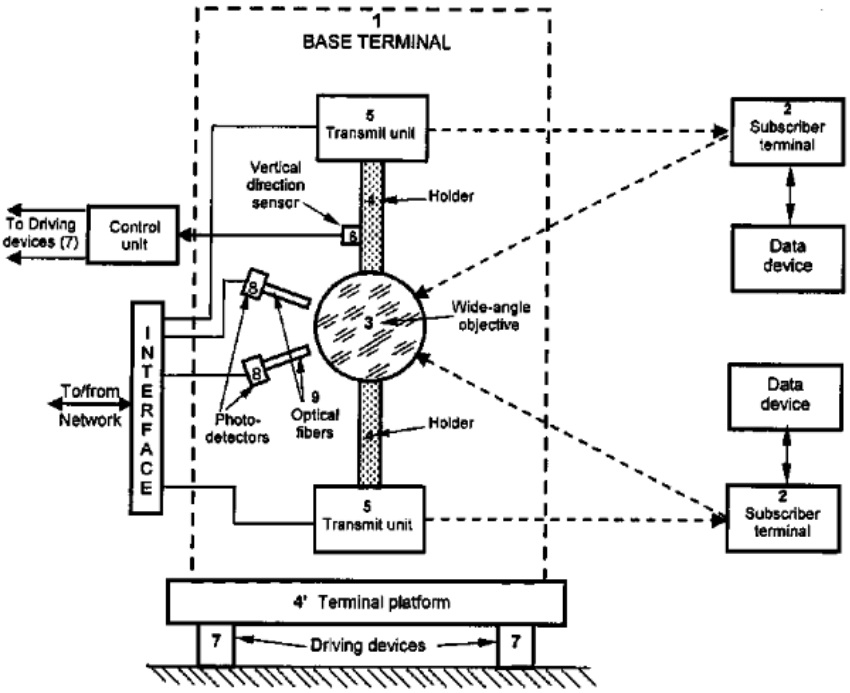

Figure 2.6: Illustrated is the patented design of a multi-beam system produced by Vladimir G. Sidorovich, Aleksei A. Leshev, Valery V. Ragulsky, Mikhail A. Sadovnikov, Mikhail V. Vasiliev, Vladimir P. Vasiliev[53]. The transmitter unit and the photo detector receiving units are separated. The transmitter being controlled separately form the receivers. The sphere acts as a single component telescope through which all the received beams pass.

The use of static transmitters and receivers would also reduce the flexibility and number of applications substantially however these should not be directly actuated but beam steered. Furthermore, sharing components for both the telescope and the optical trains would be preferable. All the above problems will be considered and tackled later in the work.

2.2. Single Beam Optical Communications

There are also numerous important design aspects which can be gained from studying the single beam optical communication systems. The problems associated with multi-beam handling will not be present. However, these designs have solved other problems which might not have been highlighted before.

Where multi-beam designs are scarce, the same cannot be said for single beam systems. There exist numerous applications which utilize laser communications. Terrestrially, applications from indoor communications, trains and building to building all the way up to deep space communications[31]. The performance and security aspects of free space optical communications are often very alluring compared to radio communications, however are also increasingly more accessible to the public. RONJA is an open source point to point laser communications system, where users are able to build their own laser communication terminals and transmit 10 Mbps over a range of 1.4 km[35]. These have been setup all around the world with success.

Communications through the atmosphere comes with its own issues. Aside from attenuation through absorption, the wavefront distortion due to turbulence and subsequent density variations can be so severe as to cause significant distortion and lead to its own attenuation. To solve these problems, the use of adaptive optics corrects the wavefront distortion and can lead to significant improvements in turbulent conditions[31]. Particularly the systems for sub-aperture wavefront correction devices, such as deformable mirrors, are interesting for multi-beam steering. This is due to their small size and arrays for micro mirrors.

For single beam communication systems in space there has been significant advancements in increasing the data rates to accommodate ever increasing data rate requirements. There now exist a

plethora of different terminals which have flown in space with many more coming in the near future[65].

A brig driver for increased data rates between satellites and ground are the Earth observation satellites. The European Data Relay System (EDRS) includes a duplex laser communication module installed on the GEO satellites. As the names suggests, it relays data for low Earth orbit applications by acting as a ground station[24]. The terminal is based on the LCT 135 by TESAT[58] and weighs around 50 kg with a power consumption of 160 W and a size of 60x60x60 cm[24]. The power transmitted is around 2.2 W and it has a telescope diameter of 13.5 cm. It is also capable of achieving 1.8 Gbps over in excess of 45,000 km[6]. Note that the system was limited to 1.8 Gbps but could perform as high as almost 5.5 Gbps. The laser terminal is hence capable of communicating at large distances and high data rates. It is illustrated in Figure 2.7.

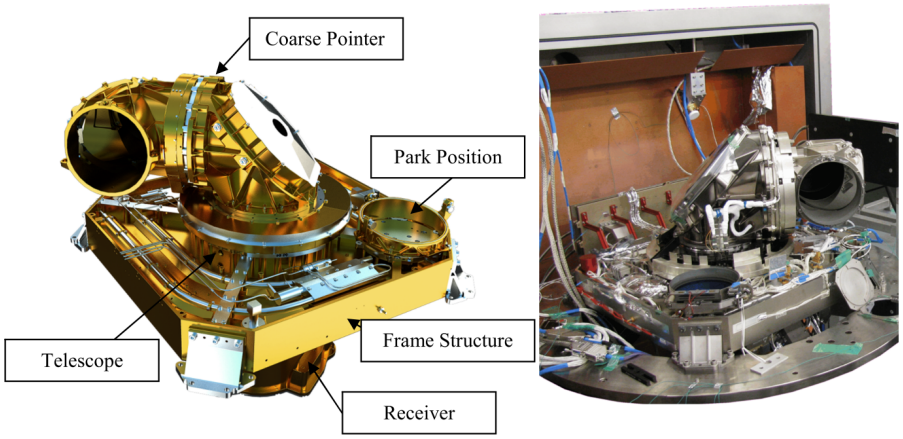

Figure 2.7: Illustrated is the laser communication terminal as used on the EDRS as illustrated in figure 2 on page 82460D-3 in ”Laser communication terminals for the European Data Relay System” by Knut Böhmer, Mark Gregory, Frank Heine, Hartmut Kämpfner, Robert Lange, Michael Lutzer and Rolf Meyer[6]. Illustrated is the coarse pointing system which points in the rough direction to the target through the use of a multi-articulated arm. The telescope is behind the coarse pointing system and contains a fine pointing mirror[24].

The pointing system consists of coarse and fine stages. The coarse pointing stage/system in the form of numerous articulated arms in which there are optical elements which re-direct the light into the telescope. This has the benefit of reducing the angular reach of the fine pointing system and also allows the telescope to have a narrow FOV. However, in this case the prospect of multiple targets would not allow for the system to narrowly point. The feedback is provided by a point and tracker and given to all the pointing systems as well as the coherent detector. The later can compensate for Doppler and indicates that these corrections can be done in the system it self.

The system is duplex and uses the same telescope for both incoming and outgoing beams as well as fine steering mirrors. These are split through the use of different polarization and frequencies. This would limit the ability for wavelength division multiplexing and polarization modulations, however that is not the problem in this case. These do have the benefit of not having to split the beam powers. The transmitter produces a seed laser and is amplified using an optical power amplifier. This indicates the use of a Master Oscillator Power Amplifier (MOPA) configuration, which combines high performance modulation (which tends to not be efficient) and efficient power amplification. This substantially improves power efficiency of the overall system when compared to a transmitter purely based on a Master Oscillator.

The use of better modulation and atmospheric compensation can improve the system substantially. A relatively similar high performance system launched later, called the Micius Coherent laser Communication Demonstration (MCLCD)[13], showed this. It did reach 5.12 Gbps between the Micius Quantum Science Satellite in LEO and a ground receiver without the need for atmospheric compensation. It too uses MOPA architectures. The closer LEO distances also aids with substantially reducing the free space losses when compared to EDRS’s GEO orbit.

The more robust and complex modulation technique used was DPSK with the demodulation occurring in large part in free space illustrated in Figure 2.8. It illustrates that receivers can be used both inside and outside of fiber hardware. However, it would likely take up more space and weigh more,

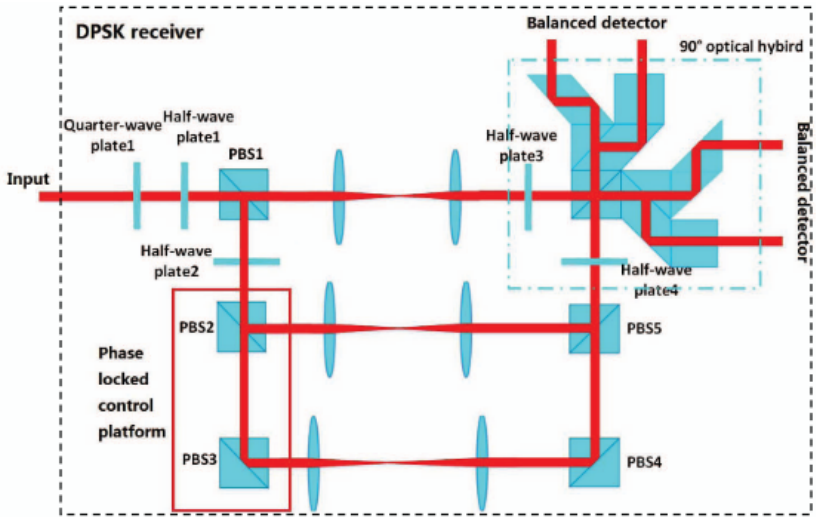

Figure 2.8: Illustrated is the DPSK receiver for MSLCD found in Figure 3 on page 261, in ”5.12Gbps Optical Communication Link Between LEO Satellite and Ground Station” by Weibiao Chen, Jianfeng Sun, Xia Hou, Ren Zhu, Peipei Hou, Yan Yang, Min Gao, Linjun Lei, Kedi Xie, Minjie Huang, Rui Li, Huaguo Zang, Yuan Wan, Enwen Dai, Yueli Xi, Wei Lu, Sentao Wei, Lei Liu and JiaWei Li[13]. The exact working and purpose of each element is out of the scope of this chapter. However, it illustrates the use of physical optical elements in the demodulation of DPSK modulation.

at least that is the impression obtained from the amount of glass present in Figure 2.8. The research team also concluded that the instability due to atmospheric effects made the link unusable and future improvements would include adaptive optics[13]. For a multi-beam system, the use of deformable mirrors for each link could result in large bulk. Hence, in line adaptive optics capabilities would be very welcome.

There are also more numerous examples of designs in space as well. Figure 2.9 compares 4 of them. As can be seen, the performance of the system is not necessarily a function of the module size alone. This is most obvious when considering OPALS, however, the reason for this will be discussed.

	Lunar Laser Communications Demonstration (MIT LL)	Optical Payload for Lasercom Science (JPL)	Optical Communication and Sensor Demonstration (The Aerospace Corporation)	Nanosatellite Optical Downlink Experiment (MIT)
Data Rate	622 Mbps	50 Mbps	40 Mbps /300 Mbps	10 Mbps / 100 Mbps
Tx Power	0.5 W	2.5 W	6 W	200 mW
Orbit	Lunar	LEO (ISS)	LEO	LEO
Payload mass	30 kg	180 kg	2 kg	1 kg
Beamwidth	2.5 urad	~0.01 deg	0.30 deg	1.3 mrad
Ground station	White Sands	OCTL 1-m	MOCAM / MAFIOT	PorTeL / OCTL

Figure 2.9: An overview of the different laser communication modules taken from slide 22 in the ”Laser Communication with CubeSats” presentation given by K. Cahoy[8].

What Figure 2.9 shows is that data rates of a few 100 Mbps should be possible for relatively little power. This is understanding that these systems are supposed to be used in LEO, with the Lunar Laser Communications Demonstrations (LLCD) as exception. Second, the Tx power is not the total power consumed by the transmitter but in the case of NODE referrers to the modulator power of the seed laser.

What it shows is that small and high performance laser communication modules are possible and the designs should be investigated further.

The laser communication terminal produced by MIT for the Nano Satellite Optical Downlink Exper-

iment (NODE)[32][9][8][33][45][14] is depicted in Figure 2.10. The system shows that small modules can also perform admirably. What is shown is that the use of a optic fiber to transport the laser to the optimal location makes the system easy to organize. Furthermore, the electronics behind the transmitter can be made high performance and compact. What is not illustrated, is that the satellite it self is used as a coarse pointing system with the FSM acting as fine steering.

The system is not duplex implying that this aspect cannot be considered. Currently, the uplink is only used to track the spot and give feedback to the FSM and coarse pointing system. Furthermore, a multi-beam system would have to serve multiple targets in the FOV implying a coarse pointing system cannot be done using the whole satellite or terminal as a whole. The FOV by the FSM is also limited which would restrict the applications for multi-beam terminals.

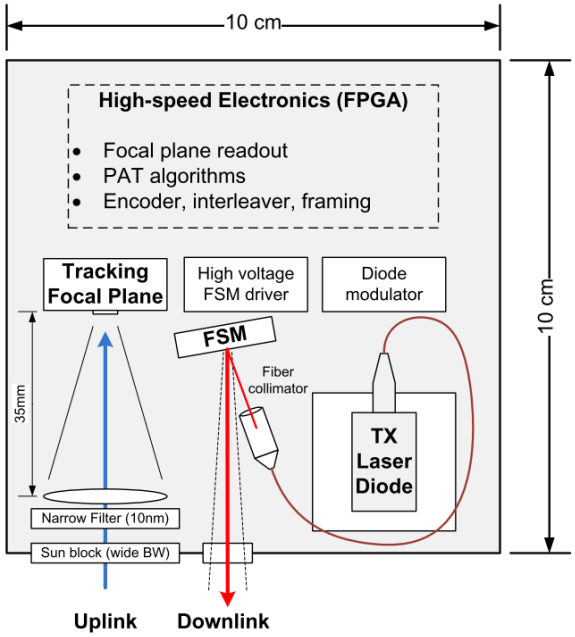

Figure 2.10: The design illustrated shows the laser communication terminal for NODE from MIT, in the paper ”Design of a Free-Space Optical Communication Module for Small Satellites” by Ryan Kingsbury, Kathleen Riesing, Prof. Kerri Cahoy on page 3[33]. Shown is that the electronics are connected to a laser diode transmitter which delivers the light via an optic fiber to the fiber collimator. The beam is then reflected off an FSM which finely steers the beam to target. The uplink consists of a number of filters after which a lens focuses the incoming light onto a tracking focal plane.

The method by which the signal beam is generated becomes more clear when considering Figure 2.11. The system uses an Master Oscillator Power Amplifier (MOPA) configuration which utilizes high performance and low efficiency modulators or Master Oscillators which seed a small signal into the fiber amplifiers. The fiber amplifiers, powered by pump lasers, are higher efficiency and hence the overall power efficiency is improved. This configuration is therefore high performance with a reasonable efficiency method for transmitting.

Alternatives would be using the CCD or a photodiode directly. These have drawbacks and benefits as well, however where lower performance compared to the MOPA[33]. However it also benefits due to a potentially smaller footprint and optical train.

NASA’s Optical Communication and Sensor Demonstration (OCSD) program too is a small satellite laser communication module[29]. The mission was meant to demonstrate both laser communication as well as proximity operations between 2 satellites. Considering the laser communications design, a different approach was taken compared to all the previous designs discussed. Instead of using a FSM, the satellite uses coarse and fine attitude determination to point the whole spacecraft into the right direction. As was determined before, it would not be possible to do this for a multi-beam system.

This design does have an extensive fiber based MOPA schematic shown in Figure 2.12. It can be seen that the power amplifier used is Yttrium based and not Erbium. The reason for this is the target wavelength 1064 nm instead of 1550 nm, which is more efficiently generated through an Yttrium fiber amplifier. What more is that there is extensive analysis on the thermal properties of the system. It

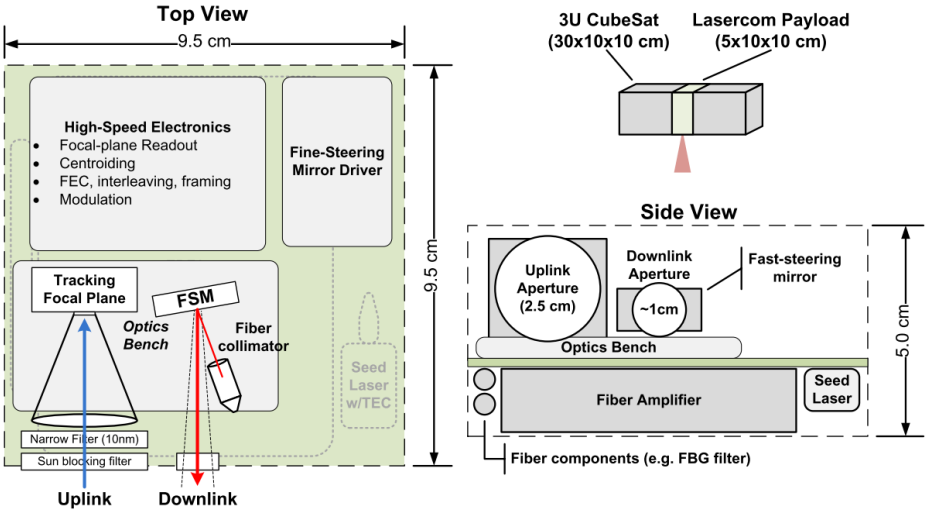

Figure 2.11: Illustrated is the transmitter design of NODE as presented on page 71 of "Optical Communications for Small Satellites" by Ryan W. Kingsbury[33]. The MOPA architecture is used where a fiber power amplifier is used to amplify the signal produced. The fiber amplifier uses multiple loops and hence takes a large portion of the space underneath the system. The seed laser is modulated with the signal generated by the high performance modulator and then amplified by the fiber amplifier. The fiber amplifier is pumped with pump lasers. The modulation power is 200 mW but including the input pump power and modulation power the total goes up to 8-10 W.

showed that even in small modules, the temperatures can be kept under 50 C.

The efficiency of the fiber amplifier is increased by matching the pump wavelength as close as possible to the output wavelength. This is because shorter wavelength photons are higher energy than longer wavelength photons and the conversion between the two are inherent losses. However, in this case it was found that a pump laser wavelength of 975 nm was in fact less efficient and unstable due to hardware constraints. The choice was then to use 915 nm instead. Should fiber amplifiers be used, this wavelength proximity should be kept as close as possible.

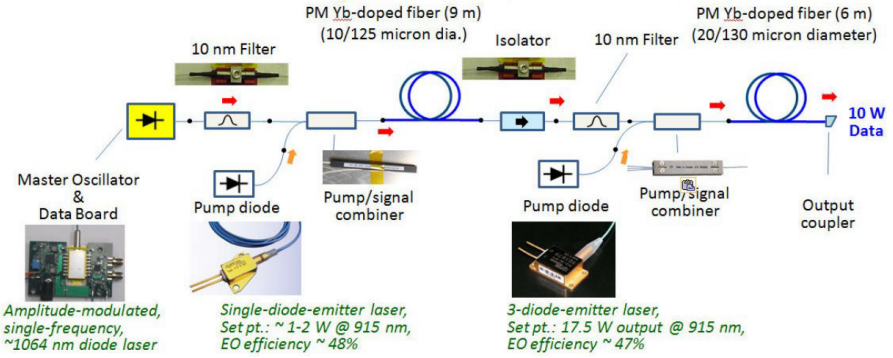

Figure 2.12: Illustrated is the laser transmitter schematic for OCSD, found as figure 4 on page 5 of "The NASA Optical Communication and Sensor Demonstration Program: An Update" by Siegfried W. Janson and Richard P. Welle[29]. It shows that the Master Oscillator produces a seed signal which is then amplified twice by 2 Yttrium doped fiber amplifiers. The first stage being 2 W and the second stage being 17.5 W. Each stage is isolated and the output laser power is 10 W.

The Optical PAyload for Lasercomm Science (OPALS) was a module installed onto the ISS to test optical communications[41][1][74]. It was designed to have a downlink of around 30-50 Mb/s with its current modulation. Due to the system being used on the ISS, it can be relatively heavy and power intensive compared to the other systems discussed. The mass is 222 kg in total, which includes the base and interface. The system also consumes a few 100 Ws at numerous voltages. The system life was also short due to it being a demonstration. The laser used 2.5 W and produced 1550 nm light.

A rendering of the system is shown in Figure 2.13. The electronic hardware used was not tested for

the space environment and instead kept under an atmosphere in an oil drum sized container. The expected life was on the order of a few months. The laser module was ruggedized for space. The system was also not duplex or built for multiplexing. Regardless, the system passed through all qualification tests.[74]

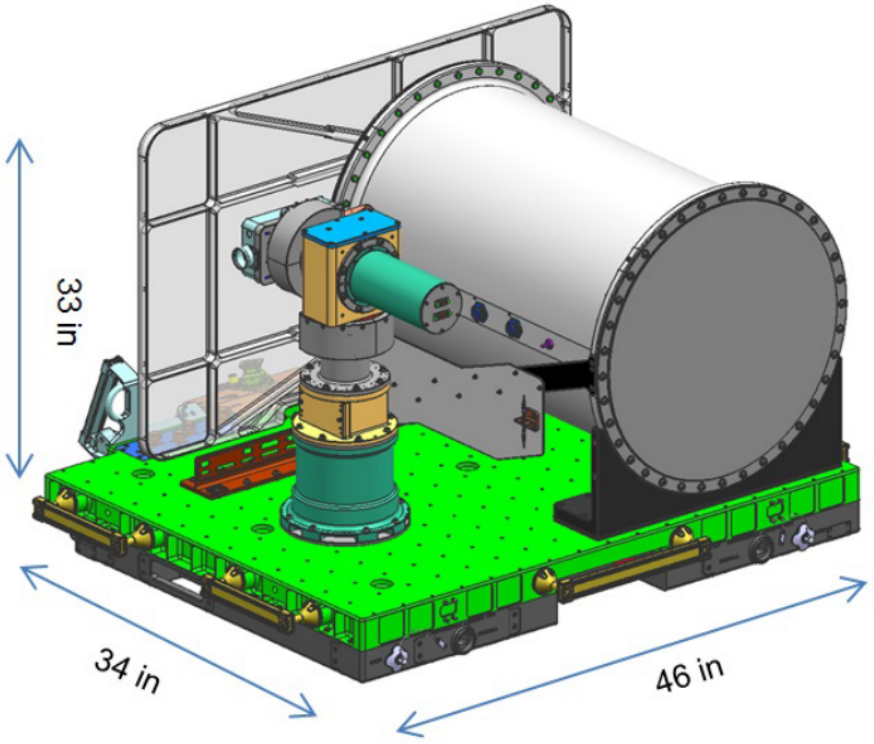

Figure 2.13: Render of the OPALS system found in figure 2 on page 3 of "OPALS: An Optical Communications Technology Demonstration from the International Space Station" by Bogdan V. Oaida, Matthew J. Abrahamson, Robert J. Witoff, Jessica N. Bowles Martinez, Daniel A. Zayas[41]. From bottom left is the platform which interfaces with the ISS. In the center of the figure is shown the laser on a mount next to a drum shaped cylinder. The Drum shaped cylinder contains all the fiber optics and electronics.

There can hence not be much said about the hardware design and layout due to the unique circumstances of the mission. During the operations however, the relative trajectories and hence the laser pointing was pre-programmed and then where subject to a control loop. The ground receiver contained a beacon which was detected by OPALS via an 8 bit CCD. This resulted in precautions having to be taken against background noise. This was particularly important considering the Sun geometry and clouds. These problems where overcome and the system was capable of acquiring an optical link numerous times. The low detection thresholds tended to result in higher reliability. Furthermore, there was no feedback from the gimbals of the laser, implying that this part of the pointing was done open loop.[1]

The feedback loop using even low 8 bit range the CCD will give substantial design flexibility and will be used. The system should also be made to work using lower threshold beam detection for better reliability. Furthermore, some additional features can be included into the system which will be designed and discussed in this work. In fact, that the steering it self is also closed loop so that offsets are corrected for over time. There should also be precautions taken to prevent over exposure to sunlight.

2.3. A Small Note on the Literature Review

A much more broad literature review was already performed during the literature study[56]. **The literature study can be found attached at the end of this report**, the parts for the thesis planning and details relating to current situations have been omitted because it is irrelevance to this work. In this literature review numerous items where already discussed and some aspects analyzed. There are

also extensive derivations and analysis of multiple topics including, but not limited to: fiber coupling, turbulence, link budgets, etc... These derivations will be referred to in this work when relevant, but will not be discussed here. The literature study also performed extensive analysis on different steering mechanisms. The trade-off performed during this work is briefly explained in Appendix E. This section will briefly discuss origins of the major requirements which drive the different technology choices.

First, numerous requirements for the system and different system design aspects where created. These are stated in Appendix C. The general design requirements mainly concern the terminal performance characteristics. They where derived from the previous laser terminal designs, such as those discussed above, to be comparable in both performance and flexibility in its application.

Then there are numerous different pointing system requirements which are based on analysis of atmospheric effects and fiber coupling. These analyses will be performed again for the given situation, however the ones specified were derived extensively and considered in the more general context of laser communication.

A small selection of requirements pertaining the selection of technology is shown in this section. Starting with the general requirement **GD-CR-004**:

GD-CR-004: The terminal shall have a FOV of 90 deg in total or the Earth + 1000 km either side (which ever comes first).

This requirement was derived to allow for a wide range of different applications for the terminal. With such a wide point of view, applications such as both far and near Earth communications can be realized. This is because the number of targets can increase with a greater range of location flexibility.

The wide FOV will come with challenges in the telescope design. The light must be picked up, without distortion, from a wide FOV. Traditionally, telescopes tend to restrict their FOV as much as possible for optimal imaging and would not accommodate these angles or cause large distortion. A different approach should therefore be taken.

GD-CR-014 directly influences the technology selections for beam steering, feedback loops and transceiver.

GD-CR-014: The terminal shall be able to produce duplex communications with all targets.

This is a very important and driving requirement. Making the system duplex increases the number of beams per target by 2 compared to a system with single directional communications. It implies that the feedback loop together with the overall system design for beam steering must be able to handle these beams. The output beam must be guided directly onto target and the exact location of the target should be determined as well. This poses strict conditions on the accuracy of the system.

For the transceiver it implies that the system must be able to handle both incoming and outgoing beams to both receiver and transmitter (hence transceiver). The design of the transceiver must therefore be doing in direct conjunction with the overall system design to accommodate duplex communications.

GD-CR-001 and **GD-CR-015** show requirements which might be unassuming at first. However, in fact drives the technology selection for the beam steering mechanism.

GD-CR-001: The terminal shall be designed to handle 10 targets.

GD-CR-015: The terminal shall be able to sustain a 10 second link without interruptions.

The they drive the selection of the steering mechanism and general system design for a number of reasons. Firstly, the number of targets are proportional to the number of beams which have to be handled. This implies that the area of the mechanism as well as the number of steering surfaces are crucial for accommodating a high number of beams.

As a result, the mechanism chosen should accommodate the number of beams while simultaneously being able to separate them from each other for a duration no shorter than 10 seconds. This implies that the proximity of the beams when the targets are moving close to each other should be handled for as much and long as possible. The system should also be fast enough, having to be able to correct for jitter and wander.

Furthermore, the feedback loop will be designed to be able to minimize the number of beams required for tracking and steering while still accommodating beam tracking in high enough resolutions. This must be done while maximizing the number of targets and maintaining flexibility. If this is opti-

mized, the system performance will be greatly increased and handle more beams without increasing SWaP. The system should also be able to identify, track and steer multiple unique beams, placing constrains on the spot/beam trackers.

For future flexibility these requirements area also indicative. The use of Adaptive Optics (AO) for turbulence correction might not always be possible at the target. If AO could be implemented in the multi-beam terminal the applications and performance will be dramatically increased for targets inside an atmosphere. For this however, a very high resolution and high speed beam steering mechanism with sub-beam diameter wavefront correcting abilities should be made possible for each beam.

The performance and resolution of the beam steering mechanisms and spot trackers are hence quite high priority. Other requirements which are crucial for selecting the transceiver technology are **GD-CR-008**, **GD-CR-016** and **RxTx-PA-005**:

GD-CR-008: The terminal shall not consume more then 500 W (50 W per link/beam).
GD-CR-016: The terminal shall be able to communicate with at least 40 Mbps per link at its Shannon Limit for OOK modulation.
RxTx-PA-005: The optical power amplifiers shall not use more power then 60W per link.

These requirements are primarily instated to limit the SWaP of the transceiver. The transceiver should hence be low power and high performance. These requirements limit the performance ranges and will hence drive the technology choice for the transceiver. It will also force the consideration of using COTS technologies outside of the current hardware flown in space.

Furthermore, the data rate and power was chosen to ensure competitiveness with single beam designs for small satellites. As shown in Figure 2.9 and other designs, the general performances of the modern medium to high-end single beam designs for small satellites are on the order of 40 Mbps and 50 W. The modulation is less important, however was chosen to be OOK to ensure the system is comparable. The system should also be able to handle other modulations, through which the limits will increase.

2.4. Summary and Conclusion

Previous designs have illustrated a multitude of different ways to achieve both multi-beam and single beam laser communication. For sustaining multiple links can be done using dynamic and flexible lenses, steering using mirrors or have no steering at all. There are also numerous different philosophies with regard to maintaining links. These include sharing one beam and splitting time vs continuous connections.

The use of steering mirrors are seen as more feasible due to their TRL and ability to maintain constant communications. The result is a system which does not depend on the number of links for its data rate capabilities as well as not being able to perform adaptive optics. Furthermore, not using steering would imply the use of very large and extensive fiber arrays with the relevant fiber optics and electronics. This is also less than ideal and likely less efficient due to circular packaging, the number of fibers, losses in fiber coupling, inability to perform adaptive optics, etc...

Furthermore the separation of the up and down links, embodied as incoming and outgoing beams, was often done by splitting based on polarization and/or wavelength. This would limit the modulation and multiplexing techniques and hence it would be interesting to remove this barrier. Furthermore, the sharing of components could be improved as well by increasing the distance followed on the same path.

The larger single beam terminals tend to use 2 sets of pointing systems, namely a coarse and a fine. This however would potentially not be possible for multi-beam applications, due to the system having to accommodate multiple targets in multiple places in the FOV. The second set usually consists of a fine steering mirror, which would have to be incorporated for every beam in the multi-beam terminal. These most likely would be in the form of SLM's or MMA's due to their superior resolution and speed respectively.

What more, the single beam terminals have shown the technological basis for high performance MOPA architectures and fiber hardware. These systems are preferred due to the seed laser being able to be generated by an inefficient but high performance Master Oscillator and the resulting amplification compensating by being higher efficiency. This technology can also be included into fiber hardware

which has a proven track record in space, good footprint and has a huge variety of components due to its use in internet. However, alternatives might be better and this should be delicately trade-off'ed. CCD's and photodiodes might have better SWaP, but require more optics to accommodate demodulation.

3

Propagation Methods and Models

The design of a multi-beam system requires verification of its working and ability to steer multiple beams to requirements. Visualization and simulation is often the best way to investigate different design aspects and choices. In order to prove the ability to control multiple beams by using a Micro Mirror Array (MMA), a Spatial Light Modulator (SLM) or other steering mechanism, through a potentially complex optical train would require accurate and representative Models. More over, different aperture sizes and shapes generate different diffraction patterns which can have a large effect on the working of the system.

Due to these reasons, it was chosen to first develop a modeling method, to then subsequently use during the design process in later chapters.

A model algorithm must be constructed that can find these effects and generate an accurate representation. This is done by propagating and combing the fields in accordance with the Huygens-Fresnel principle. Each point on the wavefront it self produces spherical waves in an isotropic linear propagation medium. When all the spherical waves from each point are combined, it produces the most accurate approximation of the wavefront and hence beams. For this, 2 main methods where chosen; Fresnel and transfer function based propagation.

First these propagation techniques are briefly discussed for those unfamiliar with them. Then, implementation of the principles into a model requires adaptation to the model tool, which in this case is Matlab. Subsequently the model algorithm is discussed. The model algorithm is then verified by comparing different propagation between Gaussian beams, transfer function propagation and Fresnel propagation. Lastly, the models are validated by performing diffraction experiments and then comparing real life diffraction patterns with simulation results. There will then be a conclusion and summary of the chapter.

3.1. Propagation Techniques

This section shall discuss the principles later used in the model algorithms, to give insight for those not familiar with the general principles behind the model. This will be done through the use of illustrations and small derivations. However, for further and more in depth understanding, it is recommended to consult textbooks and lecture materials on the subject.

3.1.1. Huygens-Fresnel Propagation

Disturbances in any medium result in a propagation of the disturbance through the medium. The propagation it self is also a disturbance in the medium and hence each point where the propagation travels through it self generates and propagates disturbance. The aggregate of these secondary propagations is equivalent to the propagation of the initial disturbance. The superposition of these can be considered the wavefront. This is in essence the principle behind the propagation of EM waves.

This is encapsulated in the Fresnel-Huygens principle. According to Hecht[23], the Huygens-Fresnel principle can be described as follows:

> ”Every unobstructed point of a wavefront, at a given instant, serves as a source of spherical secondary wavelets (with the same frequency as that of the primary wave). The amplitude

> of the optical field at any point beyond is the superposition of all these wavelets (considering their amplitudes and relative phases)." - Optics Fourth Edition, by Eugene Hecht, Chapter 10, page 445.[23]

This principle can be visually illustrated. Figure 3.1 illustrates a spherical wave depicted in 2D. The wave propagates outward from a point source. Multiple point sources can be combined/super imposed/interfered to form a wavefront as shown in Figure 3.2.

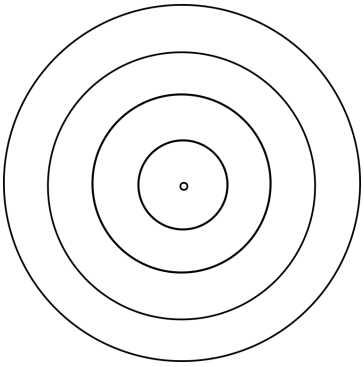

Figure 3.1: Illustrated is a spherical wave originating from a point and radiates outward.

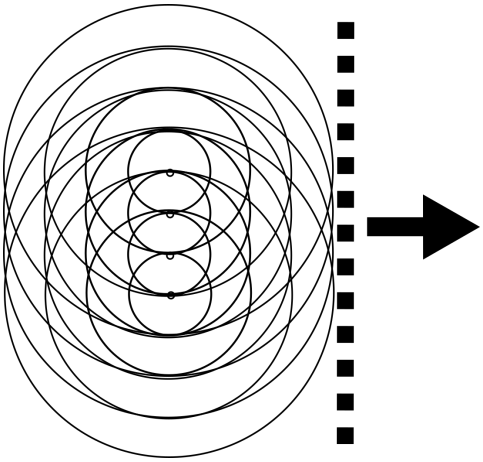

Figure 3.2: Illustrated is a series of spherical wave point sources which interfere to produce a wavefront. The wavefront is indicated why the dashed line, with the direction of travel indicated by the arrow.

There is a problem with this principle. The wavefront it self can be expressed as a series of point sources. If these point sources radiate outward symmetrically, the direction of the wave is lost. It would imply that there should be a backwards propagating/traveling wave observed as is illustrated in Figure 3.3. This is not the case however. This phenomena would also clash with other theories and descriptions of the light phenomena such as photons, information, momentum, etc...

Analysis by Kirchhoff[23] produced a solution to this in the form of oblique spherical waves, shown in Figure 3.4 and Figure 3.5. This solves the problems of back-propagating waves. Note, that the principle only concerns secondary waves, there can still exist uniformly/symmetrically radiating point sources generating spherical wavefronts. In that case, the waverfronts are described by oblique secondary wavelets which are arranged in a sphere. This is illustrated in Figure 3.6.

These phenomena lend themselves to visuals and complex mathematical notation. The electric field amplitude of a point at a distance r from spherical and oblique wave source can be expressed as follows:

$$E_I(r,t) = E_p(t)K\frac{e^{jkr}}{r} \tag{3.1}$$

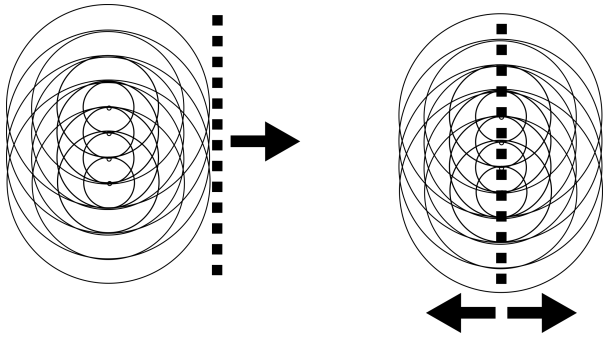

Figure 3.3: An illustration of the symmetric propagation problem associated with a perfect spherical secondary point sources. Left is shown how a number of point sources can produce a wavefront. Right is shown that when the wavefront it self is expressed as symmetric point sources, that the wavefront would travel in both directions. Hence, there would be a wavefront which back-propagates in the opposite direction of the original wavefront. This, however, is not observed in practice.

Figure 3.4: Illustration of an oblique spherical wave, with the color depth an illustration of the amplitude of the wavefront. As can be seen, the majority of the wave energy is propagated to the right of the wavefront, while none of the energy is propagated to the left.

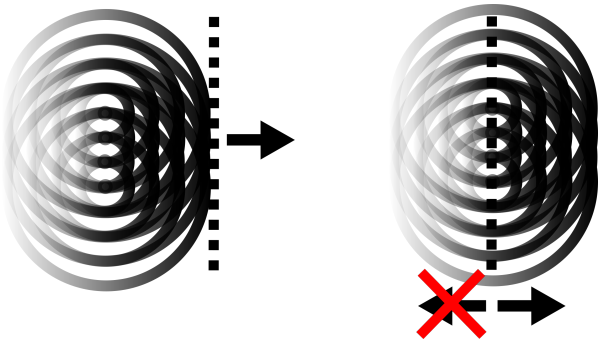

Figure 3.5: Wavefront synthesis using oblique waves. As can be seen, the wavefront (depicted by the dashed line) has the same direction of travel as the original wavefront both as a result of primary and secondary waves. This is different compared to Figure 3.3, where uniformly/symmetrically propagating spherical waves produced a wavefront traveling in 2 directions.

Where E_p is the electric field of a point which radiates spherically and is a function of time as it is periodic. Furthermore, K is the Kirchhoff's obliquity factor, r the spatial position relative to the radiating point, k the wave number ($2\pi/\lambda$), with λ being the wavelength and E is the resulting electric field at that location. The obliquity factor can be described as follows:

$$K = \frac{1}{2}(1 + cos(\theta)) \tag{3.2}$$

However, the obliqueness is not a significant effect at small angles θ.

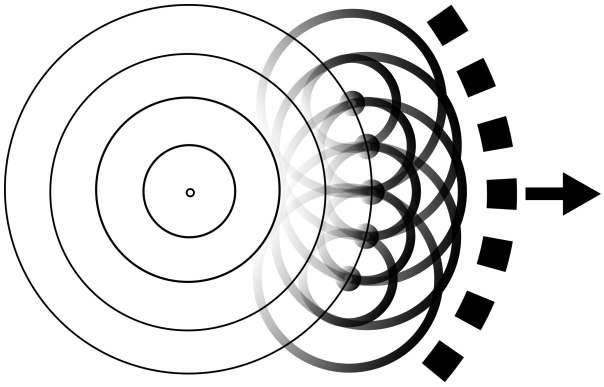

Figure 3.6: Spherical wavefronts from uniformly and symmetrically radiating sources can be expressed in oblique secondary wavelets. The wavefront from the secondary waves is illustrated by the dashed line, with the direction along the arrow. This is equivalent to the original point source wavefront illustrated by the thin lines!

3.1.2. Fresnel Propagation

When the propagation of a wavefront is analyzed, the dynamics of the wavefront must be understood and expressed in the propagation. For example, if the source is a point radiating uniformly like the one depicted in Figure 3.6, then the phase, direction and strength of the secondary waves depend on their relative distances to the source. When this wave is diffracted and propagated through an aperture, the amplitude and distribution of the field in the aperture is a function of this. Similarly, if a plane wave is incident on the aperture, the distance from the source of the plane wave does not matter. In this work, the exact amplitude and distribution of the electric field in the aperture is unknown. There is hence an assumption made that each point/pixel is independent, a plane wave incident on "ds_P" and only through their combination is the field propagated.

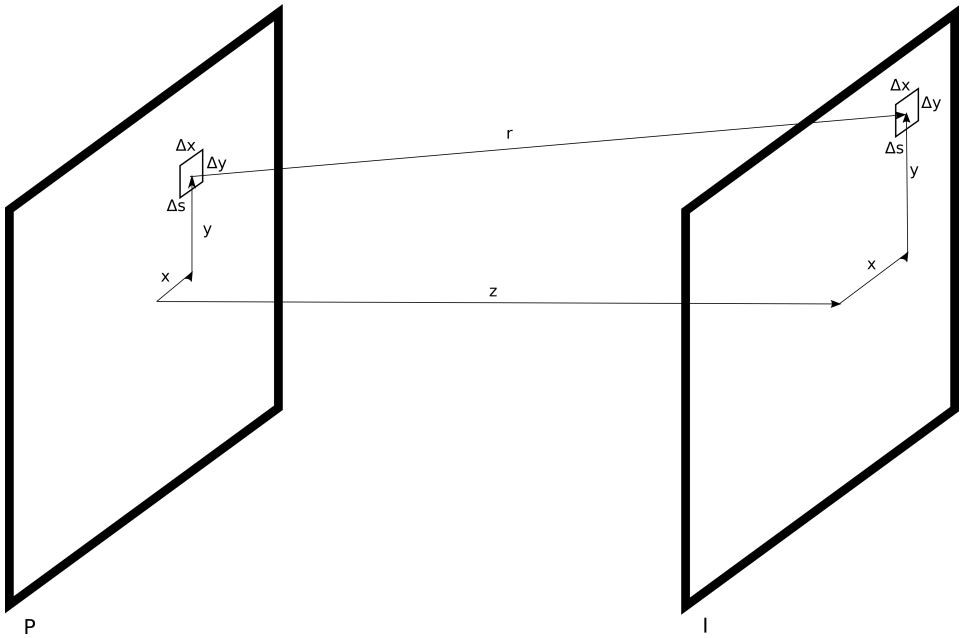

Figure 3.7: An overview of the coordinate systems and notation. The waves travel from plane P to plane I in a oblique spherical wave from a given ds_P, located at x_P and y_P. The goal is to aggregate the waves over the whole plane. In this case, the field coming from plane P has been propagated from an other source, namely the communication targets. Hence, the waves from ds_P are considered secondary waves and hence oblique. The wave propagates over distance r to ds_I on the imaging plane, located at x_I and y_I.

The simulation is performed in a computer and is hence made of finite and discrete segments/pixels. The situation for a small segment is depicted in Figure 3.7 and Figure 3.8. These are referred to as s_P and Δs_I on the projection and imaging planes respectively. Each small segment produces an electric

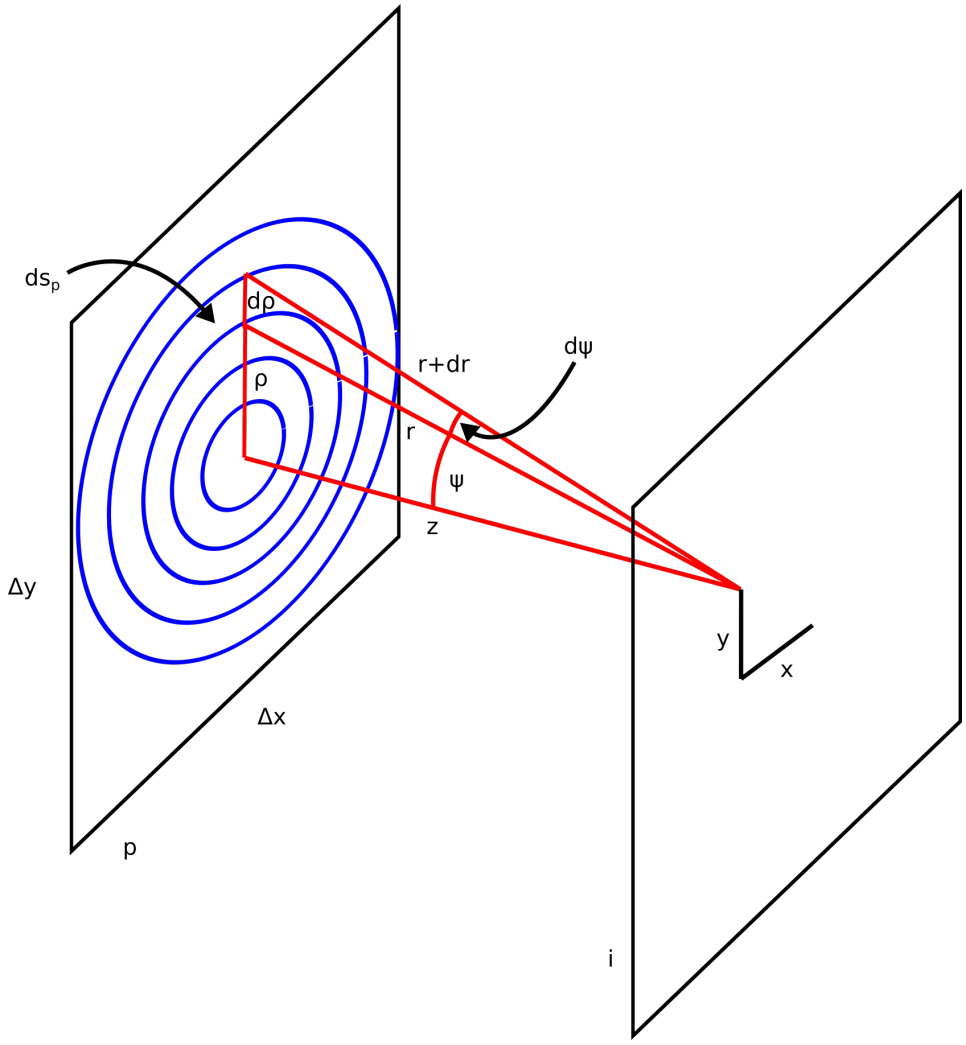

Figure 3.8: Illustration of the diffraction of one pixel p (left screen) on the imaging plane i (right screen). The the pixel has a number of zones, ds_p, at the same distance, r, from a given point on the imaging plane. These are indicated between the blue circular lines. r is composed of the horizontal distance, z, and ρ is the radial distance on the pixel plane. The angle swept by this is ψ. Note that plane i is the same size and shape as plane I in Figure 3.7, while plane p is encapsulated by the pixel of Δ s.

field, E_i, on the imaging plane which is superimposed with the other pixels on plane P to produce an overall field into E_I. Each has a plane wave electric field per unit area of E_{AP}, however only the input field, E_P, is known. The segment on the projection plane is relatively small, but can be subdivided to smaller segments ds_P and its effect on the imaging plane is denoted by dE_i, can be expressed as a planewave as follows:

$$dE_i = E_{AP} K \frac{e^{jkr}}{r} ds_p \tag{3.3}$$

$$E_i = E_P Q K e^{jkr} \tag{3.4}$$

Where, $E_P Q = E_{AP}$. What is unknown is the factor Q to correct the input data with the output data. The small area, ds_p, can be expressed in terms of the small angle $d\psi$.

$$ds_p = 2\pi\rho d\rho = 2\pi r sin(\psi) r d\psi = 2\pi r^2 sin(\psi) d\psi \tag{3.5}$$

The mixed variable function of ψ and r can be substituted as follows:

$$\frac{z}{r} = cos(\psi) \longrightarrow -\frac{z}{r^2} dr = -sin(\psi) d\psi \tag{3.6}$$

Assuming the distance between plane P and I is large compared to the size of plane P and hence ρ, leads to:

$$ds_p = 2\pi r^2 \frac{z}{r^2} dr = 2\pi z dr \approx 2\pi r dr \tag{3.7}$$

Inserting this into Equation 3.3:

$$dE_i = 2\pi E_{AP} K e^{jkr} dr \longrightarrow E_i = 2\pi E_{AP} K \frac{e^{jkr}}{jk} = \frac{\lambda}{j} E_{AP} K e^{jkr} \tag{3.8}$$

Comparing this to Equation 3.4 to find Q:

$$\frac{\lambda}{j} E_{AP} = Q E_P \longrightarrow Q = \frac{j}{\lambda} \tag{3.9}$$

$$E_i = E_P \frac{j}{\lambda} K e^{jkr} \tag{3.10}$$

This equation describes a wave who's amplitude is independent on the distance. This is expected, as the pixel was assumed to consist of a plane wave and its amplitude is independent of the distance it travels. However, in the aperture, the small pixel will diffract and hence become an oblique spherical wave. Now this spherical oblique wave can be given in terms of the data given, and the whole plane P and I analyzed:

$$dE_I = E_P \frac{j}{\lambda} \frac{e^{jkr}}{r} K ds_P \tag{3.11}$$

Where:

$$r = \sqrt{z^2 + (x_I - x_P)^2 + (y_I - y_P)^2} \tag{3.12}$$

This however, can be approximated through the use of a binomial expansion:

$$r \approx z + \frac{(x_I - x_P)^2 + (y_I - y_P)^2}{2z} \tag{3.13}$$

The inverse of the radius can be approximated further:

$$\frac{1}{r} \approx \frac{1}{z} \tag{3.14}$$

Furthermore, the obliquity factor can be re-written to include these approximations as well:

$$K = \frac{1}{2}(1 + cos(\theta)) = \frac{1}{2}\left(1 + \frac{z}{r}\right) \approx \frac{1}{2}\left(1 + \frac{z}{z}\right) = 1 \tag{3.15}$$

Hence, because of the assumption that the distance between plane P and I is large, the obliquity of the wave can be ignored. Inserting these into Equation 3.11:

$$dE_I = E_P \frac{j}{\lambda z} e^{jk\left(z + \frac{(x_I - x_P)^2 + (y_I - y_P)^2}{2z}\right)} ds_P \tag{3.16}$$

This can be re-written as follows:

$$dE_I = E_P \frac{j}{\lambda z} e^{jkz} e^{j\frac{k}{2z}(x_I^2 + y_I^2)} e^{j\frac{k}{2z}(x_P^2 + y_P^2)} e^{-j\frac{k}{z}(x_I x_P + y_I y_P)} ds_P \tag{3.17}$$

Integrating this leads to:

$$E_I = \frac{j}{\lambda z} e^{jkz} e^{j\frac{k}{2z}(x_I^2 + y_I^2)} \int_{x_{P0}}^{x_{P1}} \int_{y_{P0}}^{y_{P1}} E_P e^{j\frac{k}{2z}(x_P^2 + y_P^2)} e^{-j\frac{k}{z}(x_I x_P + y_I y_P)} dx_P dy_P \tag{3.18}$$

This is the equation that will be used to produce an approximation of the true diffraction of the radiation on the imaging plane. Note, that this is a slightly different approach and resulting equation

than the one given by Hecht[23] in chapter 10.3. The Equation 3.18 can be further simplified in its notation, as the last term in the integral can be stated in terms of spatial frequency:

$$\frac{k}{z}(x_I x_P + y_I y_P) = \frac{k}{z}x_I x_P + \frac{k}{z}y_I y_P = 2\pi(f_{xI}x_P + f_{yI}y_P) \tag{3.19}$$

Where:

$$f_{xI} = \frac{x_I}{z\lambda} \tag{3.20}$$

Inserting this into Equation 3.18:

$$E_I = \frac{j}{\lambda z}e^{jkz}e^{j\frac{k}{2z}(x_I^2+y_I^2)}\int_{x_{P0}}^{x_{P1}}\int_{y_{P0}}^{y_{P1}} E_P e^{j\frac{k}{2z}(x_P^2+y_P^2)}e^{-2\pi j(f_{xI}x_P+f_{yI}y_P)}dx_P dy_P \tag{3.21}$$

Which is the same form of a 2D Fourier transform:

$$E_I = \frac{j}{\lambda z}e^{jkz}e^{j\frac{k}{2z}(x_I^2+y_I^2)}\mathcal{F}_{2D}\left(E_P e^{j\frac{k}{2z}(x_P^2+y_P^2)}\right) \tag{3.22}$$

This analytical equation is similar to the equations given by Hecht[23], however the approach and the resulting terms at the front are not entirely the same. It is hence required to compare with a second method which has already been verified. Nevertheless, this form of the equation can easily be implemented into a computer model, which will be discussed later. However, a side effect of this approach is that the pixel size increases as a function of distance. This in effect decreases resolution of smaller artifacts in dimensional terms, however encapsulates larger structures. This allows accommodation of focusing the fields on larger components of the design. When lenses are used, the pixel size can also decrease dimension.

This method is hence versatile when moving light between different sized components. However, for consistent pixel sizes it is problematic. The following method will discuss a way to propagate the field without losing resolution.

3.1.3. Inclusion of Lenses in Fresnel Propagation

The implementation of optical elements into the models is required to simulate the whole optical train. The inclusion of the lens changes the phase distribution of the wavefront through changing the refractive index over the wavelengths. This phase change is independent of a given mono-chromatic wavefront. Hence, it can be super imposed on the wavefront. The geometry is illustrated in Figure 3.9.

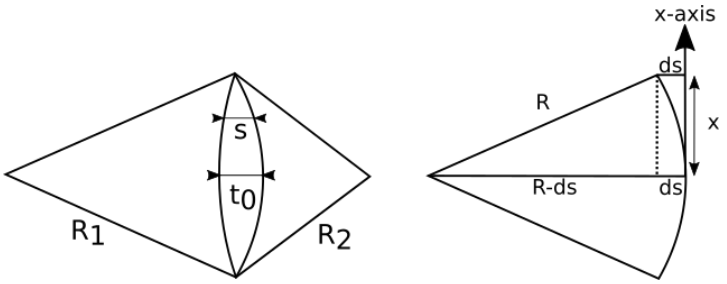

Figure 3.9: Illustration of the free-space propagation distance difference between the axial waves and the off-axial waves.

The distance traveled of the waves through the lens as a function of the location on the surface of the lens is described as,

$$d = t_0 - ds_1 + ds_2 = t_0 - \left(R_1 - \sqrt{R_1^2 - x^2 - y^2}\right) + R_2 - \sqrt{R_2^2 - x^2 - y^2} \tag{3.23}$$

Resulting in,

$$d = t_0 - R_1\left(1 - \sqrt{1 - \frac{x^2+y^2}{R_1}}\right) + R_2\left(1 - \sqrt{1 - \frac{x^2+y^2}{R_2}}\right) \tag{3.24}$$

The terms under the square root can be simplified through approximating thin lenses and the terms as,

$$d = t_0 - R_1\left(1 - \left(1 - \frac{x^2 + y^2}{2R_1^2}\right)\right) + R_2\left(1 - \left(1 - \frac{x^2 + y^2}{2R_2^2}\right)\right) \tag{3.25}$$

This too can be simplified to,

$$d = t_0 - \frac{x^2 + y^2}{2}\left(\frac{1}{R_1} - \frac{1}{R_2}\right) \tag{3.26}$$

Through adding additional free space propagation on the sides of the lens and multiplication with the wave number, $k = \frac{2\pi}{\lambda}$, the wavefront augmentation by the lens can be found as a function of x and y,

$$\Delta\phi = knt_0 - k(n-1)\frac{x^2 + y^2}{2}\left(\frac{1}{R_1} - \frac{1}{R_2}\right) = knt_0 - \frac{k}{2f}(x^2 + y^2) \tag{3.27}$$

The phase field can be superimposed by multiplying by the complex representation,

$$L = e^{jknt_0}e^{-j\frac{k}{2f}(x^2+y^2)} \tag{3.28}$$

The propagation of the projection plane through a lens system can be done in multiple stages. This is illustrated in Figure 3.10. It is assumed that the lens thickness is negligible enough compared to the propagation distances, to not require propagation. Hence, Fresnel propagation only has to be applied on the distances d_0 and d_1, while the superposition of the lens is done between these propagation stages.

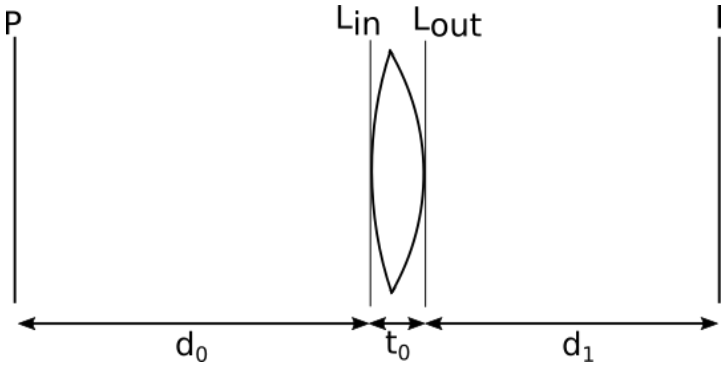

Figure 3.10: One lens optical setup. From left to right; the projection plane, P, emits light, which propagates through free space to the lens input plane, L_{in}, over distance d_0. It then propagates through the lens, over distance t_0, to the output plane of the lens L_{out}. It then propagates through free space to the imaging plane I over distance d_1.

The propagation over d_0,

$$E_{Lin} = \frac{1}{j\lambda d_0}e^{jkd_0}e^{j\frac{k}{2d_0}(x_L^2+y_L^2)}\mathcal{F}_{2D}\left(E_P e^{j\frac{k}{2d_0}(x_P^2+y_P^2)}\right) \tag{3.29}$$

The wavefront augmentation of the lens,

$$E_{Lout} = E_{Lin}L \tag{3.30}$$

The subsequent propagation over distance d_1,

$$E_I = \frac{1}{j\lambda d_1}e^{jkd_1}e^{j\frac{k}{2d_1}(x_I^2+y_I^2)}\mathcal{F}_{2D}\left(E_{Lout} e^{j\frac{k}{2d_1}(x_L^2+y_L^2)}\right) \tag{3.31}$$

Subsequently, the propagation through the lens can be described in one equation as,

$$E_I = \frac{-1}{\lambda^2 d_0 d_1} e^{jk(d_1+nt_0+d_0)} e^{j\frac{k}{2d_0}(x_I^2+y_I^2)} \mathcal{F}_{2D}\left(e^{j\frac{k}{2d_0}(\frac{1}{d_0}-\frac{1}{f})(x_L^2+y_L^2)} \mathcal{F}_{2D}\left(E_P e^{j\frac{k}{2d_0}(x_P^2+y_P^2)}\right)\right) \tag{3.32}$$

In the model these steps can be done one by one or the whole problem can be solved in this one equation.

3.1.4. Fresnel Transfer Function Approximation Verification

The previous method was derived analytically and is a mathematical representation of the propagation. This second method, presented by Voelz[70] on chapter 5 and pages 63 to 64, allows for verification and a method of propagation through which the pixel dimensions remain the same. This is a method by which a transfer function, h, is convoluted with a function, f. The convolution theorem states[23]:

$$g = f \otimes h = \mathcal{F}_{2D}^{-1}(\mathcal{F}_{2D}(h)\mathcal{F}_{2D}(f)) \tag{3.33}$$

Similarly, if the transfer function of the diffraction is known, the electric field can be propagated:

$$E_I = \mathcal{F}_{2D}^{-1}(\mathcal{F}_{2D}(h(x,y))\mathcal{F}_{2D}(E_P(x,y))) = \mathcal{F}_{2D}^{-1}(H(f_x,f_y)\mathcal{F}_{2D}(E_P(x,y))) \tag{3.34}$$

The transfer function, H, can be implemented as the Fourier transform of an impulse function, $\mathcal{F}_{2D}(h)$, or directly as a transfer function H. These are analytically the same, however computationally there are differences. In this case, Voelz[70] indicates that the implementation of transfer functions directly can be used in a wider range of propagation's compared to impulse methods. Hence, this will be used to verify the validity of the model. The transfer function given by Voelz[70] on page 63 is the following:

$$H(f_x,f_y) = e^{jkz} e^{j\frac{k}{2z}(x^2+y^2)} = e^{jkz} e^{j\pi\lambda z(f_x^2+f_y^2)} \tag{3.35}$$

Where:

$$f_x = \frac{x}{\lambda z}, \quad f_y = \frac{y}{\lambda z} \tag{3.36}$$

The subsequent algorithm ignores the e^{jkz} term because it does not affect the spatial structure of the output. Hence, the transfer function becomes:

$$H(f_x,f_y) = e^{j\pi\lambda z(f_x^2+f_y^2)} \tag{3.37}$$

A benefit of performing the calculation in terms of spatial frequency is that the spatial dimensions of the output array can be controlled allowing for higher resolutions. Another major difference between the method presented in Equation 3.22 and this method is the omission of the term $e^{j\frac{k}{2z}(x_P^2+y_P^2)}$. This omission can be done only for larger distances were:

$$z >> \frac{k}{2}(x_P^2 + y_P^2) \tag{3.38}$$

The largest structures in the aperture can only be as larger as the aperture. Taking the furthest points on a 10 cm square aperture from the center and a wavelength of 1550 nm, the following must hold true:

$$z >> 10134 \quad [m] \tag{3.39}$$

This is numerous orders of magnitudes further than can be expected for an optical communication terminal. However, the propagation is particularly important for the multi-beam control mechanism. These tend to consist of SLMs and MMAs, which can be as small as 2 cm or less. Furthermore, the beams incident on the active surfaces themselves, as well as the active surfaces them selves are smaller still. These can be as small as 1 mm or less. When 1 mm is used, the distance becomes more reasonable: z » 4 [m]. When there is little diffraction, such as when a relatively small beam is passed through a relatively larger aperture, it too is relatively accurate.

Hence, this method in theory has a larger error compared to the method presented in Equation 3.22, however maintains a higher resolution in the output array where Fresnel propagation loses resolution. This will be discussed further section 3.2.

3.1.5. Gaussian Beams and Beam Transportation for Verification

Gaussian beams refer to the electric field cross section of the beam being the 2 dimensional Gaussian distribution. This is a solution of the wave equation. Gaussian beams are a simple method by which beam behavior and transport can be analyzed for one of the most common beam profile types produced by laser sources.

Handling and transporting Gaussian beams through lenses and over distances is also relatively straightforward. This method is very ubiquitous and hence it will not be derived. The equations which describe the Gaussian beams are stated in Hobbs page 12-13[25], Verdeyen[68] and in Ram page 7[48].

The field (with the time dependent terms omitted) is described as,

$$E(r,z) = E_0 \frac{\omega_0}{\omega(z)} e^{\frac{-r^2}{\omega^2(z)} - j\left(kz + \frac{kr^2}{2R(z)} + atan\left(\frac{z}{z_0}\right)\right)} \tag{3.40}$$

Where E is the field, r a location on the perpendicular field with respect to the center of the beam, z is the axial distance from the waist, ω_0 the radius of the beam at its waist, $\omega(z)$ the beam radius at location z, z_0 the location of maximum wavefront curvature from $z = 0$, $R(z)$ is the wavefront curvature and lastly, $k = 2\pi/\lambda$ the wave number. z_0 can be expressed as,

$$z_0 = \frac{\pi\omega_0^2}{\lambda} \tag{3.41}$$

The beam also has a complex q number,

$$q(z) = z + jz_0 \tag{3.42}$$

This number is a product of the derivation of the Gaussian beam equations. However, it concisely summarizes the beam shape and propagation.

A major benefit of using Gaussian beams is the use of ray transfer matrices. For a lens this is as shown in

$$\begin{bmatrix} x_2 \\ \theta_2 \end{bmatrix} = \begin{bmatrix} A & B \\ C & D \end{bmatrix} \begin{bmatrix} x_1 \\ \theta_1 \end{bmatrix} \tag{3.43}$$

These can be used through substitution of q as well,

$$\begin{bmatrix} q_2 \\ 1 \end{bmatrix} = \begin{bmatrix} A & B \\ C & D \end{bmatrix} \begin{bmatrix} q_1 \\ 1 \end{bmatrix} \tag{3.44}$$

Which can be expressed as,

$$q_2 = \frac{Aq_1 + B}{Cq_1 + D} \tag{3.45}$$

For a lens system as described in subsection 3.1.3 and Figure 3.10, 2 matrices are required; a matrix for distance and a matrix for a lens. The matrix for distance,

$$S = \begin{bmatrix} 1 & d \\ 0 & 1 \end{bmatrix} \tag{3.46}$$

is relatively straight forward, as it simple adds to the z component of q. The lens matrix,

$$L = \begin{bmatrix} 1 & 0 \\ -\frac{1}{f} & 1 \end{bmatrix} \tag{3.47}$$

changes θ to curve towards the focal point. The multiplication of the matrices leads to the transfer of the beam through the one lens system as,

$$\begin{bmatrix} q_2 \\ 1 \end{bmatrix} = S_1 L S_0 \begin{bmatrix} q_1 \\ 1 \end{bmatrix} = \begin{bmatrix} 1 & d_1 \\ 0 & 1 \end{bmatrix} \begin{bmatrix} 1 & 0 \\ -\frac{1}{f} & 1 \end{bmatrix} \begin{bmatrix} 1 & d_0 \\ 0 & 1 \end{bmatrix} \begin{bmatrix} q_1 \\ 1 \end{bmatrix} \tag{3.48}$$

easily changing the beams from location to location. The one lens system in this case would be as follows,

$$\begin{bmatrix} q_2 \\ 1 \end{bmatrix} = \begin{bmatrix} 1 - \frac{d_2}{f} & \left(1 - \frac{d_2}{f}\right) d_1 + 1 \\ -\frac{1}{f} & -\frac{d_1}{f} \end{bmatrix} \begin{bmatrix} q_1 \\ 1 \end{bmatrix} \tag{3.49}$$

This allows for direct comparisons between the Fresnel propagation through a lens as well as the Gaussian beam. This however can only be done if the diffraction of the beam through the aperture and the control system has negligible effect. Hence, this method can only be used for verification of the Fresnel propagation of small uncontrolled Gaussian beams (relative to the aperture) and design of a optical setup and train.

3.2. Model Algorithms

The analytical equations for the propagation of the input fields have to be adapted to work for a computer model. This has to be done in such a way as to make sure the program execution is as fast as possible. Furthermore, the inputs have to be adapted for the internal functions and presented in a way that can be interpreted. This section will discuss the propagation algorithms which implement the above Equation 3.22 and Equation 3.34 in the models.

The programming was performed in MATLAB.

3.2.1. Fresnel Propagation

The algorithm for Fresnel propagation is presented in Listing 3.1.

```
1  function E = FresnelProp(E,z,lambda,D)
2  k = 2*pi/lambda;
3  [nx, ny] = size(E);
4
5  dx = D/nx;
6  dy = D/ny;
7  x1 = (-nx/2*dx : dx : nx/2*dx - dx);
8  y1 = (-ny/2*dy : dy : ny/2*dy - dy);
9  [xP,yP] = meshgrid(x1, y1);
10
11 dx2 = z*lambda/(nx  * dx);
12 dy2 = z*lambda/(ny  * dy);
13 x2 = (-nx/2*dx2 : dx2 : nx/2*dx2 - dx2);
14 y2 = (-ny/2*dy2 : dy2 : ny/2*dy2 - dy2);
15 [xI,yI] = meshgrid(x2, y2);
16
17 DI = max(max(xI))*2;
18
19 g = E.*exp(1j*k/(2*z).*(xP.^2+yP.^2))*dx*dy;
20 G = fftshift(fft2(ifftshift(g)));
21 E = (1j/(z*lambda))*exp(1j*k*z).*exp(1j*k/(2*z)*(xI.^2+yI.^2)).*G;
22
23 E = E(ceil(0.5*nx*(1-D/DI)):ceil(0.5*nx*(1+D/DI)),ceil(0.5*ny*(1-D/DI)):ceil(0.5*ny*(1+D/DI))
       );
24 [mx,~] = size(E);
25 E = imresize(E,nx/mx,'nearest');
26 end
```

Listing 3.1: Fresnel Propagation Algorithm.

In short and highlighting the most important parts, the working of Listing 3.1 is as follows:

- Line 1 to 3: Declares the function and is the start of the algorithm, with input arguments being the input field, E, the propagation distance, z, wavelength, lambda and the aperture dimension, D.

Subsequently, some basic variables are declared, namely the wave number, k, and the number of pixels in the x and y axis, denoted by nx and ny respectively.

- Line 5 to 9: Defines the dimensional size (in meters) of a pixels as dx = D/nx, where dx is the pixel size and hence the smallest spatial variation. The resulting dimensions and mesh of the input apertures are created, represented by xP and yP.
- Line 11 to 15: The propagated pixel size, dx2 and dy2, is first calculated. Subsequently, the mesh generated.
- Line 17: The new aperture dimension found.
- Line 19 to 20: The input data is put through Equation 3.22.
- Line 23 to 25: This step is optional and is done to compare with the transfer function. The newly propagated field is cut to fit the same dimensions as the input field. Furthermore, the additional pixels are inserted through the ”imresize” such that comparisons between different methods using matrix operations is easier.
- Line 26: End of function/algorithm.

The majority of the code is straight forward. However, there are a number of additions to the existing train of thought in subsection 3.1.2. These are mainly the definition of the propagated pixel size, the multiplication by dx*dy and the shifting of the results of the 2D fast fourier transform.

The definition of the pixel size for the input field is relatively straight forward, the dimension of the input field is divided by the number of pixels across the aperture. These pixels, on plane P, propagate through space to the output field on plane I.

As Gaussian beam optics has shown, the focal point of a beam is more like the waist of a beam. In the waist of the beam it is assumed that the wave is planar and the resultant divergence is the further propagation. However, the pixel it self is not the size of the waist and not the shape of Gaussian beam. Hence, the divergence of the size of a pixel is given by the diffraction limit of a pixel. The pixel is a square shape and the rectangular diffraction limit is the following:

$$dx = \frac{\lambda f}{D} \tag{3.50}$$

Here, dx, represents the resolvable length in the x-axis (note that this is the same for the y-axis for a square aperture) and f the focal length which is the propagation distance of the light. If it is assumed that the pixel on plane I is small enough to act as a point, then the diffraction distance, z, can be substituted into the focal length. Furthermore, the aperture size can also be defined in terms of the pixels on plane P:

$$dx_2 = \frac{\lambda z}{nxdx} \tag{3.51}$$

The pixels defined in plane P have the value of the point in the center of the pixel. The result of this is that the intermediate points in the pixel are ignored in the integration process. The multiplication with ”dx*dy” in line 19 in Listing 3.1 implies the pixel values become that of the area. The resulting integral implies that energy is more conserved and a closer approximation. Figure 3.11 illustrates this.

Lastly, the function ”fftshift” is required because the fft2 function in MATLAB generates a distribution with the zero frequency in the top left corner of the plot. However, the center of the aperture is the center of the spatial fourier transform for diffraction. The fftshift allows of the top left of the fourier plot to be centered and hence the plot becomes centered relative to the diffraction aperture, solving the problem. Similarly, the input of the fft2 function is ifftshift’ed as well to make sure the center of the plot is processed as the zero of the fft2 function.

3.2.2. Fresnel Propagation in a One Lens System

The algorithm for Fresnel propagation through a one lens system is presented in Listing 3.2.

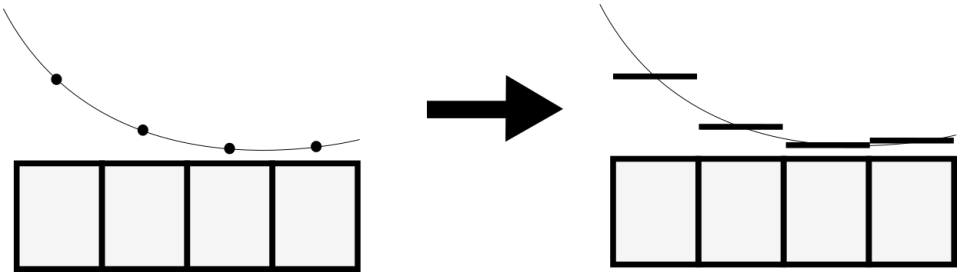

Figure 3.11: Left shows an electrical field distribution point sampled into pixels. Hence, the pixel has the value of the point in the distribution located at some point on the pixel. Here, it is illustrated in the center. The right shows when the pixel value is the value of the whole pixel at the value sampled in the middle of the pixel. When integrated, the pixels on the right is a closer approximation, however the interpolation between values is more accurate for the case on the left.

```
1  function E = FresnelPropLens(E,lambda,D,d0,d1,f,n,t0)
2  [nx, ny] = size(E);
3  dx = D/nx;
4  dy = D/ny;
5  k = 2*pi/lambda;
6
7  %"coordinates" of matrix Ain
8  x1 = (-nx/2*dx : dx : nx/2*dx - dx);
9  y1 = (-ny/2*dy : dy : ny/2*dy - dy);
10 [xP,yP] = meshgrid(x1,y1);
11
12 %dx and dy in distance d0
13 dxL = d0*lambda/(nx  * dx);
14 dyL = d0*lambda/(ny  * dy);
15 %"coordinates" of matrix Aout
16 x2 = (-nx/2*dxL : dxL : nx/2*dxL - dxL);
17 y2 = (-ny/2*dyL : dyL : ny/2*dyL - dyL);
18 [xL,yL] = meshgrid(x2, y2);
19 %Lens phase
20 dphi = -1*(k/(2*f))*(xL.^2+yL.^2);
21
22 %dx and dy in distance d1
23 dxI = d1*lambda/(nx  * dxL);
24 dyI = d1*lambda/(ny  * dyL);
25 %"coordinates" of matrix Aout
26 x2 = (-nx/2*dxI : dxI : nx/2*dxI - dxI);
27 y2 = (-ny/2*dyI : dyI : ny/2*dyI - dyI);
28 [xI,yI] = meshgrid(x2, y2);
29
30 DI = max(max(xI))*2 %Required to know when comparing to other methods
31 %D
32
33 g = E.*exp(1j*(k/(2*d0))*(xP.^2+yP.^2))*dx*dy;
34 G = fftshift(fft2(ifftshift(g)));
35 EL = -(1j/(d0*lambda))*exp(1j*k*d0).*exp(1j*(k/(2*d0))*(xL.^2+yL.^2)).*G;
36
37 EL = exp(1j*k*n*t0)*exp(1j*dphi).*EL;
38
39 gL = EL.*exp(1j*(k/(2*d1))*(xL.^2+yL.^2))*dxL*dyL;
40 GL = fftshift(fft2(ifftshift(gL)));
41 EI = -(1j/(d1*lambda))*exp(1j*k*d1).*exp(1j*(k/(2*d1))*(xI.^2+yI.^2)).*GL;
42 E = EI;
43
44 end
```

Listing 3.2: Fresnel Propagation Through a One Lens System Algorithm.

In short and highlighting the most important parts, the working of Listing 3.1 is as follows:

- Line 1 to 5: Declares the function and is the start of the algorithm, with input arguments being the input field, E, the propagation distances, d0 and d1, wavelength, lambda and the aperture dimension, D, the focal length, f, index of the glass, n, and the thickness of the lens, t0. Subsequently,

some basic variables are declared, namely the wave number, k, and the number of pixels in the x and y axis, denoted by nx and ny respectively.

- Line 7 to 28: Generates the mesh for each plane. These are denoted by P for the projection plane, L for the lens plane (both the input and the output) and I for the imaging plane. The phase term for the lens is specified in line 20.
- Line 30: Determination of the new aperture size. This is determined in order to allow for comparisons to other modeling methods.
- Line 33 to 42: Multi-step implementation for Equation 3.32.
- Line 26: End of function/algorithm.

3.2.3. Fresnel Transfer Function Approximation Verification

The algorithm for the transfer function approach is shown in Listing 3.3.

```
1  function[u2]=propTF(u1,L,lambda,z);
2  % propagation - transfer function approach
3  % assumes same x and y side lengths and
4  % uniform sampling
5  % u1 - source plane field
6  % L - source and observation plane side length
7  % lambda - wavelength
8  % z - propagation distance
9  % u2 - observation plane field
10
11 [M,N]=size(u1);           %get input field array size
12 dx=L/M;                   %sample interval
13 k=2*pi/lambda;            %wavenumber
14
15
16 fx=-1/(2*dx):1/L:1/(2*dx)-1/L; %freq coords
17 [FX,FY]=meshgrid(fx,fx);
18
19 H=exp(-j*pi*lambda*z*(FX.^2+FY.^2));  %trans func
20 H=fftshift(H);            %shift trans func
21 U1=fft2(fftshift(u1));    %shift, fft src field
22 U2=H.*U1;                 %multiply
23 u2=ifftshift(ifft2(U2));  %inv fft, center obs field
24 end
```

Listing 3.3: Fresnel Transfer Function Approximation Algorithm by Voelz[70] on page 63.

In short and highlighting the most important parts, the working of Listing 3.3 is as follows:

- Line 1: Beginning of the function. Note that all the text behind the % are comments.
- Line 11 to 13: Dimensions are encode in N and M. The subsequent pixel dimensions and wave numbers are found.
- Line 16 to 17: Define the coordinates of the frequency domain of the transfer function and a mesh is made with these coordinates.
- Line 19 to 23: First the transfer function, ”H”, is generated and the input field is transformed into the frequency domain. These are then multiplied and transformed back into the spatial domain.
- Line 24: Ending of the function.

As discussed in subsection 3.1.4, the approach defines a transfer function in the frequency domain. This is the reason why the mesh is generated in the frequency domain. Furthermore, the multiplication with the transfer function and the input frequency plane is the equivalent to convolution.

3.3. Model Verification and Validation Through Comparison

This section aims to verify the model algorithm(s), specifically the Fresnel propagation algorithm, discussed in section 3.2. This will be done primarily through comparison with Fresnel transfer function and with Gaussian beam methods (FP, TF and GB respectively). However, there will also be more qualitative comparisons with textbook examples and previous experiments in order to ensure minimization of implementation error.

The two errors of importance are the spatial distribution of the output field and the peak intensities. The spatial distribution will ensure that the output is representative for the potentially complex diffraction patterns which arise from non-aligned mirrors and changing aperture shapes. The peak intensity, which is comparable to the Strehl ratio, makes sure that the optical quality of the system is not different due to the working of the algorithm. It is also a crucial parameter for optic fiber coupling, hence for future analysis this must be corrected. The power error (PE) and the peak intensity error (PIE) are,

$$PE_{TF} = \frac{\Sigma_x \Sigma_y (|I_{FP} - I_{TF}|)}{\Sigma_x \Sigma_y |I_{FP}|} \tag{3.52}$$

$$PI_{TF} = \frac{MAX(I_{FP}) - MAX(I_{TF})}{MAX(I_{FP})} \tag{3.53}$$

$$PE_{GB} = \frac{\Sigma_x \Sigma_y (|I_{FP} - I_{GB}|)}{\Sigma_x \Sigma_y |I_{FP}|} \tag{3.54}$$

$$PI_{GB} = \frac{MAX(I_{FP}) - MAX(I_{GB})}{MAX(I_{FP})} \tag{3.55}$$

Note, that to compare differently sized apertures, the apertures where cropped and the resolutions changed to be comparable.

3.3.1. Free Space Propagation

This verification will check if the two Fresnel diffraction algorithms as well as the standard Gaussian beam equations correlate and if the differences between them are as expected. The differences will be relative to FP.

The input plane is imposed with a Gaussian distribution at its waist in the center of the plane. The radius of the distribution varies from 0.1, 1 and 10 mm. The subsequent distribution is propagated from the input plane over a number of distances. The resulting output planes are subtracted and the error normalized to the Fresnel propagation output.

The resulting data can be found in Appendix A. Particularly illustrative are the results illustrated in Figure 3.12 and Figure 3.13.

As can be seen in Figure 3.12, the error with respect to TF increases drastically at larger distances. However, the error with respect to GB does not. This is because the aperture dimensions do not change with TF. Hence the beam diameter grows beyond the size of the aperture, together with reflections caused by the Fourier Analysis on a discrete aperture. This is illustrated in Figure 3.14. This implies that simulations over these distances using TF require larger apertures for the given beam radius.

Similarly, when looking at Figure 3.13, it can be seen that the errors for both TF and BG are the same and large at small propagation distances. This is because the aperture produced by FP is smaller than the beam diameter, as shown in Figure 3.15. Hence, the beam is exceeding the aperture size and results in a similar error as with the TF at larger distances.

Similarly, PIE are shown in Appendix A, show similar patterns. This is for the same reasons as is the case for PE.

Both of these errors can be solved by increasing the aperture size for FP when closer to the input plane. Similarly, for TF, the input plane should be enlarged for longer distances to accommodate the output plane. However, for free space propagation of Gaussian beams at intermediate lengths both of these methods are accurate to within 5% for both PIE and PE. The errors that resulted where also suspected and illustrate some of the different benefits and drawbacks of using TF and FP.

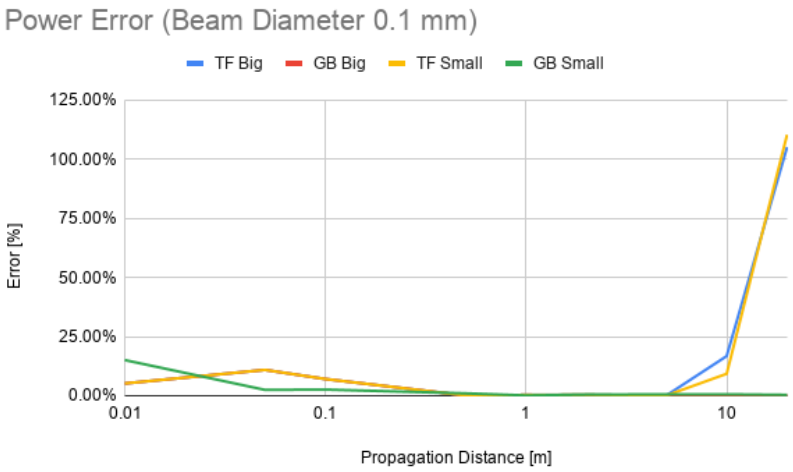

Figure 3.12: Power error of a Gaussian beam propagation of a 0.1 mm radius beam in a 0.1 m aperture. The error is relative to the Fresnel Propagation algorithm and is compared to the Fresnel Transfer Function (TF) and the standard Gaussian Beam (GB) equations. The propagation under these different algorithms change the size of the aperture, hence each output is adjusted to the largest (big) and smallest (small) apertures for comparison.

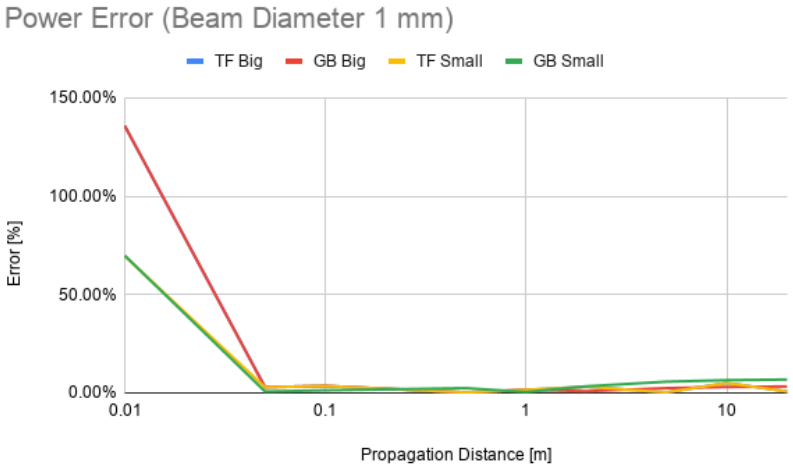

Figure 3.13: Power error of a Gaussian beam propagation of a 1 mm radius beam in a 1 m aperture. The error is relative to the Fresnel Propagation algorithm and is compared to the Fresnel Transfer Function (TF) and the standard Gaussian Beam (GB) equations. The propagation under these different algorithms change the size of the aperture, hence each output is adjusted to the largest (big) and smallest (small) apertures for comparison.

3.3.2. Aperture Diffraction

The aperture diffraction will be compared between both FP and TF. The data is presented in Appendix A. The output image, due to the image resizing, can be shifted by a pixel due to rounding. This increases the error substantially in some cases for PE. This is corrected for by shifting the image by 1 pixel.

For much the same reasons as specified in subsection 3.3.2, the errors existent close to the input plane are because of the output aperture size of FP. For distances further away from the input plane, the output aperture of TF is too small. However, for the intermediate distances there is little difference. Note, that these problems can be solved by changing the input aperture diameter, while making the circular hole the same size.

However, because the diffraction occurs through a significantly large hole compared to the aperture, in this case the approximation made in the TF method at closer distances adds to the error. This is therefore another reason as to why the outputs at larger distances are more similar. This is especially indicated by PIE for the larger apertures.

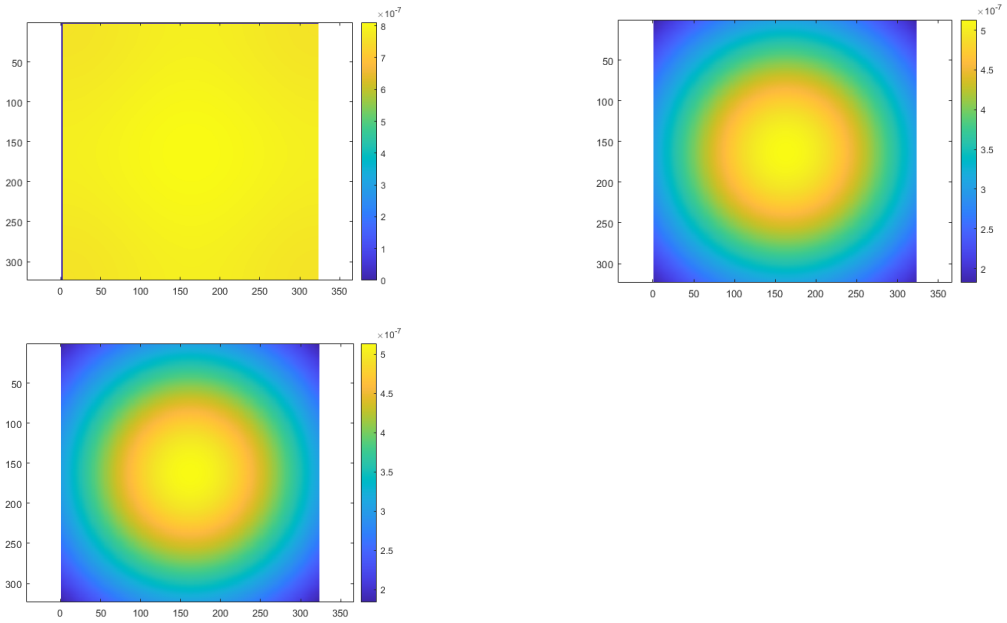

Figure 3.14: The intensity distribution of a 0.1 mm radius Gaussian beam propagated over a distance of 10 m with an aperture diameter of 0.1 m. The color scale is normalized intensity and the x and y axes note the pixels in the aperture. (a): Illustrates the propagation by TF. (b) Depicts the propagation by FP. (c) Depicts the GB propagation. As can be seen, the aperture does not represent an accurate Gaussian beam due to the beam exceeding the aperture size using TF. However, it performs better using FP and GB.

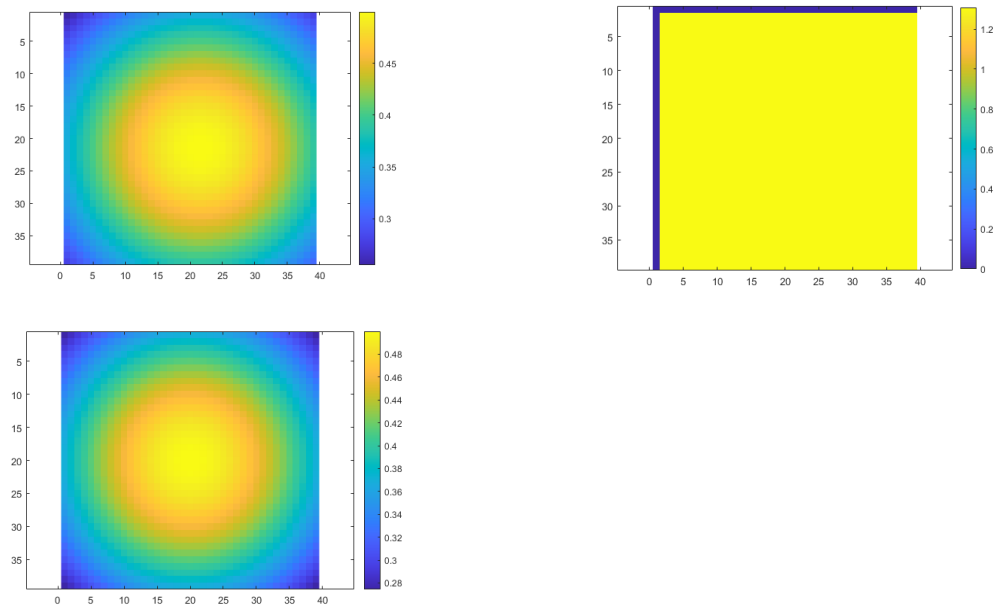

Figure 3.15: The intensity distribution of a 1 mm radius Gaussian beam propagated over a distance of 0.01 m with an aperture diameter of 0.1 m. (a): Illustrates the propagation by TF. (b) Depicts the propagation by FP. (c) Depicts the GB propagation. In this case, FP generates an aperture which is too small for the beam projected.

There are also additional errors introduced by the increasing output aperture size given by FP at larger distances. This drop in resolution must hence also be done for FT in order to facilitate comparison. However, it does make the comparison subject to rounding and averaging errors.

The conclusion is hence again, that the aperture relative to the object propagated and propagation distance must be carefully chosen for both FP and FR. However, if the pattern fits in the aperture, the

outputs are very similar and both will give a good indication. However, due to the assumptions made in FT, the closer propagation's should be done using FP while this algorithm also handles increased aperture size better at larger distances. However, this comes at a cost of resolution, which again highlights the importance of appropriate aperture size selection.

3.4. Experimental Verification and Validation Through Comparisons with Diffraction Experiments

Initially the planned experiment was meant to take place in a laboratory and the multi-beam system as a whole was to be build and demonstrated. However, at the beginning of 2020, the terrible COVID-19 global pandemic arrived in the Netherlands as well. As of writing this terrible episode in human history is still on going. The resulting measures taken by the government made the experiment as initially envisaged logistically and practically impossible.

The result of losing a physical demonstration is that a more heavy emphasis was placed on the models. The resulting FP model used, was made with less assumptions to make sure of the accuracy. The experimental goal can hence be changed and instead became to verify and validate more complected diffraction patterns.

The models created in the previous sections are sufficiently close to verify the accuracy of the Fresnel Propagation (FP) model. It also validates its use as an accurate tool for simulating the propagation of the light and get the expected results. However, it does not directly illustrate its effectiveness in simulating real world propagation of light, as the algorithms compared too have inherent assumptions. These assumptions lead to limitations which could be exceeded and so to be sure of the FP model's accuracy, an experiment was performed.

Shown is that the FP model is sufficiently accurate at predicting the diffraction patterns produced by the experimental setup.

3.4.1. Experimental Setup

A simple experiment was setup to generate numerous diffraction patterns to verify and validate both the FP (both with and without lens) and TF simulations (after lens). The goal was to verify and validate the abilities of each simulation algorithm to accurately obtain representative diffraction patterns. This would give more confidence in the resulting beam steering simulations.

The experiment had a non-existent budget and lacked a laboratory environment. The setup was hence both scavenged from parts and tools as well as setup in and around the author's place of residence. This placed constrains on the setup, as the diffraction pattern shapes had to be measured using regular calipers, paper and pencils. The pattern generated must hence be large and clear enough, while remaining complex. The setup, illustrated in Figure 3.16, was chosen. The divergent beam ensured that the diffraction pattern does not collapse into an Airy disk by the time it is large enough to trace using paper and pencil. The lens allowed for testing the theory around lenses discussed earlier as well.

A setup was chosen which generated detailed diffraction patterns from a green 532 nm laser pointer. The subsequent beam was expanded by a short 1.7 cm focal length macro lens, taken from the camera of a (broken) smart phone camera. The diffraction holes where sourced from perforated solder board, screw hole clips for ceiling lighting and a hole in the hilt of a potato peeler knife. To change the diffraction pattern, not only the hole diameter was changed but also the distance between the macro lens and the diffraction hole.

The setup is photographed in Figure 3.17, Figure 3.18, Figure 3.19, Figure 3.20 and the measurement through tracing in Figure 3.21. The setup performed admirably, depicting similar diffraction patterns to the ones illustrated in Hecht[23] chapter 10. However, the quality of the laser source and the lens as well as the quality of the circle and mirror leaves wanting. This results in a number of additional diffraction patterns imposed onto the circular diffraction pattern which are normally not associated with circular hole diffraction. These are super imposed onto the circular diffraction patterns and cause visual noise. The laser pen emitted wavelength has a self reported range of 10 nm round 532 nm, however it is unknown what the exact wavelength is or its overall spectrum, which cause alterations in the patterns.

These decrease the accuracy of the experimental setup. However, the measurement methods are also limited inherently. The transition between dark and light rings is gradual and not radially symmetric, implying a subjective choice is made as to the location of the ring. The slimmer rings are often the same

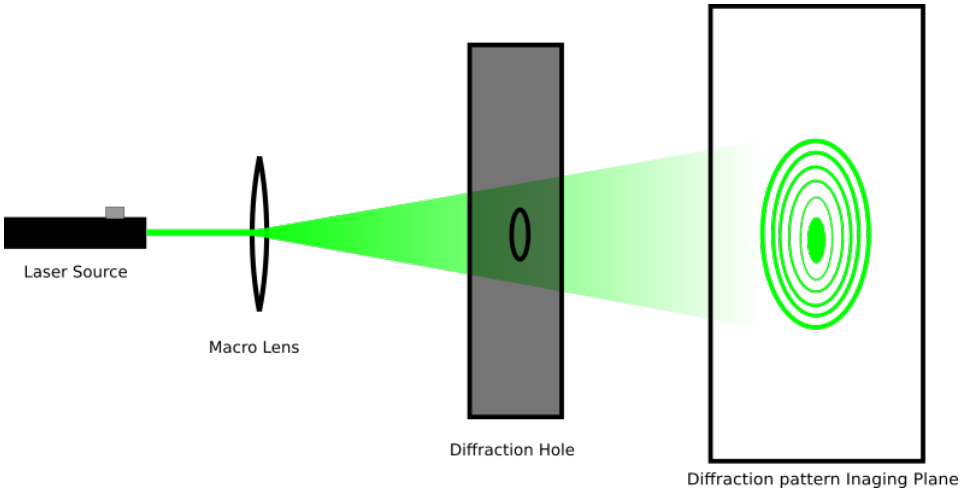

Figure 3.16: Illustration of the experimental setup used to generate diffraction patterns. From left to right, a laser source produces a narrow laser beam which is expanded by a macro lens with a focal length of 1.71 cm. The beam is then diverged for some distance to the diffraction hole. The light is than diffracted and projected onto the imaging plane.

width or smaller as the pencil line, implying there is an inherent +- 1 mm error at least. This makes the exact tracing of the diffraction patterns challenging. Lastly, the experiments performed where also limited to the practical size and variation of the patterns generated.

The error was investigated by considering the pencil line thickness and multiple marks made for multiple different tracings (note, that these are illustrated in the traces in Appendix B as well). The variance is estimated to be 3 mm.

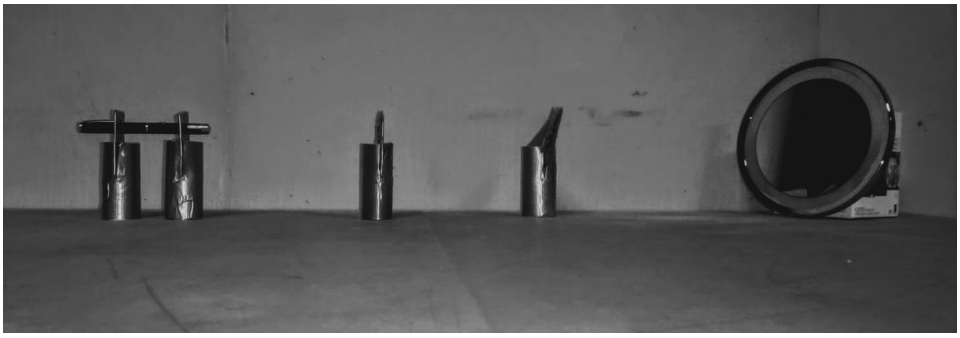

Figure 3.17: Illustrated is the optical train with each optical element shown. From left to right; the 532 nm laser source is passed through a lens contained in element 2. The 3rd element contains the diffraction hole. Then finally the mirror reflects the diffracted beam over to the wall at the appropriate distance.

3.4.2. Experiment Results

The results of both the experiments as well as all the relevant simulations of each model can be found in Appendix B. These results are presented pictorially and subsequently in a table where the accuracy can be quantified. This allows for seeing if the simulation produces patterns which behave the same as the physical patterns. The accuracy indicates how close the models can model reality, given the measurement accuracy.

When considering the general patterns. In a brief glance it can be clearly seen that the general diffraction patterns are both similar between the different models as well as the resulting physical patterns (one such is pictures in Figure 3.21). It clearly illustrates that either models can be used to create a good visual impression of the effects of different design choices and physical phenomena.

As for the accuracy, the simulation results might not always indicate coherence with the experimental results. It would be forgiven to then mark the models as inaccurate. However, when results are nuanced, a different picture emerges. Firstly, measuring the rings has an estimated accuracy of around +-1 mm due to the compass, position of the paper on the wall, calipers, distance measurements, etc...

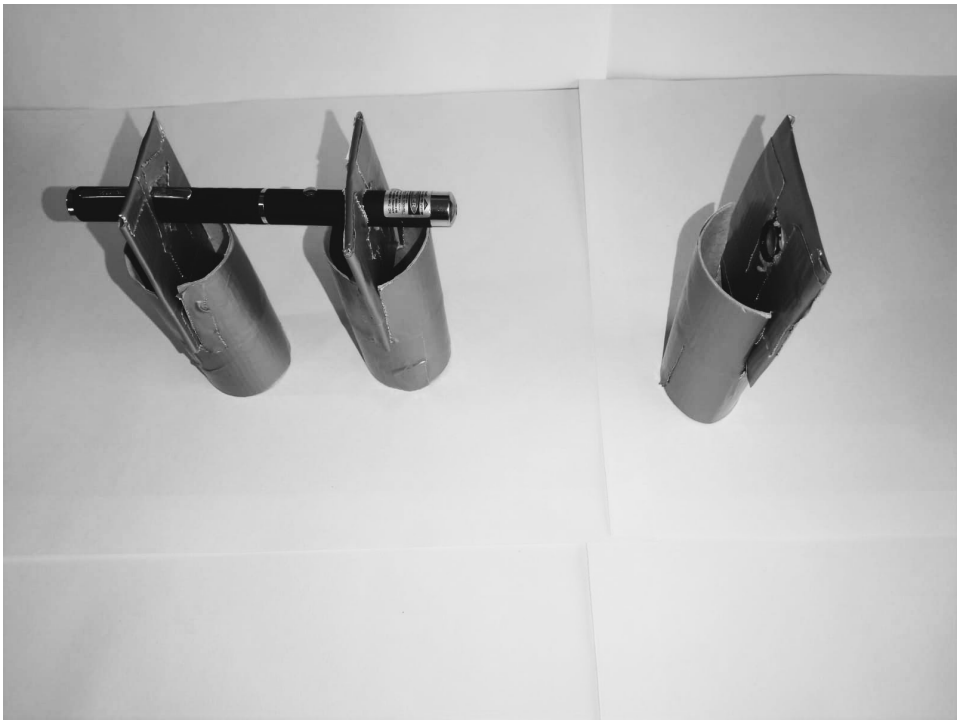

Figure 3.18: Photographed is a close-up of the laser and lens.

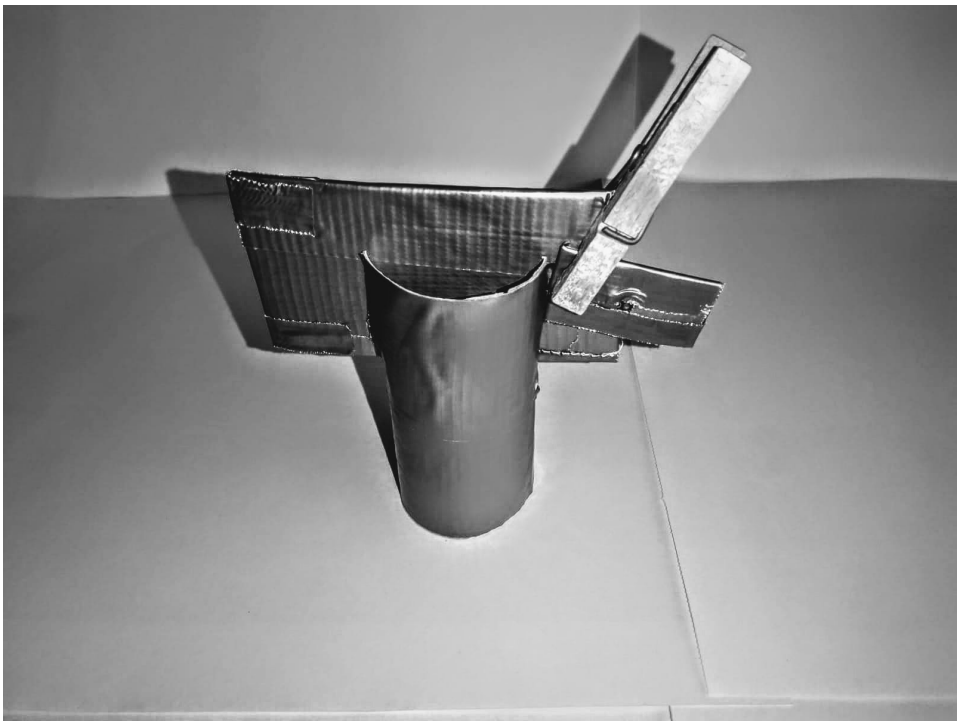

Figure 3.19: Depicted is the stand used to present the diffraction hole to the laser beam.

Secondly, the fainter fringes might not be obvious during the experiment, making it easy to accidentally miss them. This is made all the more likely due to the vertical fringes originating from the laser source, which can be seen as the dark vertical lines in Figure 3.21. The missing fringes could cause for the results to be staggered, such as seen in the results of 1 mm diffraction hole, 60 cm lens-hole distance and 5.64 m propagation distance. Where the simulation results could be staggered by one

Figure 3.20: Shown is a close-up of one of the diffraction holes, in this case the perf-board. Shown is how the other holes are covered to not interfere with the diffraction pattern.

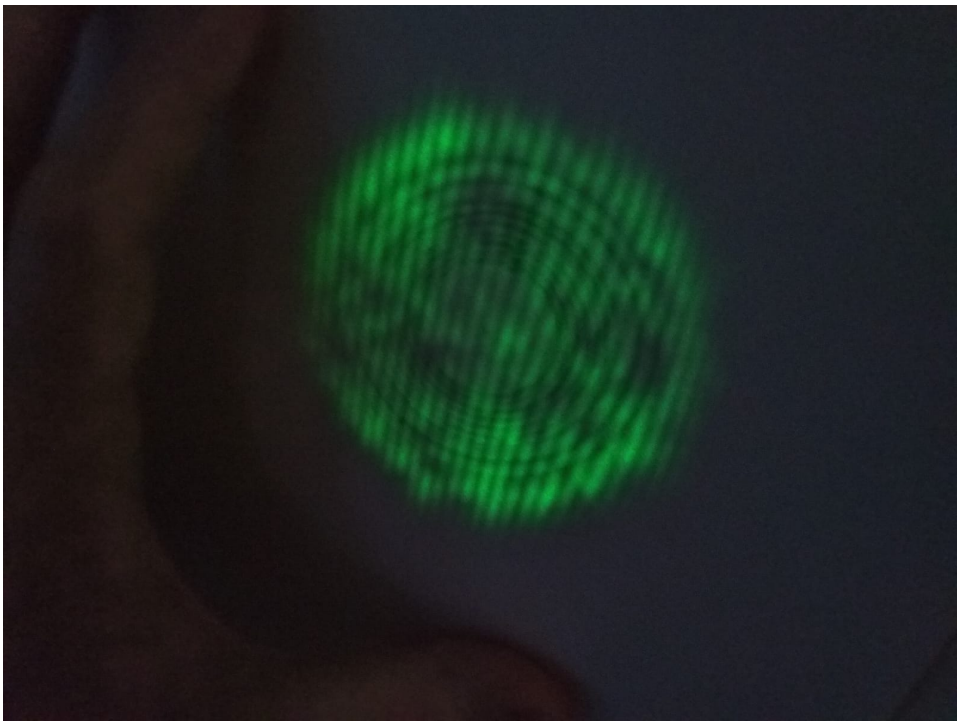

Figure 3.21: The pattern is than projected onto a wall where a black piece of paper was used to trace the dark rings using a compass.

ring.

Considering this, the FP simulations compared to the experiments in the table generally are very close and within the error margins. TF simulations slightly less so, however, also within the error margins. From the data it can be concluded that the diffraction patterns generated by the FP simulations

are likely a close approximation of the real diffraction patterns both in terms of size and shape. This gives confidence in the beam steering simulations performed later on.

3.5. Propagation Methods and Models Conclusion

The propagation of light is a highly non-linear phenomena which can lead to diffraction effects important to multiple beam steering. These effects should be taken into account when considering the design of a multi-beam system. It has been shown that it is possible to accurately simulate the diffraction and propagation of light through different apertures and optical elements. This has been shown primarily with two methods.

The first method considered in this chapter was derived from fundamentals Fresnel Propagation (FP), based on the works of Hecht[23], Blaunstein[39] and Verdeyen[68]. This method uses few assumptions and hence is close to the classical physical propagation of light. Furthermore, the inclusion of lenses and other optical elements can be done easily. However, the use of this method in a discrete input aperture implies a growing or shrinking aperture size. This implies that at small distances, the aperture calculated becomes smaller than the structures them selves leading to large errors and unusable results. However, when the input aperture diameter and propagation distances relative to the input is chosen well, these problems can be overcome. The visually, spatially and peak intensity wise, the results hold up to comparison with existing theory, namely the work and examples given by Voelz[70], Hecht[23], Blaunstein[39], Verdeyen[68] and Gaussian beams. Lastly, the method was compared with diffraction experiments performed in the real world. These also verify and validate the model's ability to predict diffraction patterns and propagate light.

This method further simplified to allow the use of Transfer Functions (TF) obtained from the work of Voelz[70] was also used. This allowed for both verifications as it has been source from established literature. However, it is the second model method that maintains the same aperture size during the propagation simulations. This allows for quicker testing as well as simulating smaller propagation distances for small (relative to the aperture) structures such as Gaussian beams and diffraction holes.

These models will be used in the coming chapters to derive system configurations, requirements and trade-off's.

4

Inherent System Losses, Limitations and Performances

This chapter will discuss the aspects of the system which cannot be changed or adjusted, but do nonetheless have implications for the overall system design and in particular on the link budget. This section will mainly discuss the issue of free-space losses, atmospheric effects and jitter. The former having effect on the signal power at the telescope entrance and the later affecting the fiber coupling efficiency of the design.

First the inherent loss due to free-space travel between two points is discussed aswell as the overall effects of the atmosphere. It will consider the losses which happen due to beam divergence over long distance, spreading the signal power over a large area and the receiving telescope having small pointing offsets. Furthermore, the pointing losses of the transmitting telescope, transmitting a beam with an Airy profile, is also considered. All the losses will be given a loss factor which can be used to determine the signal strength and performance of the system later on. Losses due to atmospheric absorption are approximated. After this, the more difficult problem of atmospheric turbulence is tackled to determine the atmospheric contribution to jitter.

The modeling of the effects of atmospheric distortion due to turbulence will not be modeled extensively. For such parameters, the values will be estimated.

The jitter and the minimal required system response speed to combat jitter is then also discussed. The result of this is a re-evaluation of the requirements and subsequently stating the minimal performance of the system in this area. It will be important when evaluating the steering hardware choices.

Finally there is a conclusion which will also summarize the findings.

Note, the next sections will discuss work in part based on the literature study[56] together with new insights.

4.1. Link Budget for Target Transceiver and Free Space Travel

This section will discuss the free-space propagation aspects of optical communication. This mainly consists of travel through the vacuum of space as well as the path through the atmosphere. The nature of this is quite complex and infinite in depth, however it will be analyzed and distilled down to what is required in a link budget. First, the propagation through vacuum over a large distance. After this, the attenuation through absorption through the atmosphere is discussed, with a selection of the optimal frequency range of the link. There will also be a discussion on the scintillation due to atmospheric turbulence, where the effects of turbulence are shown and a turbulence profile is created. Lastly, there is a small discussion on some future improvements to free-space propagation.

4.1.1. Free Space Propagation

Considering the free space propagation, the signal is transmitted and exits the transmitter telescope. It then travels through free-space and to the receiver from the transmitter. During travel, the beam spreads and hence loses intensity. The geometry is shown in Figure 4.1. The losses can then be described geometrically as,

$$L_S = \frac{A_R}{A_S} = \frac{\pi\left(\frac{D_R}{2}\right)^2}{\pi\left(\frac{D_T(1+2Ztan(\theta))}{2}\right)^2} = \left(\frac{D_R}{D_T + 2Ztan(\theta)}\right)^2 \tag{4.1}$$

Where the area after free-space propagation is denoted by A_S, the receiver telescope area A_R, their respective diameters are given by D_R and D_S, given by the trigonometric equation given by the geometry in Figure 4.1 respectively. The distance of the propagation is denoted by Z and the spread of the beam is that of the first Airy disk zero angle.

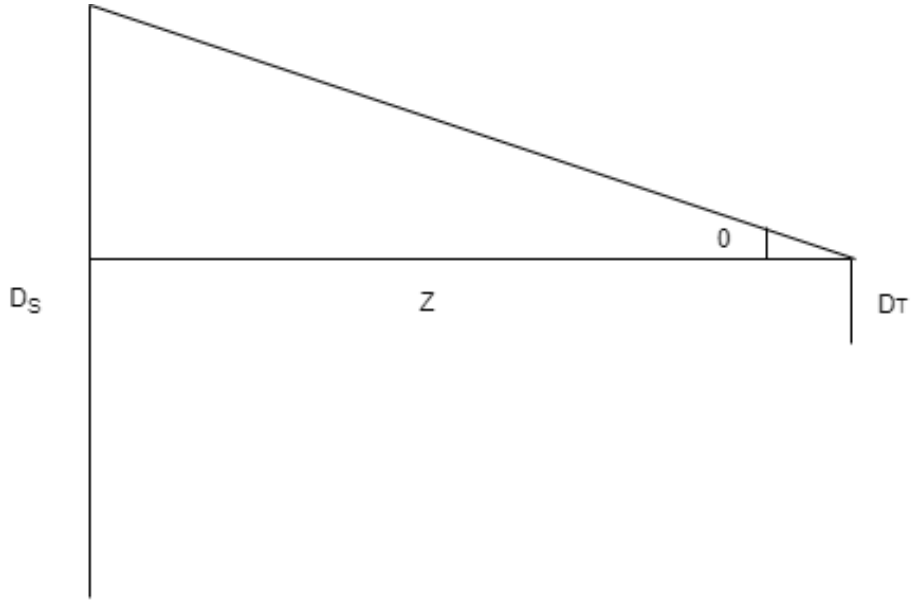

Figure 4.1: The geometry of free space propagation. The spreading angle is denoted by θ, the distance is denoted by Z, the transmitter diameter D_T and the diameter after propagation is D_S.

The subsequent telescope of the transmitter could also be pointed with an instantaneous offset angle. This implies that the beam distribution peak intensity is not incident on the receiver telescope. A spot of a diffracted beam through a circular aperture, normalized by the peak intensity, can be represented by the Bessel function,

$$I(\theta) = \left(\frac{2J_1(0.5kD_T sin(\theta))}{0.5kD_T sin(\theta)}\right)^2 \tag{4.2}$$

Where I is the intensity normalized by the peak intensity, k the wave number, D_T the telescope diameter, J_1 denotes the Bessel function of the first kind order 1, θ the angle to the observation point from the beam axis of propagation at the input aperture. This equation is zero when the Bessel function is zero is at $0.5kD_T sin(\theta) = 3.8317$, which leads to the infamous Reighley criterion,

$$sin(\theta) = \frac{3.8317}{0.5kD_T} = \frac{3.8317\lambda}{0.52\pi D_T} = \frac{1.22\lambda}{D_T} \tag{4.3}$$

Which for wavelengths round 1550 [nm] and transmitter telescope diameter on the order of 10 [cm] implies angles of 1.8e-5 [rad]. This at a distance of between 1000 [km] to 10,000 [km] implies central peak radius of 20 [m] to 200 [m]. If the receiver telescope diameter is on the order of 10 [cm], then the intensity over its input aperture can be considered uniform as a first approximation.

The angular misalignment loss factor is hence equal to the normalized intensity from Equation 4.2. The loss factor is hence,

$$L_T = I(\theta) = \left(\frac{2J_1(0.5kD_T sin(\theta))}{0.5kD_T sin(\theta)}\right)^2 \tag{4.4}$$

Where L_T is the loss factor due to pointing misalignment. When the transmitter telescope is much larger and the receiver is closer, this approximation will not hold anymore. When the spot on the receiver telescope is smaller than the input aperture, almost all the power in the beam will enter the telescope or fall completely outside it. Hence this factor will not be required for those cases other than a binary 1 or 0. For cases where there is a significant distribution over the aperture, the intensity requires to be integrated over the aperture area.

An example integration of an Airy disk is shown in Figure 5.12 for a beam with no misalignment. This was done analytically and graphed, and will be discussed in subsection 5.2.1. It shows that the central peak contains about 86% and exceeds 95% after the second fringe. Hence, L_S can be considered 1 when the telescope is larger than the second fringe of the spot in this case. However, each case must be considered individually, which makes the intermediate size more challenging to design. However in this work it is assumed not to be the case for this design.

Note here as well, that the relation in Equation 4.1 specify that smaller divergence leads to lower free space losses. The result in Equation 4.4 shows that this can only be achieved through larger telescope apertures but comes at the cost of increased required steering accuracy. This implies that the signal power, steering accuracy, telescope input aperture size and the free space losses are connected and that more accurate steering directly leads to higher data rates.

Lastly, the receiving telescope it self can be misaligned. In the case of the small receiver telescope, the loss factor can simply be,

$$L_R = cos(\phi_R) \tag{4.5}$$

Where L_R is the loss factor regarding the receiver telescope misalignment and ϕ_R the misalignment.

4.1.2. Atmospheric Absorption

For targets which are communicated with in the atmosphere, there are numerous additional losses. These are the absorption losses due to the molecules and atoms in the atmosphere as well as the turbulence causing diffraction.

The atmospheric composition implies that certain frequency bands of light are absorbed in accordance with the chemistry of the substances. A rough illustration of the absorption effects can be seen in Figure 4.2. The atmospheric absorption of light depends on the altitude as well, due to the composition and density change with altitude[27]. As a result, certain wavelengths propagate better through the atmosphere than others and hence the wavelength selection is important. Especially for targets in the atmosphere, the selection of the wavelength must also not be harmful for humans and hence cannot be in the visual or ionizing spectrum. Hence, the highest frequencies available are in the near-infra red range.

Laux et all.[36] performed an experimental study on the infra-red emissions from an air plasma, the results are shown in Figure 4.3. The inverse of the emission spectra is the equivalent of the absorption spectra, implying that the frequencies with strong emissions are also frequencies more strongly absorbed. As can be clearly seen, the wavelengths between 1.4 and 1.7 micro meters (1400 to 1700 nm) are suitable for atmospheric transmission. These are also ideal for Erbium Doped Fiber Amplifiers (EDFA's) and will allow for efficient signal amplification, which will be discussed later in detail. Furthermore, standard fiber optics used on Earth for internet infrastructure have optimized transmission windows around 1550 +- 200 nm. Hence, the system can be designed to work with existing fiber optic hardware.

In addition to absorption spectra, there also exist aerosols and condensation. These are much less predictable and depend heavily on the location and weather. Hence, it is assumed that the weather conditions are ideal in this work. The transmission is assumed to be 80% from the data given considering Figure 4.2 and Figure 4.3. This will be used later when estimating the link budget of a link. The efficiency of atmospheric transmission will hence be noted as, $\eta_A = 0.8$.

4.1.3. Atmospheric Turbulence and Adaptive Optics

The atmosphere is a very complex and constantly varying fluid medium. Turbulence and other variations cause the density of the atmosphere to vary slightly. Due to the small wavelengths this changes the phase/wave-front significantly. Subsequently, the direction and intensity of the signal is altered

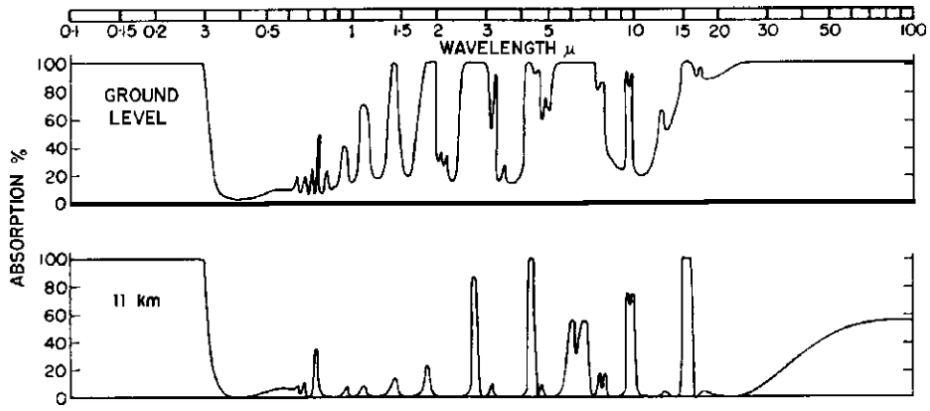

Figure 4.2: Taken from the work by Laux et all.[36], page 2, Figure 1. Shown is an illustration of the optical attenuation due to absorption. It shows how different wavelengths are absorbed differently due to different absorbance bands of present gasses. The transmission is around 80% for 1550 nm, which is good compared to other similar wavelengths.

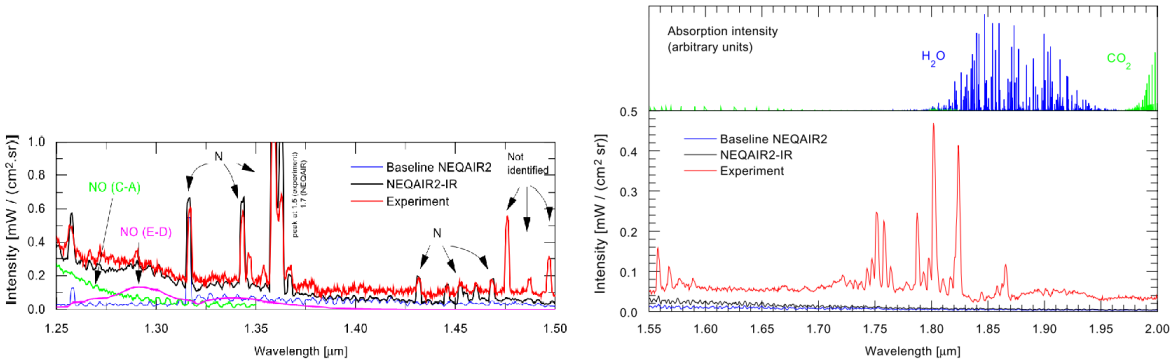

Figure 4.3: Taken from the work by Laux et all.[36], page 7, Figure 9 and page 10, Figure 10. The spectral emissions are associated with the absorption implying less emission lines are preferable around the chosen wavelengths. Again it can be seen that around 1550 nm there are relatively little emission lines.

which presents it self as scintillation, fading, aberrations and data loss. Hence the travel of the beam through the atmosphere is an important problem.[63]

The method by which this can be corrected for is through the use of Adaptive Optics (AO). These systems are able to correct the wavefront such that these problems are solved to a certain extent. However, as the wavefront spreads out through space, the relative effects of small distortions are also spread out. This implies that correction of the wavefront might be unnecessary for long distance communications and relatively small telescope apertures. However, for targets in the atmosphere or for instances when the spacecraft is in LEO, these distortions can affect the performance.

The frequency by which the system should correct the wavefront was studied by Greenwood[22] and the resulting frequency parameter has been named after him; Greenwood frequency. The expression of the Greenwood frequency is shown in Equation 4.6. It is derived from a probabilistic structure of turbulence using the Kolmogorov spectrum. The Kolmogorov spectrum, in turbulence, being a semi-statistical power distribution for vortexes in a turbulent fluid. The power spectrum arises because of larger vortexes losing their velocities to smaller vortexes and those subsequent vortexes also losing their velocities to smaller vortexes, etc... In this case, the integration limits is chosen to be from the starting altitude to the top of the chosen Hufnagel-Valley turbulence profile[63], discussed later.

$$f_G = 2.31\lambda^{-6/5}\left[sec(\zeta)\int_{z_0}^{40km} C_n^2(z)V(z)^{5/3}dz\right]^{3/5} \tag{4.6}$$

Where, ζ is the angle by which the light travels through the atmosphere, λ is the wavelength, C_n^2 is the turbulence strength, V is the wind velocity and z is the altitude. When the wavefront is corrected at this frequency, the uncorrected/rejected integrated power spectrum of the wavefront error over the entire spectrum until infinity drops by 3 [db]. Put in another way, the integrated temporal wavefront error becomes negligible.

As stated, the Kolmogorov spectrum in fact contains vortexes which are of a larger variety of sizes. The vortexes which are smaller than the telescope aperture cause wavefront errors which are smaller then the aperture. This will be referred to as sub-aperture errors. Hence, Equation 4.6 is an equation which is valid over the whole spectrum and so includes sub-aperture corrections. This causes scintillation in the form of a number of small spots which disappear when corrected for, shown in Figure 4.4.

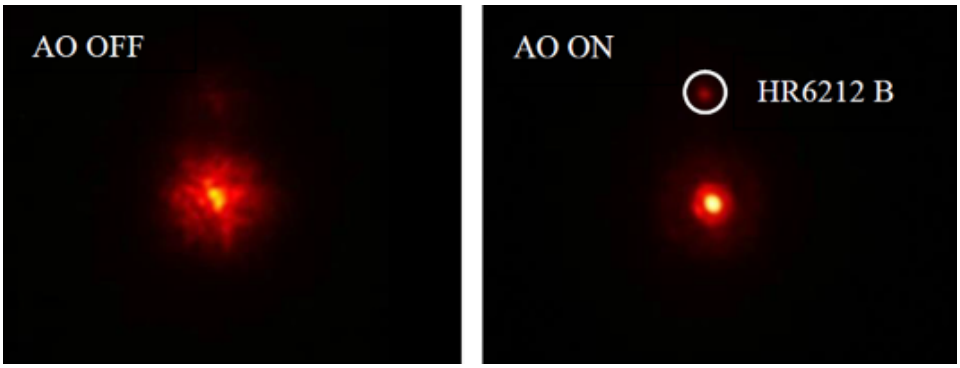

Figure 4.4: This image was taken from ALPAO[2] on their webpage on "Adaptive optics applications" url: https://www.alpao.com/adaptive-optics/alpao-applications.html. It shows an example of a scintillated image of a star left and a corrected image right. As can be seen, the scintillated image contains numerous bright spots and a distribution of the light over a larger area.

Corrections for sub-aperture might not be possible in a multi-beam system and so alternative equations for simple tip-tilt corrects are required. Glenn A. Tyler[67] derived expressions which quantifies the frequency required for tip-tilt only, shown in Equation 4.7 and Equation 4.8.

$$f_{T_G} = 0.331 D_T^{-1/6} \lambda^{-1} \left[sec(\zeta) \int_{z_0}^{40km} C_n^2(z) V^2(z) dz \right]^{1/2} \tag{4.7}$$

$$f_{T_Z} = 0.368 D_T^{-1/6} \lambda^{-1} \left[sec(\zeta) \int_{z_0}^{40km} C_n^2(z) V^2(z) dz \right]^{1/2} \tag{4.8}$$

Tyler[67] analyzed both centroid and bright spot tracking and found Equation 4.7 and Equation 4.8 respectively. Extensive analysis and simulations by Glindemann[21] showed that for tip-tilt, the highest gains can be experienced in tracking the brightest spot or peak. In fact, it far exceeded it in stronger turbulence regimes. Luckily, this is ideal for the used steering algorithm and does not change the system performance requirements for a given turbulence regime. The frequency for this type of AO is also around 9 times smaller than Greenwood frequency and would subsequently decreas the requirements on the pointing system substantially[67]. However, as can be seen, the more severe the weather conditions, such as wind and vortexes due to thermal effects, the higher the frequency. This implies a system inherently has weather limitations which must be taken into account.

Lastly, as seen in Figure 4.4, the effect of turbulence is to spread out the spot. This is as characterized by the Fried parameter[19][23] is the coherence length over the telescope and is denoted as r_0. Its importance is hence two fold, namely the additional spread causes lower intensities and is off importance for the subsequent design of the receiver and distance between spots. However, it is also an important indicator for the importance of sub-aperture wavefront errors. The equation for the Fried parameter is shown in Equation 4.9.

$$r_0 = \left[0.846 \frac{\pi^2}{\lambda^2} sec(\zeta) \int_{z_0}^{40km} C_n^2(z) dz \right]^{-3/5} \tag{4.9}$$

The resulting angular diffraction must be multiplied with a factor D_T/r_0 to obtain the diffraction angle afterwards[19]. This is shown in Equation 4.10.

$$sin(\theta) = 1.22\frac{\lambda}{D_T}\frac{D_T}{r_0} = 1.22\frac{\lambda}{r_0} \quad if \quad r_0 > D_T \tag{4.10}$$

The practical effects of this is that smaller telescopes can be diffraction limited even when turbulence is present, due to the Fried parameter being larger than the telescope aperture diameter ($r_0 > D_T$). This implies that especially for smaller telescopes the effect of relatively large turbulence structures are not important. For larger telescopes, the increased telescope diameter will not improve the spot size. According to Hecht(page 229)[23], the Fried parameter is usually smaller than 20 cm. This implies that the increased telescope sizes above 20 cm would only sever the purpose to increase the amount signal power captured but will not improve the spot size without AO.

Regardless, for larger telescopes to be used in multi-beam communications with ground targets, it is clear that each link must be individually corrected for errors at least the size of its Fried parameter. One way this can be done is through the use of high resolution beam steering methods which can also super-impose the conjugate wavefront on the steering inputs with a high enough resolution to make a difference. Also, the use of equally high resolution wavefront sensors would be required for this as well. This would immediately make lower resolution micro-mirror arrays with resolutions on the order of 10x10 unsuitable. Furthermore, operation in more severe weather conditions would also result in the r_0 being even smaller implying that for this too there is a weather limitation.

To find the effect of mild turbulence on the propagation, a turbulence profile was chosen. The Hufnagel-Valley profile, taken from David H. Tofsted et all.[63], was selected for simplicity and wide use. Approximate wind profiles were also taken from the work by Glenn A. Tyler[67], Fig. 2, page 365. This approximate profile is presented in Figure 4.5. The resulting turbulence profile is shown in Figure 4.6.

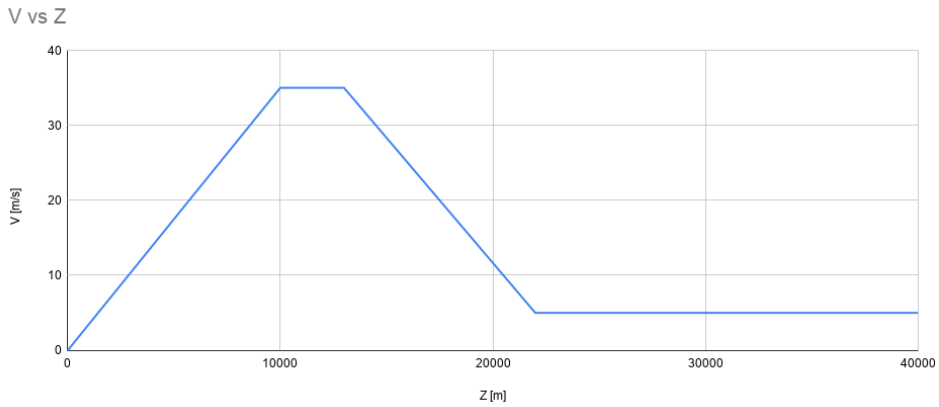

Figure 4.5: Illustrated is figure 33 found on page 82 from ”literature review” by Joshua Spaander[56]. It illustrates the approximate wind velocity profile which was taken from Fig. 2, page 365 in the work by Glenn A. Tyler[67].

4.1.4. A Word About Improvements for Free-Space Propagation

This section discusses some additional solutions, potential future improvements and developments which can be used to improve the design.

Bessel beams:

The beams discussed in this work are mostly Airy and Gaussain. However, a beam which theoretically does not diffract and subsequently does not diverge, is the Bessel beam[38]. These beams have phase corrections which follow a Bessel function of the first kind. This implies that the free-space losses due to divergence of the beam are almost eliminated. The resulting beam also has self healing properties, which implies it retains most of its shape and subsequent properties when passed through obstructions[69]. This results in the link being able to subsequently withstand stronger turbulence and so decreases the demands on an AO system[5].

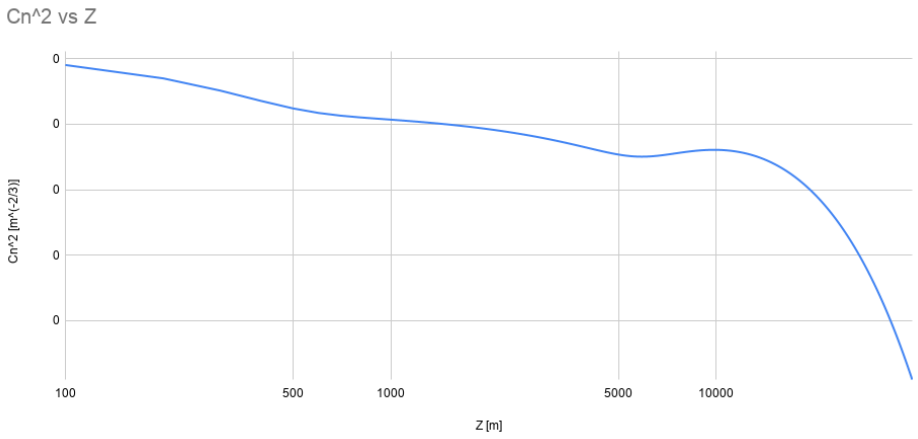

Figure 4.6: Shown is figure 34 found on page 83 from ”literature review” by Joshua Spaander[56]. It illustrates the turbulence profile for defined by Hufnagel-Valley, taken from David H. Tofsted et all.[63].

One problem with this type of beam is that they theoretically require an infinite amount of energy. However, approximations of these beams have been created successfully in the lab. Sadly, there were no practical demonstration found of such a Bessel beam traveling for longer distances than a few meters. Furthermore, the lack of divergence would also demand much stricter requirements on the pointing accuracy.

Pre-correction:

A solution to more severe weather conditions is to off-load the AO from the spacecraft and place this on the ground target instead. This is done by taking wavefront measurements from a downlink or guide star and using AO to correct these wavefronts. The resulting correction is a conjugate of the distortion that the wavefront will undergo by traveling through the atmosphere. When the out-going beam is put through the same AO, the wavefront is pre-distorted and hence the atmospheric turbulence will correct the wavefront. This is illustrated in Figure 4.7. Note that pre-correction can only be done on one side of the communication.

4.2. System Speed/Update Limitations

The speed by which the system must adjust the beam direction is dependent on numerous factors. One has already been described in section 4.1 and will be discussed in more detail. An other source of vibration is due to the spacecraft.

4.2.1. Turbulence

The already in section 4.1 discussed frequencies concern the Greenwood frequency[22] and the tip-tilt frequency by Tyler[67]. These frequencies are the required update frequency to counter the wavefront distortion due to turbulence. Considering that bright spot tracking leads to better performance and closer approximation to the algorithm compared to centroid tracking[67], this will be analyzed as well.

The term which considers the angle in Equation 4.6 at which the beam is traveling through the atmosphere, quickly grows after a few degrees. This is due to the increased distance traveled through the atmosphere and hence the beam encounters more turbulence. The maximum angle should be defined in order find the maximum frequency that can occur due to turbulence. This was chosen to be 50 degrees and was chosen to be sufficiently above the horizon. The reason for this precaution is because when beams travel too close to the horizon, the flat Earth assumption made in the equations does not hold. Furthermore, when beams travel further in turbulent media, additional effects such as branch cuts and points start occurring[20][4][57]. These are both hard to detect and correct for and hence 50 degrees is chosen.

Considering the Greenwood frequency, Equation 4.6 was numerically evaluated at 100 m discretization and at an angle of 50 degrees from the vertical, using the turbulence profile in Figure 4.5 and

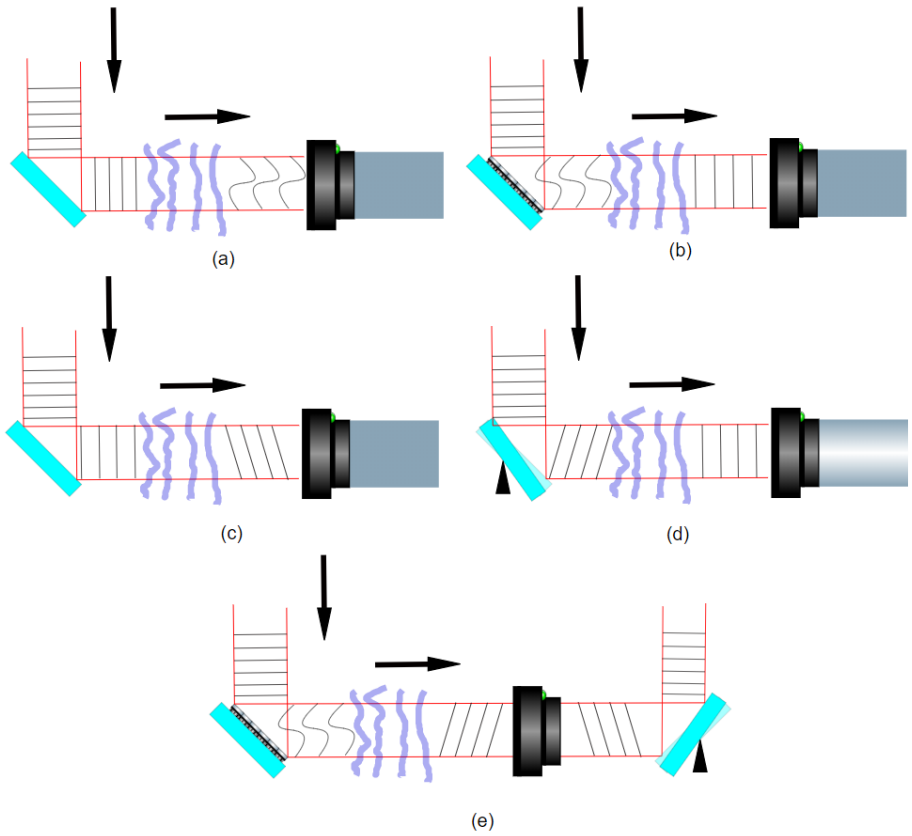

Figure 4.7: Shown is figure 32 found on page 81 from "literature review" by Joshua Spaander[56]. Shown are different methods by which adaptive optics can make improvements in the wavefront. The beams are propagated from left to right, with the transmitter on the left and the receiver on the right. (a) Shows the basic system, where the wavefront is deformed by the turbulence in the atmosphere. There is correction by a tip tilt mirror. (b) Illustrates the principle of pre-correction/pre-distortion, where a deformable mirror or other mechanism pre-distorts the wavefront in the exact opposite way the atmosphere will distort it. The result is that the atmosphere will subsequently corrects the wavefront. The light which travels back the other way would not require a second deformable mirror due to the same path principle; being distorted in the exact same way by the atmosphere and then corrected by the deformable mirror. This system would hence require only one set of adaptive optics. (c) When the structures in the turbulence are larger than the telescope optics (when the Fried parameter is proportional to the aperture diameter), the largest distortion component is the tip-tilt error. (d) Illustrates a pre-correction FSM for tip-tilt. (e) Illustrates a system with 2 tip-tilt FSMs to pre-correct for the atmosphere with a second FSM to correct for the satellite vibrations and other errors.

Figure 4.6, it was found to be 41.2 Hz. However, the frequencies for very bad weather conditions can exceed 100 Hz.

For bright spot tracking the Equation 4.8 is divided by the 6th root of the diameter of the telescope. One of the reasons is that the smaller and more frequently occurring structures in the turbulence do not cause tip-tilt corrections over the whole aperture. Analysis of the bright spot tracking frequency requires the initial sizing of the telescope diameter. Here, it is assumed that the telescope will be no smaller than 10 cm in diameter. Smaller than this will likely not allow for sufficient data rates due to the captures signal power. When the bright spot tracking is evaluated under the same conditions as the Greenwood frequency, the resulting frequency is 10 Hz. This is about a quarter of the Greenwood frequency, implying that the speed requirements are lower for a tip-tilt system. Note that it is customary to multiply with a safety factor to this of 5. This would imply a speed goal of 50 Hz.

It can be concluded that if a system is to do more comprehensive wavefront corrections, that the Greenwood frequency must be met, which is 41.2 Hz under these conditions. While a system which only corrects tip-tilt errors, under the conditions specified, should be able to update quicker than 10 Hz if it where to track the bright spot and ideally above 50 Hz.

4.2.2. Spacecraft Vibrations

The vibration of the spacecraft is hard to estimate and quantify, due to the enormous variation is spacecraft design. This work also does not design the spacecraft which supports the mutli-beam terminal. Some sources of vibrations can be considered however.

Considering pages 670 to 674 of the New SMAD[28], there are numerous values varying in the low 1-10 Hz up to 100 Hz for the fundamental frequencies. These vary between configurations, such as when in deployed state or extra stiffened for launch. Other factors include the size of the solar panels, mass, size, etc... Considering that these are the frequencies with the largest deflections, the system should be able to operate at atleast these.

Other sources of vibration are the momentum wheels, control moment gyros, or other rotating mechanisms. These can spin at very high rates. The numbers vary drastically and the size of the vibrations are hard to get by.

The New SMAD[28] recommends on page 569, in table 19-3, next to ”Jitter”, ”0.1 deg over 60 sec, 1 deg/s, 1 to 20 Hz; prevents excessive blurring of sensor data”. This was said in the context of control system requirements. Hence, the system should perform better than 20 Hz. This would already be covered by the fundamental frequency.

It can hence be concluded that for spacecraft jitter, 100 Hz should be sufficient. This was also found to be the case in the literature study[56], which can be seen in the requirements proposed and shown in Appendix C.

4.2.3. Update Rate

The requirements for the pointing system found in the literature study[56], also shown in Appendix C, mentions 5 different requirements based on similar analysis as with the turbulence and spacecraft vibrations.

1. **PS-CR-004:** The multi-beam steering/pointing system shall be able to operate at 40 Hz or higher.
2. **PS-CR-005:** The pointing system shall be able to correct for tip-tilt errors of at least 1 mrad jitter in the entire aperture at at least 100 Hz.
3. **PS-CR-006:** The pointing system shall be able to correct for at least 8.7 mrad at at least 10 Hz.
4. **PS-FC-004:** The pointing system shall be able to steer the brightest point in the spot at 100 Hz to stay within the coupling requirements.
5. **PS-FC-005:** Large perturbations of 0.5 deg/s at 10 Hz shall still be fiber coupled.

In order to satisfy the above requirements as well as the discussed sources in subsection 4.2.1 and subsection 4.2.2, it implies that the system must be able to correct the beam at a frequency/speed of 100 Hz. This also implies that the system must be able to read out the spot tracker at a frequency higher than 100 Hz.

4.3. Summary and conclusion

The free-space losses are very substantial over large distances, with the losses proportional to the signal power being smeared out over a large area due to beam divergence. There exists adjustments to the loss factor depending on the beam profile. The profile considered here is the Airy profile. Free space losses can be improved through using larger telescopes. However, the result would be more stringent pointing requirements due to the smaller angle. The result is that the free space losses, maximum telescope size and hence overall system performance are all related to the pointing accuracy. Improving the pointing accuracy would allow for larger telescopes and lower loss implying better performance. Other beam profiles, such as Bessel beams, could allow for smaller telescopes due to smaller beam divergence for similar telescope sizes, in effect decoupling this relation. However, the steering accuracy’s required would be far beyond what is deemed feasible. It is also not yet a proven technology.

It was found that the wavelengths around 1550 nm have acceptable transmission efficiencies of around 80%. This is a band of minimal absorption between 1700 nm and 1400 nm. The Erbium Doped Fiber Amplifiers would be ideally suited for amplification of these wavelengths.

Turbulence causes wavefront distortions consisting of sub-aperture distortion and tip-tilt error in the form of jitter. These affect the fiber coupling performance and hence must be considered. The atmospheric turbulence profile was estimated using the Hufnagel-Valley distribution, which is a rather mild turbulence profile. When using the relations for the Greenwood frequency and the derived expression for the tip-tilt, requirements for atmospheric corrections by the steering system were found to be between 10-50 Hz. Literature shows that the tip-tilt correction for this particular profile would suffice, however for more sever turbulence, the use adaptive optics to improve performance is required. What more, the size of the telescope on the receiver side determines the need for adaptive optics and the resulting spot size later in the system. This lends additional credence to higher resolution steering mechanisms which can also perform wavefront corrections.

The current requirements for a steering system update speed of 100 Hz seems to be suffice and taken as the lower bound.

5

Multi-beam System Design

This chapter will discuss the design of a multi-beam system in order to asses different limiting design factors. The design will attempt to full-fill the requirements set out in the literature study[56]. First a small summary will be given of the design. Then, the rest will then lead into the rest of the chapter.

Some designs have separated telescopes for incoming and outgoing beams. NODE[32][9][8][33][45][14], OCSD[29] and OPALS[41][1][74] do not support duplex optical communication but do use a different telescope for beacon tracking. Should this tracker be replaced with a receiver, it would imply that 2 telescopes are required. Work by Sidorovich et all.[53], while having a different approach, also fully separates the transmitters from the receivers, implying separate elements are required. The optical train being separated effectively implies components which are not shared. This comes at the cost of SWaP.

In contrast, ERDS[6][24], MCLCD[13], the work by Treibes et all.[66], Capots et all.[66] and Presley et all.[47] all have telescope components which are shared. Furthermore, the incoming and outgoing beams follow the same path through the telescope until split. Splitting, however, is done with free space optics. This implies there are still some components which are not shared. There is hence still room for improvement when considering sharing components.

Same path also allows for steering more beams due not having to handle incoming and outgoing beams separately. On the flip side, both angle and position of the beams must be changed. This requires 2 steering mechanisms and 2 spot trackers. To simplify the system, these spot trackers where placed at the same optical distance as the steering mechanisms, simplifying the control loop.

The design allows for the incoming and outgoing beams to follow the same path by incorporating 2 steering mechanisms. The signal is coupled into the fiber transceivers and are subsequently split there. The result is that the design created, shown in Figure 5.1, shares all the free space optical components. This implies that the resulting number of components are reduced and also allows for scaling.

The same path choice lends itself to the use of fiber based transceivers. This is because the use same path requires the incoming and outgoing beams to be pointed and located in the exact same way. The small fiber cross sections and long fibers imply there is no room for deviation, implying that signals which exit the fiber are propagated on the same axis. The fiber hardware performances are also very high, due to their extensive use on Earth for high end internet applications. The use of fiber transmitters for free space optical communications is also not new in space. In fact OCSD[29], NODE[32][9][8][33][45][14], OPALS[41][1][74] as well as all the multi-beam designs (except for Sidorovich et all.[53]) utilizes a fiber based transceivers.

For the design of the transmitter involved an investigation into the different configurations and hardware. It was found that the Master Oscillator Power Amplifier (MOPA) configuration combined high performance with acceptable efficiency. The design of the receiver allows for splitting the incoming and outgoing beams without the need for selecting for polarization or wavelength. The transceiver can be seen in Figure 5.2.

Note, that the optics and electronics required for transmitting and receiving where not designed as these are available COTS.

The coarse pointing systems are often present on single beam designs. These can be in the form of pointing the satellites, such as in NODE, or articulated members, such as EDRS[6][24] and

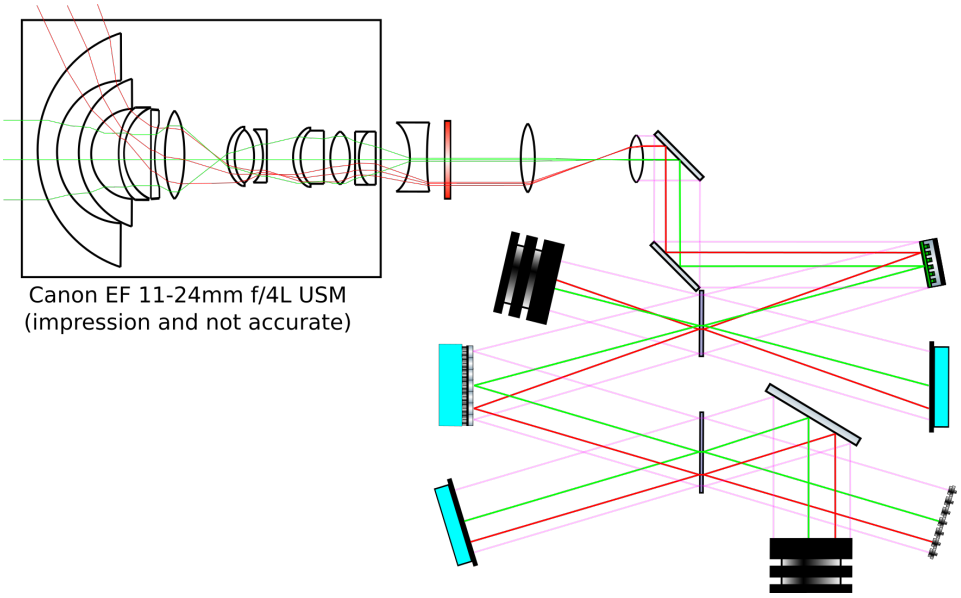

Figure 5.1: Depicted is the designed optical train. Shown are the incoming parallel rays from 2 far away targets. The first target is depicted in green and is directly on the optical axis. The second red target is at the extreme periphery of the wide angle telescope. The beams are directed into the telescope and are focused at the focal point of the lens system. Before this however, it is collimated at the appropriate beam diameter. The beams are now parallel. It is subsequently passed through an optical filter to filter out unwanted light and reflect it back out through the telescope. It then enters a re-imaging stage where the appropriate cross section and beam size is realized. Then from the perspective of the incoming beams (left to right) subsequently enter the steering stage of the system where the SLM steers the beams to the correct location on the MMA which is coupled to the fiber location. After reflecting of the MMA, it steers the beams into the correct fiber. The beams are split by beam splitter plates along their path to the spot trackers. The first of the spot trackers has the same optical path as the MMA and hence gives feedback to the SLM. The second is optically the same optical path as the fiber and hence provide feedback to the MMA's. The bi-directionallity of the system implies that incoming and outgoing beams follow the same optical path. Hence, the generated outgoing beams will also be split and are dumped into the beam dumps to prevent stray light.

OPALS[41][1][74]. However steering one optical telescope while dealing with multiple beams coming in at multiple angles, would make it impossible to accommodate all of them. Furthermore, all the multi-beam systems considered in chapter 2 do not accommodate for large angular deviations and hence do not solve this problem. All accept for the work by Sidorovich et all.[53], which employs a glass ball for wide FOV. This would cause distortion and subsequent adverse effects on fiber coupling and is hence not an ideal solution.

The system designed here solves this problem by using a rectilinear lens. This is depicted at the start of the optical train in Figure 5.1. This lens maps angles onto a grid and therefore causes minimal distortion and improved fiber coupling. The system can accommodate beams within the wide FOV hence not requiring a coarse pointing system (assuming the terminal is pointed so that its targets are within the FOV).

This chapter will go in to more detail on the design process and trade-offs. To do so, it serves to start with understanding the overall goal. The overall goal of the system is to communicate with multiple targets. Hence, the chosen measure of the system abilities is primarily the data rates. Each stage in the travel of the light between the terminal and the targets is affected. Hence, a natural method to maintain overview will be via the link budget.

The capacity per link is an important characteristic and must be comparable to current link capacities to be competitive. Here a practical approach is taken, where each stage of the signal traveling from the terminal to the ground station receiver is lumped in stages with efficiencies. The link budget is dependent on many aspects of the design of the terminal. However, the theoretical maximum link capacity is described by the Shannon–Hartley theorem:

$$C = Blog_2\left(1 + \frac{S}{N}\right) \tag{5.1}$$

Where C is the link capacity in bits per second (b/s or bps), B the bandwidth in Hz, S the signal

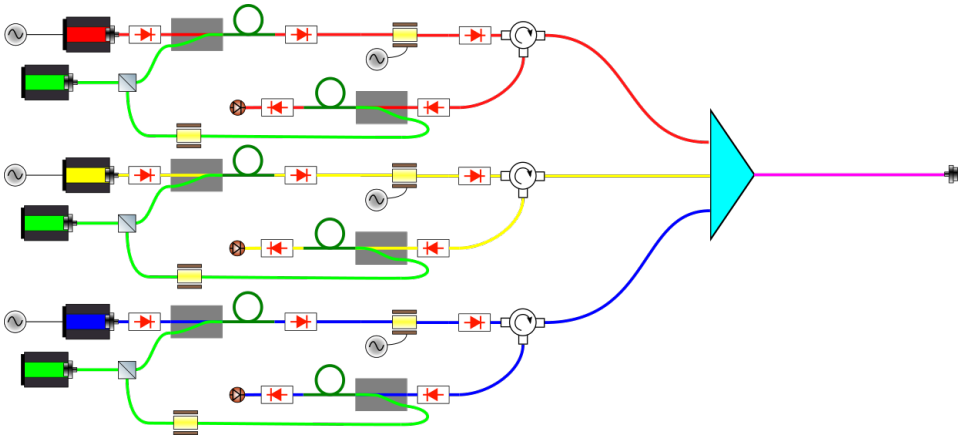

Figure 5.2: Multiplexed version of Figure 5.34 which uses a mux to separate and combine 3 different frequencies. The combined wavelengths are shown in purple while the separated frequencies are shown in red, blue and yellow. The pump laser wavelength is shown in green.

power in W and N the noise power in Watt. This will serve as a guide to evaluate the link performance. This can only be done when considering signal power. There are numerous aspects of the link budget that have to be designed and modeled for, which are also out of the scope of this report. These are for example, the design of the transceivers on the target spacecraft and ground stations.

Numerous requirements where also derived from the available literature in the literature study. These are shown in Appendix C. Not all of these are relevant for the design of this system and this will be discussed in the next relevant sections. However some will guide the design.

The next sections will discuss the link budget and are in part based on the literature study[56] together with new insights and specifically pertaining the control system.

The chapter will start with discussing the design and losses due to fiber coupling to aid in the transceiver trade-off. The effects of miss alignment, jitter and steering accuracy's on the performance will be discussed. Then the losses due to pixel allocations within the steering system will be discussed with the aid of simulations. Mainly, the effects of beam cropping and diffraction effects on the system performance will be discussed to aid in the steering mechanism choice.

Using the discussed design aspects, the optical train design will be produced. Primarily trade-offs for different hardware components and system layouts/configurations are discussed. These include the feedback loop, fiber coupling design, steering mechanism choice, telescope selection/design and final optical train assembly. This concludes with an illustration of the final optical train in Figure 5.1 as well as Figure 5.32.

This is then followed by the transceiver design, with similar trade-offs for different system configurations and hardware components. The final design is shown in Figure 5.2 and Figure 5.2.

Lastly, the final link budget is evaluated to find the theoretical maximum data rate the system can attain, followed by the conclusion and summary.

5.1. Losses and Design in Fiber Coupling

The transceiver of the system is an important aspect of the link performance. It is common to use fiber receivers due to their performance and technology readiness level. They have been used on NODE[32][9][8][45][14], Optical Communication and Sensor Demonstration[29] and OPALS[41] although notably as transmitters. They also allow out going beams to be emitted from the same location as the beams are received, which allow them to follow the same path in reverse directly to the target.

The transmission from a fiber is less interesting for this work, however, becomes much more relevant when considering the receiving aspects. This brings with it the simple sounding but complicated act of coupling the incoming beams into the fibers. In the literature study[56], the works on this have been discussed at much greater length, with all the used equations derived extensively. This work will condense it and so will not discuss derivations. It will also combine it with previously discussed aspects and derive it's approximate effects on the system as a whole.

5.1.1. Maximum Fiber Coupling Efficiency and Ideal Spot Size

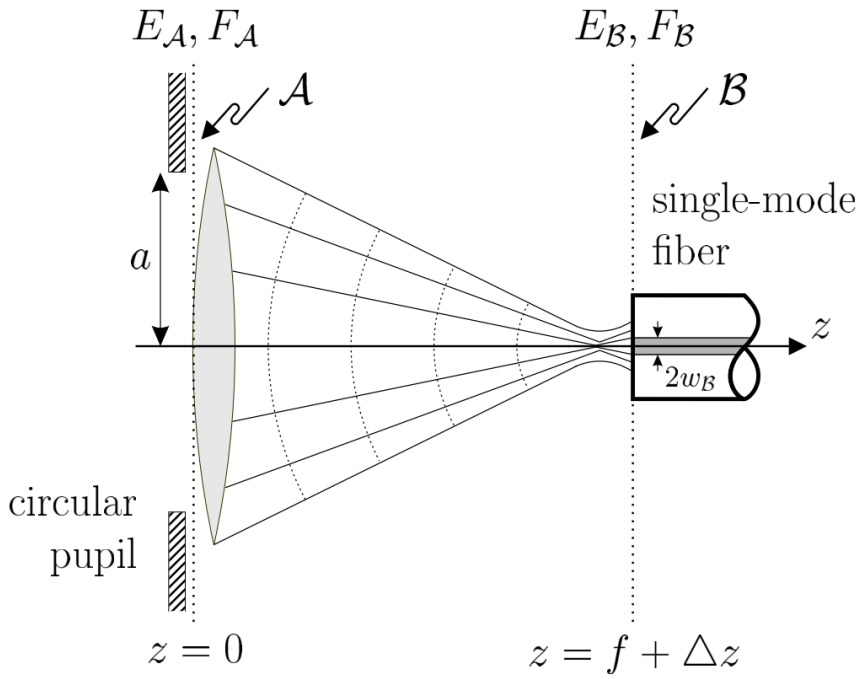

Figure 5.3: Shown is a depiction of fiber coupling, seen in Figure 1 found in page 19 in "Alignment tolerances for plane wave to single-mode fiber coupling and their mitigation by use of pigtailed collimators" by Oswald Wallner, Pater J. Winzer, Walter R[71]. The axial distance is along the z axis with the perpendicular axes on the fiber plane denoted by x and y.

The fiber has a certain width and signal mode fibers have internal beam profiles which are approximately Gaussian with a radius equal to the mode field radius with a planar wavefront. The beam projected onto the fiber has an Airy profile and the radius of this profile can be adjusted. Due to the differences in Airy beam profiles and Gaussian profiles, there is an optimum. The formula for the efficiency is given in Equation 5.2[71]. Introducing $\beta = R/\omega_A$, where β is the ratio between R, the aperture radius, and ω_A being the back propagated fiber mode field radius to the lens plane. This is is related to the fiber mode field radius, ω_B, as $\omega_A = \frac{\lambda f}{\pi \omega_B}$. The system is illustrated in Figure 5.3.

$$\eta = \frac{2}{\beta^2}\left(1 - exp\left(-\beta^2\right)\right)^2 \tag{5.2}$$

Equation 5.2 is plotted in Figure 5.4. Shown is that the maximum efficiency is around 81%, where the aperture radius is 1.2 of the back propagated mode field radius. This efficiency is the maximum coupling efficiency and will hence be the maximum efficiency of the signal power transfer. The optimal radius changes with the offset and vibration, lowering the maximum efficiency. This will be discussed later in this section.

5.1.2. Effect of Fiber Misalignment

The alignment of the beam to the fiber also changes the efficiency of the system. There are 5 offsets which can be normalized to allow for general application. The first two are the linear offsets in the perpendicular plane denoted by x, for left and right, and y, for up and down. To obtain the planar wavefront in a Gaussian beam, the waist of the beam must be at the fiber input face. Implying that axial offsets, Δz, also lead to coupling losses, the axial direction denoted by z. The fiber face and the beam could also be pointed in different directions with respect to the z axis into the x and y directions. These are denoted by ϕ_x and ϕ_y.

The normalizations are done with respect to their relevant optical parameters. For the lateral offsets, Δx and Δy, are normalized to the fiber mode field radius ω_B. The x and y coordinates are normalized to

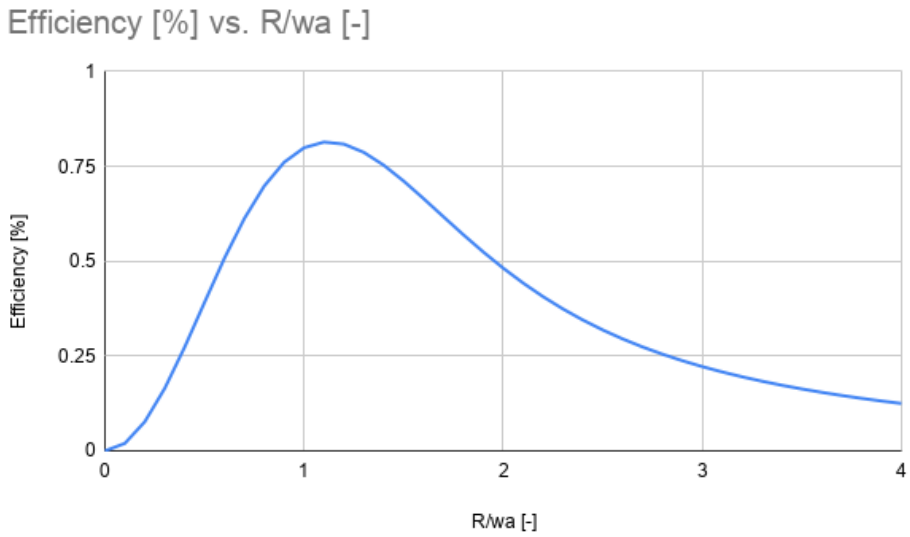

Figure 5.4: Shown is Figure 12 found on page 29 from ”literature review” by Joshua Spaander[56]. The function plotted is how an increasing spot size normalized to the mode field radius changes the efficiency of the fiber coupling assuming the spot is centered. The maximum efficiency is 81% at a 1.2 normalized radius.

the back-propagated mode field radius ω_A due to the comparison being done on the lens input plane. The angular offsets are normalized with respect to half the f-number of the lens.

$$\begin{aligned} \Delta x \rightarrow \Delta x' = \frac{\Delta x}{\omega_B} \quad \Delta y \rightarrow \Delta y' = \frac{\Delta y}{\omega_B} \quad \Delta z \rightarrow \Delta z' = \frac{\Delta z R}{f \omega_B} \\ \Delta \Phi_x \rightarrow \Delta \Phi'_x = \Delta \Phi_x \frac{f}{R} = \Delta \Phi_x \frac{N}{2}, \quad \Delta \Phi_y \rightarrow \Delta \Phi'_y = \Delta \Phi_y \frac{N}{2} \\ x \rightarrow \mu = \frac{x}{w_A} \quad y \rightarrow \nu = \frac{y}{w_A} \end{aligned} \tag{5.3}$$

The normalized expression derived by Oswald Wallner, Pater J. Winzer, Walter R. Leeb[71] is given in Equation 5.4.

$$\eta = \left| \frac{\sqrt{2}}{\pi \beta} \int \int exp\left(-\left(1 - j\frac{\Delta z'}{\beta}\right)\left((\mu - \beta \Delta \phi'_x)^2 + (\nu - \beta \Delta \phi'_y)^2\right)\right) exp\left(j2(\Delta x' \mu + \Delta y' \nu)\right) d\mu d\nu \right|^2 \tag{5.4}$$

Note that these assume relatively small errors. Much more substantial errors might result in efficiencies which divert from this expression. However, it provides a way to specify the requirements for building the system as well as being able to predict the efficiency drop due to pointing accuracy and offsets.

Equation 5.4 is a function of 6 misalignment variables of which $\Delta x'$ and $\Delta y'$ are interchangeable as well as $\Delta \phi'_x$ and $\Delta \phi'_y$, implying that there are 3 different types offsets to consider. The effects on the efficiency of each type of offset is plotted in Figure 5.5.

Figure 5.5 shows that each misalignment is not created equal. When considering each normalized misalignment, it might be alluring to say that defocus is of little concern. However, considering that the defocus is normalized to the considerably small single mode fiber mode field radius, reduces the tolerance substantially. The mode field radius is on the order of 1.5 micro meters. Consequently, the fiber angular misalignment is the most resilient due to this fact.

There is also an optical design parameter of β. This has effect on the angular and offset performance. The effect of β on the offset is shown in Figure 5.6. It is clear that smaller spots do not result in better performance with or without spots. Larger spots also perform worse, except for large offsets where larger spots start to outperform. This is due to the large spot having a larger spread implying

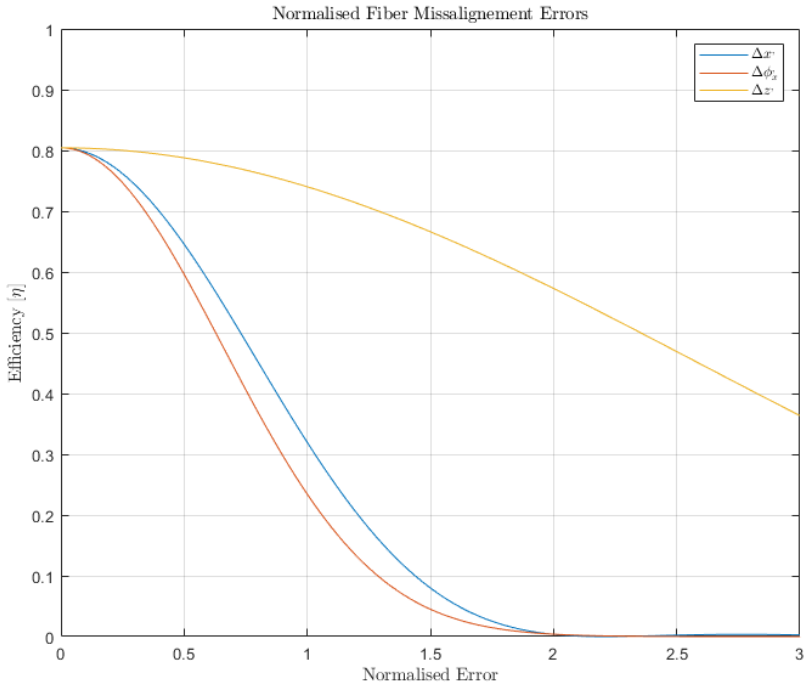

Figure 5.5: The effects of different normalized fiber misalignment errors on the efficiency of fiber coupling. 3 lines are depicted, from left to right; the left/red line depicts the normalized angular error, middle/blue line the offset error and right/yellow line the axial/defocus error. The relevant labels are shown in the top right.

more energy at the edges of the beam and hence more is coupled into the fiber. therefore, larger spot diameters will be more resilient to larger offsets. This should be adjusted as a direct result of the pointing accuracy.

When considering a typical[43] single mode fiber can have a mode field radius of 4 μm and a lens system with a focal length of 25 cm and a radius of 7 cm ($\beta = 1.1$), the following are the un-normalised 40% efficiency misalignment values are:

1. Offset: $3.52e-6$ [m]. From the lens over a 25 cm focal length = $1.41e-5$ [rad] = $8.06e-4$ [deg]
2. Angular: 0.2128 [rad] = 12.2 [deg] For two way communication: $1.41e-5$ [rad] = $8.06e-4$ [deg]
3. Defocus: $4.03e-5$ [m]

The planar offset accuracy is related to the required steering mechanism accuracy. If it can be assumed that the optical system can be reduced down to one lens, accuracy by which the angular misalignment can be tolerated is the inverse sine of the resulting triangle. The steering mechanism, which corrects for the offsets, would also be required to steer at this accuracy when placed at the focal distance away. However, due to the steering mechanism being integrated into the optical train, it can be placed closer to the fibers and relax the steering accuracy requirements.

It can be seen that the misalignment tolerances for 40% are already quite low. This has profound consequences for the system design. For example, the offset tolerances increase the steering accuracy requirements for the steering mechanism. The low defocus tolerances can also be problematic, because the path length through the optical train can vary when the targets are moving in the field of view.

One method around this problem is analyzed by Oswald Wallner, Peter J. Winzer and Walter R. Leeb[71]. The solution proposed is the introduction of a GRIN lens (GRadient-INdex) on the fiber, as illustrated in Figure 5.7. These lenses consist of a transparent media with varying refraction index gradients, in such a way as to focus the light into the fiber.

For a GRIN lens with an effective mode field radius of ω_C is an increase by a factor $A = \omega_C/\omega_B$ compared to the initial mode field radius. However, this also has converse effects that for the same

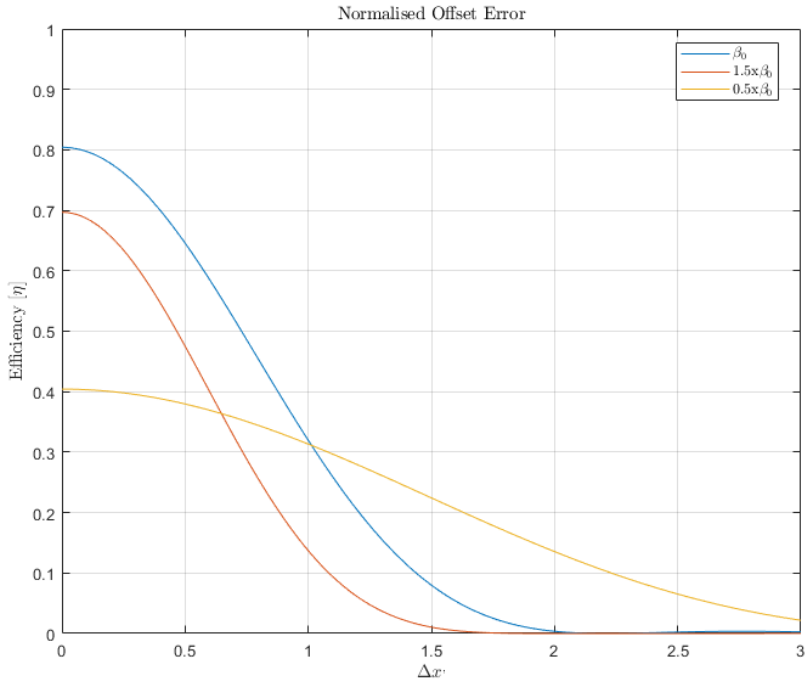

Figure 5.6: The effect of different spot sizes on the coupling efficiency. From the top/blue line; The top/blue line shows the efficiency drop due to a normalized offset with a β the highest theoretically achievable efficiency, the middle/red line is a 1.5 times that (increased lens radius or decreased field mode radius hence relatively smaller spot) and the bottom/yellow line 0.5 times (increased relative spot size).

system, the focal length and hence the volume of the system increases with the same amount. This is illustrated in Equation 5.5. It has no effect on β due to the principles of fiber coupling remaining the same, as shown in Equation 5.6.

$$f_C = Af \tag{5.5}$$

$$\begin{aligned} \beta &= \frac{\pi R \omega_c}{\lambda f_c} = \frac{\pi R A \omega}{\lambda A f} \\ &= \frac{\pi R \omega}{\lambda f} \end{aligned} \tag{5.6}$$

However, Figure 5.7 shows how the inclusion of a GRIN lens makes the fiber a larger target to hit. Hence, the pointing requirements can be relaxed by a factor A, defocus by a factor A^2 as well while angular tolerances are tightened by a factor A. This is shown in Equation 5.7 and Equation 5.8. Note, that the tolerances in the y direction are the same as for the x direction, due to these being the same type of misalignment.

$$\Delta x' = \frac{\Delta x}{\omega_C} = \frac{\Delta x}{A\omega}, \quad \Delta z' = \Delta z \frac{R}{f_c \omega_C} = \Delta z \frac{R}{A^2 f \omega} \tag{5.7}$$

$$\Delta \Phi_x' = \Delta \Phi_x \frac{f_C}{R} = \Delta \Phi_x \frac{Af}{R} \tag{5.8}$$

The reason for these alterations is due to Gaussian beam transportation. The back propagation of the Gaussian fiber profile behaves the same as a Gaussain beam because it is identical. This implies that the beam radius, which is equal to that of the fiber mode field radius, at the waist determines the beam spread. So artificially increasing the effective mode field radius would subsequently increase the effective beam waist radius. Hence, larger beam radii require longer focal lengths to produce the

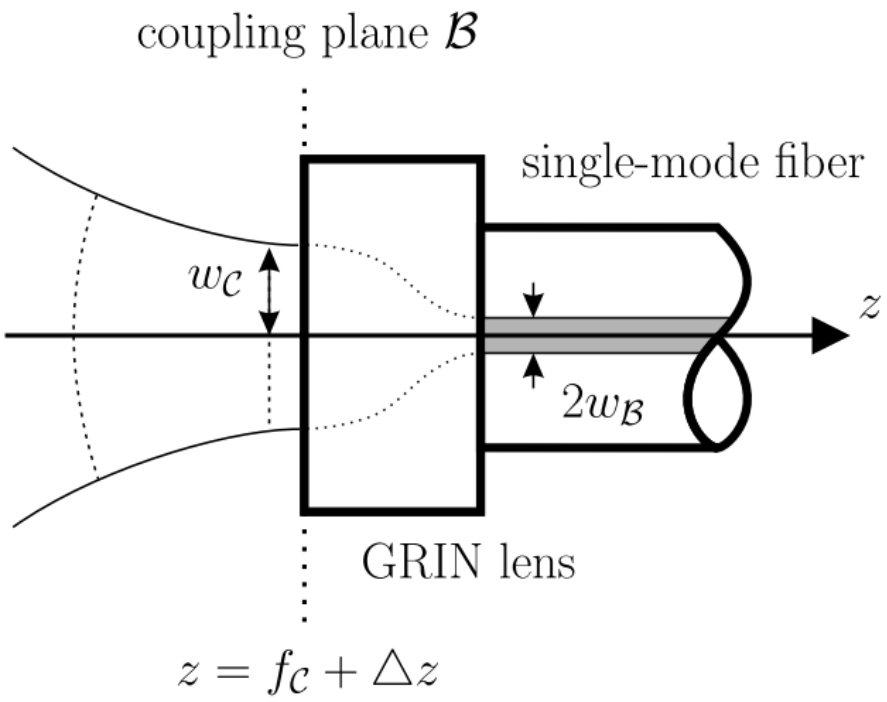

Figure 5.7: Shown is Figure 6 found on page 24 in the work "Alignment tolerances for plane-wave to single-mode fiber coupling and their mitigation by use of pigtailed collimators" by Oswald Wallner, Peter J. Winzer and Walter R. Leeb[71]. What is illustrated is the application of the GRIN lens and how it can serve as an intermediary for reducing the mode field radius to allow for fiber coupling.

target beam waist radius. The drawback is that larger angular accuracy over the longer distance due to smaller beam spread. The benefits are the larger spots, relaxing the tolerances in the offsets. However, the biggest improvement is the defocus tolerances, due to the beam radius being approximately the same radius as the waist over longer distances.

This is also true when considering the two way communication for a multi-beam terminal due to the larger focal length. The reality is that the use of a GRIN lens implies the system must be re-designed to accommodate it and that the system size will likely increase. This increases SWaP while decreasing system stability. However, if the steering mechanism can be placed closer, the requirements for the pointing accuracy can be relaxed.

Considering a situation where a GRIN lens with diameter of 1.8 [mm][34], or a radius of 0.9 mm, on a fiber end is used would result in $A = 225$. Hence, for the same system discussed, a lens system with a focal length of 225 x 25 cm and a radius of 7 cm ($\beta = 1.1$) the following are the un-normalised misalignment values for 40% efficiency:

1. Offset: $7.92e-4$ [m]. From the lens over a 225 x 25 cm focal length = $1.41e-5$ [rad] = $8.06e-4$ [deg]
2. Angular: $9.46e-4$ [rad] = $5.41e-2$ [deg] For two way and same path communication: $1.41e-5$ [rad] = $8.06e-4$ [deg]
3. Defocus: 2.04 [m]

This relaxes the tolerances considerably for offsets and especially for the defocus. In this case, unless the system dimensions are beyond 8 [m], increased path lengths of a few centimeters will not matter. This implies that GRIN lenses are crucial for use in multi-beam systems. The angular requirements remain the same due to longer focal lengths, however these can be achieved through correct fiber installation in the system and placing the steering mechanism closer to the fibers. The increase focal length from 25 cm to 112 m is unrealistic and will have to be shortened. But this can be done in the optical train.

In theory, the radius of the telescope/lens can also be reduced instead of increasing the focal length. This has consequences for the signal power captured and hence the overall system performance. More over, the spot size is also limited by atmospheric disturbance, hence, there is an inherent minimal requirement for the GRIN lens radius. Furthermore, the normalized radius β can also be optimized.

The minimal efficiency will be taken to be 60%. This would result in the maximum ranges for each normalized error being the following:

1. Normalized Offset: 0.6.
2. Normalized Angular: 0.5. Note that for 2 way communication this will have to be derived from the normalized offset and the focus length.
3. Normalized Defocus: 1.9.

5.1.3. Effect of Jitter and Fiber Coupling Efficiency

Similar to static misalignment's, there are also misalignment's which occur due to jitter. The jitter can originate from vibrations and atmospheric interference. Here, the offset jitter will be discussed and the other jitters are considered to be negligible. Both Jing Ma, Fang Zhao, Liying Tan, Siyuan Yu, Qiqi Han[30] and Morio Toyoshima[64] describe the same principles for efficiency and jitter. However, the work by Jing Ma, Fang Zhao, Liying Tan, Siyuan Yu, Qiqi Han[30] is used here, due to the use of principles of backpropagation. This makes it easier to use and more inline with the derivations on misalignements in subsection 5.1.2. Note that here too, the respective works contain brief derivations, with the literature study[56] containing slightly more in depth analysis pertaining to their derivations and use. Here, the application to the system design will be discussed.

The equation derived by Jing Ma et all.[30] and introducing $\beta = R/\omega_A$ the result of the integral is as follows:

$$\langle \eta \rangle = \frac{2}{\left(2\left(\frac{\sigma}{\omega_B}\right)^2 + 1\right)^2 \beta^2}\left(1 - exp\left(-\left(1 + \left(\frac{\sigma}{\omega_B}\right)^2\right)\beta^2\right)\right)^2 \tag{5.9}$$

Where σ is the rms jitter. The effect of the jitter on the efficiency can hence be expressed directly. When finding the optimum β for a given jitter rms, Equation 5.9 can be differentiated with respect to β and equated to zero.

$$\frac{d\langle \eta \rangle}{d\beta} = \left(2\left(\left(\frac{\sigma}{\omega_B}\right)^2 + 1\right)\beta_{opt}^2 + 1\right)exp\left(-\left(\left(\frac{\sigma}{\omega_B}\right)^2 + 1\right)\beta_{opt}^2\right) - 1 = 0 \tag{5.10}$$

When β is made the subject of the equation, Equation 5.11 results.

$$\beta_{opt} = \sqrt{\frac{1.2564}{\frac{2\sigma^2}{\omega_B^2} + 1}} \tag{5.11}$$

Through substitution back in to Equation 5.9, the maximum efficiency for a given jitter with optimum beta can be found. This is expressed in Equation 5.12.

$$\langle \eta_{max} \rangle = 0.8145 \frac{1}{\frac{2\sigma^2}{\omega_B^2} + 1} \tag{5.12}$$

When these two equations are graphed, the resulting plots are shown in Figure 5.8 and Figure 5.9. From Figure 5.8 it can be observed that the optimal β becomes smaller for a given normalized jitter rms. This would imply that the optimal spot size increases with increasing jitter, similarly to regular fiber offsets.

The efficiency, shown in Figure 5.9, indicates that the efficiency drops sharply to 25% just after one mode field radius of rms jitter. This implies that the jitter is a very important variable for the overall system performance.

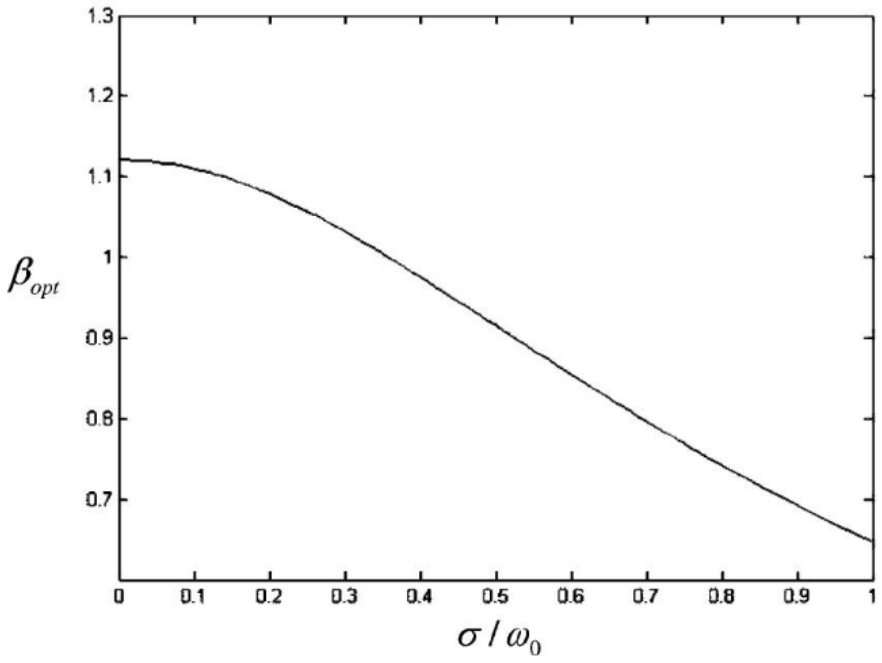

Figure 5.8: Illustrated is a plot taken from Figure 5 on page 5187 in the work "Plane wave coupling into single-mode fiber in the presence of random angular jitter" by Jing Ma, Fang Zhao, Liying Tan, Siyuan Yu, and Qiqi Han[30]. The graph plots the optimal β against the normalized jitter and shows that smaller β and hence larger spots are more optimal with increased jitter.

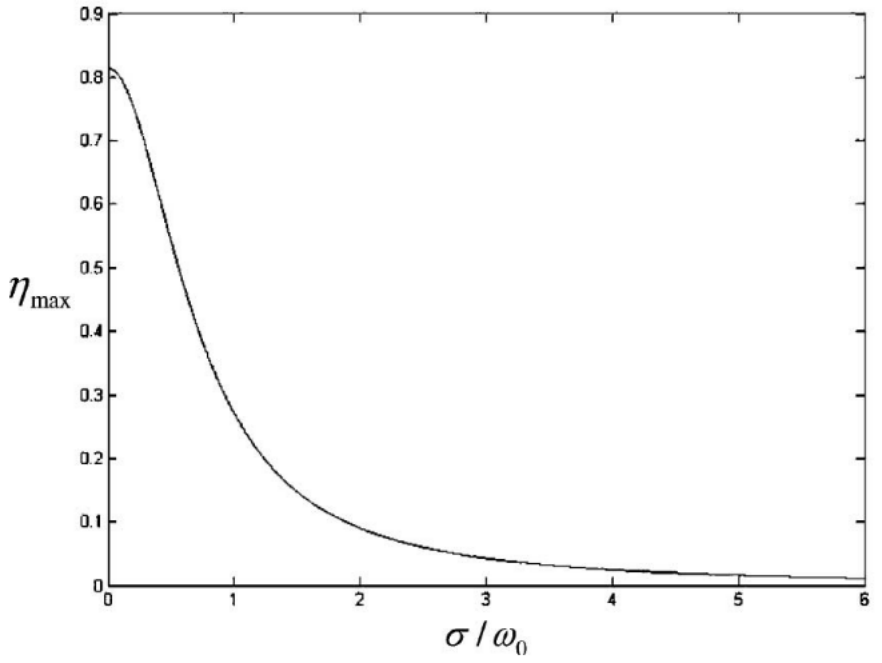

Figure 5.9: Illustrated is a plot taken from Figure 6 on page 5187 in the work "Plane wave coupling into single-mode fiber in the presence of random angular jitter" by Jing Ma, Fang Zhao, Liying Tan, Siyuan Yu, and Qiqi Han[30]. It indicates that for a given optimized spot radius for a given jitter that the maximum coupling efficiency, η, reduces. This shows that the presence of jitter will lead to decreased efficiency.

Atmospheric turbulence produces scintillation and speckles. This has been analyzed by Yamaç Dikmelik and Frederic M. Davidson[17]. Through a comprehensive derivation, the result is the following expression:

$$\eta_c = 8a^2 \int_0^1 \int_0^1 exp\left(-\left(a^2 + \frac{A_R}{A_C}\right)(x_1^2 + x_2^2)\right) I_0\left(2\frac{A_R}{A_C}x_1x_2\right) x_1x_2 dx_1 dx_2 \tag{5.13}$$

Where x_1 and x_2 are the normalized radial integration variables, expressed as $2r/D_R$, for the receiver and lens radius respectively. A_R and A_C are the receiver area and spatial coherence area. The coherence area is related to the coherence length, $A_C = \pi\rho_C^2$ which in turn is related to the diffraction structures $\rho_C = (1.46C_n^2k^2L)^{-3/5}$. The ratio between them is proportional to the number of speckles and their size. The beam energy is split among multiple speckles as well as decreased overall, implying it is an important aspect of the coupling efficiency. The coupling geometry, $a = \frac{D_R\pi\omega_B}{2\lambda f}$, describes the geometric aspects of the coupling, which too affect fiber coupling efficiency. The results for the analysis are given in Figure 5.10 with respect to the number of speckles and with respect to C_n^2 in Figure 5.11.

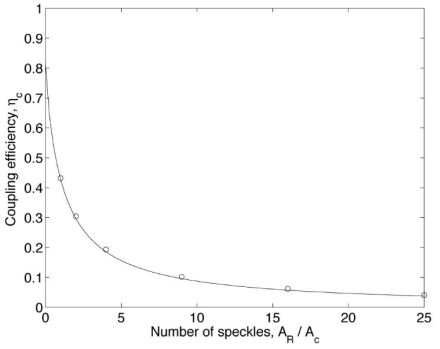

Fig. 2. Fiber-coupling efficiency as a function of the number of speckles A_R/A_C over the receiver aperture. The coupling-geometry parameter $a = 1.12$ for the curve. The circles represent the maximum coupling efficiency that can be obtained by optimizing a for six different values of A_R/A_C.

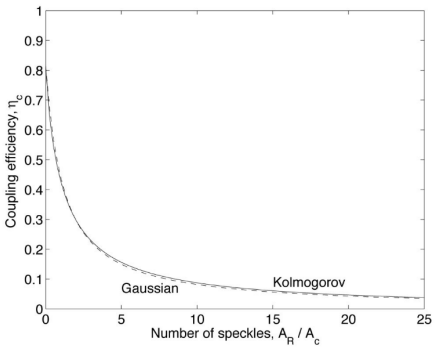

Fig. 3. Fiber-coupling efficiency as a function of the number of speckles A_R/A_C over the receiver aperture for $a = 1.12$. The two curves are obtained by using the mutual coherence function for the Kolmogorov spectrum (solid curve) and the Gaussian approximation to the mutual coherence function (dashed curve).

Figure 5.10: Shown are 2 plots taken from Figures 2 and 3 on page 4949 in the work "Fiber-coupling efficiency for free-space optical communication through atmospheric turbulence" by Yamaç Dikmelik and Frederic M. Davidson[17]. It shows that increasing number of speckles severely limit the efficiency of the subsequent fiber coupling. For both graphs, the line starts at 81% which occurs at 0 speckles. As the number of speckles are increased the efficiency drops to around 15% at 5 speckles. The curves in Fig. 2 and Fig. 3 (the Gaussian one) was made using the coupling geometry, a = 1.12. Fig. 3 shows the difference between the assumption of a Gaussian distribution and how close it is to the Kolmogorov distribution.

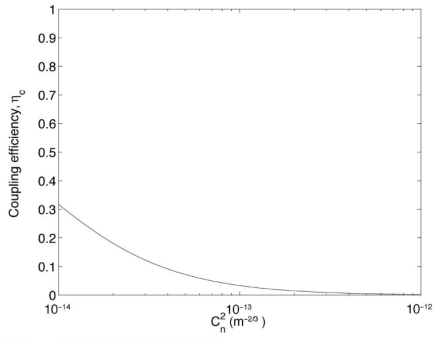

Fig. 4. Fiber-coupling efficiency as a function of C_n^2 for a link distance of 1 km, where $D_R = 10$ cm, $a = 1.12$, and $\lambda = 1.55$ μm.

Figure 5.11: Shown is a plot taken from Figure 4 on page 4950 in the work "Fiber-coupling efficiency for free-space optical communication through atmospheric turbulence" by Yamaç Dikmelik and Frederic M. Davidson[17]. The plot shows the relation between the turbulence strength (C_n^2) and the fiber coupling efficiency. Note, the plot does not start from 0. It shows that even for moderate turbulence the coupling efficiency drops substantially.

As is expected, more turbulence and more speckles result in lower fiber coupling performances. Part of the gains in using adaptive optics to correct the wavefront is increased efficiency from removing the speckles. This adds to the benefits of having high resolution steering systems.

Considering the previous limit of 60%, the effects of jitter and atmospheric effects will have to be fit into that value. This would imply that adaptive optics will be required for more turbulence applications. Hence, this aspect will be omitted as it is out of the scope of the thesis.

To achieve atleast 60% with jitter would imply the system has to limit the normalized jitter (σ/ω_B) to 0.42, when the optimal β is set to 0.96.

5.2. Losses and Design Due to Pixel Allocations

The control of the beams requires allocation of steering area on the beam control surface (MMA's, SLM's, piezo arrays, etc...). The allocation of area per spot depends on the distance between spots. When the distance is small, the resulting area allocated to the spot decreases and the shape is altered by the discrete surfaces. These are in the form of mirrors and pixels. MMA's tend to be low resolution on the order of 10x10 while SLM's are high resolutions[55][26].

The algorithm used is the one described in chapter 6.

5.2.1. High Resolution Beam Control

The allocation of area for a high resolution beam control can be approximated through a perfect circle. The size of the circle can increase and decrease as the spots move further and closer away respectively. This changes the effective size of the aperture and decreases the signal power though cropping the beam.

Considering a beam with an Airy profile, such as those expected from incoming beams. When the allocated area becomes smaller, the resulting beam is cropped and the signal strength is decreased. The equation for the intensity of an Airy disk is shown in Equation 4.2. However is simplified to the following:

$$I(x) = \left(\frac{2J_1(x)}{x}\right)^2 \tag{5.14}$$

Where in this case, $x = kD_T sin(\theta) = kD_T r/R$, with r being the distance to the view point of the center to the observation point and R is the maximum radius. The parameter x can hence be seen as a normalized radius. The integral is best done in polar coordinates.

$$P(x) = \int_0^x \int_0^{2\pi} \left(\frac{2J_1(x)}{x}\right)^2 x d\phi dx \tag{5.15}$$

When evaluating this integral in Wolfram Alpha, the result as a function of the normalized radius is shown in Equation 5.16, angular Equation 5.17 and radial Equation 5.18.

$$P(x) = -4\pi(J_0(x)^2 + J_1(x)^2 - 1) \tag{5.16}$$

$$P(\theta) = -4\pi(J_0(kD_T sin(\theta))^2 + J_1(kD_T sin(\theta))^2 - 1) \tag{5.17}$$

$$P(r) = -4\pi\left(J_0\left(kD_T\frac{r}{R}\right)^2 + J_1\left(kD_T sin\left(kD_T\frac{r}{R}\right)\right)^2 - 1\right) \tag{5.18}$$

The function plotted is shown in Figure 5.12. As can be seen, the central fringe contains 87% of the beam and 95% of the power has been captured after the first fringe. This implies that the circular area allocated to the beam in this case must be larger than the first fringe to not have a noticeable effect. Hence, if the radius of control surface is roughly twice that of the beam radius/central fringe radius than there is no noticeable effect. However, below one beam radius the signal power will drop sharply, being at half power at about 40% of the radius.

The same analysis can be done for outgoing beams which can have a Gaussian profile. The power can be found similarly considering the electric field described in Equation 5.19[68][23],

$$E = E_0\frac{\omega_0}{\omega(z)}exp\left(\frac{-r^2}{w^2(z)} - j\left(kz + \frac{kr^2}{2R(z)} + atan\left(\frac{z}{z_0}\right)\right)\right) \tag{5.19}$$

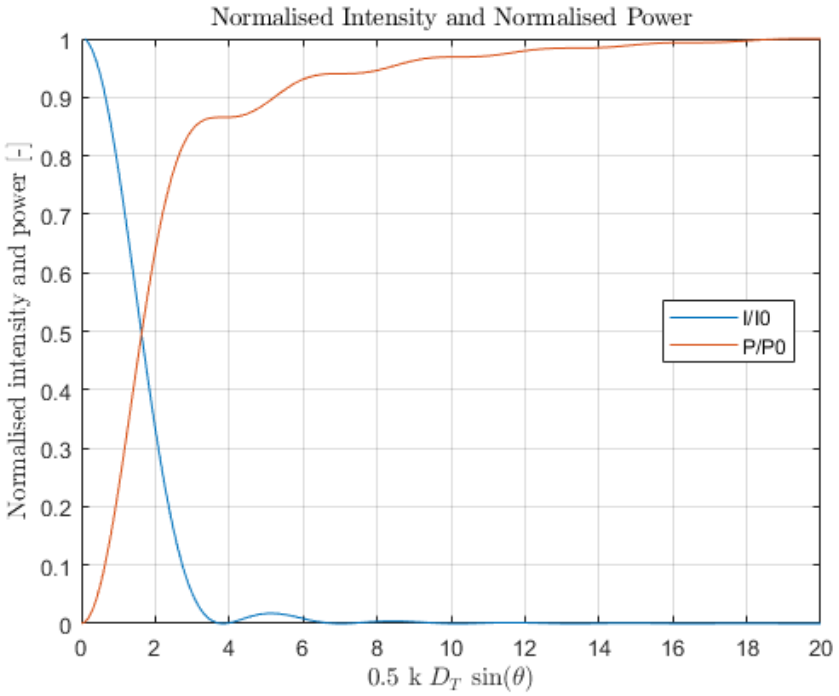

Figure 5.12: Normalized intensity and its resulting radially integrated power of an Airy disk.

where E is the field, E_0 is the peak field, ω_0 the waist beam radius, ω the beam radius, z is the axial distance from the waist, z_0 is the distance to the maximum field curvature and $R(z)$ is the field curvature. The intensity is relatively easy to obtain because the phase term can be ignored,

$$I = I_0\left(\frac{\omega_0}{\omega(z)}\right)^2 exp\left(\frac{-2r^2}{w^2(z)}\right) \tag{5.20}$$

where I is the intensity and I_0 is the peak intensity. The resulting power is to be integrated again in a polar fashion,

$$P = \int_0^r \int_0^{2\pi} I_0\left(\frac{\omega_0}{\omega}\right)^2 exp\left(\frac{-2r^2}{w^2(z)}\right) r d\phi dr \tag{5.21}$$

where P is the total power. When normalizing the radius though $x = \sqrt{2}r/\omega$, the integration becomes,

$$P = 2\pi I_0\left(\frac{\omega_0}{\omega}\right)^2\left(\frac{\omega}{\sqrt{2}}\right)\int_0^x xexp\Big(-x^2\Big)dx \tag{5.22}$$

This integration can be solved in a straightforward manner to result in,

$$P = \pi I_0 \frac{\omega_0^2}{2}\left(1 - exp\left(\frac{-2r^2}{\omega}\right)\right) = P_0\left(1 - exp\left(\frac{-2r^2}{\omega}\right)\right) \tag{5.23}$$

The power described in Equation 5.23 is graphed together with the intensity described in Equation 5.20 (normalized) in Figure 5.13. The nature of the normalization of the equation results in the plot being smaller than the Airy disk graphs in Figure 5.12. The difference in field is illustrated in Figure 5.14, however, this does not imply that Gaussian beams are inherently smaller than Airy profiled beams. Hence, it is not relevant to the following analysis.

Considering Figure 5.14, when the beam is cropped by the steering mechanism, the power initially does not vary much. When reaching $x = 1$, the power reduces by 10% and subsequently sharply falls. Half of the power remains when the cropped normalized radius is 0.6.

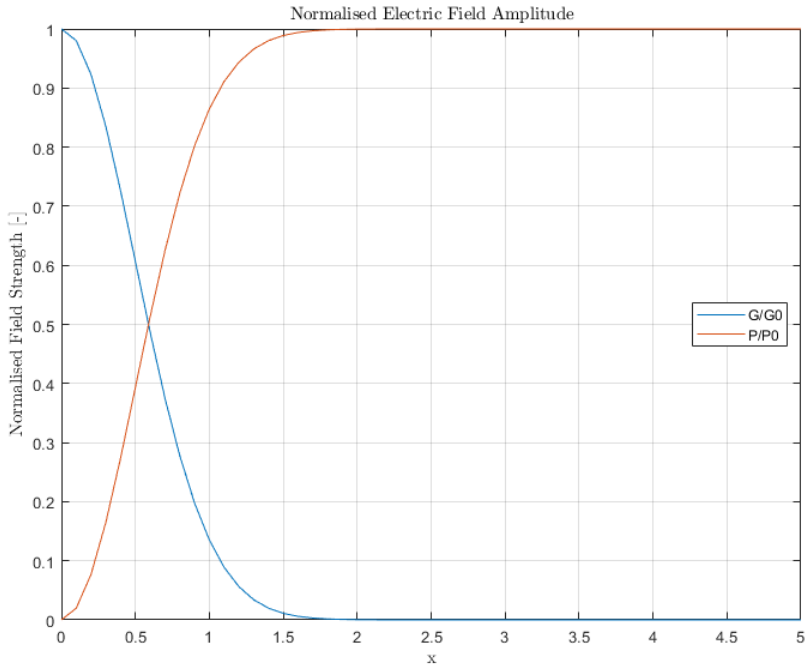

Figure 5.13: Normalized intensity and its resulting radially integrated power of a Gaussian beam.

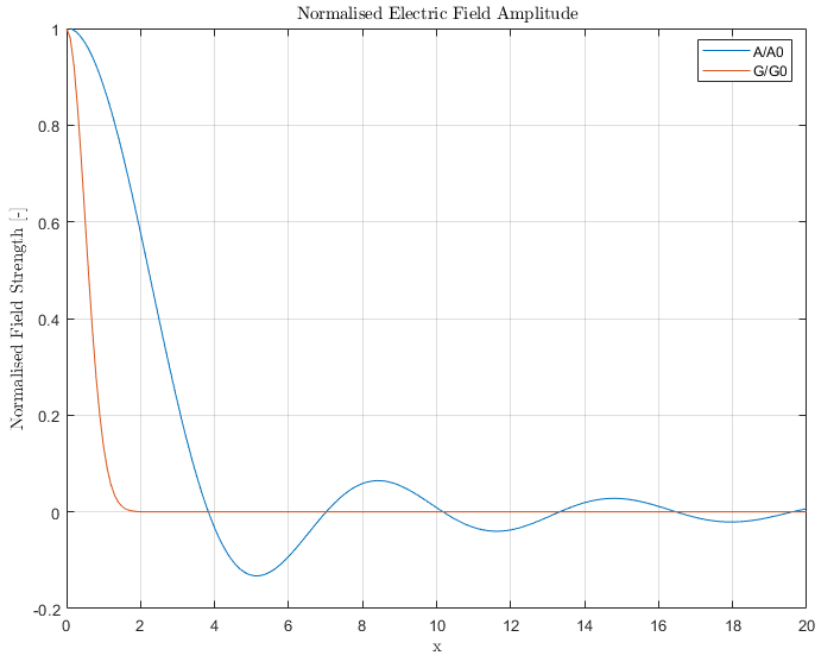

Figure 5.14: Normalized intensity and its resulting radially integrated power of a Gaussian beam and Airy beam.

When comparing cropping the central peak Airy profile and Gaussian profiles of equal radii, it is clear that cropping the Gaussian beam is more detrimental. Furthermore, considering the algorithm proposed, when the beam centers are separated by a distance greater than their combined respective radii, the drop in signal power might be considered negligible.

5.2.2. Low Resolution Beam Control

When considering the effects of decreasing the resolution of the steering system, it becomes much more challenging to find its affect analytically. The reduced resolution will cause cropping which is non-circular and the discrete boundaries between pixels pointed into different directions will cause splitting of the beams. The simulations performed in chapter 6 show numerous examples, shown in Figure 5.15, Figure 5.16, Figure 5.17 and Figure 5.18.

An example of when the beam spots are far away from each other is shown in Figure 5.15. The resulting pixels used for beam steering is shown in Figure 5.16. As can be seen, the steering area allocated to each beam is multiple times larger than the beam diameter. This results in no visible diffraction occurring in the output. Hence, there is no functional difference between lower resolution steering mechanisms when enough steering area is allocated to each beam, similarly to high resolution steering.

Figure 5.15: Illustration of 3 input beams on the left and their steered results on the right. In these images there is no noticeable diffraction of the beams. The beams are steered by the steering mechanism with the pixels shown in Figure 5.16. The steering system used has a 10x10 micro mirror resolution.

Figure 5.16: Illustration of the steering mechanism and their actuated pixels for the situation illustrated in Figure 5.15. The surfaces allocated to each beam is large enough to not cause noticeable diffraction of the beams. The steering system used has a 10x10 micro mirror resolution and the figure shows the phase field.

What happens when beams get closer is shown in Figure 5.17 and Figure 5.18. Firstly, considering

the steering area of 1 pixel relative to the beams shown is enough for negligible diffraction. This can be seen from the bottom most beam in Figure 5.17. Hence, in this case it will not result in losses due to diffraction. However it would when the beam diameter approaches the same as the dimensions of the pixels.

Secondly, the other two beams are at the edges of 2 pixels, implying part of their energy is diverted into different directions. However, this is not done evenly due to diffraction effects, which can be observed in the top two steered beams in Figure 5.17. This leads to additional signal power loss on top of the miss-direction losses.

Figure 5.17: Illustration of 3 input beams on the left and their steered results on the right. In these images there is no noticeable diffraction of the beams. The beams are steered by the steering mechanism with the pixels shown in Figure 5.18. The steering system used has a 10x10 micro mirror resolution.

Figure 5.18: Illustration of the steering mechanism and their actuated pixels for the situation illustrated in Figure 5.17. The surfaces allocated to each beam is large enough to not cause noticeable diffraction of the beams. The steering system used has a 10x10 micro mirror resolution and the figure shows the phase field.

Subsequently, when spots/beams are at an appropriate distance from each other and from a pixel edge, there is little to no difference between high and low resolution steering mechanisms. To illustrate how much worse the performance of a low resolution steering mechanism becomes due to diffraction, some larger spots are steered as depicted in Figure 5.19. This implies that low resolution steering

implies smaller diameter beams in smaller numbers at larger distances have to be used compared to high resolution steering.

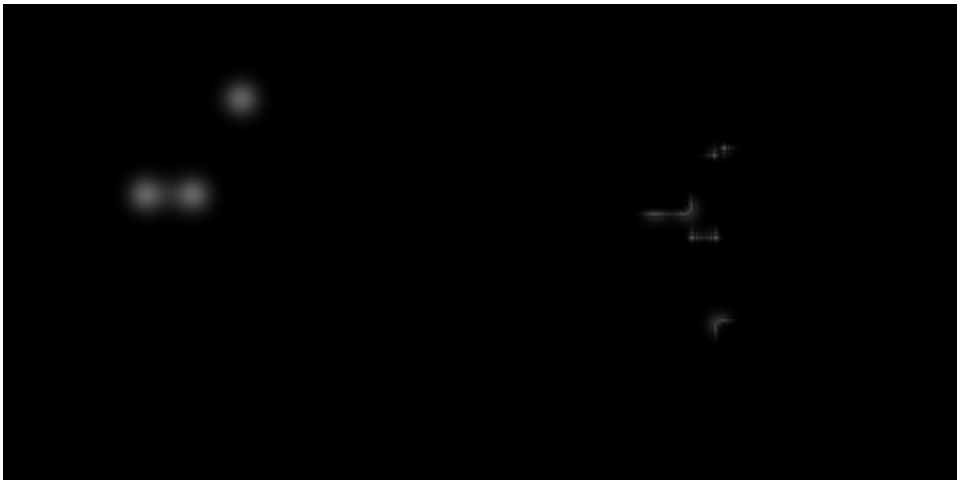

Figure 5.19: Shown here are some severe diffraction effects due to pixels that are too small and discrete compared to the beams. The patterns for off-axis and partially obscured square diffraction are clearly shown.

Low resolution steering is hence not advantageous in anyway compared to high resolution steering when purely considering beam control. However, lower resolutions can result in smaller computational loads. Furthermore, MMA's can operate in the 100's of Hertz, lending to their applications in adaptive optics. Implying that the combination between slower SLM's and faster MMA's can be beneficial. The choice of beam steering will be discussed later.

5.3. Optical Train Design

The optical train design is an important variable in the performance of the system. This is because of multiple reasons not limited to the optical efficiency, the amount of signal required for feedback, mass, etc... The design is both crucial for the practical limitations as well as general system performance.

The Shannon-Hartley theorem, as shown in Equation 5.1, indicates that increasing signal strength leads to higher data rates. On such method to increase the signal power is by increasing the telescope aperture size. Similarly, when sending the laser beam, a larger telescope results in a smaller beam divergence, implying less power spread. Larger telescopes hence help both ways. The size in this case has already been discussed in section 4.1.

However, additional design choices have to be made, namely the feedback and the beam transportation. This will primarily have effect on the amount of signal used for the feedback, size and optical complexity of the system.

5.3.1. Feedback and Beam Control

Any optical system has the choice between a pre-programmed trajectory and a feedback system. For applications where the communications are not foreseen, the pre-programmed trajectory might not always be possible. In these cases, the system requires a feedback loop on the locations of the beams. The location of the feedback system in an simple multi-beam system and its effects on the layout are shown in Figure 5.20 and Figure 5.21.

Considering Figure 5.20, the difference between the left and right illustrations is that the location of the feedback system is after or before the beam steering mechanism. The feedback is illustrated using a spot tracker in this case. The difference in the block diagram is negligible when considering that the phase field is changed during steering when the feedback is located on either side of the beam steering. This is because the goal of the system is to point the incoming beams to the transceivers and the outgoing beams to the spacecraft locations. The later of which are either beam or beacon spots on the spot tracker. When an outgoing beam spot is placed over the incoming beam spot, or vice versa, it does not matter which direction the beam goes because they now follow the exact same path. Hence, other than the orientation of the diagram, both block diagrams are identical in Figure 5.21. Hence, both

orientations will work.

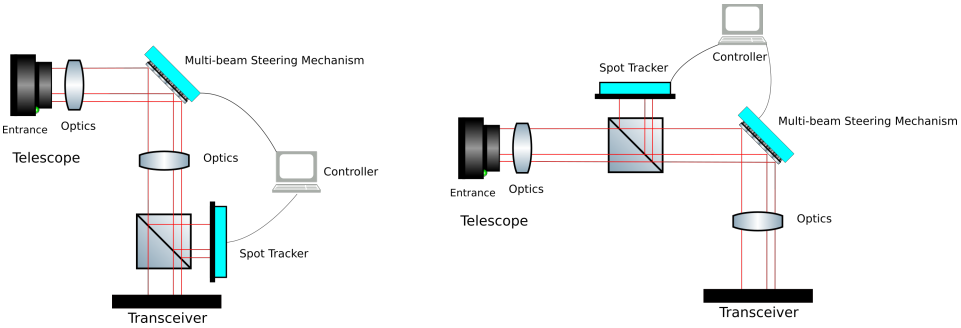

Figure 5.20: These figures shows 2 different feedback orientations for a multi-beam system. The left figure shows, from the telescope, first reflect of the beam steering mechanism before being split to the spot tracker. This configuration steers incoming beams. The right figure shows the spot tracker before the beam steering mechanism which shows outgoing beam steering. The block diagram is shown in Figure 5.21. Note that the right illustration shows a bi-directional beam splitter which can be made with multiple components.

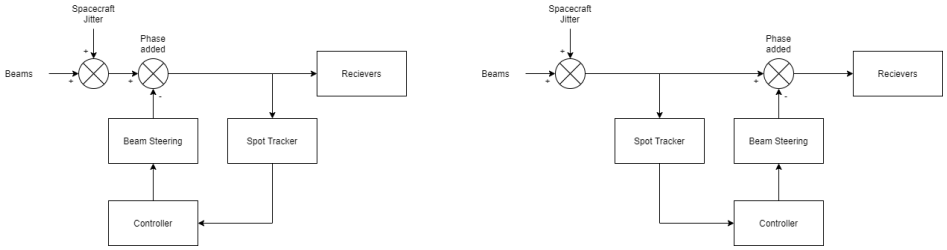

Figure 5.21: This figure shows 2 different feedback orientations for two multi-beam systems shown in Figure 5.20 in the form of a block diagram.

However, there is a difference when considering the optical aspect. In the left illustration of Figure 4.7, the incoming beams/beacons are steered to the transceivers because the spot tracker is down stream from the steering mechanism. These transceivers are in known locations, decreasing spot tracking uncertainty when trying to align 2 different spots. Furthermore, a simpler beam splitter which works one way is sufficient. This is different compared to the right illustration where the beams/beacons are steered to the targets and beams in both directions must be tracked and corrected for. Considering this, the trade off is made in Table 5.1 where the resulting design choice is to steer the incoming beams.

Table 5.1: This the trade-off for the feedback orientation.

Configuration	Incoming Beam Steering	Outgoing Beam Steering
Feasibility	Feasable	Feasable
Splitter Complexity	Low	High
Steering Complexity	Low	High
Number of Spots Tracked	High	Low

Furthermore, the resolution of the spot tracker must be higher than the steering mechanism or the expected distance between spots. Considering the different feedback methods, to achieve duplex communications with a single steering mechanism and spot tracker becomes complected. This is depicted in Figure 5.22.

There are some inherent problems with these configurations. A major one is shown in Figure 5.22, where multiple spots can cause sudden and violent miss-pointing of outgoing beams. Furthermore, distinguishing outgoing and incoming beams will require additional software complexity and development of reliable and versatile open loop control algorithms.

Two configurations have been identified through which these problems can be solved and are shown in Figure 5.23.

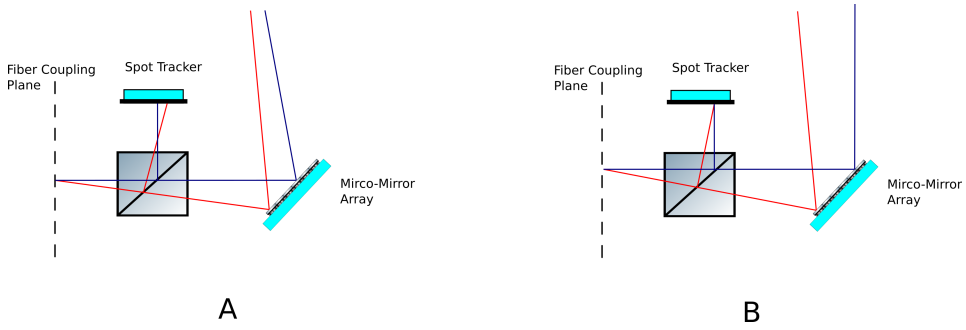

Figure 5.22: Depicted here are two situations where single stage steering is used. Incoming beams are presented in red and outgoing beams are presented in blue. Due to the outgoing beams having a different path compared to incoming beams each beam must be steered separately. (A) shows how this is possible, however note that the outgoing beams have to be controlled in an open loop. (B) shows a potential problem where the spots for the outgoing and incoming beams are in the same location on the spot tracker while following completely different paths, implying the system has certain spot configurations which will disrupt operations.

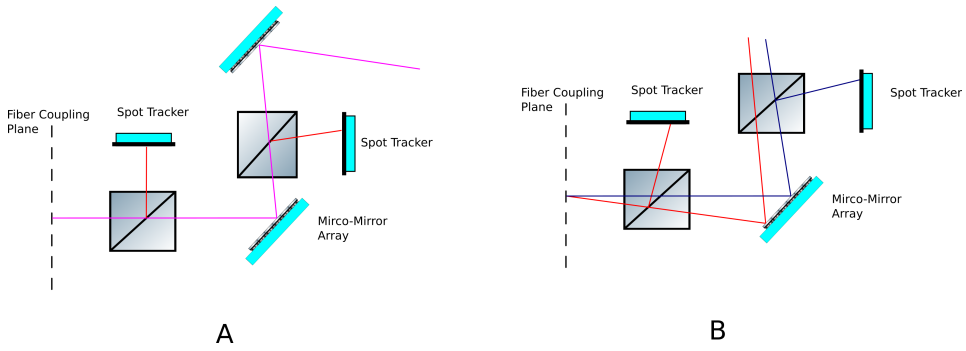

Figure 5.23: Depicted are two systems which can control the outgoing and incoming beams. (A) shows a 2 steering mechanism configuration while (B) uses a single steering mechanism. Both have the feedback scheme depicted left on both Figure 5.20 and Figure 5.21. (B) has the spot tracker for the incoming and outgoing beams after the steering. It requires measurement of both incoming and outgoing beams. (A) has both incoming and outgoing beams following the same path and only requires measurement of the incoming beam spots however twice as much.

Considering Figure 5.23 (A), to ensure duplex communications, the path for out and incoming beams must be the same. This implies that there should be two steering stages. For incoming beams, the first steering stage should separate the beams and point them to set locations on the second beam steering mechanism. The second steering mechanism then makes the approach angle to the transceivers zero for optimal fiber coupling as well as ensuring path similarity between out and incoming beams in the fiber. Each location will be referred to as a steering stage.

Considering Figure 5.23 (B), the beams will follow different paths but eventually must connect to the same two points. Due to the different paths being followed, this would require the steering of both incoming and outgoing beams and hence the spots of both must be tracked. The system should also follow the feedback schematics in Figure 5.20 and Figure 5.21. This implies the spot tracking for the incoming beams are done on the fiber coupling side and the spot tracking for the out going beams are done on the telescope input side.

There are numerous criteria to consider to trade off these two configurations. One of them is the feedback complexity. Same path configurations have low Complexity. This is due to the same path not requiring control of separate incoming and outgoing beams. Conversely, separate path configurations have a higher complexity due to twice as many moving beams having to be controlled by a single steering mechanism.

The number of components increases the SWaP of the system. The same path configuration has to support 4 components; 2 spot trackers and 2 steering mechanisms. For separate path configurations require 3 to support steering; 2 spot trackers and 1 steering mechanism. The result is that the number of components which could fail, have to be calibrated and included into the operation is higher. The result is that in this respect the separate path has the edge.

Design flexibility of each design is also a crucial consideration. The inclusion of multiple steering

stages allows for the combination of different technologies. For example, the low frequency response of a SLM can be compensated for by a higher frequency response MMA while the high resolution SLM can compensate for the lower resolution MMA. Furthermore, the same path requirement allows for an indirect measurement of the pointing to target accuracy through the fiber coupling efficiency. For this the signal strength can be used. Two steering mechanisms and spot trackers can also serve as each others hot spares and can ensure that receiving signals are still possible with closed loop control. In this event, the out going beams can still be controlled using open loop. However, separate path configurations would not allow this.

The number of beams to track is important for the specifications of the spot trackers and the feedback loop. For the same path configuration, the same path implies this is equal to the number of targets. Where as the separate path requires to keep track of the combined total of incoming and outgoing beams, hence two per target. This results in the separate path configuration to always have twice as many beams to track compared to the same path configuration.

The maximum number of steerable beams is an important parameter for the number of targets that can be sustained and the overall performance edge a multi-beam system has over a single beam system. This is related to the maximum number of spots that can be controlled. The same path configuration allows for the incoming and out going beam for each target to share a spot. Hence, twice the maximum number of spots can be controlled in terms of beams. Whereas the separate path configuration can only handle the number of beams equal to the maximum number of spots.

SWaP requirements are important for keeping mission costs low. In this case, the size/volume as well as the mass is proportional to the number of components which are of different sizes. For the same path length configurations, the mass is slightly larger due to additional imaging stages required for the extra steering mechanism. Conversely, the separate path length configuration causes for a comparatively slightly smaller total mass due to having one less imaging stage. However, compared to single beam systems, the mass saving per link is likely quickly reached.

The power is related to the number of active components, with the steering mechanism being assumed to be the most power hungry. For same path configurations require 1 more steering mechanism to power relative to the separated path configurations.

Signal power efficiency is directly related to the link performances and hence overall system performances. This parameter is hence weighted very heavily. The same path configuration requires measurement twice on the incoming signal, implying more of the incoming signal is lost. The separate path configuration also measures twice, but once for each beam direction. This implies that the incoming signal would be comparatively stronger while the outgoing signal comparatively weaker.

This trade-off is hence harder since it requires to chose between sacrificing the incoming signal or the outgoing signal. The single path configuration implies that the outgoing beam will automatically have more transmitted power, implying that the power requirement is shifted to the target. This is good for ground based targets, as the SWaP requirements are less crucial for these, however, for satellites this can be more problematic. In reality, they too might have the same system configuration, in which case the two beams are measured equally as much over the full path and it should hence not matter what the configuration is. However, when considering noise, reducing the weakest signal, the incoming signal, would likely result in proportionally more signal having to be used. It is hence likely that the separate path configuration is signal power friendlier.

The trade off is illustrated in Table 5.2, which concludes that the same path configuration is the better option.

The same path configuration results in a choice having to be made of steering mechanism for each steering stage. Each stage has its own considerations which are summarized in the trade off performed in Table 5.3.

The beams are already split in steering stage two. Hence, the resolution of the second steering mechanism does not matter as much and the locations of the transceiver fibers can be placed in such a way as to cause the least amount of diffraction losses. This leads to MMA's a becoming more attractive option, as long as it can offer at least one steering mirror slightly larger than the beam diameter. Furthermore, the use of MMA's also allow for higher frequency responses which gives the system the ability to correct for higher frequency jitter.

The feedback for both steering stages must be arranged in incoming steering configuration. The spot tracker requires to have the same/equivalent optical path as the steering mechanism to allow for accurate determination of the steering angles.

Table 5.2: Trade-off table for the steering configurations depicted in Figure 5.23. ”Single Path 2 Steering Stages” referrers to (A) and ”Dual Path 1 Steering Stage” to (B) in Figure 5.23. The result is that the Single Path 2 Steering Stages come out scoring better.

Criteria	Single Path 2 Steering Stages	Dual Path 1 Steering Stage	Weights
Feedback Complexity	1	0	4
Number of Components	0	1	2
Design Flexibility	1	0	4
Number of Beams To Track	1	0	4
Maximum Number of Steerable Beams	1	0	4
Mass	0	1	3
Power	0	1	1
Signal Power Efficiency	0	1	5
Total	16	11	27

Table 5.3: Steering stage mechanism trade-off.

Criteria	MMA	SLM	Weight Stage 1	Weight Stage 2
Speed	>300 Hz	<200 Hz & >60 Hz	1	1
Resolution	~10 x 10	>1920 x 1080	2	0
Weighted Total Stage 1	1	2		
Weighted Total Stage 2	1	0		

Hence, the system will have the incoming beams steered to have the same path as the outgoing beams. The system will have 2 steering stages and each stage will have their own feedback post steering mechanism. The first stage will control the offsets and separation as well as low frequency jitter. This stage also has the potential of wavefront corrections. The second stage will correct for angular misalignment’s while also taking care of higher frequency jitter before ultimately fiber coupling. This stage also has the potential of using the signal strength in the feedback loop. The system has potential to steer the same number of beams as the maximum number of spots and inherently has built in redundancy and design flexibility. A simplified schematic is illustrated in Figure 5.23 (A).

5.3.2. Design of Fiber Coupling

The coupling into the fiber can only be done through steering the beams into the fiber. The accuracy is limited by the steering mechanism, spot tracker and surrounding hardware. Considered will be the interfacing with the steering mechanism and the steering mechanism it self. The spot tracker resolution will also be briefly mentioned and placed in the system. After this the system will be put together.

Firstly, the accuracy of the steering mechanism depends on multiple aspects. Here, two will be discussed, the direct interfacing and the mechanism it self. These could be one of the same if the mechanism driver is attached to the mechanism, however will be discussed separately. For MMA’s, each micro mirror is controlled through a MEMS or piezo. These usually require a voltage for actuation and is subsequently divided over 3 terminals corresponding to up-down and two axis of rotations. The system could hence be analog and this is indeed the case for the majority of mirrors discussed in the overview paper by Yuanping Song, Robert M. Panas, Jonathan B. Hopkins[55]. This implies that it is possible, with in reason, to steer as accurately as one might want. However, the system operating the MMA is a digital computer with a Digital to Analog Converter (DAC) in between it and the MMA. The number of bits the DAC can distinguish or the bits allocated to the steering is the bottle neck. The number of possible mirror settings and subsequent steering accuracy is dependent on the maximum number of distinguishable bits. Similarly for the SLM, the discretization of the phase shift, or ”color depth” so to speak, of each pixel will determine the smoothness of the slope of the phase as well as the number of different possible slopes. The steering accuracy of SLM’s is hence dependent on the number of bits in a similarly as with MMA’s.

However, the devil is in the details, as there are numerous aspects which determine the steering accuracy considering the SLM. Phased array’s use delays across its antenna array, to generate signal phase differences across the array, to generate angled wavefronts. SLM’s are similar by phasing the

incoming wavefront sub-aperture in each pixel. The key aspects are shown in Figure 5.24. In theory the smallest discretised slope would be similar to the top left sketch shown in Figure 5.24, however, only the last pixel is phase stepped. For large beams and larger pixels this would likely result in wavefront distortion that are too large, causing diffraction losses due to being too near field. Hence, the pixels require to be small enough to prevent this from happening. When the pixels are small enough compared to the distance traveled, Feng Xiao and Lingjiang Kong[75] showed that far field approximations are possible. Beam steering and forming have been shown in the works by Feng Xiao and Lingjiang Kong[75] and R. Bonjour, S. Welshen, J. F. Johansson and J. Leuthold[7]. Bonjour et. all.[7] used 50x50 pixels for their beam which resulted in adequate steering.

To verify this, experiments in the simulation were performed by generating 2 mm and 0.4 mm on a SLM of 4x4 cm with a resolution of 1080x1080 pixels. The beam was propagated 1 meter and the minimum deviation of 1 pixel was required together with not observable diffraction. The setup only allowed the pixels to increase or decrease in increments rounded to the nearest $2\pi/2^8$ radians phase shift in an 8 bit pixel color format. Note that $2\pi/2^8$ radians phase shift would be equivelent to the $\Delta\phi$ depicted in Figure 5.24. These simulations indeed confirmed these findings and further also proved that going down to 10x10 pixels would also work. Furthermore, the maximum number of pixels between steps for any steering to take effect. Hence, this will be considered the minimum distance between increments and is coincidentally illustrated in the top left of Figure 5.24.

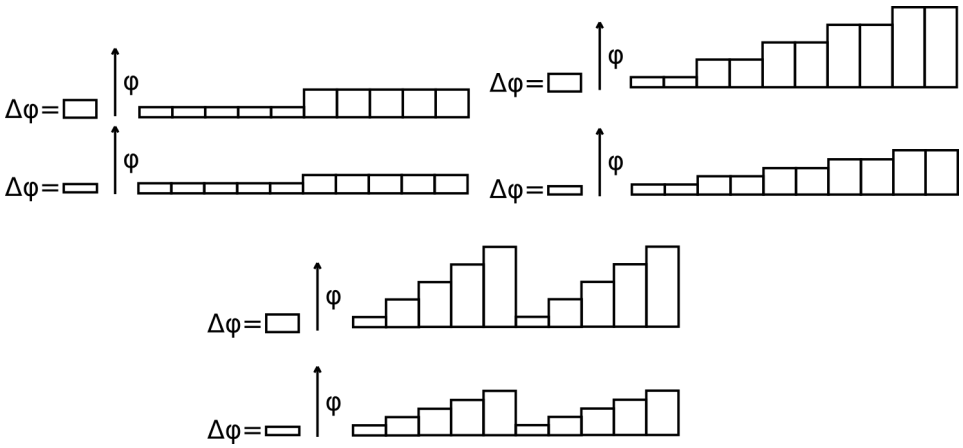

Figure 5.24: Illustrated is a visualization of discretization of phase for a number of pixels. The phase is changed to approximate a slope to reflect the light in a particular direction. Here, ϕ denotes the phase and $\Delta\phi$ is the smallest discretization of the phase. Top right is the smallest evenly distributed slope, top left is depicted a scheme where every other pixel contains a jump and lastly the bottom where every pixel is incrementally increase until the phase wraps 2π. These approaches have different diffraction patterns and different pointing accuracy's. The smaller discretization can produce a larger number of possible slops and higher steering fidelity.

The resulting steering accuracy is hence a slope of $2\pi/2^8$ over 10 pixels. 1 pixel has a length of $0.04/1080 = 3.7e-5$ meter or 37 μm, which would imply a phase slope of 66 radians per meter. Each 2π radians is equal to 1550 nm, which implies an equivalent mirror slope of 16.3 μm/m. This is equivalent to an deflection angle of 16.3 μrad or 0.9 mdeg.

In the overview paper by Song et. all.[55] it is indicated that the majority of MMA's have a rotational range of around 10-50 degrees which also contain the fastest MMA's. The rotational range is preferably small in order to get the best steering accuracy for a given DACs, however still large enough to steer each beam into any or all fiber from any angle. Assuming an MMA of 20 degrees is sufficient, this would allow for flexibility later on. Assuming the analog voltage range is linearly applied to the range of rotational motion this would imply an 8 bit DAC would result in 1.36 mrad or 0.08 deg. To get similar steering accuracy's as with the SLM, the DAC would require a 14 bit DAC and result in 21.2 μrad and 1.22 mdeg. Considering the considerable tolerance on fiber coupling in the absence of GRIN lenses, the trade-off is trivial. Hence, the 1.8 mm GRIN lens will be added as the one discussed in section 5.1. This implies an offset of 1.58 mm can be tolerated and the SLM, when considering reflection requires twice the accuracy, can be placed at a distance not exceeding 50 meters. It is very unlikely that 50 meters will be exceeded. For a defocus error of 2 meters and that the system should be manufactured with a precision of 4.73e-4 radians.

The system response speed is quicker than the expected jitter considering the fast response of the MMA and the spot trackers possibly being on the order of a few 100 Hz and the SLM on the order of 60-180 Hz or higher. Hence, the system should be tolerant to the turbulence induced jitter as well as spacecraft vibrations. The accuracy also beats the required accuracy.

5.3.3. Telescope Design

The system depicted in Figure 5.23 (A) shows a system which accepts beams at different angles of incidence and proceeds to steer them into a fiber. The beams have to be formed/focused by a telescope in front of the system which can accept beams from wide angles, focus them and then inject them into the system at divergence angles which are acceptable. This must also be done without distortion as that would severely affect the fiber coupling efficiency.

Luckily, this problem has already been encountered and successfully solved in the photography and film industry. Fish eye lenses suffer from a larger amount of distortion which can be used in an artistic way. However, they are often distracting and unusable for wide angle shots in landscapes and films. The invention and use of rectilinear lenses allows for equally wide angle shots while almost eliminating distortion. Examples of these are the Nikkor 13 mm F5.6 and the newer Canon EF 11-24mm f/4L USM, shown in Figure 5.25 and Figure 5.26.

Figure 5.25: Shown here is a picture of the Nikkor 13 mm F5.6 lens.[52]

This is done by mapping the radially incoming light into a linear 2D map by linearly spacing angles radially on the focal plane. This is illustrated in Figure 5.27, where the use of meniscus lenses is used to refract the light into a more parallel angle to the optical axis. This design principles can also be found in the Canon lens cutaway shown in Figure 5.28. This is done in such a way where the resulting image is mapped maintaining the aspect ratios of the environment being imaged. Hence, beams will remain circular and do not turn into ellipses or other types of distortions. The lenses are also designed to keep dispersion to a minimum, however, this is a less interesting aspect of the lens as the frequency spectrum used is narrow.

Hence, the use of a commercially available lens would save costs as well as being proven hardware. However, these are not designed with the strict SWaP requirements often found in space. therefore, a custom design for the flight hardware might still be required. Furthermore, these lenses will have a defined diameter which might be too small or to larger for the application. Some optics in front of the camera lens would be required to solve these issues. Another point of consideration would be the addition of optical elements to image the output image into a format accepted by the system with defined beams. The result is that some support optics have to be designed, however, due to the standardization within brands, this is possible.

The Nikkor lens dates back to the 1970s[52], significantly older and produced in smaller numbers

Figure 5.26: Shown is a picture of the Canon EF 11-24mm f/4L USM lens.[40]

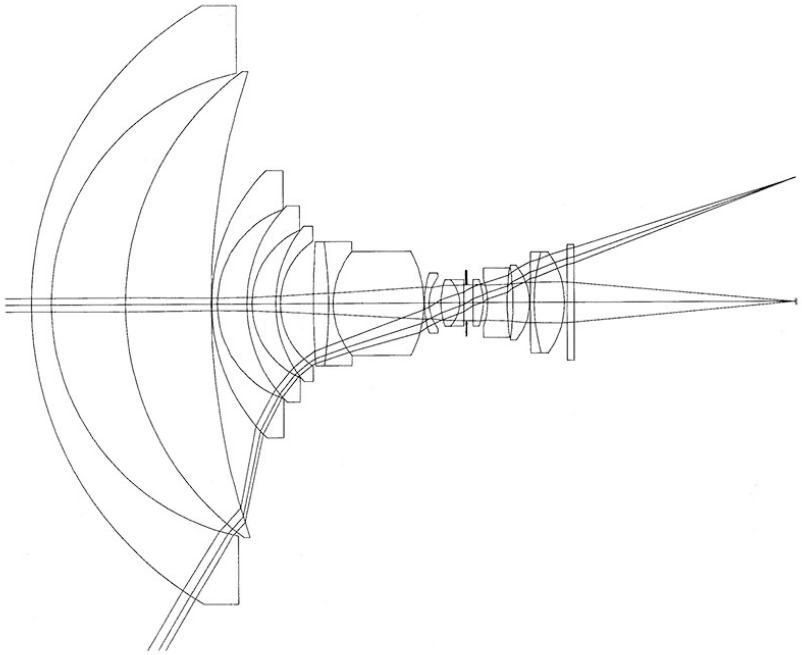

Figure 5.27: Illustrated is the lens and ray system for the NIKKOR 13mm F5.6[52]. In short from left to right, the first set of meniscus lenses (and one concave lens) transport and bend the light such that it is more parallel to the optical axis. This reduces the divergence angle substantially. Multiple lenses are used to prevent reflections and scattering by deducing the angle of incidence of the light. After this, the light travels through focusing optics and adjustable apertures in the second part of the lens to become compatible with the CCD/camera system behind the lens.

compared to the Canon lens, dating back to 2015[40]. Hence, the safer option would be the Canon lens. The FOV of the lens is different in different directions due to the baffle and the spatial dimensions of the camera device. These do not have to be present in the overall system and hence the FOV can be at least at $72\mathrm{deg}$ with the focus at infinity and aperture diameter of around 11 cm[40]. This will satisfy the **GD-CR-004** and go towards **GD-CR-005** requirement posed in Appendix C, pertaining the FOV and COTS components. This makes the subsequent design much more flexible in terms of orbit altitudes and the orbits which can be serviced by the multi-beam terminal. The compatibility between the camera lens and the rest of the system can be done with an imaging stage.

Note that from now on, the camera lens will be referred to as a lens system to avoid confusion with single lenses.

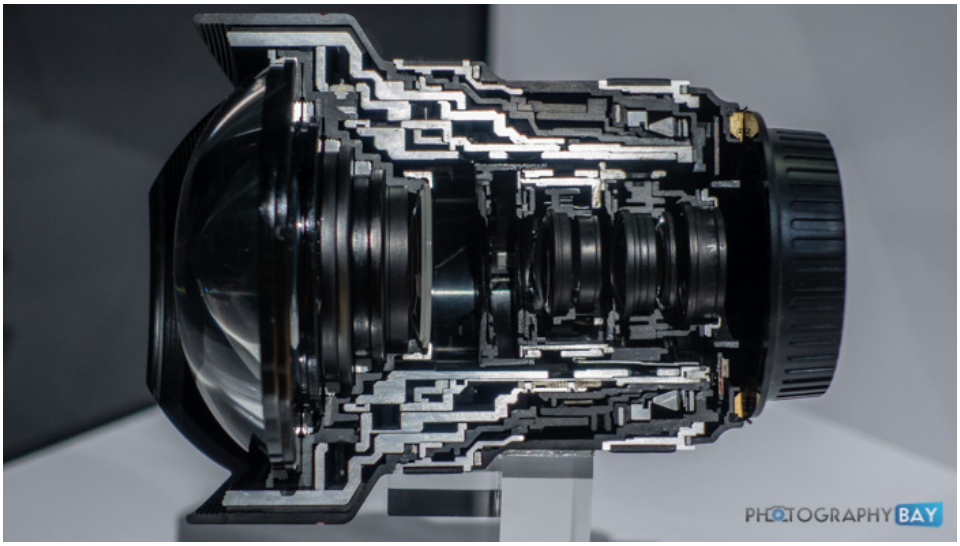

Figure 5.28: This picture shows a cutaway of the Canon EF 11-24mm f/4L USM[49]. Clearly illustrated is a similar optical layout as shown in Figure 5.27, where there are numerous meniscus lenses used to gradually and efficiently change the angles of the rays. The second stage where the image is focused onto the CCD for a camera device.

The lens system is high enough quality for use in film and photography. However, when considering fiber coupling, a diffraction limited lens system is preferred. The methods by which different aberrations affect the fiber coupling performance can be quantified, uses the same equations as shown in the Literature Study[56] (see attached). However, the exact aberrations and their effects on the system performance using this lens system is impossible to quantify without lab experiments.

A solution which can make the system as a whole closer to being diffraction limited would be using the SLM for wavefront correction and control. For this the system can be constructed and the wavefront after the SLM can me measured. The static distortions can be corrected for using the SLM, by calibrating the system to correct the wavefront as much as possible. This would in turn not require active correction during operations. Non static but predictable distortions can also by corrected for using simple standard corrections imposed on the output of the algorithms. Furthermore, this would also increase the performance for the outgoing beams through pre-corrections.

This highlights the utility of using SLM's as part of the beam steering system in improving performance as well as increasing system design flexibility.

5.3.4. Optical Train Assembly

Now that all the components and aspects of the design have been defined, the system can be put together to form the optical train. It will hence be placed in such a way as to ensure its functions optimally and to maximize efficiency. For the requirements, please consult Appendix C.

The first optical elements are those of the camera lens system found in subsection 5.3.3, the Canon EF 11-24mm f/4L USM, which will be placed facing the optimal direction. This will satisfy the **GD-CR-004** and go towards **GD-CR-005** requirements, pertaining the FOV and COTS components. These have a focal distance of around 2 cm and an output aperture of around 1.5 cm radius. The resulting beams have to be collimated by a convex lens. The exact specifications are not given by Canon, hence the exact distance as well as the collimating lens are not determinable. Hence, it is assumed that the resultant intermediate aperture size is 5 cm in diameter with beam radii of 0.5 cm. This will satisfy the critical requirement **CD-CR-001** for capabilities of handling 10 targets. The lens system setting will remain at a single setting where it focuses from infinity. This will ensure that the center of mass will not change during its life and satisfying **GD-CR-018**.

GD-CR-017 states that the system should be capable of withstanding pointing into the Sun for about 2 minutes. This can be achieved by filtering out the vast majority of the sunlight through the use of a band pass dichroic filter which then reflects the unwanted spectra back out of the telescope. This will ensure the system will not be destroyed and it has further benefits of reducing noise and stray light on the spot trackers and in the fiber receivers.

The SLM, like those sold by HOLOEYE[26] to name an example, are of the form factor 1.5x1.5 cm. Hence, the aperture must be re-imaged to have a diameter of 1.8 cm and resulting beams of 1.8 mm diameter or preferably slightly larger, so that the beam can be slowly focused down to their waist of 1.8 mm at the fiber GRIN lens. Some design principles which have been adhered to are steep incident angles onto surfaces of the optical elements to prevent reflections and maximize efficiency. This has been adhered to by the camera lens system, collimating lens and the dichroic filter. However, for re-imaging stages this implies relatively long focal lengths and thin lenses. Hence, a focal length of 10 cm was chosen of the first lens giving a convergence angle of 0.245 rad or 14 deg. This implies that the second lens would have to be 3.6 cm focal length and would be placed 13.6 cm from the first lens.

The resulting beams are then sent into the steering stage through a mirror system to optimize form factor. The system until now is depicted in Figure 5.29.

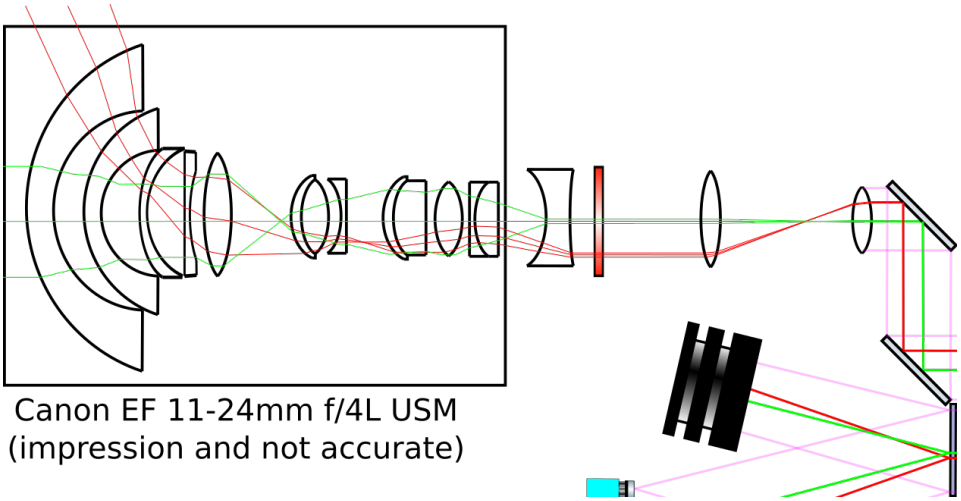

Figure 5.29: Depicted is the designed telescope and imaging system. Two targets are depicted, the green target is on the optical axis while the red target is on the maximum periphery. They are focused by the lens system and subsequently collimated to large 0.5 cm beams in an 5 cm aperture. The light is filtered for any unwanted frequencies by the dichroice filter and then re-imaged to the correct sized aperture for the steering system. The mirrors guide the beams into the steering system.

The telescope, as discussed in subsection 5.3.3, is the previously mentioned Canon EF 11-24mm f/4L USM lens system depicted in Figure 5.28. A lens system for the optical train was designed before the realization that a COTS lens could be used. The diagram and some rudimentary ray tracing had been performed and this was adjusted for diagrams shown for the purposes to illustrate the workings of the Canon EF 11-24mm f/4L USM lens system based on the cutaway shown in Figure 5.28.

The steering system uses similar design principles. After the mirrors guiding the beams into the start of the system, the beams are incident on the SLM. In theory, the beams could be deflected by a mirror such that the aperture is incident on the SLM. This then is reflected off and integrated back into the optical train. However, this adds mass and requires optical beam splitters and directional transparency.

Beam splitters work in all directions, implying that light in the opposite direction will not follow the same path but a reflection of it. This is depicted in Figure 5.30. This results in different paths being followed, some of which cannot be used or require complected optics to use back in line. Hence, the resulting unused beams must be dumped and are hence wasted. Furthermore, beam splitters also absorb some of the light implying they should be used as little as possible.

To improve efficiency, the number of beam splitters are minimized and the transparency chosen to be 90% implying that 10% is reflected. One is used for each spot tracker, of which there are two. Hence, the SLM is mounted at a shallow angle such that the steering can be done inline while allowing for enough space for the MMA and other components. The angle is preferred to be shallow to allow for the maximum transmission efficiency through the beam splitters. The SLM might have a different aperture size compared to the MMA. As long as it is within reason, this will not matter and the beams will be steered to the correct locations.

As discussed before, the spot trackers must be placed at the same optical distance as their resulting planes. Hence, the beam splitter is placed half way to the MMA and the spot tracker placed at the same distance as the MMA from the beam splitter. The spot tracker data is fed back to the SLM.

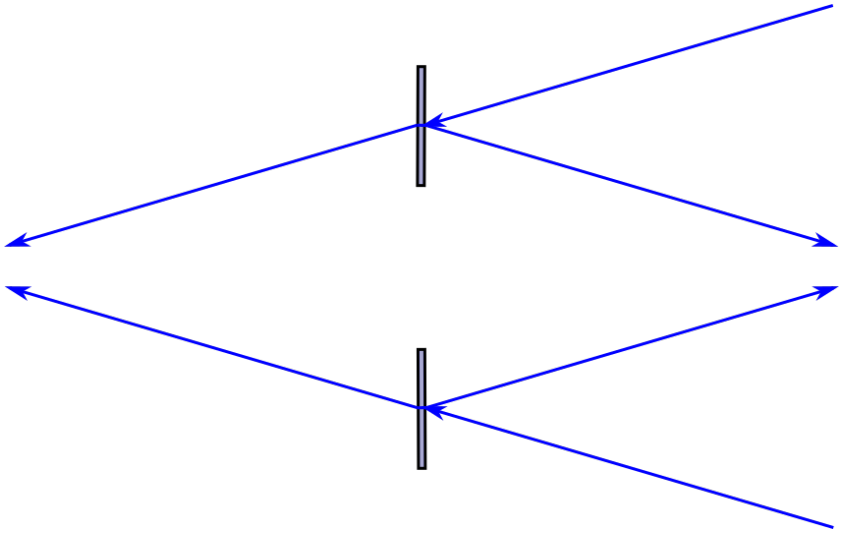

Figure 5.30: Shown are 2 different direction beams incident on two different beam splitters. The different directions cause the resulting beams to be reflected into different directions implying that two way path symmetry cannot be used with beam splitters.

The efficiencies of reflections of the MMA should be near perfect, considering the high quality continuous mirror surfaces over the diameter of the beams. The SLM however does not have a complete fill factor and perfect reflections. From a number of SLMs available, the fill factor varies from 90% to 95% and reflective efficiencies between 65% to 97%[62][26]. This implies a best case efficiency of around 92%. The fill factor for large numbers of small squares implies that this produces an optical grating effect. Assuming an optical grating, diffraction effects where analyzed as that of a grating and determined not to effect the system in its current configuration if the housing absorbs them.

The MMA is not placed at an angle, because the incident angle is already present. Note that as a result, the spot tracker is placed in the same orientation. The feedback for the fiber coupling is done in a similar way as for the SLM. Note, that the spot tracker in this case is angled normal to the incoming beams in the same way the fibers are angled to have exactly the same path.

The use of beam splitters in a system which uses the same path for incoming and outgoing beams, is that the outgoing beams also produce reflections. As was shown in Figure 5.30. These are unusable and very hard to merge back into the optical train. Hence, the beams are dumped into beam dumps, one of which uses a mirror which reflects the beams into the bottom dump to save space and not interfere with the spot trackers. The beam dumps will have to be cooled.

The steering system is shown in Figure 5.31. The overall system is depicted in the Figure 5.32.

The distances between each component are determined by the angle chosen, the dimensions which related to the steering mechanism and bound by its angular reach.

According to Song et. al.[55], there exist numerous MMA's with mirrors on the order of 1-10 mm and with a resolution of at least 10x10. This would imply that the size of the MMA can be between 1 cm to upwards of 10 cm depending on the fill factor and mirror size. Because of the design of the feedback system and optical train, the fill factor is less of an issue. The reason is that each mirror steers a separate beam, as long as the beam is not cropped, there will be no signal lost between the mirrors. For a 1.8 mm radius GRIN lens and respective beam, this implies a 4x4 mm mirror. The size of the MMA must be larger than 4x4 cm with at least 10 mirrors to communicate with 10 targets as to be in accordance with **CD-CR-001**.

The GRIN lenses of the fibers must be placed in such a way that they align exactly with their respective mirrors during production. Therefore, the number of mirrors must be exactly the same or larger than the number of fibers and the size of the mirrors must be greater than the diameter of the GRIN lenses. Hence, the receiver fiber array must be the same dimensions as the MMA and so be 4x4 cm at least, with 10 fibers in the same pattern.

Furthermore, the CCD also requires to be the same outer dimensions as the MMA, or an re-imaging stage is required. However, CCD's exist in that form factor and hence it was chosen not to include an imaging stage. The beam dumps must be the same size as the MMA's to ensure the whole aperture is

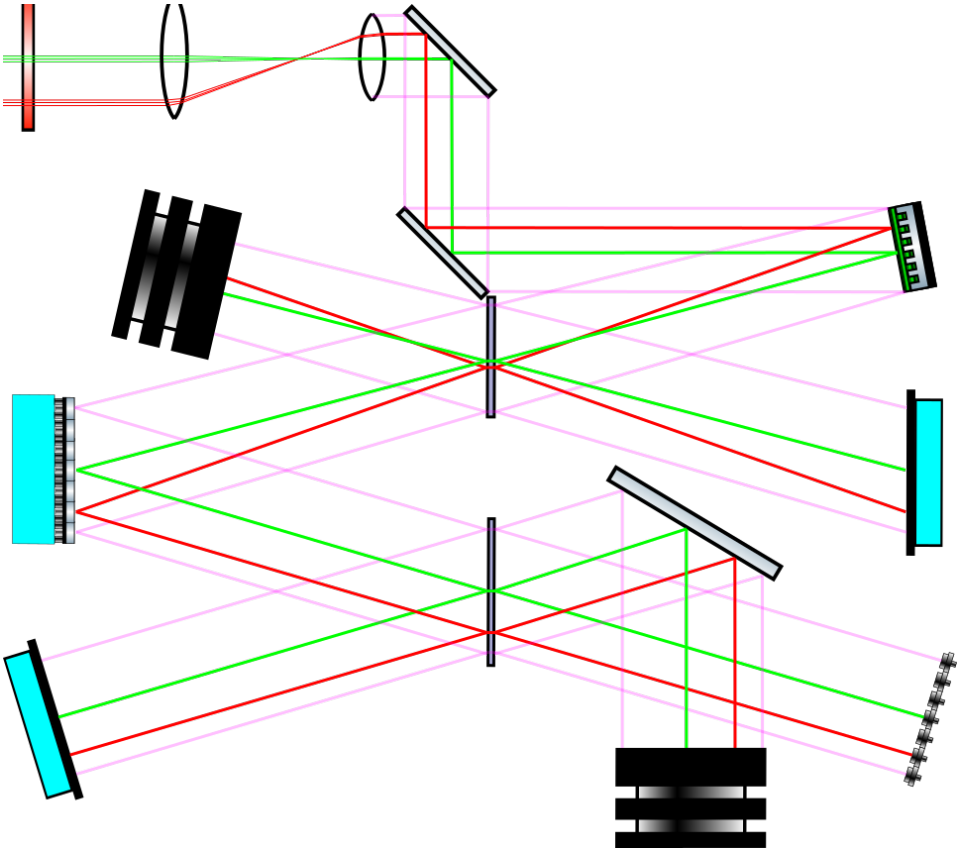

Figure 5.31: Depicted is the designed beam steering system. From the top where the beams are directed by the second mirror to the SLM, two beams originating from two targets depicted in red and green, are directed to the SLM. The light purple beams on the peripheries denotes the aperture size or the extreme locations where the beams can exist. The SLM steers the beams onto the MMA. In between the MMA is a beam splitter which directs some of the energy towards the first spot tracker which is used for the SLM feedback and has the same optical path as the MMA. The MMA subsequently steers the beams to the fibers. The spot tracker for the MMA is supplied by the second beam splitter. The beam splitters also direct some of the energy of the outgoing beams which are unusable. These are directed and dumped into the beam dumps.

dumped and light is not allowed to go astray.

The angle from the horizontal chosen is 15 degrees, which gives relatively good packing efficiency while simultaneously keeping the system compact enough. This implies that the distance between the horizontal to the center of the MMA, when accommodating the beam dump, requires 8 cm of drop. Hence, the distance between the SLM and the MMA is 62 cm, with 60 cm horizontal and 8 cm drop. As shown in Figure 5.31, the beam is then reflected an other 62cm to the fibers. Note that the beam splitter is half way between the MMA and the SLM and between the MMA and the fibers, such that the spot trackers fit.

The total volume of the steering system is 8x70x20 = 11200 cm^3 or 11.2e-3 m^3 when including some margins. The telescope is 25 cm long and has a diameter of 8 cm, with an exclusion volume which includes margins is assumed to be 35 cm long and 13 cm diameter. This implies the cubic volume of 5915 cm^3 or 5.915-3 m^3. Furthermore, the colimator, filter, re-imaging stage and mirrors will have about 60 cm long and 5 cm diameter volume, with margins of 70 cm and 10 cm. This implies a cubic volume of roughly 7000 cm^3 or 7e-3 m^3. The total volume would then be 24115 cm^3 or 0.024 m^3, which is well below the 1 m^3 specified by **GD-CR-009**. The system overall can be seen in Figure 5.32.

5.4. Transceiver Design

The choice of transceiver through a trade-off was already made before the design of the pointing system. This section will explain the trade-off and the different aspects of the transceiver design. A number of technology and system choices where considered as viable options for the receiver design in two main categories; fiber and non-fiber systems. High Power Master Oscillators (HP MO's) directly pro-

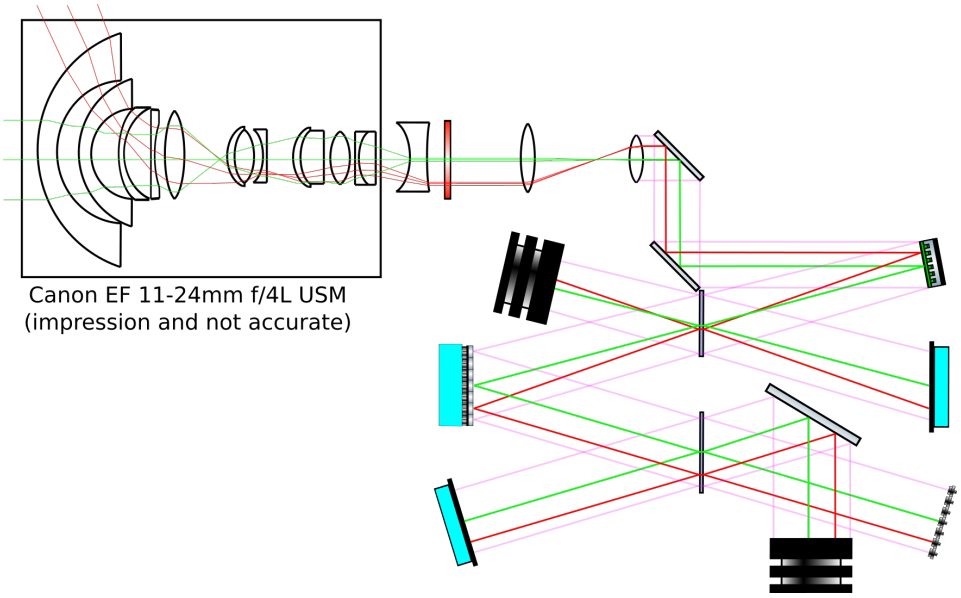

Figure 5.32: Depicted is the designed optical train. Shown are the incoming parallel rays from 2 far away targets. The first target is depicted in green and is directly on the optical axis. The second red target is at the extreme periphery of the wide angle telescope. The beams are directed into the telescope and are focused at the focal point of the lens system. Before this however, it is collimated at the appropriate beam diameter. The beams are now parallel. It is subsequently passed through an optical filter to filter out unwanted light and reflect it back out through the telescope. It then enters a re-imaging stage where the appropriate cross section and beam size is realized. Then from the perspective of the incoming beams (left to right) subsequently enter the steering stage of the system where the SLM steers the beams to the correct location on the MMA which is coupled to the fiber location. After reflecting of the MMA, it steers the beams into the correct fiber. The beams are split by beam splitter plates along their path to the spot trackers. The first of the spot trackers has the same optical path as the MMA and hence gives feedback to the SLM. The second is optically the same optical path as the fiber and hence provide feedback to the MMA's. The bi-directionallity of the system implies that incoming and outgoing beams follow the same optical path. Hence, the generated outgoing beams will also be split and are dumped into the beam dumps to prevent stray light.

ducing modulated light and ejecting it into the steering system. This can perhaps be done by directly modulating a laser diode or by placing a laser light emitting diode laser and propagating the light through an Electric Optical Modulator (EOM). The fiber equivalent would also have the laser diode either directly modulated or with an in fiber EOM. The Master Oscillator Power Amplifier (MOPA), which would utilize a lower power MO which is then amplified in free space by a crystal or as such. The in fiber MOPA would use a fiber amplifier instead of free space amplification.

One of the criteria is the data rate, where having high data rates are very preferable. Related to the design, there exist limitations in the extinction ratio and the modulation techniques. An EOM in space would likely be either piezo or gas based and so has numerous data rate disadvantages in terms of speed and spacecraft compatibility. Furthermore, larger diodes have stronger influence on the frequency due to their altering of the electric circuits and introduction of stray capacitance. Furthermore, general physical limitations of diodes decreasing the bandwidth and severely limit the modulation options. The extinction ratio is an important factor in increasing SNR, which are better when the signal power is small and is amplified post signal generation. Lastly, pointing losses are also causes for data rate losses. The pointing accuracy and the small signal criteria disadvantages the non-fiber non-MOPA designs significantly. Hence, the fiber MOPA is the better choice.[32][25][33]

High performance MO's with large bandwidths and high frequencies tend to not be very efficient[32][33]. Furthermore, the amplification of non-fiber systems would also have to be done in free space which requires more detailed optical design making it less space efficient and reliable. The use of a fiber would greatly deduce the optical complexity and allow for greater isolation and variation between different links. Hence, the fiber MOPA options would be the best for this.

Leakages of the pump laser light as well as other light sources can be prevented through optically isolating the fiber amplifier. However, the shot and beat noise of fiber amplifiers are notoriously bad according to Hobbs page 290[25]. The alternatives of using crystal amplifiers in free space will have similar problems. However, these problems can ultimately be overcome through using more isolators, although this is expensive, putting MOPA's at an disadvantage. This noise would hence not be present

directing in MO designs making these more attractive in this respect.

The design flexibility of fiber based systems are greater than the other designs. This is due to their relative space and mass efficiency, together with a large variety of COTS hardware. Furthermore, the optics exist in an optical fiber which allows for very easy form factors. This also has benefits for the same path, reffering to the incomming and outgoing beams occupying the same space, and pointing abilities which can be built into the system due to their flexibility. The TRL of fiber MOPA hardware is also very high for terestrial applications and also has had an extensive flight history in space.

The trade-off has been performed with their relative weighting shown in Table 5.4. The resulting transmitter technology and system chosen was the fiber MOPA design. MOPA will from now on be used to referrer to the fiber MOPA.

Table 5.4: Trade-off table for the system transmitter technology and layout. HP MO (High Power Master Oscillator) is a transmitter which directly produces modulated laser light which is released into the system. Fiber HP MO first couples it into a fiber after which it is transmitted. MOPA (Master Oscillator Power Amplifier) uses a low power MO and then amplifies the signal using a device in the free space path. Lastly, the Fiber MOPA which uses fiber amplifiers and low powered fiber coupled MO's.

Criteria:	Weight:	HP MO	Fiber HP MO	MOPA	Fiber MOPA
Date Rate	10	-1	-1	-1	1
SWaP	8	-1	-1	-1	1
Noise	5	1	1	0	0
Design Flexibility	7	-1	1	-1	1
Same Path Abilities	10	-1	1	-1	1
TRL/Flight History	9	-1	0	-1	1
Total:	49	-39	4	-44	44

The receiver technology can also be traded-off using the same criteria. In this case CCD, diode and fiber detectors have been traded-off as likely candidates. CCD's and Diodes have numerous problems associated with them regarding their ability to de-modulate the signal. The reason for this is that these technologies inherently measure intensity and hence are likely only compatible with OOK modulation. More complex modulation would require building de-modulation into the optical train, making this a very complex and expensive endeavor. This hence has implications for the data rates and the SWaP should more complex modulations be chosen. However, should this be implemented regardless, then the diode and the fiber recievers would likely perform similarly due to similar technologies likely being used. The CCD in particular is inherently slower due to the number of pixels having to be read out and the required de-modulation optics would have to work over a spatial area the size of the CCD. The design and operation of this would likely be a nightmare.

Furthermore, the CCD and Diode probably has to be cooled and prepared to maximize the performance and minimize noise. The fiber based systems have been designed for high data rate applications and hence do not have to be cooled. The diode as a result can be brought to work with little noise and some optical design. The CCD however has some inherent noise characteristics which are harder to remove. However, the use of fiber amplifiers, as stated before, can cause increased noise.

The use of fiber based systems increase the design flexibility greatly, have good TRL and have the benefit of being able to provide same path capabilities for the reasons stated before. The CCD has been used extensively in space instrumentation, however not as a high performance communication device. The CCD and diode lacks same path capabilities as well as having severe design flexibility limitations due to not being incorporated into a fiber.

The receiver trade-off is shown in Table 5.5. The result is that the fiber detector is the winner of the trade-off.

The fiber transceivers are common in high data rate applications such as those found in terrestrial applications such as the global internet optic fiber network. Fiber based transmitters have also been used in notable single beam applications. Currently, the most applicable hardware which as flown in space come in the form of a MOPA (Master Oscilator Power Amplifier) configuration due to their high performance and efficiency. Previous flights of the MOPA configuration include Optical Payload for Lasercom Science (OPALS)[41][73], Optical Communication and Sensor Demonstration (OCSD)[29] and Nanosatellite Optical Downlink Experiment (NODE)[10][11][8][9][33][14][45]. As the name suggests, the system consists of a high performance modulator for the laser light in the form of a Master Oscillator (MO) and is capable of different modulations. The MO is not energy efficient and so the sig-

Table 5.5: Trade-off table for the system receiver technology and layout considering the previous trade-off for the transmitter in Table 5.4. The CCD is a imaging sensor which us used to directly detect the amplitude oscillations in the signal spot. The diode is a single avalanche diode onto which the laser light is directly focused onto. Lastly, the fiber detector has a fiber as an input.

Criteria:	Weight:	CCD	Diode	Fiber Detector
Date Rate	10	-1	1	1
SWaP	8	-1	-1	0
Noise	5	-1	1	0
Design Flexibility	7	1	1	1
Same Path Abilities	10	-1	-1	1
TRL/Flight History	9	0	-1	1
Total:	49	-26	-5	36

nal power is kept low to waste as little energy as possible down to almost 3% according to Kingsbury on page 65 just below figure 3-4[33]. The weak signal is then amplified with a doped fiber amplifier as the Power Amplifier (PA), such as an EDFA (Erbium Doped Fiber Amplifier) or YDFA (Yttrium Doped Fiber Amplifier).[32]

The choice has to be made as to which fiber amplifier has to be chosen. Hobbs on page 290 specifies that there are different types of dopants for fiber amplifiers, namely Erbium, Neodynium and Holium. Erbium as a dopant would be best for 850, 990 and 1550 nm while Neodynium for 1060 and 1320 nm and Holium at 1380 nm. Furthermore, there also exists Yttrium as used by Janson and Welle[29], which is optimal for 1050 nm[33]. The optimal dopant would hence be Erbium because of its performance around 1550 nm, which is the target wavelength as discussed in section 4.1 and will satisfy **GD-CR-019**.

Erbium can be pumped at 980 nm or 1490 nm. The pump wavelength should be chosen to be as close to the signal wavelength of 1550 nm, as this will result in the least losses. The reason for this is because the photon energy of a 1490 nm photon is 1239.8/1490 = 0.83 eV, for 980 nm 1.27 eV and for 1550 nm 0.80 eV. This implies that a pump laser with a wavelength of 980 nm is fundamentally limited to 62% efficiency. Where as the 1490 nm pumping would result in 96% maximum efficiency[72]. This will also reduce the thermal loads on the system due to the lost energy not being dissipated as heat. Hence, the pump wavelength is preferred to be 1490 nm. However, in combination with the laser diode for 1490 nm should it self require an efficiency which can exceed the 980 nm diode fiber combination. Furthermore, the diode laser setup has to be chosen which can operate stable at the operating temperature.

For an indication of the overall efficiency and a hardware layout which can be expected, the design produced by Janson and Welle[29], as can be seen depicted in Figure 5.33, will be discussed. This system utilizes an Yttrium fiber amplifier and so there could be efficiency differences. It is claimed that the laser pump diodes used are around 47% efficient and use a 1-2 W pump laser and a second 17.5 W pump 3 diode laser. The signal wavelength of 1064 nm and a pump wavelength of 915 nm would result in a $\frac{915}{1064} = 0.86$ theoretical maximum amplifier efficiency. This leads to an overall efficiency of both amplifier stages of roughly 40% when combined. The final result is that the system has an electrical input power of 50 W and an optical output power of around 10 W, giving an overall efficiency of 20%. The remaining losses are due to the energy consumption of the master oscillator and data board as well as the losses in the optical elements such as the isolators, pump combiners, etc...

Note, that the power transmitted by EDRS[24][6] are on the same order, while being at GEO. However, comparable nonetheless with other laser communication hardware. Conversely, the effective aperture diameter is smaller, implying more severe beam divergence. This would likely lead to lower data rates compared to the larger aperture systems such as EDRS.

NODE has a 0.2 W transmitted power with an input power of 15 W according to the Integration and Testing of the Nanosatellite Optical Downlink Experiment presentation given by Cahoy on slide 3[8]. This would work out to an efficiency of 1.3%. This indicates that large variation in efficiency can be found due to design differences.

A duplex transceiver design was created which allows for same path duplex communications for a given fiber out of the 10 available fibers. It hence represents one link. This design is shown in Figure 5.34. A pre-amplifier for the receiver is included in the case where for a given BER and jitter the transmitted power to the system can be minimized, effectively increasing the performance[46]. This

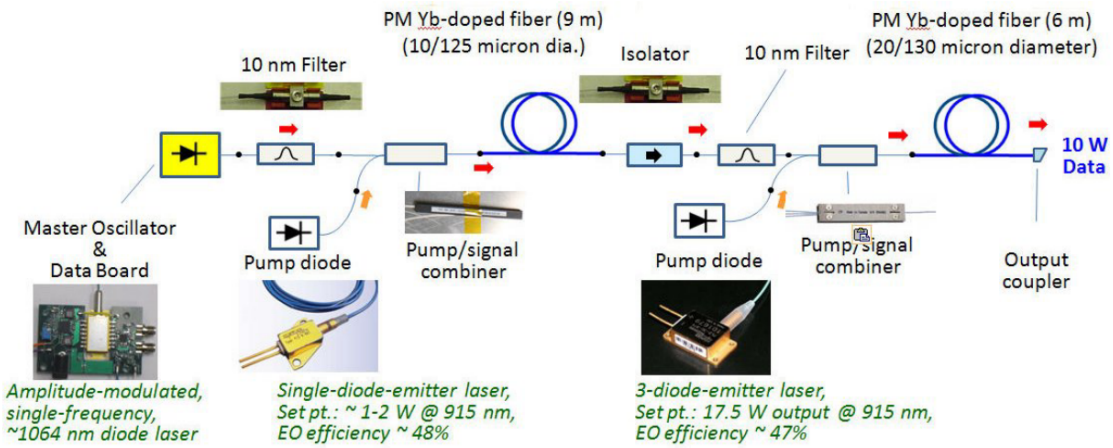

Figure 5.33: Illustrated is the laser downlink transmitter hardware schematic depicted in Figure 4 on page 5 found in "The NASA Optical Communication and Sensor Demonstration Program: An Update" by Siegfried W. Janson and Richard P. Welle[29]. From left to right, the Master Oscillator (MO) generates a modulated seed laser and is then amplified by a lower powered Yb-doped fiber amplifier, which is pumped by a single laser. It is then passed through an isolator which checks the direction of light. The signal is then amplified again through a higher powered Yb-doped fiber amplifier, which is pumped by 3 lasers. The signal is then sent out of the system towards the target.

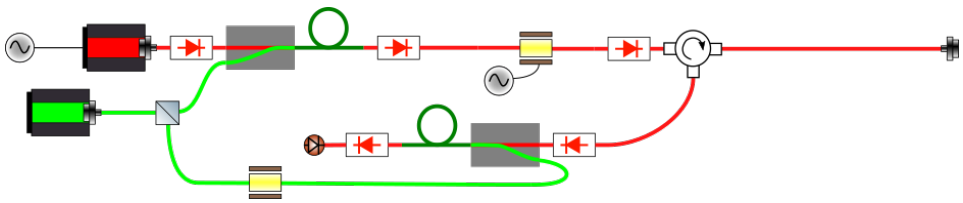

Figure 5.34: Duplex transceiver design for a single fiber. From right to left and following the path of an incoming beam, the GRIN lens couples the incoming laser beam into the fiber where it travels until it meets the optical circulator. This then diverts the beam down into the receiver fiber. There is a fiber amplifier which can be switched on and off when a given situation calls for a pre-amplifier in the form of an EDFA. The resulting beam is then detected by the fiber detector. From right to left at the top and following the out going beam, starts with a low power MO. The signal is then amplified by the EDFA and then sent through an additional regulator in case a situation calls for post modulation, pulsing, beaconing or other. It is then sent into an optical circulate which directs the beam into the outgoing fiber and subsequent GRIN lens. The fiber lasers are each pumped by a high efficiency 1490 nm laser diode. The signal wavelength of 1550 nm is shown in red and the pump laser wavelength of 1490 nm is shown in green.

should be controlled and actively optimized based on a feedback from the receiver power.

The system shown in Figure 5.34 it self is slightly different compared to the architecture shown in Figure 5.33, however the number of components in the fiber is similar. The connection losses shown where found to be similar and the relative efficiencies are similar at 20%.

Multiplexing is an important aspect of increasing the data rate of a given optical link, by modulating multiple frequencies of light and sending them along the same path. This effectively increases the number of communication channels and hence the data rate. To accommodate this in the optical train as well as the same path philosophy, Dense Wavelength Division Multiplexing (DWDM), with channels spaced 0.8 nm, can be used to ensure minimal dispersion[50]. This also makes them highly used in the long distance fiber communication and satisfies requirement **CG-CR-020**. Note, that not all the wavelengths of a regular DWDM might be usable. The exact specifics should be within the ranges specified in section 4.1.

For this a mux splits the incoming frequencies and combines the outgoing frequencies into one fiber. The same system can then be placed behind the mux.

This work will assume the efficiencies given by Janson and Welle[29], as these are comparable to the expected power efficiencies for high end 1450 nm pig tailed laser diodes at Thorlabs[59]. These are lower efficiency, around 30% instead of 48%, but it is assumed that even better diodes will be

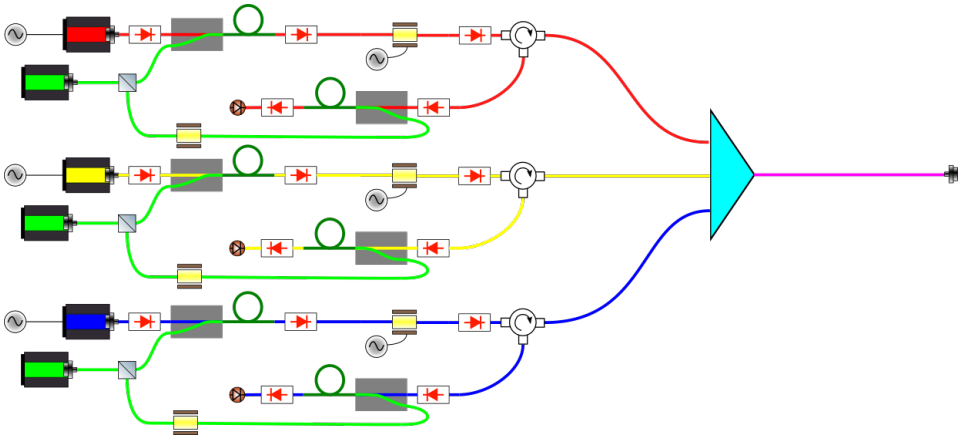

Figure 5.35: Multiplexed version of Figure 5.34 which uses a mux to separate and combine 3 different frequencies. The combined wavelengths are shown in purple while the separated frequencies are shown in red, blue and yellow. The pump laser wavelength is shown in green.

available elsewhere which are around 40% efficient. Furthermore, the increased wavelength conversion efficiency of 96% given by EDFA's pumped by 1490 nm instead of 86% makes up part for this discrepancy. This will also increase efficiency by maintaining a lower fiber temperature due to higher efficiencies in the fiber[3]. The system architecture is also inspired by Janson and Welle[29] as well as the system architecture used in internet infrastructure depicted in figure 2.2 by Wang[72]. The system efficiency, considering the efficiency of the SLM as well, will hence be assumed to be 20% for the transmission and 35% for the receiving pre-amplifier.

This assumption was verified by comparing the insertion losses and efficiencies of the components. The system does not contain a 10 nm filter or the same number of insulators and less optical amplifiers compared to Figure 5.33. However does contain optical circulators and modulators. Optical circulators work in multiple directions for a range of wavelengths and maintain polarization. These are used in many communications applications to route signals in multiple directions along the same fiber using a similar structure as optical isolators and also act as such. These have similar losses compared to optical isolators[60][61].

For a 10 W optical link it would imply a consumption of 50 W electrical power meeting **GD-CR-008** and **RxTx-PA-005**. Furthermore, the components are standard components which can be purchased COTS, meeting **GD-CR-005**. The power consumption and efficiency are the same as previous designs. In fact, the fiber temperature is in all likelihood lower than found by Janson and Welle[29], meeting **RxTX-PA-001**. The radiation will probably also not be a problem as found by Williams and so **RxTX-PA-002** will likely be met. As discussed before, the efficiency of the fibers will be above 40% meeting **RxTx-PA-003**. However, not when considering the laser diode in the system. The pre-amplifier is used conditionally, meeting **RxTx-PA-004**.

Lastly, the emission of 10 beams at 10 W would imply a total incident power of around 100 W. These powers might cause thermal issues for SLM's, implying that these must be cooled[26][62].

5.5. Final Link Budget

This section will shortly summarize the efficiencies and signal path to find a basic link capacity according to the Shannon-Hartley theorem discussed at the start of the chapter and shown in Equation 5.1. This simple analysis will be done between two of the same multi-beam systems and will specify the Shannon-Hartley limit of a hypothetical link budget. This will be considered per 0.8 nm channel of the DWDM and implies a 0.1 THz bandwidth.

Starting at the transceiver, where the input power of 50 W with an efficiency of η_{Tx} = 20%, which leads to an optical signal power output of 10 W. The associated noise for the EDFA is harder to estimate. Hobbs on page 290 under "8.7.4 Fiber Amplifiers"[25] in the first paragraph mentions that the spontaneous emission noise increases through the use of fiber amplifiers. Perhaps not unexpectedly considering that the system works through pumping electrons to quasi stable states. Amplified Spontaneous Emission (ASE) noise can be calculated using the Equation 2.7 on page 9 in the work by

Wang[72], which assuming an population inversion factor of 1 and a gain of 20 dB, would result in a noise power of 1.2 μW. However, the amount of noise found by Paschotta[44] for a gain of 40-30 dB at the same wavelengths gain is closer to an order of 3 dB which would result in 2 W. Considering this, it was chosen to take the larger noise value of 2 W on a signal of 10 W.

The beam splitters chosen have a transparency of 90% and hence reflect 10% of the outgoing beam into the beam dump. There are two beam splitters implying an optical train efficiency of η_{OT} = 81%. The rest of the optical train is assumed to have negligible losses. Due to the receiving system also having the same optical train, this too will have the same optical train efficiency.

The telescope pointing accuracy is not relevant due to the wide FOV, making L_R = 1. The pointing limitations pointing accuracy of the system is equal to that of the SLM when transmitting. This is due to the spot having to be pointed onto the target and offsets can cause the less intense fringes on the sides of the spot to be received instead. This is expressed by Equation 4.4. Considering the optical train depicted in Figure 5.32, the telescope diameter is not completely utilized and instead only a smaller portion is used. The diameter of the telescope is around 8 cm and hence it is assumed that the effective diameter is 4 cm. The Rayleigh formula produces a divergence angle of 47.28 μrad, implying that L_T is 57.26% considering the 16.3 μrad SLM pointing accuracy found in subsection 5.3.2.

The distance to the target was set at 10,000 km to simulate large distances and 100 km to simulate propagation at an angle through the atmosphere. The free space propagation losses are described in Equation 4.1 and L_S = 1.75e-9. The propagation can pass through the atmosphere and additional losses due to absorption, discussed in subsection 4.1.2, is η_A = 80% for 100 km of atmospheric propagation.

The signal now reaches the telescope of the receiver. The same optical train efficiency is applied of η_{OT} = 81%. The difference now is that the beam must be fiber coupled. The steering systems should allow for optimal fiber coupling, the maximum efficiency of which is η_{FC} = 81% efficiency. Due to the corrected jitter, it is assumed that the pre-amplifier is not required.

The final expression for the arrived signal is hence as follows:

$$S_R = \eta_{FC}\eta_{OT}\eta_A L_S L_R L_T \eta_{OT}\eta_{Tx} S_T \tag{5.24}$$

S_R, the final signal power received at the detector, was found to be 3.41e-9 W. With the noise calculated in the same way, resulting in 0.68e-9 W. This would result in a Shannon-Hartley limit data rate of 258 Gbps, noting the previously found 0.1 THz bandwidth. This exceeds the **GD-CR-016** requirement of 40 Mbps. When considering the DWDM this number could be increased by orders of magnitude. Although terrestrial fiber optic cables can transport data in the order of Tbps, this result quite unlikely to be close to the real performance. There are numerous performance and practical limitations when considering signals of such low powers. Detection of such small signals is already a great challenge and so is the presence of unconsidered noise such as the detector noise and thermal radiation.

It is clear however, that the majority of the problems would be at the receiver. To illustrate how unreliable the link would be, consider a situation where in the final stage some noise of -50 dBw or 10 μW is added either in the receiver, fiber optics and/or optical train. The system's Shannon-Hartley limit would fall to 50 Mbps. Moving closer to the target at a distance of 2500 km, the received signal becomes much more reasonable to 0.1 μW and increase the limit to 740 Mbps with the same noise input. The only real way to solve the signal power problems is simply transferring larger signal powers. This can be accomplished by increasing the transmission power, finding shorter distance applications or larger telescopes with more accurate steering.

5.6. Summary and Conclusion

The final design of the optical train can be seen in Figure 5.32 and the transceiver in Figure 5.35.

Fiber coupling into a fiber end is exceedingly difficult due to the small size of the fiber. These requirements can be softened by inclusion of a GRIN lens. Additional benefits of a GRIN lens is that the beam divergence is insignificant when propagated through the optical train. It was chosen to use a 1.8 mm diameter GRIN lens with the accompanying 1.8 mm diameter beam. This increased the tolerable planar offsets by a factor 450, to 1.58 mm and 450^2 for defocus to 8.16 meters for 40% efficiency. This is up from 3.52 μm and 40.3 μm respectively. This was hence included. The effects of jitter where deemed minor and out of the scope of this thesis for the chosen turbulence profile.

It was found that the allocation and the size of the pixels (pixels referring to mirrors or SLM pixels) to each beam used had significant effects on the system performance. This was gleamed from the use of

simulations and beam profile analysis. The proximity of beams would require smaller control surfaces allocated to them, which in turn would eventually result in cropping the beams are subsequent signal loss. High resolution steering mechanisms allow for the smallest and finest control pixel allocations and would hence allow for closer beam proximity. The proximity limit is equal to the spot resolving limit.

Bigger problems arise when large discrete steering surfaces are used such as in a mirror array. These occur when beams cross the boundary between pixels and when 2 beams populate the same pixel. These issues are more pronounced with larger beams and could result in complete signal loss for all of the links at once. The result of these problems with larger pixels and the potential for AO, the higher resolution SLM was chosen for separating the beams in the first steering mechanism. The larger surfaces for the second steering mechanism due to better speed performances and not requiring fine pixel allocations.

The feedback loop was designed with 2 steering mechanisms to allow for the transmitting and incoming beams to follow the same path. The result of this is that they system increases beam handling capacity by factor 2 at the cost of one additional component. It also results in added system redundancy compared to the multi-path systems and allows for using the best of both worlds of low and high resolution steering mechanisms.

It was subsequently decided to have a high resolution SLM for the first steering stage and a low resolution MMA for the second stage. The feedback loop is closed through a spot tracker for each steering stage. The spot tracker is placed at a optically equivalent path as the target plane of the steering stage, in order to make the system as simple and accurate as possible.

The steering accuracy of the SLM and MMA where investigated. Using simulations the minimal slope of the SLM was investigated. Once the slope of the pixels exceeded 1 phase increment after every 5 pixels was sufficient. Based on this, it was found that an analog MMA with an 8 bit DAC and an SLM with 8 bit color depth would be sufficient, however 16 bits would be more preferred for both. There exist numerous COTS SLM's and MMA's which can achieve this.

The design of a telescope is crucial in the sense that it must not distort the beams and have a large field of view. The distortion would have negative effects on the fiber coupling and the wide field of view allows for more utility and diverse applications. This would imply that fish-eye lenses are not suitable for these applications. However, the film and photography industry solved this problem using rectilinear lenses, which can map angles into grids. The result is that an easily integratable and durable COTS camera "lens" can be used as a telescope. In this case the Canon EF 11-24mm f/4L USM was chosen, but alternatives do exist.

The transceivers where designed in the MOPA fiber based architecture. The main reason for the MOPA architecture is the higher performance for tolerable energy efficiencies. This allows for high performance applications while maintaining a low swap. Basing it on fiber technology allows for the system to use same-path communication. Fiber technology is also very established and widely used on Earth for high data rate applications. The transceiver can hence be fully COTS.

The Shannon-Hartely limit is harder to find good representative values especially at large distances. When moving closer to the target at a distance of 2500 km, the received signal becomes much more reasonable to 0.1 μW and increase the limit to 740 Mbps. This, with the right modulation and multiplexing, could result in comparable data rates of current small satellite laser communication systems. Larger receiving telescopes and signal power would increase this substantially understanding the limits discussed in chapter 4.

The resulting system meets all relevant design requirements and will be verified and validated to do so in the coming chapters.

6

Beam Control, Algorithm and System Performance Simulation

The steering is a challenge for both a single beam and a multi-beam system which have common themes and crucial differences. The method by which the system controls their beams has already been discussed and the hardware layout given. This chapter will discuss closing the control loop in software and perform a simulation to verify and validate the design.

The single beam systems discussed in chapter 2, illustrate some of the challenges and solutions for single beam steering. Two examples which illustrate a general scheme are the EDRS and NODE systems. EDRS uses the system shown in Figure 6.1. Considering this design, there are in fact multiple closed loops identifiable which use the same point and track controller. Namely, the feedback data is used for both coarse and fine pointing assemblies. The adjustment of the coarse. The system utilizes a feedback loop form the receivers to the different pointing systems. The feedback loop is entirely contained within the system it self and is a closed loop system. The work does not present a clear way as to how the coherent receiver or other produces a spatial signal.

The second example, that of NODE, is shown in Figure 6.2. The system in fact has 2 feedback loops, one for the ADCS subsystem which provides coarse pointing and the other for the fine steering mechanism for fine pointing. The ADCS feedback loop is closed. The beacon tracker and algorithms will send the offset signal to the ADCS, after which the satellite will adjust its attitude changing the signal, in effect which closes the loop.

For the second loop is either open or closed. The adjustments of the fine steering mechanisms does not alter the position of the spot on the beam tracker, making it open loop. However, when the signal strength of the receiver is sent up via radio link to the spacecraft, there can be some feedback. In this case, the feedback would not be spatial but in the form of signal amplitudes. There would also be a delay depending on the speed of the detection, processing and transmission.

The coarse pointing stage, as discussed previously in chapter 2 and chapter 5, is both unfeasible for multiple beams and not required. Instead, wide FOV optics where chosen which removed the need for pointing either the whole spacecraft or an arm. What more, is that these systems follow singular beam tracking. This implies that an algorithm must be developed which can distinguish between different beams.

Because the multi-beam system designed is duplex with a same path approach to incoming and outgoing beams, is it somewhat comparable to ERDS which also is a duplex system. The incoming and outgoing beams even follow roughly the same path through the telescopes. However, due to it being single beam it does not require control of both angle and location of the beam. The result is that the system only requires one set of fine steering mechanisms. As discussed before, the multi-beam system must also be able to control both the location as well as the angle of the beams. The result is that twice the number of spot trackers and control mechanisms are required to be controlled and a solution to this must be found.

A number of multi-beam designs discussed in chapter 2 have different approaches to the control loop. However, the multi-beam design by Treibes et al.[66] shown in Figure 2.3, has a similar beam tracking and steering system philosophy. The design uses a multi-spot tracker on the focal plane of

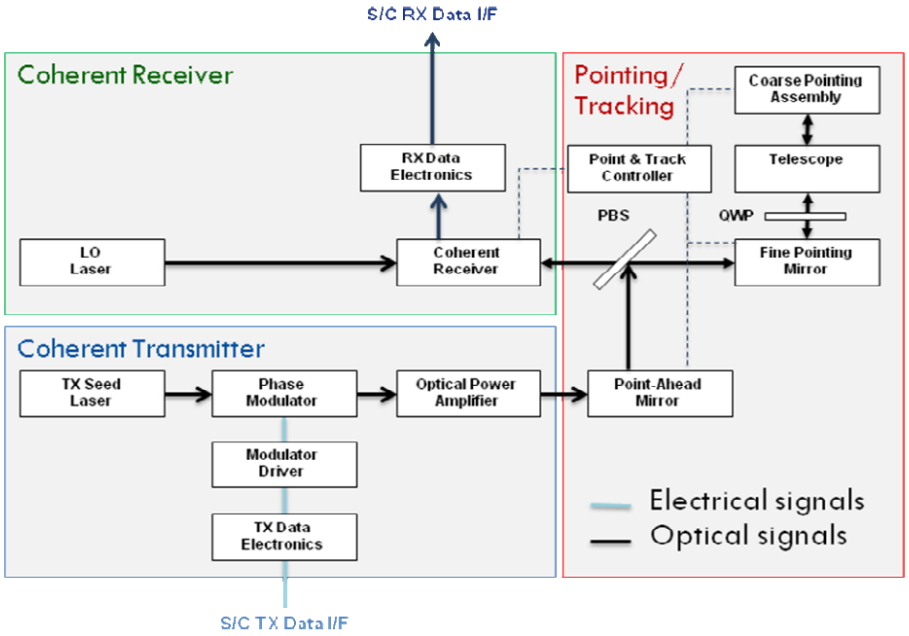

Figure 6.1: Illustrated is a block diagram depicted on page 284 in Figure 1, in the work "The European Data Relay System, High Speed Laser Based Data Links" by Frank Heine, Gerd Mühlnikel, Herwig Zech, Sabine Philipp-May and Rolf Meyer[24]. Considering the feedback loop for beam steering, the coherent receiver provides feedback to the point and track controller. This controller adjusts the coarse and fine pointing systems. This subsequently changes the input on the coherent receiver, closing the loop.

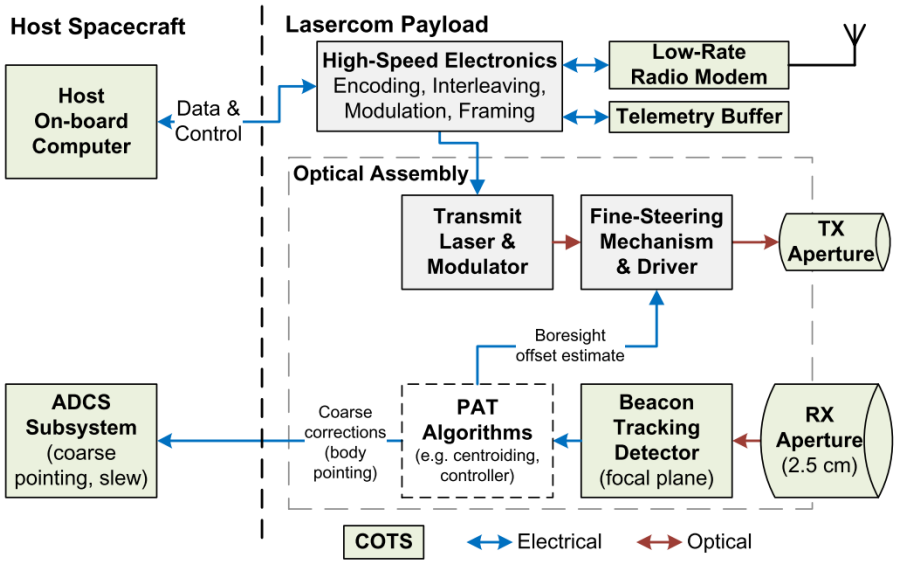

Figure 6.2: Illustrated is the block diagram of NODE, depicted in Figure 2-2 on page 42 in the work "Optical Communications for Small Satellites" by Ryan W. Kingsbury and also shown on slide 27 in "Laser Communication with CubeSats" by K. Cahoy. Considering the feedback system for beam steering, the system obtains the beacon location by reading out the beam tracking detectors. This is placed on the RX Aperture focal plane. The detector is read out and subsequently analyzed by the Pointing, Acquisition and Tracking (PAT) Algorithms. This provides attitude and steering data to the ADCS System for coarse pointing and the fine steering mechanism for fine pointing respectively.

the telescope. The resulting spots are tracked and the receiver fibers displaced to their locations. The resulting transmitter sources/fibers are also displaced to allow their spots to overlap with the received spots. The system therefor uses a closed control loop for each incoming and out going beams. The design does contains a fast steering mirror but it does not control the beams individually.

Due to there being 2 sets of movable receivers and transmitters, it could be forgiven to think these would be equivalent to having 2 control mechanisms. However, these are not equivalent to the two steering mechanisms using in the multi-beam terminal design discussed here. The difference lies in that in this system the orientation and location of the beams are controlled while the design by Treibes et al.[66] controls only the location of the transmitters and receivers. This design philosophy was not use for this system, as it would restrict the FOV and could not guaranty same path.

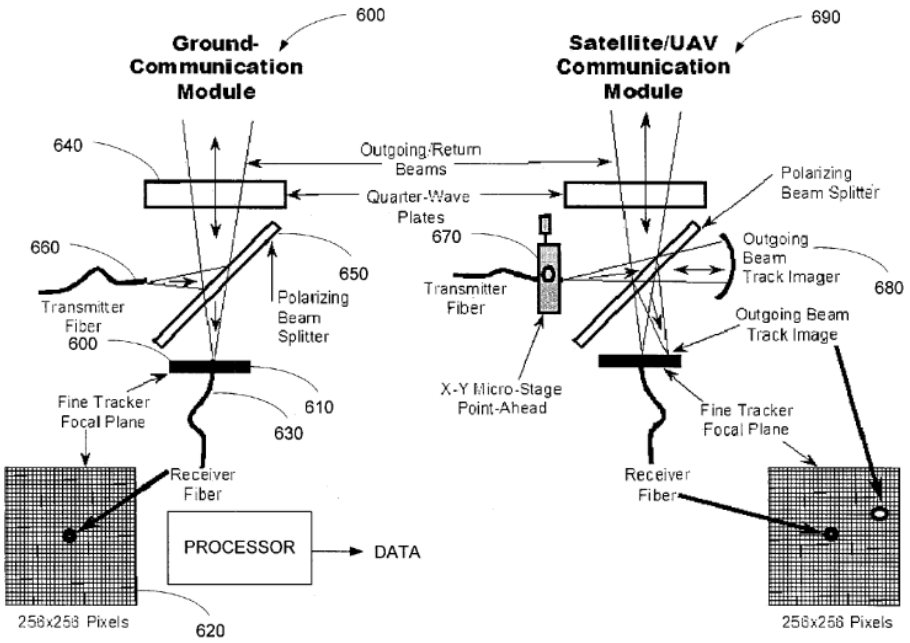

Figure 6.3: Illustrated is the patented design of different communication modules produced by Larry H. Capots, Robert Sigler, Kenneth Triebes[12], the figure can be found in figure 4 on page 5. Here, the communication module considered is the satellite communication module. The light arrives through a quarter waveplate and is then focused on a spot tracker. The receiver is embedded into the spot tracker. The outgoing beams are steered to overlap with the receiver fiber automatically pointing into the correct direction by large steering mirrors. The latter can be seen in Figure 2.4.

In terms of same path pointing, the design by Capots et al.[12], might seem to be more representative close to the current system design. However, this is not the case. The principle in the design by Capots et al.[12] shown in Figure 2.4 and Figure 6.3 is to align the spots such that both incoming and out going beams. This indeed causes them to be on the same path. However, the difference with the system designed in this work, is that a large steering mirror is used for each beam separately. This is equivalent to having a separate telescope for each beam. Consequently, the resulting beam position is automatically correct, leaving only the angular error. Furthermore, the beams are split in the fibers and not with free space optics. The beam control for this design should be able to handle both angular and positional errors.

The design produced in this work would hence have to be able able to have a completely closed control loop for all beams in the system, it should do this by being able to identify and separate each beam, the control must be done with 2 steering mechanisms and should be able to do all that with 2 spot trackers.

This chapter discusses the beam steering algorithm and it will simulate the designed steering system. The steering algorithm was designed to be compatible with the feedback method designed and closes the feedback loop on the software side. The algorithm will then be verified by putting it through its paces. A number of simulations have been performed of the steering system described in chapter 5 using the model and algorithms discussed in chapter 3. During these simulations, the input beams were detected and subsequently steered to target locations where the receivers would normally be. The results show that the system meets the designed performance and all the remaining requirements. It will also show some of the associated issues with the algorithm, both in its working and in its unavoidable physical limitations.

First, the working principle of the beam steering algorithm used will be discussed. The script of

the algorithm will be subsequently explained using the Matlab®programming environment. Subsequent simulations are performed of the designed steering system and the results discussed. Lastly, the chapter will be summarized and concluded.

6.1. Working Principle of the Algorithm and Model

The algorithm working principle is derived from the feedback system discussed in subsection 5.3.1. Each steering surface receives feedback from the associated spot tracker which depicts through same path the locations of the spots at either the MMA or GRIN lenses. The model and the algorithm is depicted in the block diagram shown in Figure 6.4. It is important to note, that each steering surface has independent control loops. Hence, the same algorithm can be used for the SLM and the MMA. However, the MMA will not require steering area allocation so this can be omitted for the MMA.

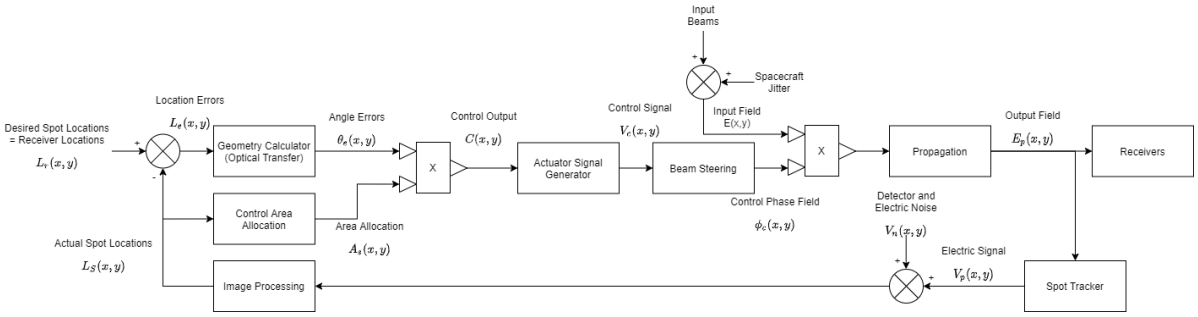

Figure 6.4: Illustrated is the block diagram of the model and algorithm.

Considering Figure 6.4, the simulation starts with the input beams which contain the atmospheric jitter. The spacecraft jitter is added and the resulting electric field is referred to as the input field, $E(x,y)$. This is located at the input aperture and is incident onto the steering surface. The steering surface, when active, will produce a phase field for the SLM and tilted mirrors for the MMA. Both can be expressed as phase fields however, with different discretizations. The fields are kept in their complex representation, implying that multiplication with the control phase field and the input electric field will yield the steered electric field and subsequently the steered beams.

This field is propagated through the steering system until the beam splitter, steering surface or GRIN lens of the receivers. The beam splitter sends some of the beam energy to the spot tracker in the form of the propagated output field, $E_p(x,y)$. The intensity of which is measured by the spot tracker and converted to an electric signal in the form of an array, $V_p(x,y)$. Some detector noise can be added here in the form of $V_n(x,y)$, however in this work it will be ignored. The signal is then inserted into the algorithm.

The algorithm was built separate from the model, with the input from each spot tracker supplied as a virtual 1080x1080 pixel spot tracker image in the form of an array. As far as the algorithm is concerned, it is connected to a spot tracker. The input field is generated by placing spots and moving them between frames in the simulation. The resulting intensity field is imaged by the spot tracker and contained in an array with an intensity value allocated to each pixel. This is then inserted into the algorithm. The algorithm produces a phase field/mirror angles in the form of a phase field. The model then super imposes this on the electric field and propagates the beams over 61 cm through the steering system.

The algorithm was included in the general block diagram depicted in Figure 6.4 and is shown in isolation in Figure 6.5.

From the image processing an array of pixel intensity data is received. The actual spot locations are derived through considering the central prominence of each spot in the form of $L_S(x,y)$. The algorithm then splits to perform 2 tasks; control area allocation and geometry/pointing of the steering.

The control area allocation finds the relative distances between each spot and then produces appropriate areas which are as large and round as possible in the form of $A_s(x,y)$. The large rounds areas allow for as little diffraction as possible.

For the geometry/pointing, the desired spot locations are the locations of the GRIN lenses of the transceivers, $L_r(x,y)$. The actual locations are subtracted from this resulting in the location errors, $L_e(x,y)$. The geometry then allows for the calculation of the angle errors which are expressed as

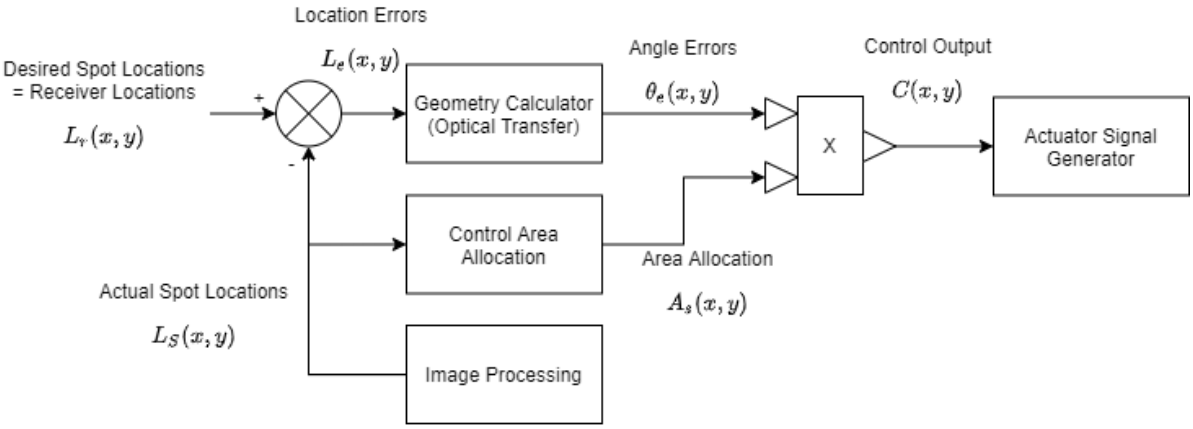

Figure 6.5: Illustrated is the block diagram of the algorithm.

phases or mirror angles and referred to as $\theta_e(x,y)$.

When these are multiplied and imposed into the control area allocation, the signal to the actuator can be generated. This intermediate step is required to ensure the correct and interpretive signal is sent to the steering mechanisms. The electrical signal, $V_e(x,y)$ shown in Table 5.1, is then put into the steering mechanism. The mechanism generates a phase field which is then multiplied with the input field. This completes the loop.

The algorithm hence takes the input from the spot tracker as an array of intensity values. From this array, it finds and identifies the spots from each beam. Subsequently, the best reflection angle to the transceiver GRIN lens locations is calculated. The locations of each transceiver is known and the propagation distance is also known. The maximum circular steering area is allocated to each beam to minimize diffraction losses as well as reflecting the maximum amount of power. Lastly the phase field/mirror angle is imposed onto the image and sent back to the model.

The locations of the transceivers are known to the algorithm. The resulting location of the spots after the steering system on the output is recorded in 2 dimensions and compared. This is done, presented, analyzed and discussed in section 6.3. The code for the algorithm is discussed in section 6.2.

6.2. Steering Algorithm Code and Working

This section shall discuss the steering algorithm. First the working of the code is presented and subsequently a short verification of its working is done.

6.2.1. Algorithm Code

Considering Figure 6.6. The algorithm functions every cycle and reacts to the changing situation. Firstly, the algorithm imports the data from the model which contains the current simulated positions of the beams. This consists of an array, with values corresponding to the intensity distribution as detected by the spot tracker.

The resulting array is then used to distinguish different spots and find their locations based on the intensity prominence. The detection of beams in itself using this method brings with it inherent drawbacks. Increasing the minimum prominence threshold would decrease the amount of noise detected as beams. This is especially useful when diffraction patterns are present. However, fainter beams might not be detected as a result.

With the location of the beams known, the vector between the beam location and the relevant receiver can be made. The relevant receiver currently is chosen based on proximity, but this criteria can be changed through the addition of some logic to the algorithm. The vector can be easily made because the position of the receiver is fixed and known. The geometry and path of the optical transfer can then be calculated.

The area is allocated by finding the halfway distance between the two closest spots and subsequently allocating the maximum area between these. The other beams are given appropriate area's as well.

Once this is done, the steering phase field is generated for each beam. This is effectively the

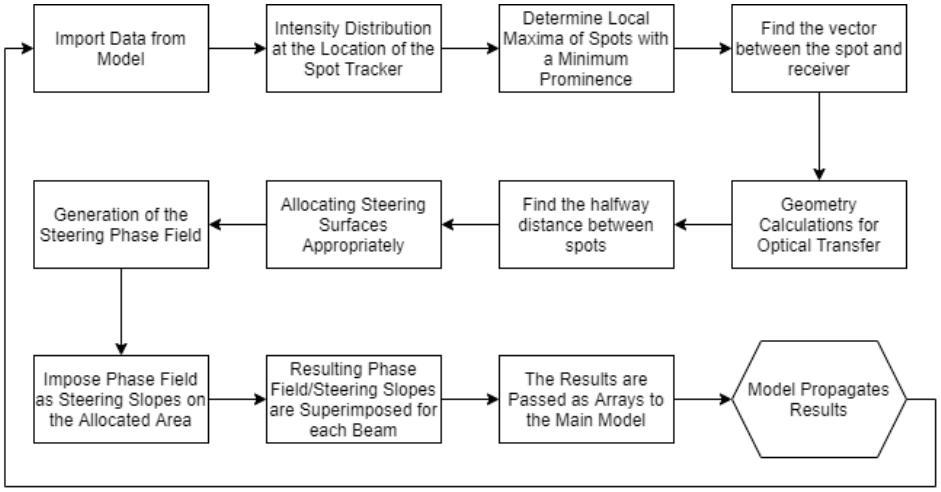

Figure 6.6: Illustrated is the functional block diagram of the algorithm. Each block shortly describes the actions performed in the algorithm.

steering slope of the mirrors or the phase distribution of the SLM. These are then imposed on their steering area's. These are done for each beam and subsequently compiled and super imposed. The resulting phase field is then sent back to the propagation model and simulated to the relevant location.

6.2.2. Algorithm Verification

To verify the algorithm, a number of tests are performed. Firstly, a test is done to see if the system can identify 3 beams. This will prove its ability to identify and distinguish multiple beams. Then a second test where the beams are steered from multiple locations in an open loop. This will prove its ability to calculate the geometry.

All the verification testing was done with a 4x4 cm input aperture at a distance of 61 cm. The wavelength is 1550 nm. All the resulting data can be found in Appendix D specifically in section D.1. Considering the first tables, it indicates that the spot tracker used was a 1080x1080 pixel camera.

First the identification of each beam. The algorithm is supposed to identify each beam uniquely and be able to locate it accurately. There were 3 beams generated, r1, r2 and r3, in 10 different locations each time to make sure the algorithm is able to perform everywhere. The x and y locations of each beam in the aperture have been recorded in the table titled ”Positions”. The goal of the algorithm is to find values as closely to these as possible.

The location data is originally expressed in terms of pixels. These are shown in ”Raw Pixels”. One will note that there is a line without data, this is because the proximity between the r1 and r2 beams was to close. The result is that the proximity calculations fail to resolve 2 beams and instead result multiple phantom beam detection. All the phantom beam locations have been shown in ”Frame 3: (detected r1&r2)”. This aspect will be discussed further during the full simulation section.

The pixel coordinates have been changed into the same scales and axis system as compared to ”Positions” in ”Detected”. At a first glance, these values are not the same. However, when observing closely, the same values can be found. After the proximity issues, the tracking of r1 and r2 resulted in flipping the order and identity of the beams tracked. The sorted data is shown in ”Detected Sorted”.

When comparing the ”Detected Sorted”, the detected beam positions, with the data in ”Positions”, the actual beam positions, it can be clearly seen that the spot tracker-algorithm combinations are very accurate. In fact, they are practically spot on. This clearly illustrates that the algorithm is very capable of multiple beam detection and tracking each uniquely for extended periods of time.

The second test, the steering, is shown in ”Steering Results”. The target locations where placed at (2083,2500), (2500,2500) and (2917,2500). As can be seen, the targets for each beam was hit within +- 1 pixel. This shows that the algorithm can perform the individual unique steering for each beam very accurately. The operation was done in an open loop which implies that even in open loop configuration, the system is very accurate.

The conclusion is that the operation of the algorithm has been verified and meets expectations. In

the next sections the full system will be simulated.

6.3. Simulation and Results

The simulation was setup to prove the steering system as a whole. During the simulation, 3 spots moved across the input aperture at different speeds and in different directions. Of the 3 spots, 2 of them would move close enough to each other that would not allow resolving between them. The 3 transceiver GRIN lenses where placed in a vertical row spanning 2 cm along the y-axis to simulate the aperture extremes of the MMA and the SLM. The simulation was chosen to contain 5000x5000 pixels while the spot trackers and SLM where allocated a more realistic 1080x1080 pixels.

The square aperture size was set to 4x4 cm and is propagated by the modified Fresnel propagation model over a distance of 61 cm. This results in and output aperture of 12.01x12.01 cm. The targets are therefor located at pixel (x,y) coordinates of (2500,2083.6), (2500,2500) and (2500,2916.3) designated ”Transceiver 1”, ”Transceiver 2” and ”Transceiver 3” respectively. With the simulation resolution, each simulation pixel spanning 24 μm on the output aperture implying that this is also the error resolution. Errors which are 0 where given the designation of 1e-5 [m] to allow for better graph viewing. The simulation duration was set to 800 frames as the targets moved across the input aperture.

A GIF was produced of the input and output aperture, however the limitations of static PDF’s and paper formats will not allow showing of this. Instead, stills from this GIF will be shown instead to illustrate different aspects. These GIF’s will hopefully be made accessible online for the interested viewer. Note that the MMA’s are not interesting to show its result due to their purpose being correcting the angle of the beam using individual mirrors and hence have no special cases.

The results for normal operation is shown in Figure 6.7 with the SLM steering shown in Figure 6.8. It can clearly be seen that the steering stage corrects the spot locations well and that the allocation of area is dynamic. The spots are also well formed with no observable diffraction effects distorting the spots.

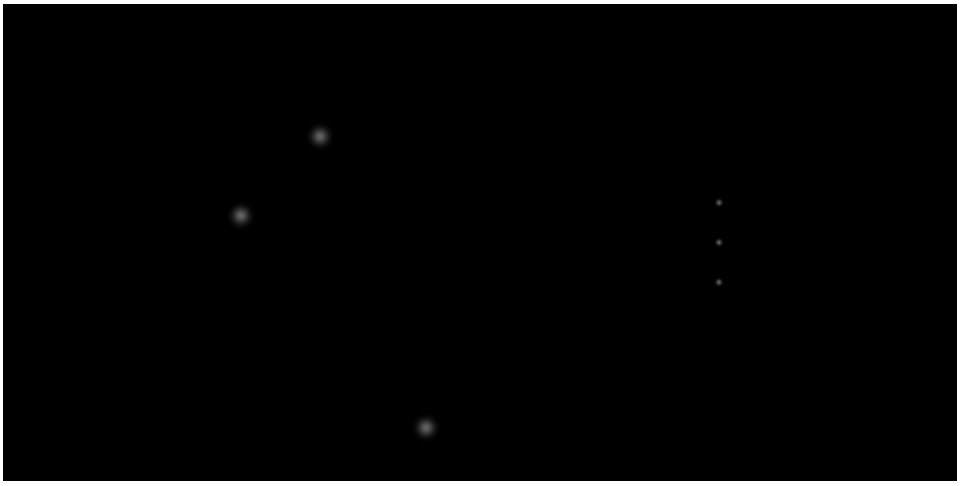

Figure 6.7: Shown is the system working normally. The figure shown contains the 4x4 cm input aperture on the left and the 12.01x12.01 cm output aperture on the right. As can be seen, the locations of the spots in the input aperture are not aligned while in the output apertures they are positioned (almost) exactly over the transceivers.

Some edge cases exist however. These arise in multiple instances, namely when 2 spots become unsolvable and when the spots exit the aperture. When 2 spots are at a distance of 1 beam radius away from each other, the spot tracker will lose the ability to distinguish the 2 spots due to the spots being unresolvable imaging wise. The algorithm will start seeing the 2 spots as 1 and steer it to a transceiver. The steering phase diagram by the SLM is shown in Figure 6.9a illustrates this phenomena.

However, in the transition during unresolving and re-resolving, the algorithm will interpret the strange shapes and intensity distribution as multiple oddly shaped beams in close proximity. The result is that the algorithm is thrown off and the steering calculations as well as area allocations cause diffraction effects. This is illustrated in Figure 6.9b with the result of the thrown off steering shown in Figure 6.10, diffraction clearly visible.

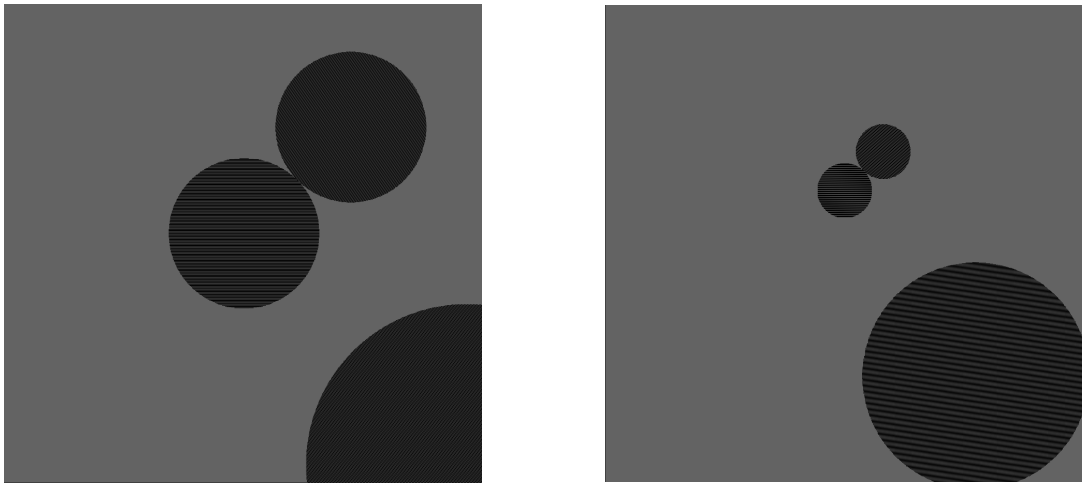

(a) (b)

Figure 6.8: 2 instances where dynamic allocation of steering area is clearly shown. The spots closer together get smaller steering areas compared to the spot further way.

During the transition process, the spots which are unaffiliated and well clear of the proximity of the other spots are also affected by the thrown off algorithm. This bug must be fixed before the implementation of this algorithm in real life specific to the application. However, the effect on the pointing during the transition between resolved and unresolved would be, for example, that suddenly all transceivers lose their spots. The result is severely increased pointing errors and complete loss of the associated signals. Once the spots become one, the pointing accuracy for 2 of the Transceivers will decrease, while for the 3rd one it increases to maximum. The same would then happen in reverse during the re-resolving transition and the system will go back to normal operation.

This beams being unresolvable is a fundamental issue in multi-beam communications and cannot be solved. All the previous designs mentioned in chapter 2 have this problem. If the system is made larger or the beams made smaller, then the number spots crossing each other can be reduced. However, it can also be tolerated and the data subsequently separated in the transceiver.

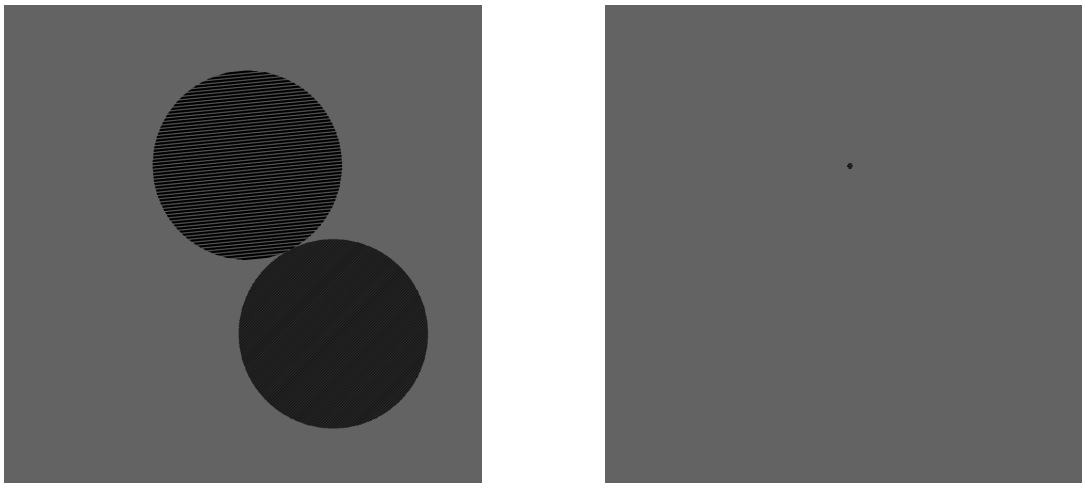

(a) (b)

Figure 6.9: A: Shows that the algorithm will treat 2 unresolved spots the same as 1 spot. B: Shows that the algorithm will be thrown off when the spots are in the transition of being unresolved.

When the spots exit the aperture, the spots are cut in half causing diffraction patterns and is shown in Figure 6.11. The algorithm will then stop steering them and the resulting pointing errors will increase for all the transceivers while the signal is completely lost.

The spot locations were measured during the experiment/simulation to find the system pointing

Figure 6.10: Shown is the exact moment when 2 spots transition to becoming unresolved. Due to the spots generating a different shape with multiple centers the algorithm is thrown off. The steering allocation for this moment is shown in Figure 6.8a. This causes a diffraction pattern and the algorithm also stops working for the unaffiliated spot on the bottom.

Figure 6.11: Shown are edge effects on the algorithm once the spots reach the edges of the aperture.

errors. The pointing errors were determined by finding the distance between the transceiver locations and the closest spot centers. What can be clearly seen is exactly what was predicted, the 2 error spikes on Transceivers 1 and 2 with Transceiver 3 maxing out due to having no beams allocated. This confirms the behavior when the spots become unresolvable and re-resolvable. The same prediction was true for the spots exiting the aperture at the end. What also can be seen is the steering accuracy. From the oscillating shapes in the data, the steering accuracy would be equal to that of one simulation pixel, which is expected since higher accuracy's are immeasurable.

The reading the plot in Figure 6.12 could be quite hard. The reason for this is that the model is discrete and hence the data jumps between different errors. From the graphs it is hard to determine the pointing errors during normal steady operation due to the noisy nature of discrete pointing. To make the behavior more clear, a 5 frame moving average of the previous 5 frames are plotted in Figure 6.13.

The same features can be seen in the moving average plots but representative. From the data, the average error is around 2e-5 m. If this were to be inserted into the normalized fiber coupling identities in Equation 5.3, it would result in a normalized displacement error of 0.013. This is indistinguishable from perfect fiber coupling conditions as can be seen in Figure 5.6 and exceeds all the associated requirements.

During the time between the unresolving and re-resolving it can be seen that the error drops to the regular levels for transceivers 1 and 2. The error for transceiver 3 maxes out, due to the system assuming that the beam is steered out of the spot tracker bounds. Hence, this can be ignored as the

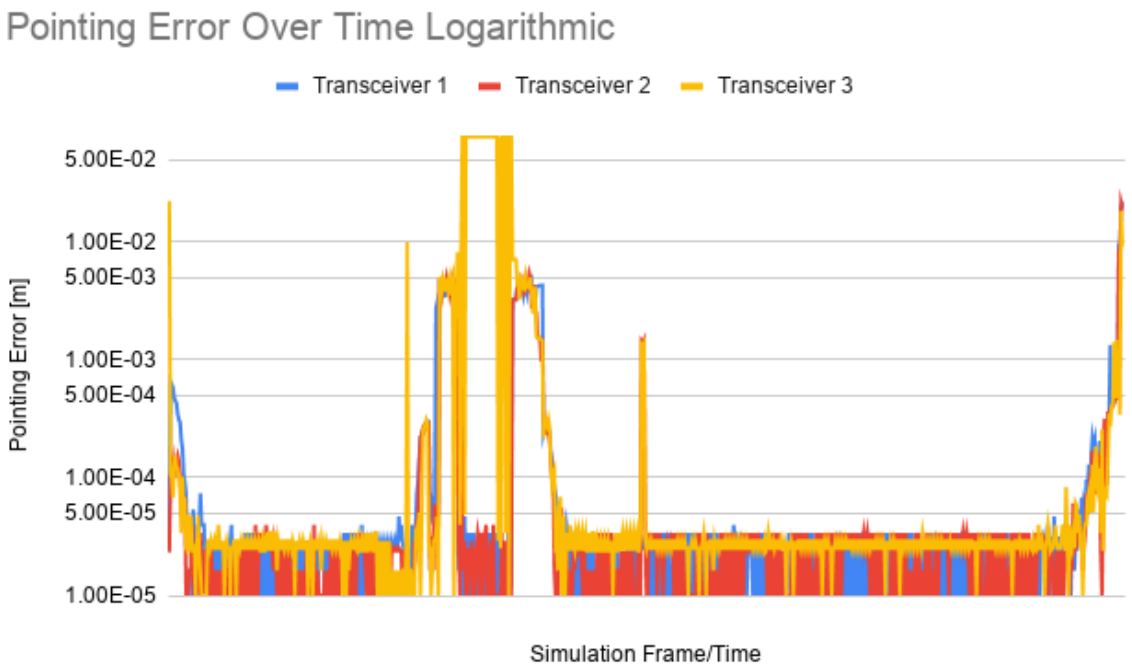

Figure 6.12: Illustrated is a logarithmic graph of the pointing error in the simulation over time for each transceiver. As can be seen in the graph, the errors generally oscillate at around 2e-5 m, which might be more clear when considering Figure 6.13. The first period of increased error are the spots entering the FOV. The second occurs due to 2 spots becoming unresolvable and then again resolvable during which it throws off the algorithm. The second is due to the spots leaving the input aperture and hence being diffracted by the aperture walls. Note that 0 values where allocated 1e-5 m.

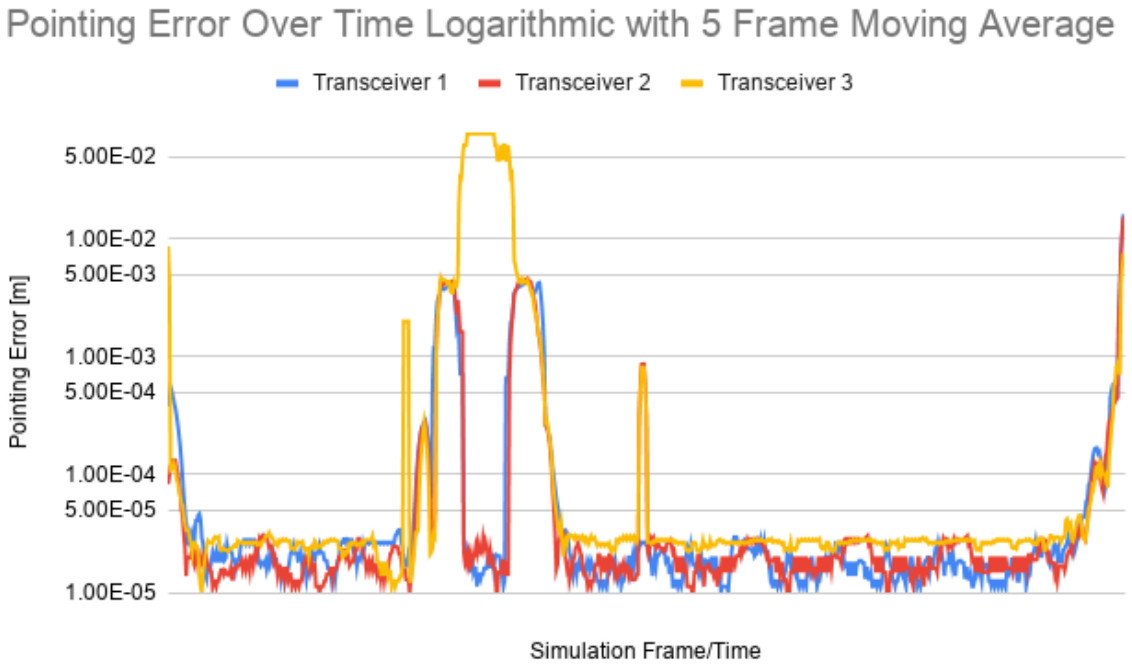

Figure 6.13: Illustrated is the same graph as illustrated in Figure 6.12 with a 5 frame moving average to make it more visually easy to view. This shows a more steady an easily viewable graph.

3rd beam cannot be resolved and so effectively does not exist as far as the system is concerned.

The time for each complete signal outage due to spots crossing paths in this case are around 15-20 frames each. The 2 spots are entwined for about 44 frames in total. This implies those 2 links are lost for about 11% of the time if they cannot be detected when coupled into the same fiber. For the 2 spots which are crossed, if the transit time is assumed to be longer than 2.3 minutes, the system would meet **GD-CR-017**. The transit time for a LEO satellite can be longer than 2.3 minutes when located at the appropriate distance. The system will therefore be more than likely able to keep the link active continuously for longer than 2 minutes, meeting the requirements.

The unaffiliated 3rd spot is lost for 5% of the time using this algorithm, which would still meet the requirements. Assuming the bug is fixed, this would imply a constant link for unaffiliated spots during the entire time they exist in the FOV. It should also work when the aperture is filled with the full 10 spots with the fixed bug.

In conclusion, according to the simulations, the system can work and will produce very good fiber coupling results. However, there is a bug that has to be taken out to prevent complete signal loss of all links when 2 or more spots cross paths. Other than that, the system exceeds requirements as a whole.

6.4. Summary and Conclusion

The algorithm has been fitted to the feedback system and the loop has been successfully closed. The working algorithm proves that the feedback loop can be closed for each steering mechanism separately and work semi-autonomously. It uses prominence to determine and distinguish between different beams, perform geometric calculations and is capable of allocating the steering area. The feedback loop is shown in detail in Figure 6.4.

The system described in chapter 5 was simulated using Fresnel propagation discussed in chapter 3. It showed that the steering system is capable of steering the beam accurately and within requirements. The control algorithm was capable of distinguishing and allocating the correct control input to the steering mechanism. Furthermore, the control area allocation was continuously round and allocated the maximum area to the two closest beams/spots. The resulting steered beams where also not diffracted and had good quality. The algorithm was also capable of controlling completely differently spaced and moving beams without prerequisite knowledge. Lastly, it demonstrated it was capable of re-acquisition of lost beams and re-assigning a transceiver on its own.

It also showed some problems. These where namely that when the beam proximity was reduced to the point where they became unresolvable. The transition between 2 beams to 1 and then back to 2 caused the system to lose all communications include that of other links. The output was also subsequently diffracted beyond use. The algorithm must be adjusted to handle these problems. However, after the transition from 2 beams becoming unresolvable into 1 the system was able to recover and re-allocate transceivers to a satisfactory accuracy.

The time frame between these beam proximity errors were within requirements and around 15% for the close encountered beams and 12.5% for the other beam. This finally indicates that a working multi-beam system can be designed and made to work within all design requirements posed in Appendix C.

7

Conclusion and Recommendations

This section shall conclude the report by summarizing its findings and discussing its implications. These will specifically pertain to the design and what it means for potential future multi-beam terminal designs. Then there will be a reflection on the design process and the research questions will be answered. The research questions themselves require reflection on the design process and work. Lastly recommendations and future work will be discussed.

7.1. Summary and Implications

The current state of the art, presented in chapter 2, has shown that there are many different methods to make multi- and single beam communication possible. Furthermore, the literature study introduced and discussed at length the different steering mechanisms which could be used as well as the requirements where a good multi-beam system should adhere to. Different aspects of the previous multi-beam designs where discussed. There where numerous good and bad aspects to each design found.

It was found that implementation of a mechanism which splits time between targets would not be beneficial. This would adversely affect the data rate with increasing number of targets. Instead, the use of steering surfaces and individual transceivers would allow for constant communication to the targets. Furthermore, the use of modulation and multiplexing would be enhanced greatly if the system would not split beams based on wavelength or polarization. Increasing the complexity of the modulation would result in greater data rates and performances. Sharing as many components as possible would also result in improved SWaP and these components should be COTS. Lastly, the steering elements used should be made as small as possible, be flexible, have the right combination of attributes and allow for the implementation of further adaptive optics features.

A system which could solve all these problems would be a good contribute to the field.

Considering this, the resulting design space was reduced and distilled to a system which can steer beams individually with steering surfaces. Steering these beams with discrete steering surfaces together with a potentially complex optical train could result in diffraction effects impacting the performance substantially. A model for the propagation of light was build from Fresnel propagation principles. This was verified by comparing the results to existing algorithms and validated by comparing it to real life diffraction patterns. The simulation algorithm produced proved accurate and proved its worth later in the design process.

The path of the beam through free space and the atmosphere was analyzed. The turbulence was assumed to be the mild Hufnagel-Valley turbulence profile. The resulting tip-tilt performance requirements where determined to be around 10-50 Hz. The propagation through free space showed that the strictness of steering requirements, data rates, telescope size and free space losses are all proportional. This is thanks to beam convergence being smaller for larger telescopes implying that less energy is ”smeered” out over a larger area. However, the smaller divergence implies the steering must be more accurate for a given distance implying these are directly related. Larger telescopes also capture more signal increasing the received data rates. Hence, the steering accuracy is directly proportional to the system performance.

The system layout was decided to allow for the incoming and outgoing beams to occupy the same

path for each target. The result of this is that twice the number of beams (and subsequently twice the number of targets) can be controlled. This choice results in a small penalty of requiring a second steering mechanism and a small increase in system size. The system will also have a semi-redundant beam steering built in as a result.

Diffraction patterns and the simulation algorithms became especially relevant when choosing the steering mechanisms. The steering mechanisms should also have the optimal combination of speed, accuracy and resolution. It is the later, when the steering surfaces are large and the resolution is low, generate severe diffraction patterns when beams become too close in their proximity. These diffraction patterns severely reduce the system performance because the resulting single strength at the receiver is reduced or even absent all together. These problems manifests it self more often with increasing number of beams and implies that low resolution steering mechanisms would not be able to handle more than a hand full of beams. High resolution beam steering is hence required in places where beams are moving and can get in close proximity. It was hence chosen to use the SLM for this. However, the second steering mechanism does not require to steer closely positioned beams and hence can be an MMA. The MMA being used allow for high speed corrections of small errors.

The transceiver design was chosen to be MOPA and fiber based. This is because the performance of this system is high while having acceptable energy efficiency. The fiber based hardware has the benefit of being used on Earth for high speed internet. This implies that using fiber hardware allows for leveraging off a long and diverse history of terrestrial use as well. It also allows the transceivers to be compatible with most multiplexing and modulation.

A rectilinear telescope was chosen to allow for wide FOV operations. This leads to high flexibility in its operation. Together with the spot trackers required for feedback, the final system layout of the optical train is shown in Figure 5.32.

A system was hence derived which could meet all the relevant requirements.

7.2. Reflection on the Design Process and Answering the Research Questions

Reflecting on the design process and explicit answering of the research questions was an important goal of this work. Now that the design of the multi-beam terminal has taken place, these can now be explicitly answered. This section will answer and discuss the research questions and provide a relevant insight into the multi-beam terminal design process.

How can a multi-beam free-space optical communication terminal be designed using COTS technologies and components?

(a) Which technologies can be used to handle multiple beams?

(b) How do different technologies affect the performance of the terminal?

(c) What aspects of the design where the most driving?

How the terminal can be designed has been illustrated during the previous chapters. The design meets all the relevant critical and non-critical requirements. There are some problematic issues with the multi-beam steering algorithm concerning the duration by which the system can maintain contact for a given link. This is because the algorithm identifies the resulting diffraction patterns as beams and the resulting number of transceivers are overwhelmed. The left over beams are then not steered and the links is subsequently lost. This issue needs to be solved for stricter requirements, however, in the current situation the system meets the requirements. The number of targets and the constant duration of a link are also harder to achieve in terms of requirements.

Other driving requirements are those of the transceivers. The data rates and requirements for multiplexing stipulated that complex and high performance hardware is required. This led to the need for fiber hardware which could handle multiple wavelengths. The resulting efficiency and power requirements, specifically **RxTx-PA-003**, is met when not considering the master oscillator's power consumption. However, this implies that the efficiency and consumption was in a certain sense not met. The fiber amplifiers and in particular master oscillators have not yet achieved the desired energy efficiency.

Another requirement which comes to mind is the FOV requirement. This requirement determined the search for a wide FOV rectilinear telescope which can collimate the beams into parallel beams.

1. What are some of the practical limitations of the design?
    (a) What are the usage limitations?
    (b) Could these limitations be pushed or changed by a non-COTS custom part?
    (c) Where there any dead ends?
    (d) Why where these dead ends?
    (e) How much of the design process was affected by the facilities and other resources available?
    (f) How would a more streamlined design process look like?
    (g) Could the design process be different by use of a non-COTS custom part?

The main practical limitations are the number of beams which can be handled, the speed of the system and the total power output/efficiency. The quantity of beams which can be handled are limited by a number of factors. The first is primarily limited by the size of the beams, number of micro-mirrors and the size of the steering mechanisms. The size of the beams relative to the aperture should preferably be as small as possible to keep spots resolvable and prevent one link from obstructing the other. The size of the components, counter intuitively, should increase while the SLM pixels remain the same size or smaller. Furthermore, the number of transceivers are limited by the number of mirrors on the micro-mirror array. Increasing the number of mirrors, packing them more efficiently and have a fully reflective surface would improve the number of beams which are capable of being steered.

Increasing the speed of the system, in particular for the SLM and spot trackers, would allow for more advanced and effective turbulence mitigation. Aside from being able to combat more severe jitter, in the case of the SLM, it would allow for sub-aperture wavefront corrections while steering. This would also reduce scintillation and speckles to improve the data rates and compatibility with more severe turbulence.

Increasing the total power output and/or efficiency would increase the signal to noise ratio and subsequent performance. The signal to noise ration reduces the range at which the communications can be performed effectively. The fiber amplifiers might increase in efficiency, however, the majority of the performance gains are in the master oscillator. Furthermore, should these systems become more efficient, then the reliance on fiber amplifiers could also be decreased, which in turn improves SWaP. A larger telescope would also help with the overall performance. Lastly, currently the beams are split and the unused beams are dumped. If this signal can be put back into the system it would also improve performance significantly.

The design process was mainly governed by multi-beam steering and how the beams were guided between the targets and transceivers. In particular the nature of same-path and multi-path systems had the greatest effect on system layout. It was found that the issues concerning the maximum capacity and the effectiveness/performance made multi-path methods less favorable. This was despite the option of using one less steering mechanism. Same path designs are also easier to deal with as a result of its benefits. This was hence a significant dead end.

The design was not based on the facilities available, which is due to the experiment becoming impossible due to the Coronavirus pandemic. However, this would change the design process, namely that there would be a practical aspect to it. The resulting performance of the system would be verified and validated to give stronger confidence in its working.

The design process would be changed with more compliant and dedicated steering mechanisms. The resulting limitations specified before would not need as much consideration and the design effort could be focused on other aspects.

2. What sensitivities exist in the design?
    (a) When a sensitivity analysis on different design aspects on the performance is done, what particular aspects are most sensitive?
    (b) How crucial is the application/use case?
    (c) What aspect of the design drives the design?

The sensitivities that were discussed before were mainly the number of beams interfering with each other, turbulence and steering mechanism resolutions for the reasons previously specified. The latter

being less sensitive due to the already high resolutions available for SLM's. However, for sub-aperture corrections, increasing the resolutions would improve turbulence performance. Turbulence induces jitter and scintillation which would reduce the performance substantially by reducing the fiber coupled signal power. These drive the design together with the beam handling. The system can be used in many different use cases and this is hence not crucial.

3. Is the SWaP of each link lower than single beam terminal links?
   (a) What aspects of the design are more SWaP intensive?
   (b) What aspects of the design are less SWaP insentive?
   (c) How would non-COTS or future COTS components change the SWaP?
   (d) Why are the SWaP costs different per link?
   (e) What is the effect of use case on the SWaP?
   (f) What is the minimum number of links required before the multi-beam terminal has lower SWaP per link as a with single-beam terminals?

This design does not have a particular application or use case, hence the SWaP is not dependent on this. Some adjustments can be made given an application which could improve SWaP, such as changing the range. The exact SWaP can only be known when considering the housing and support systems as well, which where not designed. However, and indication can be gained.

The designed terminal shares all components except for those in the transceivers. The transceivers are duplex and hence takes more components. However, the transmitter part is no less SWaP intensive and hence, for duplex communications, the SWaP of the transceiver would likely be similar to single beam applications.

The optical train is completely shared and is compact. It is therefor likely to be lighter compared to the multi-beam system designs presented in chapter 2. Compared to large systems, such as OPALS or the terminal used for ERDS, the designed terminal is smaller and more compact. The result is a significantly better SWaP per beam. Furthermore, the larger multi-beam systems presented in section 2.1, such as those by Capots et. all[12] and Treibes et. all[66], suffer from not sharing all the components between the beams. The exact sizes of these systems are unknown, however, are likely as large or in the case of Figure 2.4 (considering the human hand for scale), significantly larger.

However cubesat terminals, such as NODE or OCSD, tend to have 1 lens and a set of filters. Particularly the chosen rectilinear lens implies more glass is used in the design compared to that used in single beam terminals for cubesats. Hence the optical train of the design presented has an order of magnitude more glass components in comparison. Furthermore, the size and volume of the system is also significantly larger. However, should the rectilinear lens system be optimized to a dedicated non-cots component to reduce the number of lenses this would improve SWaP. Furthermore, for valid comparison, the optical trains of NODE and OCSD must be made duplex.

When these are accounted for, the system designed in this work is still more SWaP intensive due to the need for 2 spot trackers and steering mechanisms. This implies that the break even point could happen after at most 2-3 beams.

7.3. Recommendations and Future Work

Currently, the system has been designed to tackle multi-beam steering. However there are a number of things which still have to be designed for. Furthermore, some other things can be investigated to lead more credence and improve the design.

Firstly, the design of the housing. The construction of the housing is an important factor in the same path design, as the orientation of the fiber GRIN lens is crucial. Furthermore, the protection from the space environment and stray light are important factors in the performance and reliability of the system. What more, the SWaP is dependent on the structure of the system and hence it is important to optimize it.

The algorithm currently cannot handle the unresolving and re-resolving of beams. This was not fixed because the system met all requirements and the fix would require further designs and trade-offs. Furthermore, the operations during any more server turbulence would likely require much more complex applications such as machine learning and adaptive optics. This is hence exactly what would

be good to do in future work; generating a robust method by which multiple beams can be steered during stronger turbulence and with more interactions between beams.

The application of adaptive optics for multi-beam applications in it self is a good topic for further study. This would require methods for detecting wavefront distortions at speeds appropriate for corrections. Furthermore, the wavefront sensing hardware would require much higher resolutions compared to a similar single beam terminals. This is due to each beam having to have a similar wavefront resolution as a single beam terminal to achieve the same performance. Hence, there might be more clever solutions to this or interesting design aspects which would have to be researched.

The rectilinear lens or lens system design should be improved to allow for better SWaP. This would make the multi-beam terminal more competitive to multiple single beam terminals. Furthermore, the exact size and shapes of the terminal can also be optimized as a result.

Larger and higher resolution SLM's and MMA's would substantially improve the flexibility and effectiveness of the multi-beam system. Smaller components would result in smaller beams which more rapidly diverge, implying that more optics is required to keep them bound by the system. Furthermore, increasing the beam cross sectional size would allow for better adaptive optics. As a result, investigations into keeping the system proportions and performance but accommodating for more beams could require larger components.

Improving the speed and accuracy of SLMs would also substantially increase the system performance. Increasing the speed would allow for greater compatibility for adaptive optics. The jitter correction performance would also increase allowing spacecraft jitter to be less disruptive and performance in stronger turbulence to improve. The increased accuracy can be achieved by improving the ”color” depth of SLMs to higher bits, such as 32 and 64 bits. This would make SLMs much more versatile.

Experiments to prove the system in practice would serve as the ultimate proof of concept. It could further prove the compatibility of SLMs and fiber coupling. Furthermore, the feedback loop with the algorithm can be proven to work.

Lastly, the design of a mission including the satellite would provide context in which the system can operate and examine more fine detail the movements, intensity, variety, etc... of the targets and relative positions.

Appendices

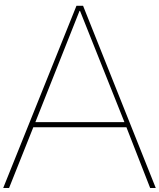

Simulation Accuracy Verification Results

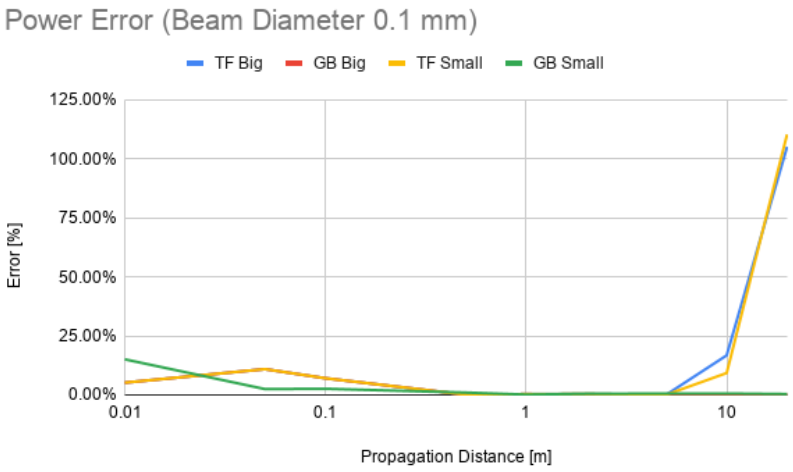

Figure A.1: Power error (y-axis) as the difference in power between a propagated Gaussian beam according to the theory of Gaussian Beam (GB) and Transfer Function (TF) algorithm with the developed Fresnel Propagation (FP) algorithm at different propagation distances (x-axis). In this case, a beam diameter of 0.1 mm is shown. The output aperture is not the same size. Hence, both the Big (requiring padding of the smaller aperture) and Small (requiring cropping of the larger aperture) to illustrate the errors resulting from those. The power error is the distributed error of each pixel added together afterwards.

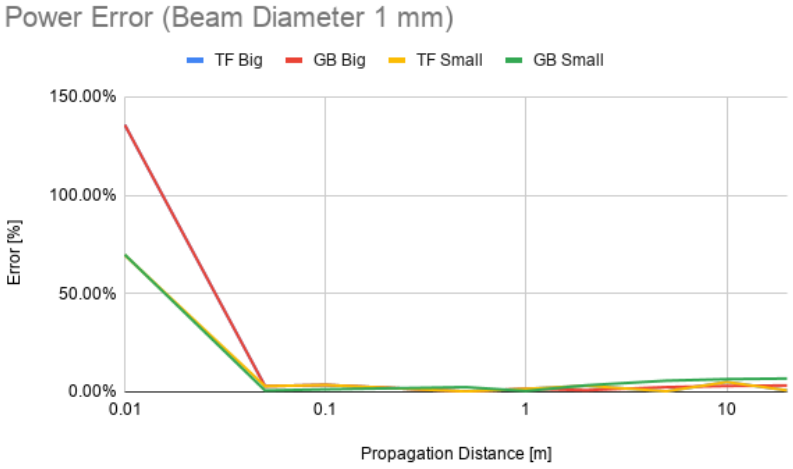

Figure A.2: Power error (y-axis) as the difference in power between a propagated Gaussian beam according to the theory of Gaussian Beam (GB) and Transfer Function (TF) algorithm with the developed Fresnel Propagation (FP) algorithm at different propagation distances (x-axis). In this case, a beam diameter of 1 mm is shown. The output aperture is not the same size. Hence, both the Big (requiring padding of the smaller aperture) and Small (requiring cropping of the larger aperture) to illustrate the errors resulting from those. The power error is the distributed error of each pixel added together afterwards.

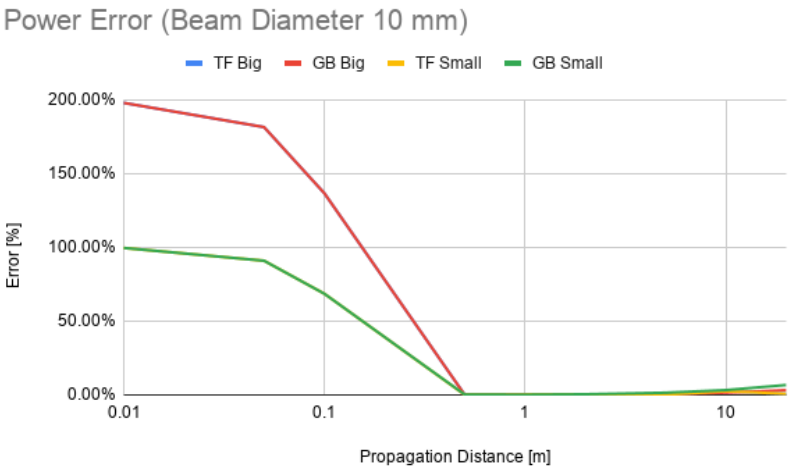

Figure A.3: Power error (y-axis) as the difference in power between a propagated Gaussian beam according to the theory of Gaussian Beam (GB) and Transfer Function (TF) algorithm with the developed Fresnel Propagation (FP) algorithm at different propagation distances (x-axis). In this case, a beam diameter of 10 mm is shown. The output aperture is not the same size. Hence, both the Big (requiring padding of the smaller aperture) and Small (requiring cropping of the larger aperture) to illustrate the errors resulting from those. The power error is the distributed error of each pixel added together afterwards.

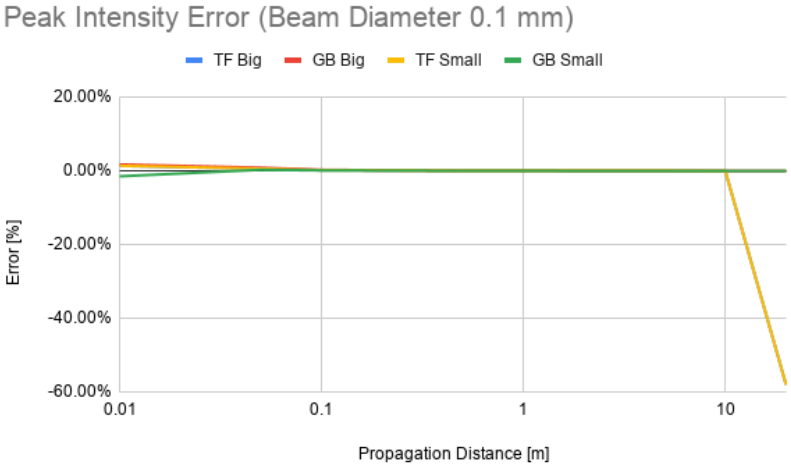

Figure A.4: Peak intensity error (y-axis) as the difference in peak intensity between a propagated Gaussian beam according to the theory of Gaussian Beam (GB) and Transfer Function (TF) algorithm with the developed Fresnel Propagation (FP) algorithm at different propagation distances (x-axis). In this case, a beam diameter of 0.1 mm is shown. The output aperture is not the same size. Hence, both the Big (requiring padding of the smaller aperture) and Small (requiring cropping of the larger aperture) to illustrate the errors resulting from those.

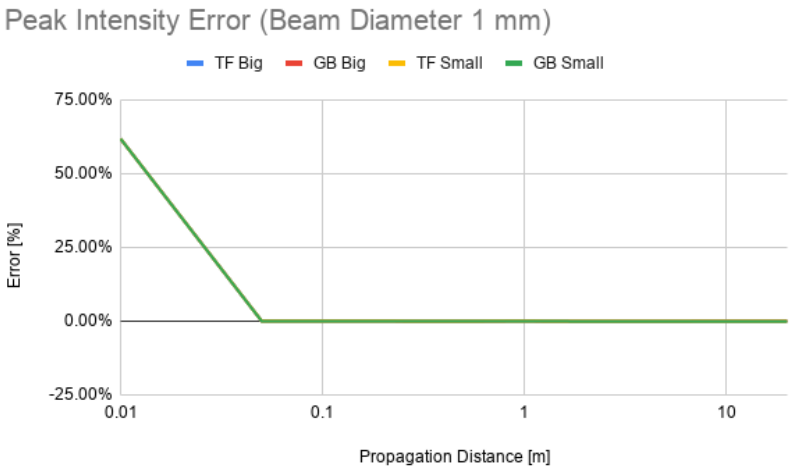

Figure A.5: Peak intensity error (y-axis) as the difference in peak intensity between a propagated Gaussian beam according to the theory of Gaussian Beam (GB) and Transfer Function (TF) algorithm with the developed Fresnel Propagation (FP) algorithm at different propagation distances (x-axis). In this case, a beam diameter of 1 mm is shown. The output aperture is not the same size. Hence, both the Big (requiring padding of the smaller aperture) and Small (requiring cropping of the larger aperture) to illustrate the errors resulting from those.

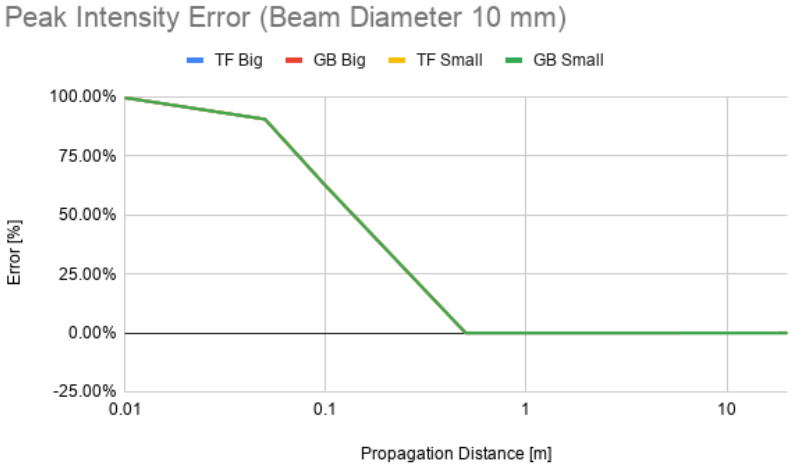

Figure A.6: Peak intensity error (y-axis) as the difference in peak intensity between a propagated Gaussian beam according to the theory of Gaussian Beam (GB) and Transfer Function (TF) algorithm with the developed Fresnel Propagation (FP) algorithm at different propagation distances (x-axis). In this case, a beam diameter of 10 mm is shown. The output aperture is not the same size. Hence, both the Big (requiring padding of the smaller aperture) and Small (requiring cropping of the larger aperture) to illustrate the errors resulting from those.

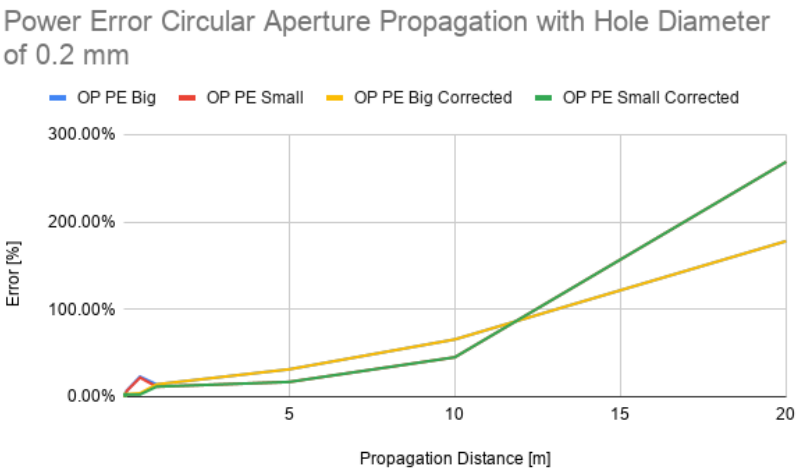

Figure A.7: Illustrated is the power error (y-axis) of a plane wave diffracted through a 0.2 mm hole after the propagation distance (x-axis). The error being between the resulting diffraction patterns of the Transfer Function (TF) and Fresnel Propagation (FP) algorithms. The power error is the distributed error of each pixel added together afterwards.

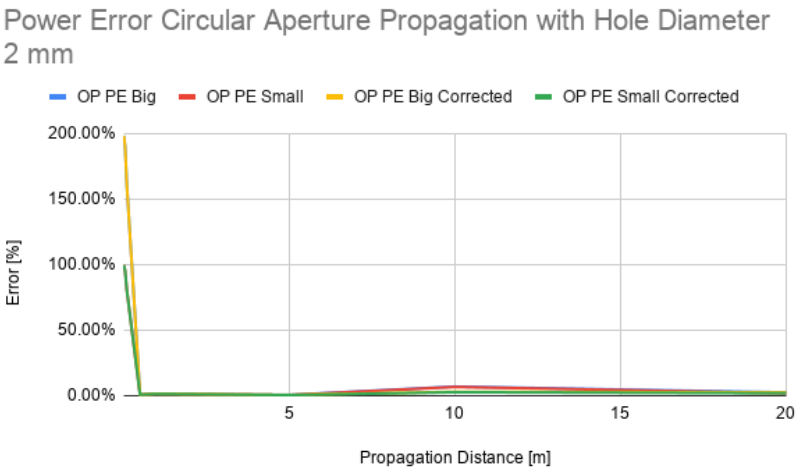

Figure A.8: Illustrated is the power error (y-axis) of a plane wave diffracted through a 2 mm hole after the propagation distance (x-axis). The error being between the resulting diffraction patterns of the Transfer Function (TF) and Fresnel Propagation (FP) algorithms. The power error is the distributed error of each pixel added together afterwards.

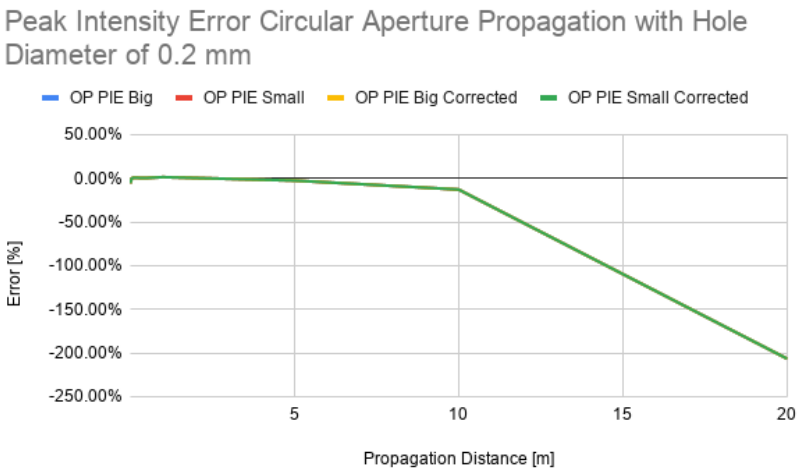

Figure A.9: Illustrated is the peak intensity error (y-axis) of a plane wave diffracted through a 0.2 mm hole after the propagation distance (x-axis). The error being between the peak intensity of the resulting diffraction patterns of the Transfer Function (TF) and Fresnel Propagation (FP) algorithms.

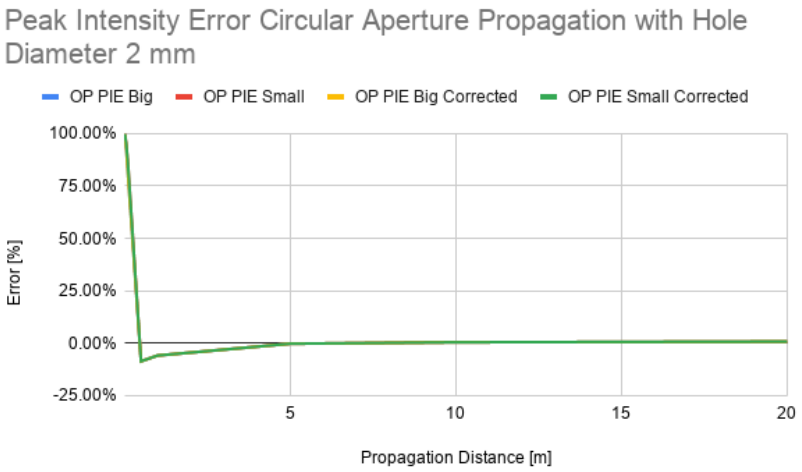

Figure A.10: Illustrated is the peak intensity error (y-axis) of a plane wave diffracted through a 2 mm hole after the propagation distance (x-axis). The error being between the peak intensity of the resulting diffraction patterns of the Transfer Function (TF) and Fresnel Propagation (FP) algorithms.

B

Experimental Verification and Validation of Simulation Results

This appendix contains the raw data on the different diffraction patterns. The images shown are not to scale, however, the relevant dimensions are mentioned in the description

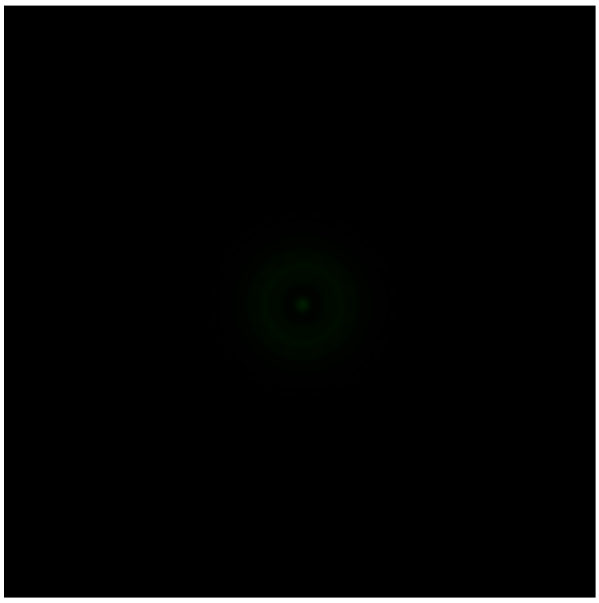

Figure B.1: The results of the Fresnel Propagation simulation for the experimental setup for a 532 nm expanding beam diffraction through a 1 mm hole at a distance of 6.5 m.

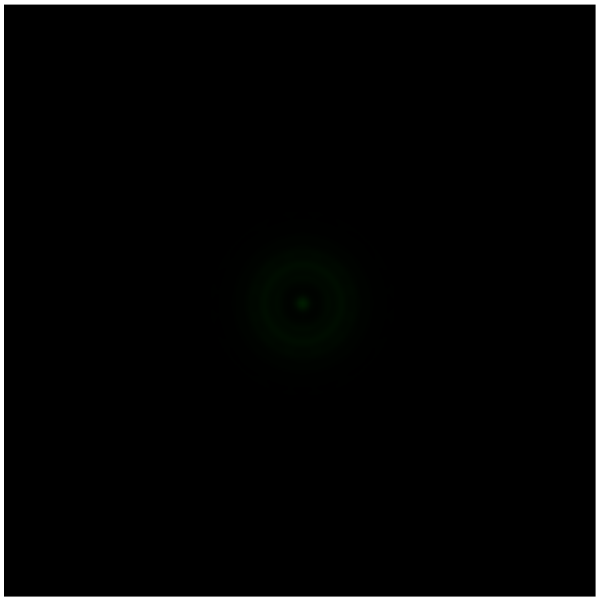

Figure B.2: The results of the Transfer Function simulation for the experimental setup for a 532 nm expanding beam diffraction through a 1 mm hole at a distance of 6.5 m.

Figure B.3: The trace of dark rings for a 532 nm expanding beam diffraction through a 1 mm hole at a distance of 6.5 m. The inner circle was measured with a caliper to be 7.3 mm from the inside line.

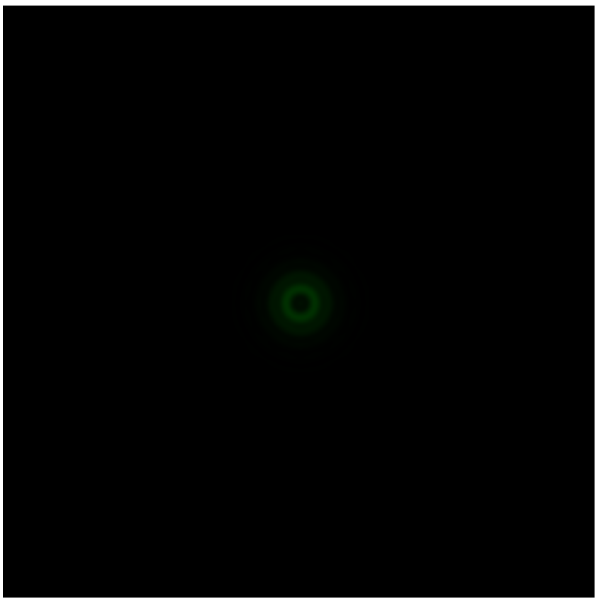

Figure B.4: The results of the Fresnel Propagation simulation for the experimental setup for a 532 nm expanding beam diffraction through a 1 mm hole at a distance of 6.08 m.

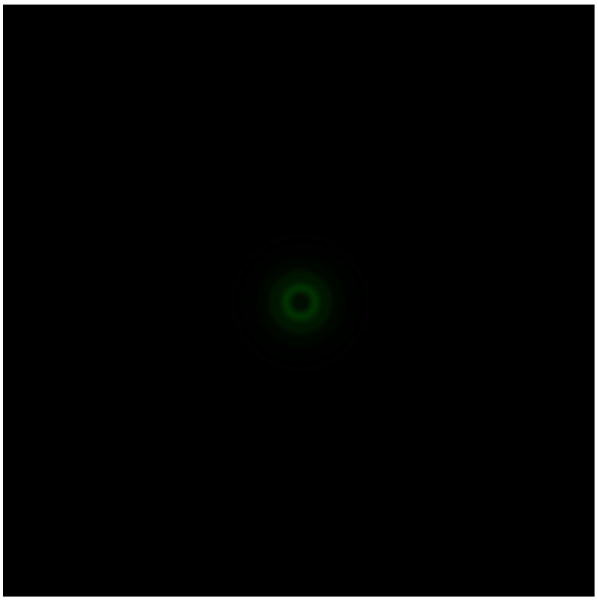

Figure B.5: The results of the Transfer Function simulation for the experimental setup for a 532 nm expanding beam diffraction through a 1 mm hole at a distance of 6.08 m.

Figure B.6: The trace of dark rings for a 532 nm expanding beam diffraction through a 1 mm hole at a distance of 6.08 m. The inner circle was measured with a caliper to be 15.6 mm from the inside line.

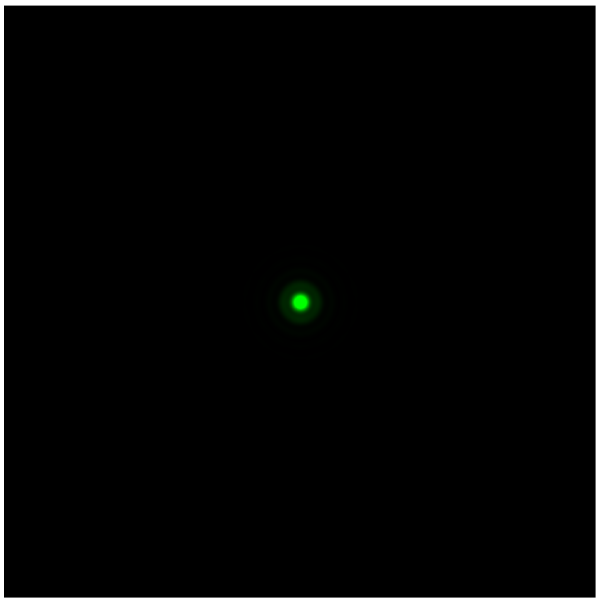

Figure B.7: The results of the Fresnel Propagation simulation for the experimental setup for a 532 nm expanding beam diffraction through a 1 mm hole at a distance of 5.64 m.

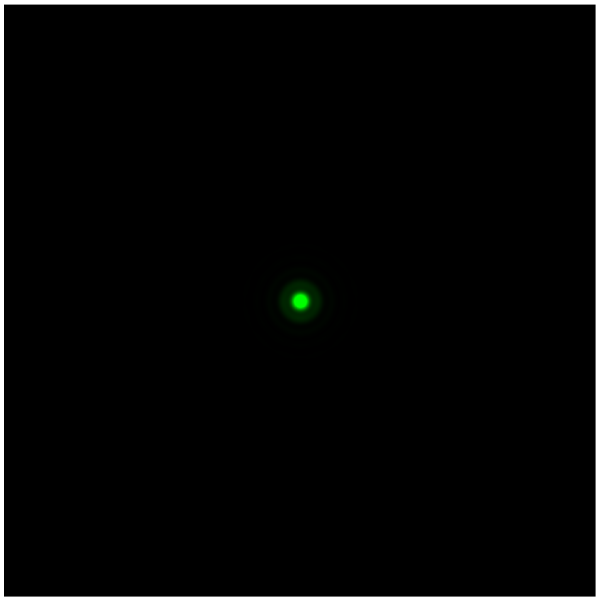

Figure B.8: The results of the Transfer Function simulation for the experimental setup for a 532 nm expanding beam diffraction through a 1 mm hole at a distance of 5.64 m.

Figure B.9: The trace of dark rings for a 532 nm expanding beam diffraction through a 1 mm hole at a distance of 5.64 m. The outer circle was measured with a caliper to be 68.4 mm from the outisde line.

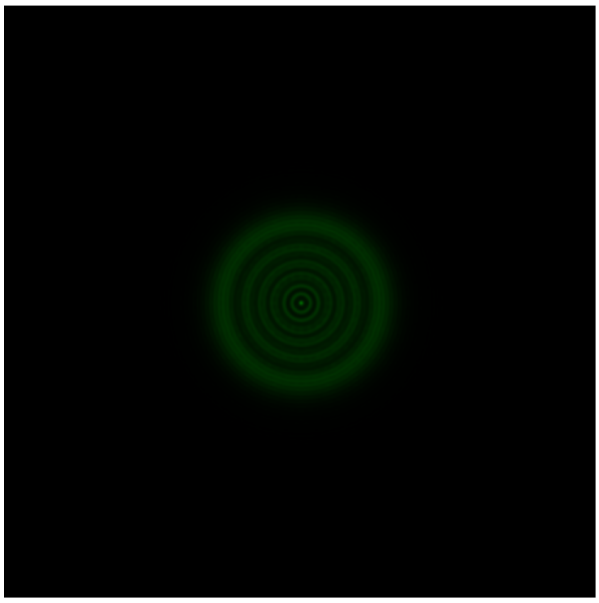

Figure B.10: The results of the Fresnel Propagation simulation for the experimental setup for a 532 nm expanding beam diffraction through a 3 mm hole at a distance of 6.04 m.

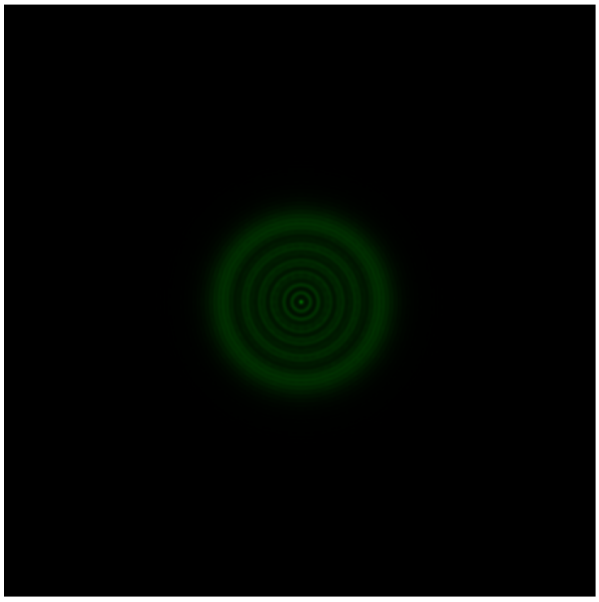

Figure B.11: The results of the Transfer Function simulation for the experimental setup for a 532 nm expanding beam diffraction through a 3 mm hole at a distance of 6.04 m.

Figure B.12: The trace of dark rings for a 532 nm expanding beam diffraction through a 3 mm hole at a distance of 6.04 m. The inner circle was measured with a caliper to be 61.0 mm from the inside line.

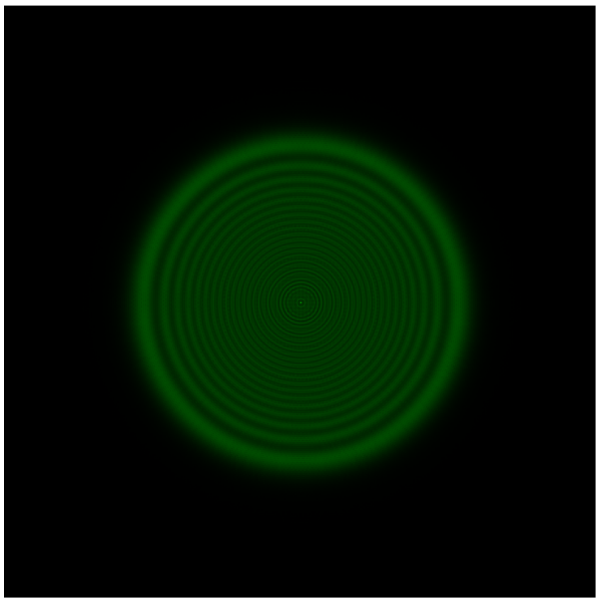

Figure B.13: The results of the Fresnel Propagation simulation for the experimental setup for a 532 nm expanding beam diffraction through a 6.5 mm hole at a distance of 5.96 m.

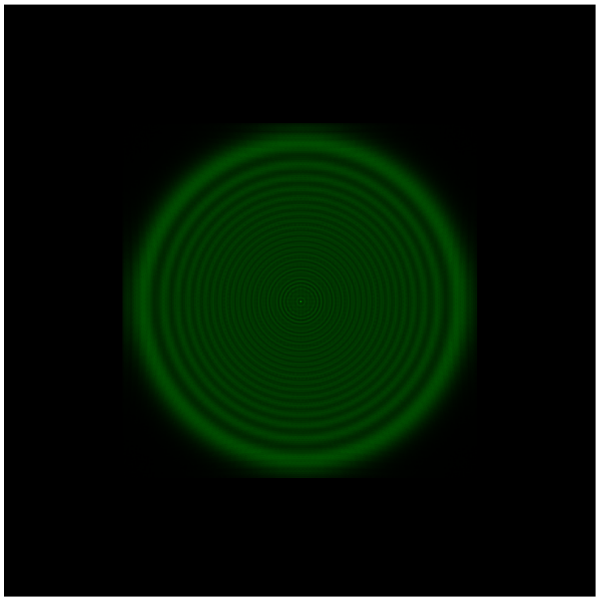

Figure B.14: The results of the Transfer Function simulation for the experimental setup for a 532 nm expanding beam diffraction through a 6.5 mm hole at a distance of 5.96 m.

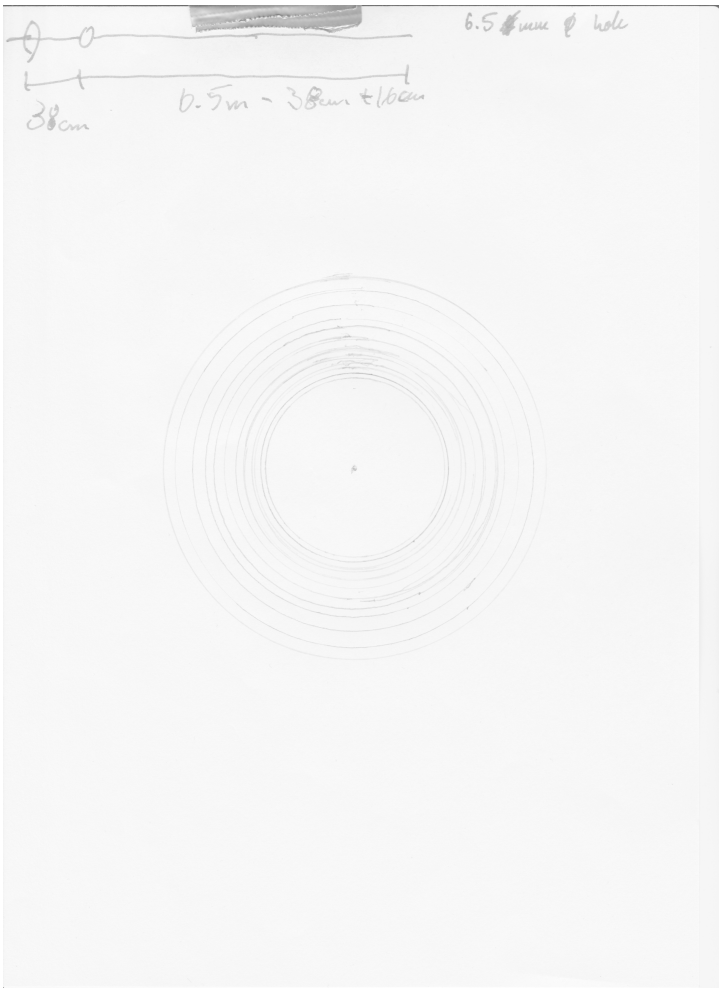

Figure B.15: The trace of dark rings for a 532 nm expanding beam diffraction through a 6.5 mm hole at a distance of 5.96 m. The outer circle was measured with a caliper to be 115.7 mm from the outside line.

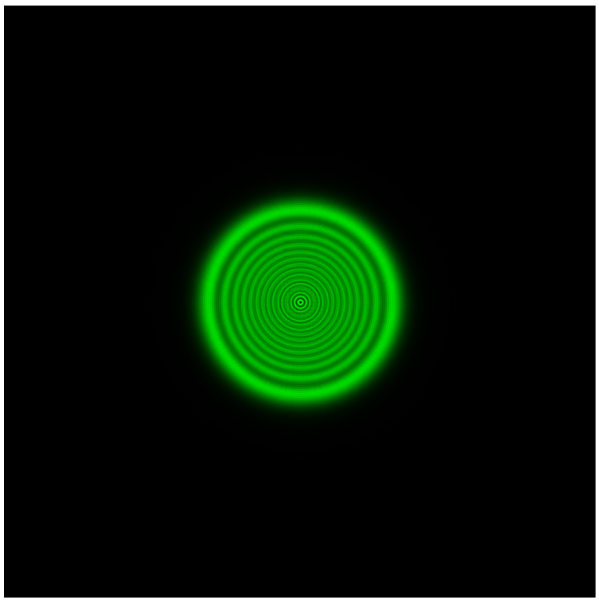

Figure B.16: The results of the Fresnel Propagation simulation for the experimental setup for a 532 nm expanding beam diffraction through a 6.5 mm hole at a distance of 5.74 m.

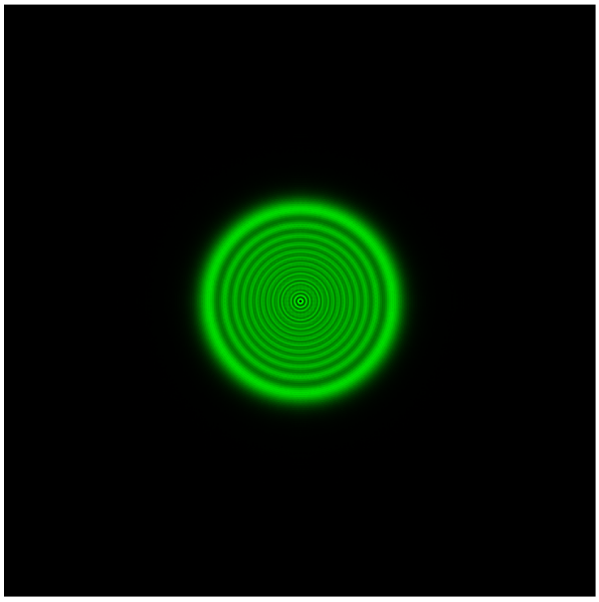

Figure B.17: The results of the Transfer Function simulation for the experimental setup for a 532 nm expanding beam diffraction through a 6.5 mm hole at a distance of 5.74 m.

Figure B.18: The trace of dark rings for a 532 nm expanding beam diffraction through a 6.5 mm hole at a distance of 5.74 m. The outer circle was measured with a caliper to be 65.8 mm from the outside line (top down).

Hole Diameter	1	mm	Wavelength	532	nm
Lens-Hole Distance	16	cm	Resolution	5000	pix width
Propagation Distance	6.5	m	Simulated input field width	0.1	m
Direction of ring numbering	inside to out		D out	0.1729	m

	Radius Difference Between Visible Dark Rings				
Rings on trace	Trace [mm]	FP Simulation [pix]	FP Simulation [mm]	TF Simulation [pix]	TF Simulation [mm]
0 to 1	4.15	120	4.15	125	4.32
1 to 2	10.80	386	13.35	501	17.32
2 to 3	6.00	121	4.18	98	3.39
3 to 4	6.10	96	3.32	65	2.25

Hole Diameter	1	mm	Wavelength	532	nm
Lens-Hole Distance	26	cm	Resolution	5000	pix width
Propagation Distance	6.08	m	Simulated input field width	0.1	m
Direction of ring numbering	inside to ouside		D out	0.1617	m

	Radius Difference Between Visible Dark Rings				
Rings on trace	Trace [mm]	FP Simulation [pix]	FP Simulation [mm]	TF Simulation [pix]	TF Simulation [mm]
0 to 1	15.00	445	14.39	422	13.65
1 to 2	4.10	83	2.68	109	3.53
2 to 3	4.00	121	3.91	111	3.59
3 to 4	3.00	96	3.11	103	3.33

Hole Diameter	1	mm	Wavelength	532	nm
Lens-Hole Distance	60	cm	Resolution	5000	pix width
Propagation Distance	5.64	m	Simulated input field width	0.1	m
Direction of ring numbering	inside to ouside		D out	0.1500	m

	Radius Difference Between Visible Dark Rings				
Rings on trace	Trace [mm]	FP Simulation [pix]	FP Simulation [mm]	TF Simulation [pix]	TF Simulation [mm]
0 to 1	4.30	112	3.36	110	3.30
1 to 2	3.40	108	3.24	102	3.06
2 to 3	3.10	109	3.27	115	3.45
3 to 4	3.00	99	2.97	104	3.12

Hole Diameter	3	mm	Wavelength	532	nm
Lens-Hole Distance	30	cm	Resolution	5000	pix width
Propagation Distance	6.04	m	Simulated input field width	0.1	m
Direction of ring numbering	inside to out		D out	0.1607	m

	Radius Difference Between Visible Dark Rings				
Rings on trace	Trace [mm]	FP Simulation [pix]	FP Simulation [mm]	TF Simulation [pix]	TF Simulation [mm]
0 to 1	6.00	174	6.02	177	5.69
1 to 2	3.30	105	3.63	104	3.34
2 to 3	6.50	150	5.19	149	4.79
3 to 4	2.60	131	4.53	129	4.15

Hole Diameter	6.5	mm	Wavelength	532	nm
Lens-Hole Distance	38	cm	Resolution	5000	pix width
Propagation Distance	5.96	m	Simulated input field width	0.1	m
Direction of ring numbering	Outside to in		D out	0.1585	m

	Radius Difference Between Visible Dark Rings				
Rings on trace	Trace [mm]	FP Simulation [pix]	FP Simulation [mm]	TF Simulation [pix]	TF Simulation [mm]
0 to 1	5.00	136	4.70	140	4.44
1 to 2	3.75	96	3.32	94	2.98
2 to 3	2.60	93	3.22	92	2.92
3 to 4	2.9	78	2.70	78	2.47

Hole Diameter	6.5	mm	Wavelength	532	nm
Lens-Hole Distance	60	cm	Resolution	5000	pix width
Propagation Distance	5.74	m	Simulated input field width	0.1	m
Direction of ring numbering	Outside to in		D out	0.1527	m

	Radius Difference Between Visible Dark Rings				
Rings on trace	Trace [mm]	FP Simulation [pix]	FP Simulation [mm]	TF Simulation [pix]	TF Simulation [mm]
0 to 1	3.60	107	3.70	104	3.18
1 to 2	2.10	78	2.70	77	2.35
2 to 3	1.50	51	1.76	66	2.02
3 to 4	1.5	52	1.80	64	1.95

C

Literature Study Derived System Requirements

Through the literature study[56], many requirements where proposed. These are shown below:

C.1. (Multi-Beam) Terminal System Requirements

C.1.1. Critical General Design Requirements:

GD-CR-001: The terminal shall be designed to handle 10 targets.
GD-CR-002: The terminal shall be able to communicate with ground targets.
GD-CR-003: The terminal shall be able to communicate with LEO satellites.
GD-CR-004: The terminal shall have a FOV of 90 deg in total or the Earth + 1000 km either side (which ever comes first).
GD-CR-005: The terminal shall use COTS components.
GD-CR-006: The terminal shall be able to interface with the spacecraft through previously used Rx hardware.
GD-CR-007: The terminal shall weight no more then 10 kg.
GD-CR-008: The terminal shall not consume more then 500 W (50 W per link/beam).
GD-CR-009: The terminal shall not be larger then 1 m^3.
GD-CR-010: The terminal shall not exceed component thermal limits.
GD-CR-011: The terminal shall not exceed component structural limits.
GD-CR-012: The terminal shall be able to handle launch loads.
GD-CR-013: The terminal shall be able to handle the space environment in GEO.
GD-CR-014: The terminal shall be able to produce duplex communications with all targets.
GD-CR-015: The terminal shall be able to sustain a 10 second link without interruptions.
GD-CR-016: The terminal shall be able to communicate with at least 40 Mbps per link at its Shannon Limit for OOK modulation.
GD-CR-017: The terminal shall be able to withstand pointing towards the sun directly for 2 minutes.
GD-CR-018: The terminal shall not change its average center of mass during its life.
GD-CR-019: The transmission wavelength of the terminal shall be 1550nm +- 200 nm.
GD-CR-020: If Wave Division Multiplexing (WDM) is used, it shall be done using Dense Wavelength Division Multiplexing (DWDM).

C.1.2. Non-Critical General Design Requirements:

GD-NCR-001: The terminal shall preferably be capable of only increasing the number of steering and Rx-Tx components when scaled up to 20+ targets (scaling).
GD-NCR-002: The terminal design shall be capable of scaling to a multiple of 6 without increasing the projected mass by a multiple of 2. (Only rough estimation will suffice.)

GD-NCR-003: The link budget according to the Shannon-Hartely theorem shall be greater then 100 Mbps.

C.1.3. Transceiver Design Requirements:

RxTx-PA-001: The system shall be designed to deliver the required amplification at the highest expected temperature of operation.
RxTx-PA-002: The power amplifiers shall be designed to meet the requirements at EOL radiation doses or at -0.5 dB which ever power output is lower.
RxTx-PA-003: Efficiency of the optical amplifiers shall not be below 40% from input electrical power to output optical power at the exit of the amplifier.
RxTx-PA-004: Pre-amplifiers shall be included only if the jitter BER is dominant.
RxTx-PA-005: The optical power amplifiers shall not use more power then 60W per link.

C.2. Pointing Sub-System Requirements:

C.2.1. Critical Design Requirements:

PS-CR-001: All 10 targets shall share pointing components or arrays.
PS-CR-002: The FOR of the pointing mechanism, should it be used, shall be greater then 3 degrees.
PS-CR-003: The spot tracker shall have a frame rate higher then the pointing system.
PS-CR-004: The multi-beam steering/pointing system shall be able to operate at 40 Hz or higher.
PS-CR-005: The pointing system shall be able to correct for tip-tilt errors of at least 1 mrad jitter in the entire aperture at at least 100 Hz.
PS-CR-006: The pointing system shall be able to correct for at least 8.7 mrad at at least 10 Hz.

C.2.2. Non-Critical Design requirements:

PS-NCR-001: The pointing component (DM, RM, FSM, etc...) shall preferably have the hardware capability to correct for higher order turbulence for each link independently should this be implemented.
PS-NCR-002: There shall be no duplicate hardware components in the design.

C.2.3. Fiber Coupling Requirements:

PS-FC-001: The normalized angular fiber misalignment, expressed as $\Delta\Phi' = \Delta\Phi f/R$, shall be less then 0.05.
PS-FC-002: The normalized axial misalignment, expressed as $\Delta z' = \Delta z R/(f\omega_B)$, shall be less then 0.001.
PS-FC-003: The normalized lateral misalignment, expressed as $\Delta x' = \Delta x/\omega_B$, shall not be less then 0.35.
PS-FC-004: The pointing system shall be able to steer the brightest point in the spot at 100 Hz to stay within the coupling requirements.
PS-FC-005: Large perturbations of 0.5 deg/s at 10 Hz shall still be fiber coupled.
PS-FC-006: The pointing system shall be able to correct for first order jitter and turbulence (pointing errors) for each link independently.

C.2.4. Deformable Mirror Requirements:

PS-DM-001: The deformable mirror shall be a discrete array of mirrors.
PS-DM-002: The temperature range of the DM shall not go out side a range of 250 K to 320 K respectively.
PS-DM-003: The DM shall be able to withstand launch amplitude vibration on its first 3 eigenmodes for 10 minutes without fracture or shall have its first eigenmode outside of the launch vibrational spectrum.
PS-DM-004: The fill factor shall not be lower then 80%.
PS-DM-005: The reflection of the light between the mirrors shall not induce noise by 3db.

PS-DM-006: The resolution/mirror size and pitch combination of the DM shall be twice as small as the required spatial separation/resolution of the FOV of the system or the Rayleigh criterion, which ever is bigger.

C.2.5. Fine and Fast Steering Mirror Array Requirements:

PS-FSM-001: The temperature range of the FSM shall not go out side a range of 250 K to 320 K respectively.
PS-FSM-002: The FSM shall be able to withstand launch amplitude vibration on its first 3 eigenmodes for 10 minutes without fracture or shall have its first eigenmode outside of the launch vibrational spectrum.
PS-FSM-003: The fill factor shall not be lower then 80%.
PS-FSM-004: The reflection of the light between the mirrors shall not induce noise by 3db.
PS-FSM-005: The resolution/mirror size and pitch combination of the FSM shall be twice as small as the required spatial separation/resolution of the FOV of the system or the Rayleigh criterion, which ever is bigger.

C.2.6. Reflective Modulator Requirements:

PS-RM-001: The RM shall not be exposed to UV light.
PS-RM-002: The RM temperature when active shall not be outside the temperature range of 270 K to 300 K.
PS-RM-003: The temperature range of the RM during the entire life shall not fall outside of 150 K to 330K.
PS-RM-004: The system shall correct for RM drift over time using a closed loop control system.
PS-RM-005: The frame rate of the RM shall not fall below the jitter frequency due to beam quality improvements.

C.2.7. Piezo Actuator Array Requirements:

PS-PAA-001: Mirror shall be angles such that there is less then 10% shadow.
PS-PAA-002: The mirror shall be a discrete array of mirrors.
PS-PAA-003: The temperature range of the DM shall not go out side a range of 250 K to 320 K respectively.
PS-PAA-004: The PAA shall be able to withstand launch amplitude vibration on its first 3 eigenmodes for 10 minutes without fracture or shall have its first eigenmode outside of the launch vibrational spectrum.
PS-PAA-005: The fill factor shall not be lower then 80%.
PS-PAA-006: The reflection of the light between the mirrors shall not induce noise by 3dB.
PS-PAA-007: The resolution/mirror size and pitch combination of the PAA shall be twice as small as the required spatial separation/resolution of the FOV of the system or the Rayleigh criterion, which ever is bigger.

C.3. Pointing Sub-System Experiment Requirements:

C.3.1. Critical Experiment Requirements:

EXP-CR-001: The pointing system design must be build able within the facility constraints:

(a) Half an optical bench.

(b) Components must be available or within time and financial budget.

EXP-CR-002: Experiment must be completed no later then 2 months before draft.

D

Algorithm Code

D.1. Verification of Algorithm Raw Data

	x	y		Frame 3:	375	544
Resolution	1080	1080		(detected r1&r2)	374	545
Lengths	0.04	0.04			365	554
Leng per pixel	0.00003704	0.00003704			356	563
					355	564

Positions						
Frame	r1 x	r1 y	r2 x	r2 y	r3 x	r3 y
1	0.002	0.000	0.009	0.007	-0.016	0.016
2	0.004	0.000	0.008	0.004	-0.012	0.012
3	0.006	0.000	0.007	0.001	-0.008	0.008
4	0.008	0.000	0.006	-0.002	-0.004	0.004
5	0.010	0.000	0.005	-0.005	0.000	0.000
6	0.012	0.000	0.004	-0.008	0.004	-0.004
7	0.014	0.000	0.003	-0.011	0.008	-0.008
8	0.016	0.000	0.002	-0.014	0.012	-0.012
9	0.018	0.000	0.001	-0.017	0.016	-0.016
10	0.020	0.000	0.000	-0.020	0.020	-0.020

Detected Sorted						
Frame	r1 x	r1 y	r2 x	r2 y	r3 x	r3 y
1	0.002	0.000	0.009	0.007	-0.016	0.016
2	0.004	0.000	0.008	0.004	-0.012	0.012
3	0.020	-0.020	0.020	-0.020	-0.008	0.008
4	0.008	0.000	0.006	-0.002	-0.004	0.004
5	0.010	0.000	0.005	-0.005	0.000	0.000
6	0.012	0.000	0.004	-0.008	0.004	-0.004
7	0.014	0.000	0.003	-0.011	0.008	-0.008
8	0.016	0.000	0.002	-0.014	0.012	-0.012
9	0.018	0.000	0.001	-0.017	0.016	-0.016
10	0.020	-0.020	0.020	-0.020	0.020	-0.020

Raw Pixels						
Frame	r1 x	r1 y	r2 x	r2 y	r3 x	r3 y
1	487	540	298	729	972	972
2	433	540	325	648	864	864
3					756	756
4	379	487	325	540	648	648
5	406	406	271	540	540	540
6	433	325	433	433	217	540
7	460	244	325	325	163	540
8	487	163	217	217	109	540
9	514	82	109	109	55	540
10						

Detected						
Frame	r1 x	r1 y	r2 x	r2 y	r3 x	r3 y
1	0.002	0.000	0.009	0.007	-0.016	0.016
2	0.004	0.000	0.008	0.004	-0.012	0.012
3	0.020	-0.020	0.020	-0.020	-0.008	0.008
4	0.006	-0.002	0.008	0.000	-0.004	0.004
5	0.005	-0.005	0.010	0.000	0.000	0.000
6	0.004	-0.008	0.004	-0.004	0.012	0.000
7	0.003	-0.011	0.008	-0.008	0.014	0.000
8	0.002	-0.014	0.012	-0.012	0.016	0.000
9	0.001	-0.017	0.016	-0.016	0.018	0.000
10	0.020	-0.020	0.020	-0.020	0.020	-0.020

Steering Results						
Frame	r1 x	r1 y	r2 x	r2 y	r3 x	r3 y
1	2083	2501	2499	2501	2917	2501
2	2083	2501	2499	2501	2917	2501
3	2260	2492	2261	2493	2916	2500
4	2084	2490	2085	2491	2075	2493
5	2083	2499	2499	2501	2917	2501
6	2083	2499	2499	2499	2916	2501
7	2083	2499	2499	2499	2916	2501
8	2499	2499	2083	2500	2916	2501
9	2500	2499	2083	2500	2916	2501
10	1693	1693	2501	1693	1693	2501

E

Trade-off Multi-beam Steering Systems

The research done in the literature study[56] into multi-beam steering methods/mechanisms considered a number of different technologies. These are namely: Deformable Mirror (DM) (referred to here as Micro Mirror Arrays (MMA's)), Reflective Modulator (RM) (in this work referred to as Spatial Light Modulator (SLM)), Fine and Fast Steering Mirror (FSM) and the Piezo Actuator Array (PAA). These requirements were made for them independently based on literature such that there was the design flexibility during the design process. It also allows the use of 2 or more different steering mechanisms to be used in a defined way, which indeed came in handy as will be discussed later in this work.

However, there were analyses and comparisons made between these steering mechanisms nonetheless. There where 2 trade-offs done based on general criteria in order to gauge which benefits each steering mechanism has, in relation to requirements. The trade-off also results in a ranked list. For each criteria, the steering mechanism was given 1 for exceeding required, 0 for just meeting required and -1 for not meeting required.

The first trade-off is regarding the ability to steer multiple beams. The exact trade-off performed in the literature study is illustrated in Table E.1. The winner of the trade-off is the SLM (RM), with MMA's (DM) coming in second while FSM and PAA are third and fourth respectively. The SLM's have the benefit of very high resolutions implying they have the abilities for sub-aperture wavefront corrections and also have high optical efficiencies. Due to the analog and optimized nature of DM's, being used extensively in adaptive optics, it has increased accuracy's and higher speeds. The application of each of these mechanisms will in the end be deterministic. The use of FSM's mainly lost on packing efficiencies and size implying arrays and optical systems would become bulky. However these too are very high performance and used in high performance applications. The PAA's, which are inclined mirrors mounted on piezo actuators, were also quite accurate but it has substantial drawbacks in accommodation of multiple beams. This is unless it is used as a MMA, but then it would become an MMA.

Table E.1: Trade-off table for multi-beam steering systems. This table can be found as table 11 on page 89 in "Literature Review" by Joshua Spaander[56].

	DM	RM	FSM	PAA	Weight
Pointing accuracy	1	0	1	1	1
Pointing FOR	1	1	1	-1	0.5
Resolution	0	1	-1	0	0.4
Frame rate	1	1	1	1	1
Precision optics dependent	1	1	-1	-1	1
Optical complexity	1	1	-1	-1	0.3
Mass	1	1	-1	1	0.3
Size	1	1	-1	1	1
Optical efficiency	0	1	-1	0	0.8
Environment effects	0	1	1	1	1
Total	5.1	6.3	-0.3	2.5	7.3

To illustrate the differences, when specifically the spacecraft jitter is considered, the results change.

The spacecraft jitter only affects the total input aperture and hence the whole aperture must be corrected for. The second trade-off was for the correction of jitter and is illustrated in Table E.2. It shows that in this case the FSM is best with MMA's as a close second.

Table E.2: Trade-off table for spacecraft jitter and vibration mitigation systems. This table can be found as table 12 on page 90 in "Literature Review" by Joshua Spaander[56].

	DM	RM	FSM	PAA	Weight
Pointing accuracy	1	0	1	1	1
Frame rate	1	-1	1	1	1
Mass	1	1	1	1	1
Environment effects	0	1	1	1	0.5
Optical complexity	1	1	1	-1	1
Total	4	1.5	4.5	2.5	4.5

What can be seen is that MMA's can be used in a lot of high performance applications when considering both beam steering and vibration corrections. However, the SLM can also include sub-aperture wavefront correction.

Bibliography

[1] Matthew J. Abrahamson, Bogdan V. Oaida, Oleg Sindiy, and Abhijit Biswas. Achieving operational two-way laser acquisition for OPALS payload on the International Space Station. *SPIE*, 9354 (March 2015):935408, 2015. ISSN 1996756X. doi: 10.1117/12.2182473.

[2] ALPAO. Adaptive optics applications, 2020. URL https://www.alpao.com/adaptive-optics/alpao-applications.html.

[3] John A. Bebawi, Ishac Kandas, Mohamed A. El-Osairy, and Moustafa H. Aly. A comprehensive study on EDFA characteristics: Temperature impact. *Applied Sciences (Switzerland)*, 8(9), 2018. ISSN 20763417. doi: 10.3390/app8091640.

[4] Eric-olivier Le Bigot and Walter J Wild. Theory of branch-point detection and its implementation. *Optical Society of America*, 16(7):1724–1729, 1999.

[5] Philip Birch, Iniabasi Ituen, Rupert Young, and Chris Chatwin. Long-distance Bessel beam propagation through Kolmogorov turbulence. *Journal of the Optical Society of America A*, 32(11):2066, 2015. ISSN 1084-7529. doi: 10.1364/josaa.32.002066.

[6] Knut Böhmer, Mark Gregory, Frank Heine, Hartmut Kämpfner, Robert Lange, Michael Lutzer, and Rolf Meyer. Laser communication terminals for the European Data Relay System. *Free-Space Laser Communication Technologies XXIV*, 8246(February 2012):82460D, 2012. ISSN 0277786X. doi: 10.1117/12.906798.

[7] R Bonjour, S Welschen, J F Johansson, and J Leuthold. Steering and Shaping of Multiple Beams with a Spatial Light Modulator based Beamformer. *2018 International Topical Meeting on Microwave Photonics (MWP)*, (1):1–4, 2018.

[8] K Cahoy. Laser Communication with CubeSats. Technical report, 2018. URL https://directory.eoportal.org/web/eoportal/s.

[9] K. Cahoy, R. W. Kingsbury, T. Nguyen, and K. Riesing. Fast-steering solutions for cubesat-scale optical communications. page 169. SPIE-Intl Soc Optical Eng, nov 2017. ISBN 9781510616158. doi: 10.1117/12.2304229.

[10] Kerri L Cahoy, Anne D Marinan, Benjamin Novak, Matthew Webber, Kerri L Cahoy, Anne D Marinan, Benjamin Novak, and Caitlin Kerr. Wavefront control in space with MEMS deformable mirrors. *SPIE*, 861708(March 2013), 2013. doi: 10.1117/12.2005685. URL https://www.spiedigitallibrary.org/conference-proceedings-of-spie.

[11] Kerri L Cahoy, Anne D Marinan, Benjamin Novak, Caitlin Kerr, Tam Nguyen Thuc Nguyen, Matthew Webber, Grant Falkenburg, and Andrew Barg. Wavefront control in space with MEMS deformable mirrors for exoplanet direct imaging mirrors for exoplanet direct imaging. *SPIE*, 2014. doi: 10.1117/1.JMM.13.1.011105. URL https://www.spiedigitallibrary.org/journals/Journal-of-Micro/Nanolithography,-MEMS,-and-MOEMS.

[12] Triebes K Capots L, Sigler R. Multi-channel wide-field laser communications method and apparatus. URL https://patentimages.storage.googleapis.com/d5/9e/75/926b6463d607a7/US7292789B1.pdf.

[13] Weibiao Chen, Jianfeng Sun, Xia Hou, Ren Zhu, Peipei Hou, Yan Yang, Min Gao, Linjun Lei, Kedi Xie, and A The Mclcd. 5.12Gbps Optical Communication Link Between LEO Satellite and Ground Station. *IEEE International Confrence on Space Optical Systems and Applications*, pages 260–263, 2017.

[14] Emily Clements, Derek Barnes, Iñigo Portillo, Caleb Ziegler, Emily Clements, Raichelle Aniceto, Derek Barnes, David Caplan, James Clark, Iñigo Portillo, Christian Haughwout, Maxim Khatsenko, Ryan Kingsbury, Myron Lee, Rachel Morgan, Jonathan Twichell, Kathleen Riesing, Hyosang Yoon, Caleb Ziegler, and Kerri Cahoy. Nanosatellite optical downlink experiment : design , simulation , and prototyping. *SPIE*, 55(11), 2016. doi: 10.1117/1.OE.55.11.111610.

[15] Corning. Corning® varioptic® lenses (variable and autofocus lenses): Driver for robust adjustable lenses. URL https://www.corning.com/worldwide/en/innovation/corning-emerging-innovations/corning-varioptic-lenses.html.

[16] Corning Technology Center. Corning ® Varioptic ® Lenses. *Corning*, (November), 2017. URL https://www.corning.com/media/worldwide/Innovation/documents/FINAL{_}CorningVariopticLenses{_}productbrochure{_}5.4.18{_}lowresWEB.pdf.

[17] Yamaç Dikmelik and Frederic M Davidson. Fiber-Coupling Efficiency for Free-Space Optical Communication Through Atmospheric Turbulence. *Applied Optics*, 44(23), 2005.

[18] Faisal Fogle, Ondrej Cierny, Paula Do Vale Pereira, William Kammerer, and Kerri Cahoy. Miniature Optical Steerable Antenna for Intersatellite Communications Liquid Lens Characterization. *IEEE Aerospace Conference Proceedings*, 2020. ISSN 1095323X. doi: 10.1109/AERO47225.2020.9172448.

[19] D. L. Fried. Optical Resolution Through a Randomly Inhomogeneous Medium for Very Long and Very Short Exposures. *Journal of the Optical Society of America*, 56(10):1372, 1966. ISSN 0030-3941. doi: 10.1364/josa.56.001372.

[20] David L Fried. Branch point problem in adaptive optics. *Optical Society of America*, 15(10):2759–2768, 1998.

[21] Andreas Glindemann. Relevant Parameters for Tip-Tilt Systems of Large Telescopes. *Publications of the Astronomical Society of the Pacific*, 109(1976):682–687, 1997. ISSN 0004-6280. doi: 10.1086/133932.

[22] Darryl P. Greenwood. Bandwidth specification for adaptive optics systems. *Lincoln Labratory*, (December):87–90, 1977.

[23] Eugene Hecht. *Optics Fourth Edition*. Addison Wesley, 2002. ISBN 0321188780.

[24] Frank Heine, Gerd Mühlnikel, Herwig Zech, Sabine Philipp-May, and Rolf Meyer. The European Data Relay System, high speed laser based data links. *2014 7th Advanced Satellite Multimedia Systems Conference and the 13th Signal Processing for Space Communications Workshop, ASMS/SPSC 2014*, 2014-January:284–286, 2014. doi: 10.1109/ASMS-SPSC.2014.6934556.

[25] Philip .C.D. Hobbs. *Building Electro-Optical Systems*. WILEY, 2009. ISBN 978-0-470-40229-0.

[26] HOLOEYE. Spatial Light Modulators.

[27] Imke de Pater Jack J. Lissauer. *Fundamental Planetary Science*. Cambridge University Press, 2015. ISBN 978-0-521-61855-7.

[28] Jeffery J. Puschell Et. all James R. Wertz, David F. Everett. *Space Mission Engineering: The New SMAD*. Microcosm Press, 2011. ISBN 978-1-881-883-15-9.

[29] Siegfried W. Janson and Richard P. Welle. The NASA Optical Communication and Sensor Demonstration Program: An Update. *AIAA/USU*, 2014. URL https://digitalcommons.usu.edu/cgi/viewcontent.cgi?article=3100{&}context=smallsat.

[30] Ma Jing, Zhao Fang, Tan Liying, Yu Siyuan, and Han Qiqi. Plane wave coupling into single-mode fiber in the presence of random angular jitter. *Applied Optics*, 48(27):5184–5189, 2009. ISSN 15394522. doi: 10.1364/AO.48.005184.

[31] Yagiz Kaymak, Roberto Rojas-Cessa, Jianghua Feng, Nirwan Ansari, Mengchu Zhou, and Tairan Zhang. A Survey on Acquisition, Tracking, and Pointing Mechanisms for Mobile Free-Space Optical Communications. *IEEE Communications Surveys and Tutorials*, 20(2):1104–1123, 2018. ISSN 1553877X. doi: 10.1109/COMST.2018.2804323.

[32] Ryan Kingsbury, Kathleen Riesing, and Kerri Cahoy. Design of a Free-Space Optical Communication Module for Small Satellites. *AIAA/USU*, 2014. URL https://digitalcommons.usu.edu/cgi/viewcontent.cgi?article=3086{&}context=smallsat.

[33] Ryan W Kingsbury. Optical Communications for Small Satellites. *Technology*, (2015):127, 2015. URL https://dspace.mit.edu/handle/1721.1/101444.

[34] Thor Labs, . URL https://www.thorlabs.com/newgrouppage9.cfm?objectgroup_id=1209.

[35] Twibright Labs. Ronja tetrapolis specification, . URL http://ronja.twibright.com/tetrapolis/spec.php.

[36] Christophe O. Laux, Richard J. Gessman, Benoit Hilbert, and Charles H. Kruger. EXPERIMENTAL STUDY AND MODELING OF INFRARED AIR PLASMA RADIATION. *American Institute of Aeronautics and Astronautics*, 1995.

[37] Claudio Mazzali. Next generation optical fibers: Challenges and opportunities. *Proceedings of 2007 9th International Conference on Transparent Optical Networks, ICTON 2007*, 1:313–316, 2007. doi: 10.1109/ICTON.2007.4296096.

[38] David Mcgloin and Kishan Dholakia. Bessel beams: Diffraction in a new light. *Contemporary Physics*, 46(1):15–28, 2005. ISSN 00107514. doi: 10.1080/0010751042000275259.

[39] Evgenii Krouk Mikhail Sergeev Nathan Blaunstein, Shlomo Engelberg. *Fiber Optic and Atmospheric Optical Communication*. 2020. ISBN 9781119601999.

[40] Canon Netherlands. Canon ef 11-24mm f/4l usm -specification - lenses - camera photo lenses. URL https://www.canon.nl/lenses/ef-11-24mm-f-4l-usm-lens/specification.html.

[41] Bogdan V. Oaida, Matthew J. Abrahamson, Robert J. Witoff, Jessica N. Bowles Martinez, and Daniel A. Zayas. OPALS: An Optical Communications Technology Demonstration from the International Space Station. *IEEE*, 2013. URL https://ieeexplore.ieee.org/stamp/stamp.jsp?arnumber=6497167.

[42] Optotune. Tunable lenses. URL https://www.optotune.com/tunable-lenses?gclid=CjwKCAiAirb_BRBNEiwALHlnD9lDRh4zo-m7uHSyAYjcHqCIiPZ-kTDBfyX9_dwHF94mTmd4pjFy2hoCfZQQAvD_BwE.

[43] Paschotta. Passive fiber optics, Apr 2020. URL https://www.rp-photonics.com/passive_fiber_optics3.html.

[44] Rüdiger Paschotta. Fiber amplifiers, Apr 2020. URL https://www.rp-photonics.com/tutorial_fiber_amplifiers9.html.

[45] Cadence Payne, Alexa Aguilar, Derek Barnes, Rodrigo Diez, Joseph Kusters, Peter Grenfell, Raichelle Aniceto, Chloe Sackier, Gregory Allan, and Kerri Cahoy. Integration and Testing of the Nanosatellite Optical Downlink Experiment. *AIAA/USU Conference on Small Satellites*, SSC18-XII-, 2018. ISSN 0022-0981. URL http://digitalcommons.usu.edu/smallsat/2017/all2017/11.

[46] Anna Polishuk and Shlomi Arnon. Optimization of a laser satellite communication system with an optical preamplifier. *Optical Society of America*, 21(7):1307–1315, 2004.

[47] Harry Presly and Michael O'Reilly. Agile Multi-Beam Free-Space Optical Communication Apparatus, 2003.

[48] Michel Ram. A method for investigating off-axis gaussian beams. *University of Utrecht Library*, 2014.

[49] Eric Reagan. Canon ef 16-35mm f/4l is usm and ef 11-24mm f/4l usm lens cutaways, Sep 2015. URL https://photographybay.com/2015/09/14/canon-ef-16-35mm-f4l-is-usm-and-ef-11-24mm-f4l-usm-lens-cutaways/.

[50] S Robinson and R Pavithra. Investigation on Multi-Beam Hybrid WDM for Free Space Optical Communication System. *International Journal of Photonics and Optical Technology*, (June 2016): 24–28, 2016.

[51] Taiji Sakamoto, Takayoshi Mori, and Takashi Matsui. Feature Articles : State-of-the-art Space Division Multiplexing Technologies for Future High-capacity Optical Transport Networks Research and Development of Next Generation Optical Fiber Using Multiple Spatial Channels. *NTT Technical Review*, 15(6), 2017.

[52] Haruo Sato. Imaging products. URL https://imaging.nikon.com/history/story/0009/index.htm.

[53] Vladimir G. Sidorovich, Aleksei A. Leshev, Valery V Ragulsky, Mikhail A. Sadovnikov, Mikhail V. Vasiliev, and Vladimir P. Vasiliev. Free-Space Optical Communication System with Spatial Multiplexing, 2004.

[54] Vladimir G. Sidorovich, Aleksei A. Leshev, and Valery V Ragulsky. Free-Space Optical Communication System, 2006.

[55] Yuanping Song, Robert M. Panas, and Jonathan B. Hopkins. A review of micromirror arrays. *Precision Engineering*, 51(August 2017):729–761, 2018. ISSN 01416359. doi: 10.1016/j.precisioneng.2017.08.012. URL https://doi.org/10.1016/j.precisioneng.2017.08.012.

[56] Joshua Spaander. Literature review, 2020.

[57] Mark F Spencer and Salvatore J Cusumano. blooming and turbulence blooming and turbulence. *SPIE*, 816503(September 2011), 2011. doi: 10.1117/12.894079.

[58] TESAT. Products, Jan 2021. URL https://www.tesat.de/products#laser.

[59] Thorlabs, . URL https://www.thorlabs.com/.

[60] Thorlabs, . URL https://www.thorlabs.com/newgrouppage9.cfm?objectgroup_id=6178.

[61] Thorlabs, . URL https://www.thorlabs.com/NewGroupPage9.cfm?ObjectGroup_ID=3404&pn=OC-L-1550#6193.

[62] Thorlabs, . URL https://www.thorlabs.com/newgrouppage9.cfm?objectgroup_id=10378.

[63] David H. Tofsted, Sean G. O'Brien, and Gail T. Vaucher. An Atmospheric Turbulence Profile Model for Use in Army Wargaming Applications I. Technical Report ARL-TR-3748, 2006.

[64] Morio Toyoshima. Maximum fiber coupling efficiency and optimum beam size in the presence of random angular jitter for free-space laser systems and their applications. *Optical Society of America*, 23(9):2246–2250, 2006.

[65] Morio Toyoshima. Recent Trends in Space Laser Communications for Small Satellites and Constellations. *Journal of Lightwave Technology*, 8724(c):1–1, 2020. ISSN 0733-8724. doi: 10.1109/jlt.2020.3009505.

[66] Capots L Treibes K, Enoch M. Multi-beam laser communications system and method. URL https://patentimages.storage.googleapis.com/9b/4d/8d/f8cee9f6dfb5e3/US7292788B2.pdf.

[67] Glenn A. Tyler. Bandwidth considerations for tracking through turbulence. *Journal of the Optical Society of America*, 11(1):358–367, 1994. ISSN 1084-7529. doi: 10.1364/josaa.11.000358.

[68] Joseph T. Verdeyen. *Laser Electronics*. Prentice Hall, 1995. ISBN 0-13-706666-X.

[69] Christian Vetter, Ralf Steinkopf, Klaus Bergner, Marco Ornigotti, Stefan Nolte, Herbert Gross, and Alexander Szameit. Realization of Free-Space Long-Distance Self-Healing Bessel Beams. *Laser and Photonics Reviews*, 13(10):1–6, 2019. ISSN 18638899. doi: 10.1002/lpor.201900103.

[70] David Voelz. *Computational Fourier Optics*. SPIE, 2011. ISBN 978-0-8194-8204-4.

[71] Oswald Wallner, Peter J. Winzer, and Walter R. Leeb. Alignment tolerances for plane-wave to single-mode fiber coupling and their mitigation by use of pigtailed collimators. *Applied Optics*, 41 (4):637–644, 2002. ISSN 15394522. doi: 10.1364/AO.41.000637.

[72] Peng Wang. *The Energy Efficiency of EDFA and Raman Fiber Amplifier*. Master of engineering thesis, University of Melbourne, 2016.

[73] M. W. Wright, M. W. Wilkerson, and Ray R. Tang. Qualification testing of fiber-based laser transmitters and on-orbit validation of a commercial laser system. *SPIE*, 10563(ICSO October), 2014. ISSN 1996756X. doi: 10.1117/12.2304100.

[74] M. W. Wright, M. W. Wilkerson, and Ray R. Tang. Qualification testing of fiber-based laser transmitters and on-orbit validation of a commercial laser system. *SPIE*, 10563(ICSO October), 2014. ISSN 1996756X. doi: 10.1117/12.2304100.

[75] Feng Xiao and Lingjiang Kong. Optical multi-beam forming method based on a liquid crystal optical phased array. *Optical Society of America*, 56(36):9854–9861, 2017.

Literature Review

Joshua Spaander

March 2020

Contents

1 Introduction

An important part of spaceflight is the communication between the ground and the spacecraft and between spacecraft. Historically this has been done using radio frequencies, with ever more complicated antenna designs and higher frequency carrier waves. However, there are numerous problems with this technology. These include crowed frequency bands, low energy efficiency, large apparatus, etc... As a result of these problems, often the full amount of data gathered cannot be communicated fully and therefor not exploited. Furthermore, this is a cost barrier to further space exploration and exploitation due to satellites being more expensive due to the SWaP (Size, Weight and Power) consumption/cost of radio communication modules.

In the last 1-2 decades, there has been a significant advancement in free-space optical communication for space. The use of optical frequencies, usually through lasers, allows for smaller bundles sizes which improves power efficiency, increases data rates, no conflicts in frequency bandwidth allocation, smaller modules, private communication, etc... Free-space optical demonstrations and modules have shown comparable data rates with high end regular radio communication systems at a fraction of their SWaP costs with performance increasing rapidly over time.

However, these demonstrations use a single beam per module. This indicates a use case where only one link can be sustained and used. This limits satellites to be multi-user, part of a network to relay information, use multiple ground stations, etc... Hence, there is significant opportunity for multi-beam systems.

My thesis topic is hence on designing a multi-beam optical communication terminal designs for spacecraft. This thesis will be characterized by an endeavor to see what an efficient and scale-able system which can communicate with multiple targets can look like.

This literature study and thesis plan shall present available literature by which key concepts and overviews are created on this thesis topic. Subsequent goals, requirements and research objectives are then distilled together with how to meet them. Finally, the thesis activities are planned.

A full design and demonstration of such a system is not achievable within the given time frame. Hence, the focus shall be on the multi-beam pointing system required in a multi-beam system. However, the overall architectural layout and surrounding technical challenges have affect on the pointing system. Hence, the goal of the thesis is to produce a transceiver design and pointing system. The resulting pointing system will also be investigated through a demonstration. This design will be done through the use of existing technology which is COTS (Commercial Off The Shelf).

Part I
Literature Review

This part shall discuss the available literature on the topic of multi-beam free-space optical communication and free-space optical communication in general. It will first discuss the previous multi- and single-beam designs. Here, an analysis of design aspects will become use full for taking inspiration and understanding what is expected of these terminals.

After this, a detailed analysis and review of different optical hardware components which can be used in the multi-beam terminal. There will also be a discussion on the fundamental theoretical foundation particularly on the fundamental challenges in optical terminal design. Here, requirements which are relevant to the design of terminal will also be derived. There is also an analysis on the expected link budget and the expected effects of misalignment. This leads to a general trade-off to see which components are most compatible with this use case.

Lastly, there is a reflection on the available literature, to summaries the discussed concepts and content.

2 Existing Designs for Multi-Beam Optical Communication Systems

This section shall discuss the previous work performed on multi-beam designs. First a summary will be made on the available literature, after which design aspects will be discussed. There is in this case a particular prevalence of patents. This too is reflected upon.

2.1 Literature

In Table 1 summarizes different works. From left to right, the title is presented, the date released, the names of the authors and the citation to the bibliography and lastly a short summary of its content.

Table 1: Literature on Previous Designs.

Literature Overview Existing Designs			
Title	Date	Authors & Reference	Content Summary
Multi-Point Free Space Optical Communication System	2018	Segura B, Mathlouthi W [30]	This is a patent. It describes a system which uses a set of fine steering optics before the telescope to redirect the beams. The beams are generated through multiple transceiver modules at different frequencies and multiplexed. This multiplexed beam is then demultiplexed by frequency through a prism, grating or other. The resulting split beams are then distributed spatially across the FOV by a FSO array. Lastly, beacons are used to track target locations and beam pointing. Separate bandwidth is given to these.
Multi-Beam Laser Communications System and Method	2007	Treibes K, Enoch M, Capots L [39]	This is a patent. The patent describes a system which utilises a telescope that can image the in coming beams on an optical train while the outgoing beams on the FOV. The optical train splits the light based on polarisation for in and outgoing beams. The outgoing beams are sampled and the samples are imaged onto the spot tracker. The rest is guided to the telescope. The incoming beams are split and coupled into the receiver fibers while the rest of the beam is imaged onto a spot tracker. The primary telescope has a wide FOV allowing for the transmitted signals to be imaged on the spot tracker such that these do not have to be scanned for. The transmitted beams are bundeled into a much smaller FOV, for energy efficiency. The fibers are steered to point the beams by a set of actuators into the FOV. The transmitting and receiving fibers are separate before entering the telescope.

Literature Overview Existing Designs Continued			
Title	Date	Authors & Reference	Content Summary
Multi-Channel Wide-Field Laser Communications Method and Apparatus	2007	Capots L, Sigler R, Triebes S [8]	This is a patent. The patent describes a system which uses a wide FOV acquisition tracker. This tracker can locate potential communication requests and use its FPO's to direct these to the target. The incoming and outgoing beams are directed accurately through an array of steering flats. These are reflected to a set of static pick-off mirrors which reflects the beams to the optical telescope. This in turn focuses the beams onto a multi-channel focal plane assembly. Here, incoming beams are coupled into the receiving fibers. The static ground channels are treated differently then the then moving channels. The static ground channels are given a static pre-determined position on the imaging plane and are hence not moved and require no pointing mechanism. Moving targets are accommodated differently. For the moving target the fibers are steered and a specialized spot tracker for reach transceiver where the receiving fiber is centered.
Agile Multi-Beam Free-Space Optical Communication Apparatus	2003	Harry Presley, Harris Corporation[27]	A patent, which describes the use of an array of transmitters and an array of receivers (separated) which are connected to cross bar switches. The specific receiver and transmitters are selected based on a CCD tracking array imaging the subscriber beams. The cross bar switches subsequently allow the beam to be directed without moving parts to a particular target by changing the transmitter. The same is done with the selected receiver. In this case, the beams are steered through a set of lenses which refract the light in different directions depending on the location of the selected transmitter. The incoming signals and out going signals are separated by a dichroic mirror which selects the wavelengths. The cross bar switches can be done for both electrical signals using and electrical cross bar switch and/or optical with an fiber optic cross bar switch.

Literature Overview Existing Designs Continued			
Title	Date	Authors & Reference	Content Summary
Multi-Target-Tracking optical Sensor-Array Technology	2009	Daniel G. O'Connell, Ken C. K. Cheung[24]	This patent describes a system which is capable of tracking and discriminating multiple targets through the use of a sensor array. This system is mean for projectile tracking for defense purposes however has insights which is useful for multi-tracking of target in multi-beam optical communications. The system incorporates information from starting optical sensors, steered optical sensors, radar sensors among others and uses algorithms to be able to discriminate between targets.
Free-Space Optical Communication System with Spatial Multiplexing	2004	Vladimir G. Sidorovich, Aleksei A. Leshev, Valery V. Ragulsky, Mikhail A. Sadovnikov, Mikhail V. Vasiliev, Vladimir P. Vasiliev[31]	This patent describes a system which serves to connect optical communication networks and relay/repeat messages between transmitter and receiver terminals. The terminals consists of a large spherical lens (referred to as the wide angle objective lens) which focuses incoming beams onto a set of receivers. These convert the optical signal into an electrical signal and is then passed on to the network. In turn, messages for transmission arrive from the network and is converted to an optical signal. The optical beam is then passed through the spherical lens to a set of fine steering mirrors on the peripheral of the sphere. The method by which these beams are steered, detected and links acquired is not described. However, considering the multitude of methods which have been presented and will be presented, tracking systems can be implemented.
End Literature Overview Multi-Beam Terminal Designs			

2.2 Spatial Separation vs Multiplexing within the Terminal

From the above presented designs there are a couple of designs and their features which stand out. These designs mainly use one telescope structure however the method by which the links are separated in the terminal are different.

The aperture captures a mixture of beams from all the links. In the considered works, the resulting beams are either multiplexed through the use of different wavelengths as is the case with Treibes K et all.[39] and polarization such as Segura B et all.[30]. It is also possible to use spatial separation from

the start as is the case with Capots L et all.[8]. These designs are shown in Figure 1, Figure 2 and Figure 3.

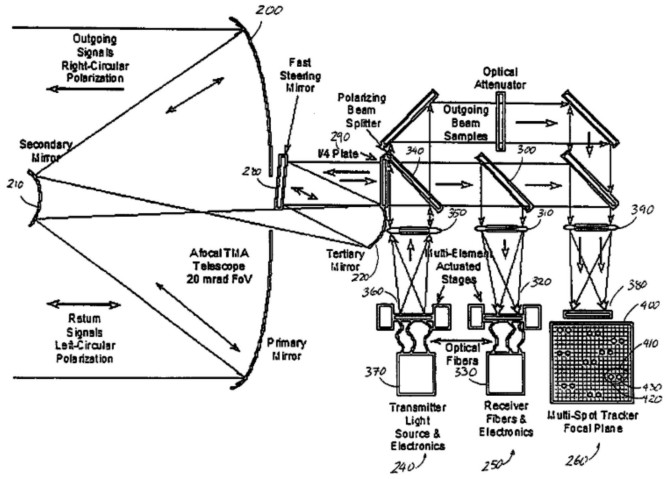

Figure 1: This design by Treibes K et all.[39] shows how a main primary mirror captures multiple beams. The system then focuses them into an optical train where the transmission and receiver channels are separated by polarization.

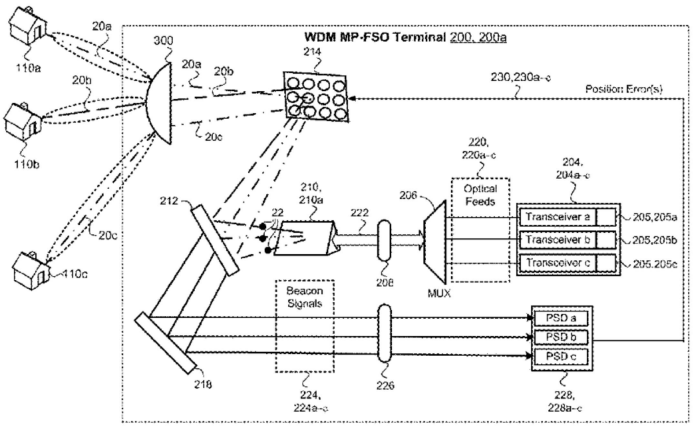

Figure 2: The design by Segura B et all.[30] shows a use of different wavelengths being separated and used for different links. The system uses a single aperture inlet for the telescope and focuses this onto a mirror array.

None of these solutions presented divides the FOV and uses one channel to

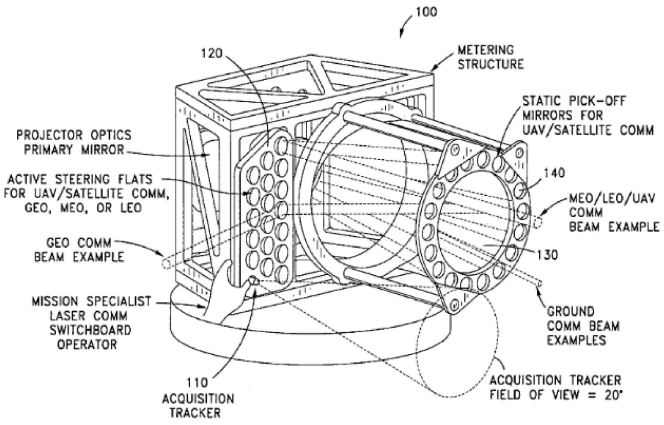

Figure 3: The design by Capots L et all.[8] shows how an array of FSMs can be used to control the direction of the outgoing beams. The incoming beams are focused onto transceivers using a large telescope. To use the pick-off mirror arrays. The result of this however, are limited aperture sizes.

service one area spatially per channel. They are target oriented and follow these target with individual channels. This is likely to reduce power requirements for sufficient signal to noise and to maintain the benefits of optical communications.

The benefit of spatial separation is that it requires less multiplexing methods required for link separation allowing these to be implemented for higher data rates. The drawback is that the system dimensions and mass scales proportional to the number of links. This is because additional hardware is required in proportion to the number of channels for spatial separation. This is hence harder to scale for multiple users.

The idea presented in Capots L et all.[8] attempts to reduce the hardware requirements for static targets and moving targets. This in turn leads to a few number of actuators and tracing sensors required. This would require a geostationary orbit or an adjustment to move the entire terminal in high orbits. Which in turn would limit the number of applications, reduce the data rates due to signal strength losses and increase the required laser powers to name a few.

In addition to this, the design presented in Capots L et all.[8] requires multiple FSMs and/or FSOs which in turn have limited aperture sizes. Smaller aperture sizes leads to lower transfer rates however more channels/beams can be implemented. This leads to a trade-off where larger optical elements would lead to higher performance but lower numbers of links for the same size and mass.

Multiplexing hence reduces the hardware requirements but limits the data budget per link. The design presented in Segura B et all.[30] illustrates as-

signing frequencies spatially, allowing for multiple transmitters operating in the same spectrum with different modulations/multiplexing methods. This does increase the link capacity however if the number of targets exceed the frequency allocations they have to start sharing link capacity.

These problems are exacerbated by the fact that separated frequencies are used for beacons in Segura B et all.[30]. This reduces the diversity of the amount of frequencies used. However this can be overcome quite simply through the use of beam splitters and using the signal it self as a beacon.

The design presented in Treibes K et all.[39] shows a completely static optical train where the beam steering occurs at the fiber. This decreases the demands on the telescope while the steering mechanisms can be made smaller. The system still has the same problems as with Segura B et all.[30] when it comes to multiplexing and frequency allocations. However, the distances and accuracy by which it has to be moved by the fibers would be harder then exploiting existing mirror systems.

2.3 Prevalence of Patents in the Multi-Beam Terminal Literature and Discussion of Other Designs

When researching, it has become clear that a significant prevalence of patents in the field and relatively little research papers. When compared to the literature on single beam communications, see Table 2, research papers are more common. This subsection discusses the motivation and applications of the designs and concepts present in these patents. Furthermore, an attempt will be made to determine the general direction of industry in the past and current on multi-beaming with the bulk in the late 2000's.

A relatively old patent is of the invention by Sprague and Scifres[33], from 1984, describes a multi-lens system which uses multiple beams to read optical disks among other applications as described in the abstract and background. This use is not directly related to optical communications for satellites, however does illustrates some benefits of increased bandwidths through the use of multi-beam data transfer. The use of micro lens arrays for the application in spatially separating and forming different laser beams. The design is shown in Figure 4.

The design invented by Daniel G. O'Connell and Ken C.K. Cheung[24] specifies the "Field of Invention" to be; "The invention provides sensor technology and method for missile defense (target tracking and discrimination), battlefield management, artillery/gunfire locator, SAM defense, space-based warhead launch detection with superior speed and accuracy." It is hence mainly defense oriented meant for the tracking of multiple targets, in this case primarily projectiles. This is hence not directly related to multi-beam communication however is related in the multi-target sense, since the multi-beam system too requires tracking of multiple targets. The design is shown in Figure 5.

The invention by Sidorovich, Leshev, Ragulsky, Sadovnikov, Vasiliev, and Vasiliev[31] describes an optical repeater system which can be used to relay and maintain a separation between individual receivers and/or transmitters. This is not directly dedicated to satellite multi-beaming concepts, instead stating in

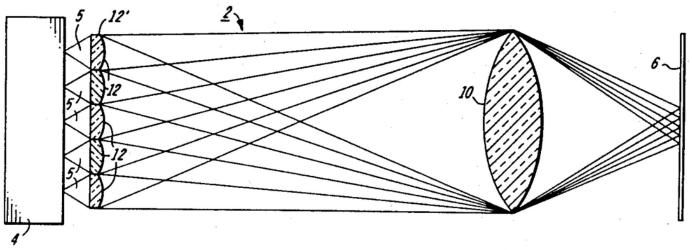

Figure 4: The design by Sprague and Scifres[33] shows a method which looks like the mirco-lens array of a Shack-Hartman wavefront sensor. This in combination with a larger lens allows for the separation and focusing. If this was used for communication, the micro-lens array could serve to couple into closely spaced optic fibers. However, the density of the fibers must be high enough for efficient coupling.

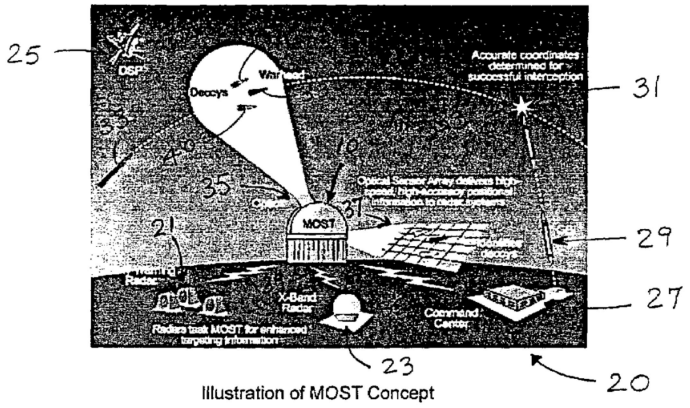

Figure 5: This illustration by O'Connell and Cheung[24] shows the application of the system in tracking multiple targets using a CCD and actuated telescopes.

the "Field of the Invention"; "The present invention relates to free-space optical communication systems and may be used for wireless/fiberless two-way information transfer between remote objects, including situations with many objects participating in point-to-point or point-to-multipoint information exchanges." This patent is still related to multi-beam communications, since this design incorporates many concepts which can be used. The design is shown in Figure 6.

The tracking of projectiles and relay of signals are very specific goals, especially compared to Capots, Sigler and Triebes's[8] inventions. The invention by Capots, Sigler and Triebes[8] explicitly mention a more diverse selection of

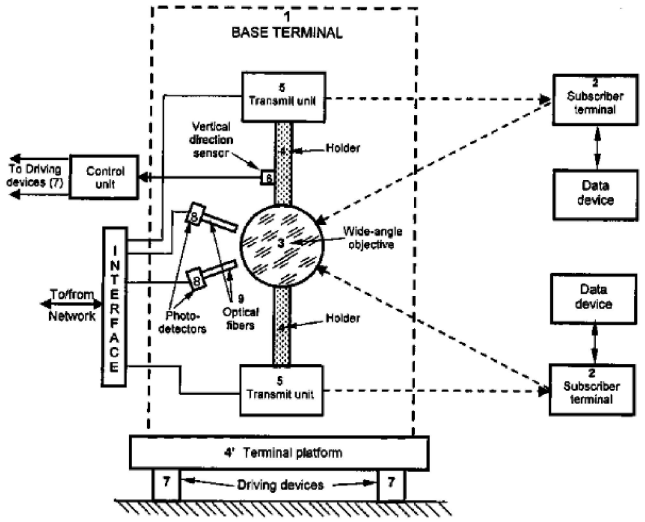

Figure 6: The design by Sidorovich et all.[31] shows a system which uses separate transmitter and receiver units. The circular lens allows for dynamic placement of the fiber while a separate transmitter unit allows for independent steering of transmitter beams. How the system performs steering and active correction is not shown here. These aspects however might be quite challenging, considering the relatively little optical elements in the system and hence little space for spot trackers and correction systems.

applications. These range from ground, mobile, aerial and satellite platforms. Furthermore, the design can be used in various satellite missions.

Segura and Mathlouthi's[30] invention patent describes a system which uses multi-beam optical free-space communications. However, the figures depict communications between households and buildings in a system which is similar to local area networks. According to the contents of the "Background" section, applications include replacing local wire and fiber networks with the more flexible free-space network links. Its application hence is not specifically dedicated to satellite multi-beam free-space optical communication, however indicates an aim for the terrestrial networking market and infrastructure. This patent is from 2018 and hence indicates some of the recent trends in the industry.

Presley and O'Reilly's[27]. The system proposed in Presley and O'Reilly's[27] does not propose a large field of application directly, however is specified to be used for multiple user targets. This open ended description can imply a very broad field of application, and their concept can likely be adapted to fit a broad number of uses. Similarly, the invention of Sidorovich, Leshev and Ragulsky[31] also presents a similarly open ended and broad application of a general multi-point communication systems. The design can be seen in Figure 7.

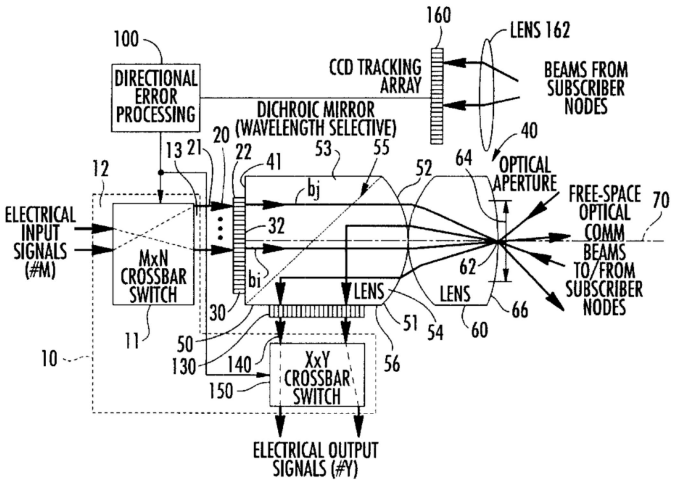

Figure 7: The design by Presley and O'Reilly's[27] is quite extensive design which uses a open feedback loop for beam pointing. The beam pointing is not done using active mirror arrays or actuators. However, it uses a fiber array which is conjugated geographically and a crossbar switch to select a fiber based on this. Similarly, the receiver is an optic fiber array with a crossbar switch. This system would require a high density of optical fibers in the fiber array. Furthermore, for efficient fiber coupling would require a diffraction limited fiber coupling with high stability and off-set corrections. This systems ability to react to this is limited.

The design of multi-beam communication related systems discussed above, have a diverse and multi-goal applications. These applications range from mobile networks to defense. However, also designs specifically dedicated to multiple uses including multi-beam satellite communications. The applications them selves do not specifically dedicate to satellite systems or mention the use of mirco-mirror arrays. Furthermore, the most recent patent indicates the use of free-space optical communications mainly for local networks and inter-building communications.

3 Single-Beam Terminal Previous Designs

This work and subsequent thesis will focus on designing and building a multi-beam free-space optical communication terminal. However, these systems will share concepts and components in common. This section shall discuss different previous designs for free-space optical communication.

3.1 Literature

The summary of different works selected is shown in Table 2.

Table 2: Literature on Previous Designs of Single Beam Terminals.

Literature on Previous Designs of Single Beam Terminals			
Title	Date	Authors & Reference	Content Summary
Design of a Free-Space Optical Communication Module for Small Satellites	2014	Ryan Kingsbury, Kathleen Riesing, Kerri Cahoy [17]	A design is presented where a single channel optical communication terminal for a cube sat is presented. This utilizes a single laser diode coupled into a fiber and directed onto a flat FSM.The is subsequently then pointed to the target. The module it self can obtain a +- 2.5 deg FOR and a beam divergence of 2.1 mrad/0.12 deg. The module it self does not use larger gimbals because of the SWaP requirements. Hence it relies on the SC to point in the general direction. The uplink does not carry data in this case and is purely used for acquisition and tracking. The acquisition happens after an elevation angle of 20 deg. The transmitter it self uses a 1W laser. The exact design of the laser system at the time of the paper being written is not yet completely done.
The NASA Optical Communication and Sensor Demonstration Program: An Update	2014	Siegfried W. Jason, Richard P. Welle [15]	The design illustrates both the ground and SC terminals. The chosen modulation is amplitude modulation. Initially a 975 nm wavelength was used but this was switched for a less power efficient 915 nm due to this being less temperature unstable. It uses a MOPA which is isolated and amplified again. This had an input power of 50W and an output power of around 10W.

Literature on Previous Designs of Single Beam Terminals Continued			
Title	Date	Authors & Reference	Content Summary
OPALS: An Optical Communications Technology Demonstration from the International Space Station	2013	Bogdan V. Oaida, Matthew J. Abrahamson, Robert J. Witoff, Jessica N. Bowles Martinez, Daniel A. Zayas [23]	OPALS is/was a system meant to increase understanding in a few areas of the field. The system was designed to have a downlink of 30-50 Mb/s. The laser used is on the order of 1-4 Watts and the mass of the whole system is. The budgets for this module are very generous, with 490 lb (222 kg) and many 100s of Watts on a variety of different voltages. The system only used an optical downlink while the optical beacon was sent from the ground station. The avionics used are COTS and housed in a 1ATM oil drum in part for cooling. The system was meant to interface with the ISS and hence is much larger and heavier then cube sat designs. The system is capable of transmitting DVD quality video. From the text it is unclear, however one gible axis actuates the whole module and is attached to the ISS structure. There exists a second set of gimbals for the transceiver, which can do so along 2 axis and can point within the requirements.. This system was designed for a range of 700 km.
Fast-Steering Solutions for Cubesat-Scale Optical Communications	2014	R.W. Kingsbury, T. Nguyen, K. Riesing, K. Cohoy [5]	The design and writers of the system design are the same as in [17], and this document seems to compliment the previous work done. The paper motivates the choice for a MEMS mirror. The paper investigated 3 main types of FSMs, mechanical, Piezoelectric and MEMS. The mechanical mirrors did not meet size and vibration constraints, which are problems related to their size and mass. The Piezoelectric mirrors did fit the SWaP requirements but the controller did not at the time. The MEMS mirrors where chosen because both the mirrors and the controllers meet the SWaP. The designers chose for an electrostatic chip sized mirror, since the electromagnetic mirrors which not in production anymore.

Literature on Previous Designs of Single Beam Terminals Continued			
Title	Date	Authors & Reference	Content Summary
Laser Communication with CubeSats	2018	K. Cahoy[4]	A presentation which has created an overview of the technologies and advancement at that time. On slide 22, there is a clear illustration of the different SWaP performances. Namely the Nanosatellite Optical Downlink Experiment both with a relatively light and power efficient platform and with relatively good performance compared to OPALS and Optical Communication and Sensor Demonstration.
Integration and Testing of the Nanosatellite Optical Downlink Experiment	2018	Payne Et. Al[25]	This is a presentation given by Emily Clements on the integration and testing of the NODE (Nanosatellite Optical Downlink Experiment). The presentation provides an overview of the layout of the module. The design shows the use of a beacon receiver for finding the target and adjust the fine steering mirror to optimally steer the beam from a COTS Collimator. The ground station is a modified amateur telescope. The group developed their own electronics boards. There where hardware demonstrations in the lab. It was demonstrated that the fine pointing can reach below the required pointing error of 0.6 mrad. Tests where with the COTS EDFA from NuPhoton under radiation doses show temporary problems occure and then nominal operation at 3krad or 6 year LEO dose.

Literature on Previous Designs of Single Beam Terminals Continued			
Title	Date	Authors & Reference	Content Summary
Nanosatellite Optical Downlink Experiment: Design, Simulation, and Prototyping	2016	Clements Et. Al.[9]	A general overview document for NODE, which is more specific in design details compared to the presentation[25]. It outlines that coarse pointing is done by the spacecraft it self and that the remaining error is then reduced through the use of an FSM. The combination of these results in a far lower pointing error. This paper also sheds more light on the transmitter design. The transmitter is a fiber coupled laser diode MOPA. The fiber is placed in a racetrack to improve the quality of the beam. After each stage the light is sampled to measure the performance of that stage. This is done with the extinction fiber, after the extinction fiber and EDFA. The laser diode temperature is monitored as well, with an electric cooler in case of overheating. Light before and at the end of the extinction fiber allows for measuring the quality of the laser light and pollution (in the laser spectrum). It hence indicates the performance of the system.
End Literature on Previous Designs of Single Beam Terminals			

3.2 Module Requirements Considerations

There are some clear limitations when it comes to the budgeting, which drive the design of the system. For larger systems such as the ISS, mass and power is not an issue and hence this system is very inefficient SWaP. For cubesats these tend to be more important.

The OPALS system for example uses an atmosphere in an oil drum to prevent the COTS components from being exposed to the harsh space environment. Furthermore, the system interface with the ISS allows it to use a mounting base. Furthermore, the equipment used is not the most efficient.

For use in systems with stringent SWaP requirements the system has to therefor use more power and mass efficient systems. A method by which this is done for example is by exposing the hardware to the vacuum of space and to use efficient power amplifiers. This also implies that the pointing mechanisms will, unlike OPALS, be done in part by the SC self and more efficient electrostatic and electromagnetic MEMS.

All in all it says however, that through system optimizations, significant gains in efficiency can be made such that these systems can become feasible.

3.3 Performance in Hardware and Architecture

	Lunar Laser Communications Demonstration (MIT LL)	Optical Payload for Lasercom Science (JPL)	Optical Communication and Sensor Demonstration (The Aerospace Corporation)	Nanosatellite Optical Downlink Experiment (MIT)
Data Rate	622 Mbps	50 Mbps	40 Mbps /300 Mbps	10 Mbps / 100 Mbps
Tx Power	0.5 W	2.5 W	6 W	200 mW
Orbit	Lunar	LEO (ISS)	LEO	LEO
Payload mass	30 kg	180 kg	2 kg	1 kg
Beamwidth	2.5 urad	~0.01 deg	0.30 deg	1.3 mrad
Ground station	White Sands	OCTL 1-m	MOCAM / MAFIOT	PorTeL / OCTL

Figure 8: Comparisons between small laser communication missions (slide 22 [4])

Considering Figure 8, it can clearly be seen that there is a significant difference between different modules and their performances. Considering for example the differences between the Nanosatellite Optical Downlink Experiment (from now on referred to as NODE) achieves similar performances as the Optical Communication and Sensor Demonstration (from now on referred to as OPALS) for data rates. However, OPALS weighs 179 kg more and produces a transmitter power 12.5 times higher. There are a number of reasons for this which can be seen from each design. The designers of the OPALS system had to meet less strict design criteria compared with those found on a nanosatellite because OPALS would be tested on the ISS. Hence, this mass likely includes the attachment points, interfacing hardware and makes use of the ISS's plenty full power. This lead to a less efficient design[23]. The used is a ruggedized military-grade laser unit does not allow for a design insight.

However, some design aspects of an optical fiber train can be seen in Figure 9.

Figure 9 shows a design which is representative for a more efficient design used in the the Optical Communication and Sensor Demonstration [15]. This design is not as efficient as the one proposed for NODE, however illustrates that the energy efficiency can be achieved through efficient power amplification.

Although the exact specifications are not fully stated, a qualification document of the OPALS laser however states that it too uses a MOPA-fiber amplifier combination[45]. This results in multiple hundreds of Mpbs, however the use of OOK it is limited to 50 Mbps (see 1st page second introduction paragraph[45]). OOK was chosen for ground receiver constraints[45].

The system architecture for space optical communication is hence very similar and the differences here can be found in specific hardware choices. However, the modulation and multiplexing techniques used are very important.

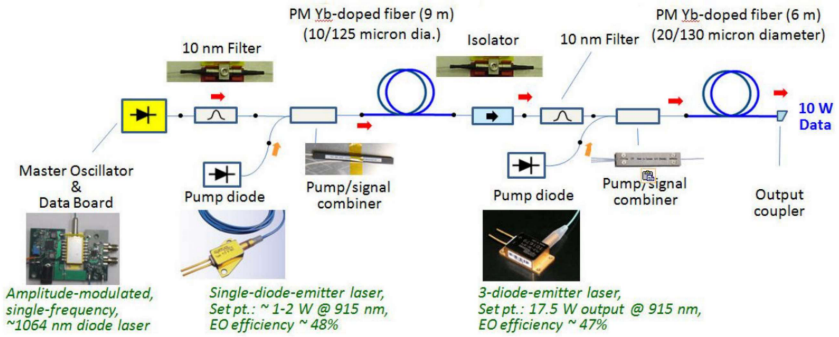

Figure 9: The Master Oscillator (MO) produces a signal which is subsequently amplified by pumping with a single diode Yttrium (Yb) doped fiber and a single diode laser. These two combined are the MOPA or Master Oscillator Power Amplifier. After this is passed through an isolator, after which the signal is pumped again with a 3 diode Yb fiber amplifier. This allows the MOPA to be low power which ensures that its power efficiency is less important and its design can be focused on data performance. The second signal amplifier can then be optimized for the best energy efficiency improving the overall system efficiency. This design is used for the Optical Communication and Sensor Demonstration[15].

4 Optical Train

This section will discuss different aspects of the optical train design for the mutli-beam terminal. There are many interdependence in the system which should be address before designing and building a mutli-beaming terminal.

4.1 Fiber Performance

If the transceiver requires the beams to be coupled into fibers, then the optical train and mirrors should meet the requirements for it to couple into the fibers and for the fibers to effectively meet the requirements. Here, the basic theory and the effects of misalignment will be explored and discussed. Special attention to jitter from atmospheric turbulence will be considered, with a discussion made on the effects on a multi-beam terminal. After this, a number of enhancements which can be made to a fiber coupling system will be considered and discussed.

Special attention will be given to the mathematical aspects of this section, since the pointing requirements will be derived from this.

Table 3: Literature on fiber coupling efficiency.

Literature on fiber coupling efficiency			
Title	Date	Authors & Reference	Content Summary
Alignment tolerances for plane wave to single-mode fiber coupling and their mitigation by use of pigtailed collimators	2002	Oswald Wallner, Pater J. Winzer, Walter R. Leeb[41]	This paper builds up and describes and builds a method for modeling and predicting the loss in fiber coupling efficiency due to miss-alignment. This methods is very similar and comparable to the methods used by other papers in this list, can hence will serve as a fundamental theoretical basis for fiber coupling. The results of these derivations are analyzed with conclusions as to the importance of different alignment tolerances. It is concluded that the angle and axial off-set of the fiber is not as important as the lateral off-sets. A method by which these tolerances can be relaxed is through the use of a pigtailed collimator through the use of a GRIN (Gradient Refractive Index Lens) lens for example. The effects of including such an optical element on the overall optical design is also discussed.
Maximum fiber coupling efficiency and optimum beam size in the presence of random angular jitter for free-space laser systems and their applications	2006	Morio Toyoshima[38]	This paper discusses the same principles discussed in [34]. However, considers jitter in general. It makes a mathematical model that models off-set spots and different sized spots and their affect the fiber coupling efficiency. When jitter is then added for displacement for different spot sizes, the resulting performance also varies. The conclusion is that for certain variance sizes due to jitter, the spot size on the fiber has an optimum efficiency fiber coupling.

Literature on fiber coupling efficiency Continued			
Title	Date	Authors & Reference	Content Summary
Plane wave coupling into single-mode fiber in the presence of random angular jitter	2009	Jing Ma, Fang Zhao, Liying Tan, Siyuan Yu, Qiqi Han[16]	This paper derives and discussed the effects of jitter on fiber coupling perfromance from first principles, similar to work of Toyoshima[38]. However, the method use is a simpler method for achieving the same results compared to Toyoshima's[38] work, and will be used as a basis to build off. This is because the fiber coupling geometry is backpropagated to the apperture plane instead of being solved on the fiber plane.
Study on the fiber coupling efficiency for ground-to-satellite laser communication links	2010	Hideki Takenaka, Morio Toyoshima[34]	A numerical approach is made to investigate the effect of turbulence on different beam sizes and wavelengths. It has unsurprisingly shown that stronger turbulence results in lower coupling efficiencies. The beam width, compared to the mode radius, results in an optimum when varied. This optimum varies for different turbulence strengths, and it has been found the mode-radius-Airy disk ratio decreases. It has also been found that larger coupling lens diameters increase the coupling efficiency. Lastly, the coupling efficiency is higher for longer wavelengths for a given turbulence. The use of a FSM improves the performance of the system, suppressing especially the lower frequencies in the error power spectrum.

Literature on fiber coupling efficiency Continued			
Title	Date	Authors & Reference	Content Summary
Fiber-coupling efficiency for free-space optical communication through atmospheric turbulence	2005	Yamac Dikmelik, Frederic M. Davidson[10]	This paper describes a method by which the fiber coupling efficiency in the presence of turbulence can be numerically approximated. After this it proposes the use of coherent fiber arrays to improve the overall performance. The method used is to calculate the efficiency is similar to the super position of spots as used in other papers in this list. The syntheses however differs, in the sense that it is assumed that the distribution in the fiber follows a Gaussian distribution instead of Rician distributions. The same maximum coupling efficiency is found as in [38]. This paper however, explores the use of a coherent fiber array, which effectively is a bundle of fibers artificially increasing the aperture. This also has the benefit of the smaller apertures being less affected by speckling. Although not mentioned, this is because the turbulence simulated in the models has a Fried parameter which is larger then the fiber sub-apertures. The system is hence an array of sub-apertures which are combined to receive the signal. The combination is more complex and leads to design considerations. The same system could also be used as a phased array for steering the signal as demonstrated by HRL, and hence can be used to steer more precisely.
End Literature on fiber coupling efficiency			

4.1.1 Effects of Fiber Misalignment and Pointing Errors on Fiber Coupling Efficiency

The basics of misalignment effects on the efficiency of the fiber coupling. The work of Oswald Wallner, Pater J. Winzer, Walter R. Leeb[41] will be discussed here in detail, with some additional points added for clarity. However, the names and variables used will be changed to ensure cohesion with the work described later. Fiber coupling is the process by which a beam from a different media is inserted/coupled into an optic fiber. In the case of a free-space optics terminal, these beams come from the free-space as its media and is coupled into a receiving optical fiber.

These fibers are often single mode fibers, this means that one mode of light

can be transmitted through it which preserves the signal quality and coherence during transport in the fiber. The result is however, that the fiber core is very small. This is because higher order fundamental lateral modes inside a optic fiber requires more cross-sectional area compared to the first fundamental mode. Hence, fiber coupling is done through a fiber coupling lens as shown in Figure 10.

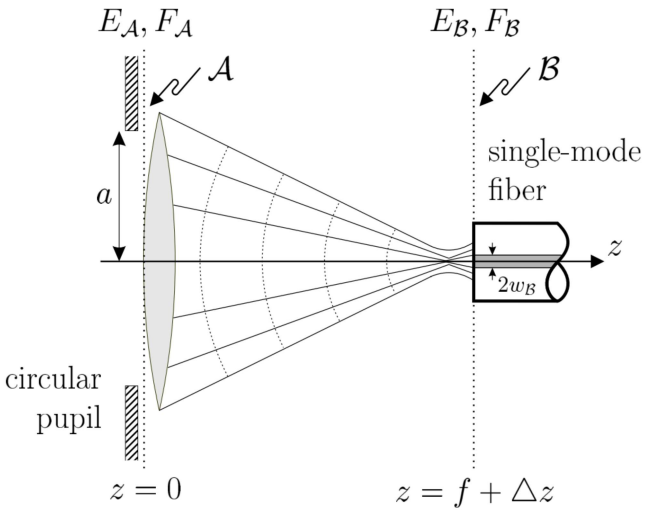

Figure 10: An illustration of fiber coupling by Oswald Wallner, Pater J. Winzer, Walter R. Leeb[41] on page 19, Figure 1. Note that the axis system perpendicular to the optical axis is denoted by the x and y axis.

The analysis begins with the realization that light is the oscillation of an electromagnetic field which is incident on the aperture of the lens and is subsequently focused onto the fiber aperture. These are described by $E_A(x, y)$ and $E_B(x, y)$ in the lens aperture plane and the fiber entrance plane. This is shown in Figure 10. The incident field takes different shapes based on the aperture geometry, refractive index, etc... The resulting change in shape of the wavefront is the product/superposition of the electric field, E_A, and the normalized complex field $F_A(x, y)$ and $F_B(x, y)$ in the lens aperture plane and the fiber entrance plane. This is shown in Figure 10. These are normalized such that:

$$\int\int_A |F_A(x, y)|^2 dxdy = 1 \tag{1}$$

This complex field is equivalent to the phase front of the wave. This is to ensure the conservation of energy. The resulting fiber coupling efficiency is the total energy loss when the incident field is formed into the field distribution of

the fundamental mode. This can be found as follows:

$$\eta = \frac{|\int\int_A E_A^*(x,y) \cdot F_A(x,y)dxdy|^2}{\int\int_A |E_A(x,y)|^2 dxdy} \tag{2}$$

Where η is the efficiency. The sources in the literature presented in Table 3 use a Gaussian/normal distribution for the fundamental fiber mode. This is an approximation of the distribution which is the result of solving the Maxwell equations. This distribution is given by:

$$F_A(x,y) = \sqrt{\frac{2}{\pi\omega_A^2}} exp(-\frac{1}{\omega_A^2}(x^2+y^2)) \tag{3}$$

Where ω_A is the mode-field radius of the fiber when backpropargated to the lens aperture plane. Similarly in the fiber plane:

$$F_B(x,y) = \sqrt{\frac{2}{\pi\omega_B^2}} exp(-\frac{1}{\omega_B^2}(x^2+y^2)) \tag{4}$$

However, this is will not be used since the backpropagated analysis is easier. This is due to the equations for a plane wave being easier to work with then Airy disks. The backpropagation of the fiber mode is done as follows:

$$\omega_A = \frac{\lambda f}{\pi\omega_B} \tag{5}$$

Where f is the focal length and ω_B is the mode field radius. The different misalignment's considered in this analysis are the lateral offsets, angular offsets and axial misplacement. All of these change the phase front of the field incident on the fiber, due to different distances that the light travels. This has to be adjusted in the complex field.

An offset changes the complex normalized field on the aperture, because of a slightly larger distance as depicted in Figure 11.

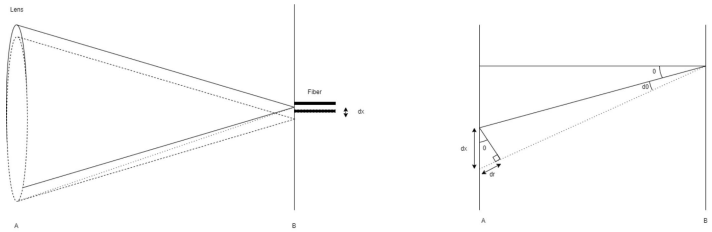

Figure 11: Geometry of a lateral offset.

The effective change in the phase front from a difference in distance traveled by the light can be found as follows:

$$\Delta\phi(t) = 2\pi\frac{t-t_0}{T} \rightarrow \Delta\phi(r) = 2\pi\left(\frac{r}{c} - \frac{r_0}{c}\right)\frac{c}{\lambda} = 2\pi\frac{\Delta r}{\lambda} \tag{6}$$

This can be described in a complex representation such that it can be multiplied as a factor to the complex field is as follows:

$$F_A(\Delta\phi(r)) = exp(j\Delta\phi) = exp\bigg(j\frac{2\pi}{\lambda}\Delta r\bigg) \tag{7}$$

A lateral offset in the x-axis will result in a path difference, derived from Figure 11, expressed as follows:

$$\frac{\Delta r}{\Delta x} = tan(\theta) = \frac{x}{f} \rightarrow \Delta r = \frac{x\Delta x}{f} \tag{8}$$

Inserting this into the formula for $\Delta\phi$:

$$F_A(\Delta\phi(x)) = exp\bigg(j\frac{2\pi}{\lambda}\frac{x\Delta x}{f}\bigg) \tag{9}$$

When this is done for both the x and y-axis, the following phase front adjustment for a lateral offset can be done:

$$F_A(\Delta\phi(x,y)) = exp\bigg(j\frac{2\pi}{\lambda f}(x\Delta x + y\Delta y)\bigg) \tag{10}$$

For a fiber tilt, the resulting complex field shifts by a distance of $-f\Delta\Phi_{[]}$ when backpropagated:

$$F_A(x,y) \rightarrow F_A(x - f\Delta\Phi_x, y - f\Delta\Phi_y) \tag{11}$$

Lastly, the axial displacement. If the axial displacement, if small compared to the focal length, the displacement can be similarly backpropagated as the mode field radius:

$$F_A(\Delta z) = exp\bigg(-j\frac{\pi\Delta z}{\lambda f^2}(x^2 + y^2)\bigg) \tag{12}$$

The resulting equation including all the offsets is as follows:

$$\begin{aligned} F_A(x,y) = \sqrt{\frac{2}{\pi\omega_A^2}} exp\bigg(-\bigg(\frac{1}{\omega_A^2} - j\frac{\pi A\Delta z}{\lambda f^2}\bigg)((x - f\Delta\Phi_x)^2 + (y - f\Delta\Phi_y)^2)\bigg) \\ exp\bigg(j\frac{2\pi}{\lambda f}((x - f\Delta\Phi_x)\Delta x + (y - f\Delta\Phi_y)\Delta y)\bigg) \end{aligned} \tag{13}$$

If the input electric field is assumed to be that of a plane wave, with amplitude 1, which is invariant over time and location in the aperture then $E_A = 1$.

The efficiency can be expressed as follows:

$$\eta = \left| \sqrt{\frac{2}{\pi\omega_A^2}} \int\int_A exp\Big(- \Big(\frac{1}{\omega_A^2} - j\frac{\pi A \Delta z}{\lambda f^2} \Big)((x - f\Delta\Phi_x)^2 + (y - f\Delta\Phi_y)^2) \Big) \right.$$
$$\left. exp\Big(j\frac{2\pi}{\lambda f}((x - f\Delta\Phi_x)\Delta x + (y - f\Delta\Phi_y)\Delta y) \Big) dxdy \right|^2 \tag{14}$$

To find the best coupling efficiency possible, the if all the misalignment's are 0, then the integral can be evaluated. The integral becomes:

$$\eta = \left| \sqrt{\frac{2}{\pi\omega_A^2}} \int\int_A exp\Big(- \Big(\frac{1}{\omega_A^2} \Big)(x^2 + y^2) \Big) dxdy \right|^2 \tag{15}$$

For this it is convenient to normalize the radius of the aperture, which because of back propagation is equivalent to the spot size, to the backpropagated fiber mode field radius:

$$\beta = \frac{R}{w_A} \tag{16}$$

The evaluated integral to the following:

$$\eta = \frac{2}{\beta^2}\Big(1 - exp\Big(- \beta^2 \Big) \Big)^2 \tag{17}$$

When considering the above equation, it can be seen that the efficiency is proportional to the ratio between the radius of the aperture as well as the backpropagated mode field radius. This is equivalent to the spot radius to mode field radius on the fiber plane. When this result is plotted with respect to this ratio, the result is depicted in Figure 12.

Figure 12 shows the effect of different spot sizes on the efficiency. It shows that very small spots are not very efficient. Increasing the spot size hence initially improves the efficiency until $\beta_0 = 1.121$. The maximum efficiency is $\eta_0 = 0.81$. This result will be compared later with the inclusion of Jitter.

Equation 14 allows the analysis of the magnitudes of the different misalignment effects. This can be best illustrated through normalization of all the parameters as follows:

$$\begin{aligned} \Delta x \rightarrow \Delta x' = \frac{\Delta x}{\omega_B} \quad \Delta y \rightarrow \Delta y' = \frac{\Delta y}{\omega_B} \quad \Delta z \rightarrow \Delta z' = \frac{\Delta z R}{f\omega_B} \\ \Delta\Phi_x \rightarrow \Delta\Phi'_x = \Delta\Phi_x \frac{f}{R} = \Delta\Phi_x \frac{N}{2}, \quad \Delta\Phi_x \rightarrow \Delta\Phi'_y = \Delta\Phi_x \frac{N}{2} \\ x \rightarrow \mu = \frac{x}{w_A} \quad y \rightarrow \nu = \frac{y}{w_A} \end{aligned} \tag{18}$$

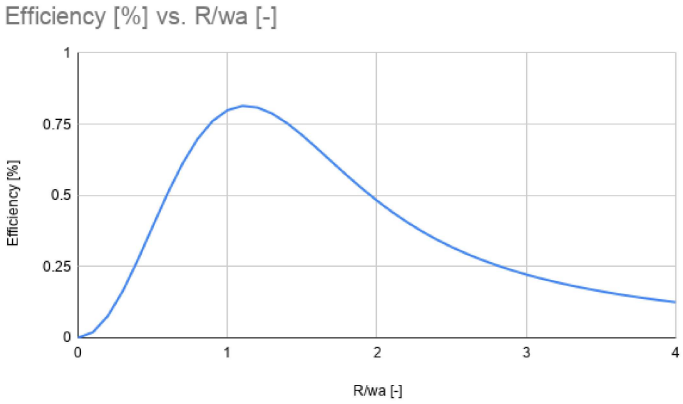

Figure 12: Depicted is the effect of spot size normalized with the mode field radius on the efficiency.

Where N is the numerical aperture. Equation 14 can hence be re-written:

$$\eta = \left| \frac{\sqrt{2}}{\pi\beta} \int\int exp\Big(- \left(\frac{1}{\omega_A^2} - j\frac{\pi A \Delta z}{\lambda f^2} \right) ((x - f\Delta\Phi_x)^2 + (y - f\Delta\Phi_y)^2) \Big) \right. \\ \left. exp\left(j\frac{2\pi}{\lambda f}((x - f\Delta\Phi_x)\Delta x + (y - f\Delta\Phi_y)\Delta y) \right) dxdy \right|^2 \tag{19}$$

Considering the lateral offsets, the misalignment laterally is divided by the mode field radius when normalized, which is a very small number for typical single mode fibers. See:

$$\frac{\Delta x}{\omega_B}, \quad \frac{\Delta y}{\omega_B} \tag{20}$$

This causes the effects of such misalignment's to be very critical. Hence, the tolerance of lateral misalignment's is very low. Oswald Wallner, Pater J. Winzer, Walter R. Leeb[41] show that a misalignment of the optimal spot size by 80% of the mode field radius already decreases the efficiency by 50% of η_0.

However, the spot sizes above β_0 has a beneficial effect on the coupling efficiency for larger misalignment's. This is because the larger spot overlaps for larger misalignment's purely because of the larger radius. This will later be exploited to find other optimal spot sizes for jitter and bias errors.

The angle misalignment tolerance is dependent on the numerical aperture. This numerical aperture would need to be large. For small numerical apertures and small misalignment angles this tolerance higher compared to the lateral tolerance. For example, a numerical aperture of 0.4 with a 11.5 degrees misalignment results in a 24% loss compared to η_0. Knowing this, the tolerance for

the angle will likely be multiple orders of magnitude smaller when the system is set up, implying that this is not an important design aspect. However, here too the larger spots are more optimal for larger angle misalignment's.

The axial misalignment is also tolerant compared to the lateral misalignment tolerances. This is because $\Delta z'$ is divided by the square of focal length. This implies that when this offset is less then 10% of the focal length, it has a negligible effect on the coupling performances.

Hence, considering that the only critical tolerances are the lateral tolerances, these will be analyzed further.

4.1.2 The Effect of Jitter on Fiber Coupling Efficiencies

The work of both Jing Ma, Fang Zhao, Liying Tan, Siyuan Yu, Qiqi Han[16] and Morio Toyoshima[38] describe the same principles. However, the work by Jing Ma, Fang Zhao, Liying Tan, Siyuan Yu, Qiqi Han[16] is used here because it too uses the principle of backpropagation and is hence easier to use. First the effect of jitter will be found, after which the addition of a bias angle will be investigated. The results from this will be a reflection and a discussion on the spot size. In this analysis, only the lateral offset will be considered, as this is has been found to be the most critical in subsubsection 4.1.1. The situation is hence as shown in Figure 13.

Jitter can be understood to be the same as the definition given by Jing Ma et. all.[16]:

> "Random angular jitter refers to the uncertainty of the instantaneous direction of the received optic axis with respect to a nominal axis of the fiber." - Jing Ma, Fang Zhao, Liying Tan, Siyuan Yu, Qiqi Han[16], page 2 first paragraph section 2 B.

The jitter it self however is not necessarily an uncertainty since it can be measured as a random motion around an optical axis. However, the motion cannot be predicted and hence its time varying magnitude will be modeled as a probability distribution. The probability density function of jitter without bias error can be modeled as a normal distribution pdf around the optical axis:

$$f(\theta) = \frac{\theta}{\sigma^2} exp\left(- \frac{\theta^2}{2\sigma^2} \right) \tag{21}$$

Where θ is the random jitter angle. This leads to a random lateral offset normal pdf:

$$f(\Delta r) = \frac{\Delta r}{\sigma^2} exp\left(- \frac{\Delta r^2}{2\sigma^2} \right) \tag{22}$$

The complex backpropagated fiber mode, as discussed in subsubsection 4.1.1,

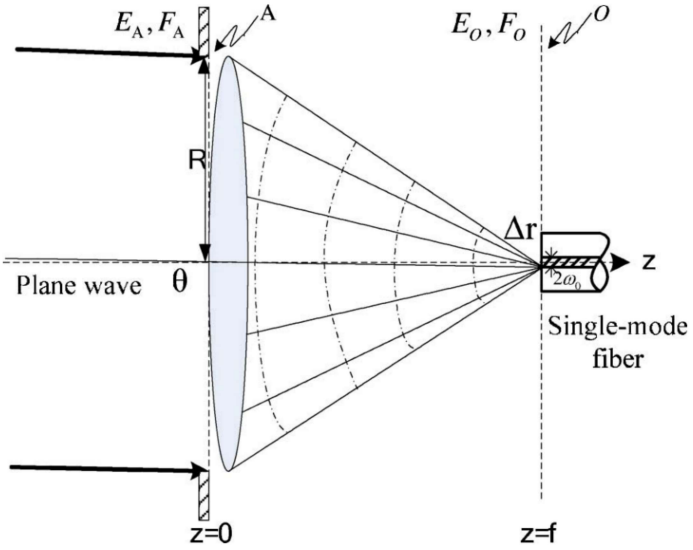

Figure 13: Coupling geometry as depicted in the work by Jing Ma, Fang Zhao, Liying Tan, Siyuan Yu, Qiqi Han[16] on page 2, Fig. 1 (note that the O is referred to in this text as B). As can be seen, it is similar to the depiction by Oswald Wallner, Pater J. Winzer, Walter R. Leeb[41] shown in Figure 10, however the axial misalignment is not considered in this analysis and is hence not depicted. Instead, the fiber plane is at the focal length from the aperture plane of the lens. The image further depicts a plane wave incident at a random angle on to the aperture plane at z=0. This causes a lateral misalignment on the fiber coupling plane of Δr.

is the mode field depicted in Equation 3 multiplied with the lateral offset correction in Equation 12:

$$F_A(r) = \sqrt{\frac{2}{\pi\omega_A^2}} exp\Big(- \frac{r^2}{\omega_A^2}\Big) exp\Big(j\frac{2\pi}{\lambda f}(x\Delta x + y\Delta y)\Big) \tag{23}$$

To unify the variables, the identities for $x = rcos(\theta)$, $\Delta x = \Delta rcos(\Omega)$, $y = rsin(\theta)$ and $\Delta y = \Delta rsin(\Omega)$. Where, in this case the angle of the offset vector, Δr, relative to the x-axis is Ω.

$$x\Delta x + y\Delta y = r\Delta rcos(\theta)cos(\Omega) + r\Delta rsin(\theta)sin(\Omega) = cos(\theta - \Omega)r\Delta r \tag{24}$$

The fiber mode can be rewritten as follows:

$$F_A(r) = \sqrt{\frac{2}{\pi\omega_A^2}} exp\Big(- \frac{r^2}{\omega_A^2}\Big) exp\Big(j\frac{2\pi}{\lambda f} cos(\theta - \Omega)r\Delta r\Big) \tag{25}$$

The efficiency at any point in time cannot be predicted. Hence, an average/expected efficiency can be produced. This can be done as follows:

$$\langle \eta \rangle = \frac{\langle | \int \int_A E_A(r,\theta) F_A(r,\theta,\Omega) r dr d\theta |^2 \rangle}{\langle \int \int_A |E_A(r,\theta)|^2 r dr d\theta \rangle} \tag{26}$$

Where $\langle ... \rangle$ is the average or expected value of a parameter. This can be found by multiplying the expression inside the integral in the numerator by the jitter pdf:

$$\langle \eta \rangle = \frac{| \int \int_A \int_0^\infty E_A(r,\theta) F_A(r,\theta,\Omega) f(\Delta r) r d\Delta r dr d\theta |^2}{\langle \int \int_A |E_A(r,\theta)|^2 r dr d\theta \rangle} \tag{27}$$

Similarly as in subsubsection 4.1.1, the plane wave assumption results in $E_A(r) = 1$ over time. The integral in the denominator is then:

$$\langle \int \int_A |E_A(r,\theta)|^2 r dr d\theta \rangle = \int_0^{2\pi} \int_0^R r dr d\theta = \pi R^2 \tag{28}$$

Hence, through substitution the following is found:

$$\begin{aligned} \langle \eta \rangle = \frac{1}{\pi R^2} \Bigg| \int \int_A \int_0^\infty \sqrt{\frac{2}{\pi \omega_A^2}} exp\Big(- \frac{r^2}{\omega_A^2} \Big) exp\Big(j \frac{2\pi}{\lambda f} cos(\theta - \Omega) r \Delta r \Big) \\ \frac{\Delta r}{\sigma^2} exp\Big(- \frac{\Delta r^2}{2\sigma^2} \Big) r d\Delta r dr d\theta \Bigg|^2 \end{aligned} \tag{29}$$

The expression can be separated and put differently as follows:

$$\begin{aligned} \langle \eta \rangle = \frac{1}{\pi R^2} \Bigg| \sqrt{\frac{2}{\pi \omega_A^2}} \int_0^R r exp\Big(- \frac{r^2}{\omega_A^2} \Big) \\ \int_0^\infty \frac{\Delta r}{\sigma^2} exp\Big(- \frac{\Delta r^2}{2\sigma^2} \Big) \int_0^{2\pi} exp\Big(j \frac{2\pi}{\lambda f} cos(\theta - \Omega) r \Delta r \Big) d\theta d\Delta r dr \Bigg|^2 \end{aligned} \tag{30}$$

The integral considering the angle θ is the same as for Bessel functions of the first kind and 0th order:

$$J_0(x) = \frac{1}{2\pi} \int_0^\infty exp(-jxcos(\theta)) d\theta \tag{31}$$

This allows the simplification, when considering the offset of angle due to the jitter, Ω, is assumed 0 because Δr is in the same direction as the offset (note the multiplication with 2π:

$$\langle \eta \rangle = \frac{8}{R^2 \omega_A^2} \Bigg| \int_0^R r exp\Big(- \frac{r^2}{\omega_A^2} \Big) \int_0^\infty \frac{\Delta r}{\sigma^2} exp\Big(- \frac{\Delta r^2}{2\sigma^2} \Big) J_0\Big(\frac{2\pi}{\lambda f} r \Delta r \Big) d\Delta r dr \Bigg|^2 \tag{32}$$

A second standard integral can be used for the integral regarding Δr:

$$\int_0^\infty xexp(-\alpha x^2)I_\nu(\beta x)J_\nu(\gamma x)dx = \frac{1}{2\alpha}exp\left(\frac{\beta^2-\gamma^2}{4\alpha}\right)J_\nu\left(\frac{\gamma\beta}{2\alpha}\right) \tag{33}$$

When used for $x = \Delta r$, $\alpha = 1/(2\sigma^2)$, $\beta = 0$ (note: not the same β as the field mode normalized radius) and $\gamma = (2\pi/(\lambda f))r$ this results in:

$$\langle\eta\rangle = \frac{8}{R^2\omega_A^2}\left|\int_0^R rexp\left(\left(-\frac{2\pi^2\sigma^2}{\lambda^2 f^2}-\frac{1}{\omega_a^2}\right)r^2\right)dr\right|^2 \tag{34}$$

Introducing $\beta = R/\omega_A$ the result of the integral is as follows:

$$\langle\eta\rangle = \frac{2}{\left(2\left(\frac{\sigma}{\omega_B}\right)^2+1\right)^2\beta^2}\left(1-exp\left(-\left(1+\left(\frac{\sigma}{\omega_B}\right)^2\right)\beta^2\right)\right)^2 \tag{35}$$

There are hence 2 parameters normalized with respect to the mode field radius important when considering the expected efficiency. These are the standard deviation and the aperture/spot radius. Considering that in a system the only design parameter in this case would be β. The optimum β for a given ω_A and σ can be found by differentiating the equation with respect to β and setting it to 0:

$$\frac{d\langle\eta\rangle}{d\beta} = \left(2\left(\left(\frac{\sigma}{\omega_B}\right)^2+1\right)\beta_{opt}^2+1\right)exp\left(-\left(\left(\frac{\sigma}{\omega_B}\right)^2+1\right)\beta_{opt}^2\right)-1=0 \tag{36}$$

When re-arranged:

$$\beta_{opt} = \sqrt{\frac{1.2564}{\frac{2\sigma^2}{\omega_B^2}+1}} \tag{37}$$

When this is substituted back into Equation 35 the highest efficiency in the presence of jitter can be found:

$$\langle\eta_{max}\rangle = 0.8145\frac{1}{\frac{2\sigma^2}{\omega_B^2}+1} \tag{38}$$

There equations are plotted in Figure 14 and Figure 15. As can be seen in Figure 14, β_{opt} decreases as the jitter (which is proportional to σ) increases. This implies that the relative radius of the aperture decreases and as a result the spot size increases for a higher coupling performance for larger jitter. This is because a larger spot spread implies a higher intensity for a randomly selected point for a larger given area. In layman terms, this is because with a larger spot it is easier to hit the small fiber target.

However, the efficiency also decreases as a result of worse overlap between F_B and E_B or equivalently F_A and E_A. This can be seen in Figure 15. Hence, minimization of this jitter through active optics would be enviable.

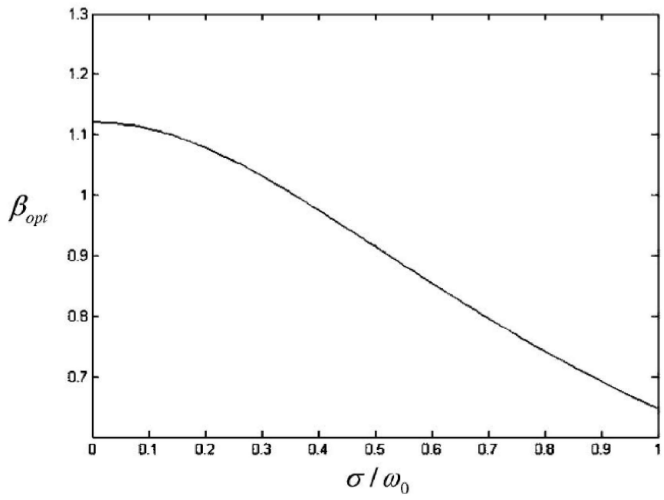

Figure 14: This graph shows the optimal β with respect to the normalized jitter. It shows that the optimal β decreases with increased jitter, indicating that larger spots on the fiber coupling plane improve the fiber coupling performance. Taken from the work by Jing Ma et all.[16], page 5187 Fig 5.

4.1.3 The Effect of Jitter from Atmospheric Turbulence on Fiber Coupling Efficiencies

Jitter can result from multiple sources. These can be on board, due to rotating objects such as CMGs and reaction wheels. Outside sources can be, for example, the atmosphere. Here an analysis of the effects of atmospheric turbulence is done. Here, an analysis will be done to see if this jitter is significant to the fiber coupling efficiency.

Here the work by Yamaç Dikmelik and Frederic M Davidson[10] is used, however the varaibles have been changed to fit the rest of the report. Yamaç Dikmelik and Frederic M Davidson[10] use the mutual coherence of the light passing through the atmosphere to model the jitter effect. The efficiency was adjusted to consider the average power focused on the fiber denoted by $\langle \cdot \rangle$:

$$\langle \eta \rangle = \frac{\langle | \int U_B(\mathbf{r}) F_B(\mathbf{r}) d\mathbf{r}|^2 \rangle}{\langle \int |U_B(\mathbf{r})|^2 d\mathbf{r} \rangle} = \frac{P_c}{P_A} \tag{39}$$

In this case, $U_B(\mathbf{r})$ and $F_B(\mathbf{r})$ are fields incident and in the normalized fiber profile respectively. Furthermore, P_c is the power coupled into the fiber and P_A the incident power on it. The vectors allows the exploitation of the vector identifies to produce a mutual coherence function. In this case, this will present

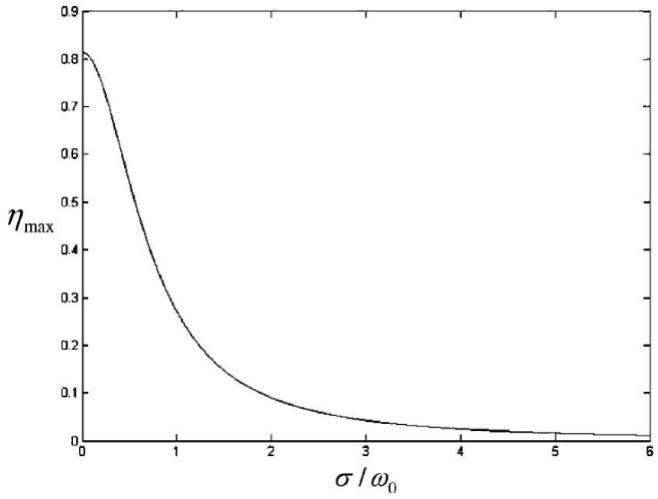

Figure 15: This graph shows the maximum coupling efficiency, η, with respect to the normalized jitter. It shows that the optimal η decreases with increased jitter, indicating that regardless of optimized spots the efficiency falls. Taken from the work by Jing Ma et all.[16], page 5187 Fig 6.

it self once the equation is re-written exploiting vector algebra:

$$\eta_c = \frac{1}{\langle P_A \rangle} \int \int_A \Gamma_i(\mathbf{r}_1, \mathbf{r_2}) F_B^*(\mathbf{r_1}) F_B(\mathbf{r_2}) d\mathbf{r_1} d\mathbf{r_2} \tag{40}$$

In this case, $\Gamma_i(\mathbf{r}_1, \mathbf{r_2}) = \langle U_B(\mathbf{r}) U_B^*(\mathbf{r}) \rangle$ is the mutual coherence function which is distorted by atmospheric turbulence. In this case, Dikmelik and Davidson chose to simulate a weak turbulence and assumed a Kolmogorov power-law spectrum:

$$\Gamma_i(\mathbf{r}_1, \mathbf{r_2}) = I_i exp(-1.46 C_n^2 k^2 L |\mathbf{r_1} - \mathbf{r_2}|^{\frac{5}{3}}) \tag{41}$$

This distribution is approximated to be equal to a Gaussian spatial dependence, which is easier to process and is used often:

$$\begin{aligned} \Gamma_i(\mathbf{r}_1, \mathbf{r_2}) &= I_i exp\bigg(- \frac{|\mathbf{r_1} - \mathbf{r_2}|^2}{((1.46 C_n^2 k^2 L)^{\frac{-3}{5}})^2} \bigg) \\ &= I_i exp\bigg(- \frac{|\mathbf{r_1} - \mathbf{r_2}|^2}{\rho_c^2} \bigg) \end{aligned} \tag{42}$$

Here the approximation is $3/5 \approx 2$. The complex field on the fiber, F_B, is

presented as follows:

$$F_B(\mathbf{r}) = \frac{kW_m}{\sqrt{2\pi}f} exp\bigg(- \bigg(\frac{kW_m}{2f}\bigg)^2 r^2 \bigg) \tag{43}$$

Where k is the wave number, W_m is the fiber-mode field radius and f the focal length. This is equivalent to the complex fields used before. This results in the following:

$$\begin{aligned} \eta_c = \frac{2\pi W_m^2}{(\lambda f)^2 A_R} \int_0^{D_R/2} \int_0^{D_R/2} \int_0^{2\pi} \int_0^{2\pi} exp\bigg(- \bigg(\frac{\pi W_m}{\lambda}\bigg)^2 (r1^2 + r_2^2) \bigg) \\ exp\bigg(- \frac{|\mathbf{r_1} - \mathbf{r_2}|^2}{\rho_c^2} \bigg) r_1 r_2 d\theta_1 d\theta_2 dr_1 dr_2 \end{aligned} \tag{44}$$

Where D_R is the diameter of the aperture and $A_R = \pi D_R^2/4 = \pi R^2$ is the area of the aperture. Understanding the cosine rule:

$$|\mathbf{r_1} - \mathbf{r_2}|^2 = r_1^2 + r_2^2 - 2r_1 r_2 cos(\theta_1 - \theta_2) \tag{45}$$

All the integrals regarding θ can be simplified:

$$I = \int_0^{2\pi} \int_0^{2\pi} exp\bigg(- \frac{r_1^2 + r_2^2 - 2r_1 r_2 cos(\theta_1 - \theta_2)}{\rho_c^2} \bigg) d\theta_1 d\theta_2 \tag{46}$$

Changing variables to $\theta_d = \theta_1 - \theta_2$ and $\theta = \theta_2$. The variable θ_d is only meaning full when in the range of $0 - \pi$ when considering vectors and the Jacobian is 2:

$$\begin{aligned} I &= 2 \int_0^{2\pi} \int_0^{\pi} exp\bigg(- \frac{r_1^2 + r_2^2 - 2r_1 r_2 cos(\theta_d)}{\rho_c^2} \bigg) d\theta_d d\theta \\ &= 4\pi \int_0^{\pi} exp\bigg(- \frac{r_1^2 + r_2^2 - 2r_1 r_2 cos(\theta_d)}{\rho_c^2} \bigg) d\theta_d \\ &= \pi exp\bigg(- \frac{A_R}{A_C}(x_1^2 + x_2^2) \bigg) I_0\bigg(2\frac{A_R}{A_C} x_1 x_2 \bigg) \end{aligned} \tag{47}$$

Note that the same standard integrals where used in the previous section. However, the radii where normalized to $x_1 = 2r_1/D_R$ and $x_2 = 2r_2/D_R$. After evaluation and normalization of $a = D_R \pi W_m/(2\lambda f)$, the results in:

$$\eta_c = 8a^2 \int_0^1 \int_0^1 exp\bigg(- \bigg(a^2 + \frac{A_R}{A_C}\bigg)(x_1^2 + x_2^2) \bigg) I_0\bigg(2\frac{A_R}{A_C} x_1 x_2 \bigg) x_1 x_2 dx_1 dx_2 \tag{48}$$

Where in this case, x_1 and x_2 are the normalized radial integration variables to for the receiver and lens radius respectively. A_R and A_C are the being the receiver area and spatial coherence area and the ratio between the two

indicate the number of speckles and their size. Lastly, the coupling geometry $a = \frac{D_R \pi W_m}{2\lambda f}$. The fiber coupling efficiency hence depends on the number of speckles and the coupling geometry. When the equation is numerically evaluated, the following results are reported:

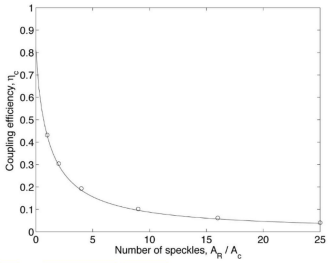

Fig. 2. Fiber-coupling efficiency as a function of the number of speckles A_R/A_C over the receiver aperture. The coupling-geometry parameter $a = 1.12$ for the curve. The circles represent the maximum coupling efficiency that can be obtained by optimizing a for six different values of A_R/A_C.

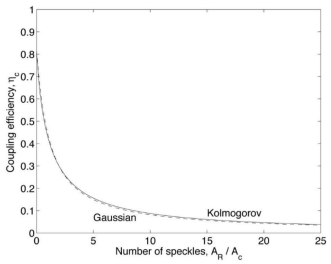

Fig. 3. Fiber-coupling efficiency as a function of the number of speckles A_R/A_C over the receiver aperture for $a = 1.12$. The two curves are obtained by using the mutual coherence function for the Kolmogorov spectrum (solid curve) and the Gaussian approximation to the mutual coherence function (dashed curve).

Figure 16: 2 graphs from Dikmelik and Davidson on page 4[10]. The results show that increasing number of speckles severely limit the efficiency of the fiber coupling for a given coupling geometry. The maximum efficiency of 0.81 can be reached with a = 1.12 with no speckles. Improvement in "a"/coupling geometry results in the circles shown in "Fig. 2". It shows that a change in geometry in this case changes very little. "Fig. 3" shows the effect of the Gaussian assumption instead of the Kolmogorov for the turbulence spectrum. It shows that the performance is close to one another.

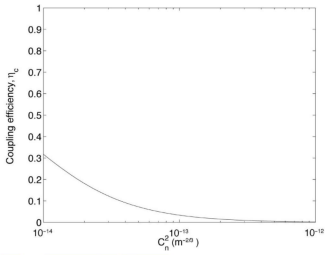

Fig. 4. Fiber-coupling efficiency as a function of C_n^2 for a link distance of 1 km, where $D_R = 10$ cm, $a = 1.12$, and $\lambda = 1.55$ μm.

Figure 17: A graph from Dikmelik and Davidson on page 5[10]. This shows the coupling efficiency depending on the turbulence strength (C_n^2) of the system in the same configuration as in Figure 16. It shows that even for moderate turbulence, the efficiency rapidly falls.

From the evaluations by Dikmelik and Davidson[10], it is clear that turbulence strongly effects the coupling efficiency of the system. Hence, mitigation of this effect is required.

4.1.4 The effect of Bias Pointing Errors on Fiber Coupling Efficiencies

The work of Jing Ma, Fang Zhao, Liying Tan, Siyuan Yu, Qiqi Han[16] includes an analysis of a bias angle. This builds off from the analysis on jitter, explained in subsubsection 4.1.2. This will be modeled by adjusting the normal distribution of jitter to be offset in a 2D plane from the optical axis. This is done through a Nakagami-Rice distribution when in 2D:

$$f(\Delta r, r_0) = \frac{\Delta r}{\sigma^2} exp\Big(- \frac{\Delta r^2 + r_0^2}{2\sigma^2}\Big) I_0\Big(\frac{\Delta r}{\sigma^2}, \frac{r_0}{\sigma^2}\Big) \tag{49}$$

Where I_0 is the modified Bessel function of the first kind and r_0 is the bias error. The resulting coupling efficiency is as follows:

$$\langle \eta \rangle = \frac{1}{\pi R^2}\Big|\sqrt{\frac{2}{\pi\omega_A^2}}\int_0^R r exp\Big(- \frac{r^2}{\omega_A^2}\Big)\int_0^\infty \frac{\Delta r}{\sigma^2} exp\Big(- \frac{\Delta r^2}{2\sigma^2}\Big) I_0\Big(\frac{\Delta r}{\sigma^2}, \frac{r_0}{\sigma^2}\Big) \int_0^{2\pi} exp\Big(j\frac{2\pi}{\lambda f} cos(\theta - \Omega) r\Delta r\Big) d\theta d\Delta r dr\Big|^2 \tag{50}$$

Using the identities:

$$J_0(x) = \frac{1}{2\pi}\int_0^\infty exp(-jxcos(\theta))d\theta \tag{51}$$

$$\int_0^\infty x exp(-\alpha x^2) I_\nu(\beta x) J_\nu(\gamma x) dx = \frac{1}{2\alpha} exp\Big(\frac{\beta^2 - \gamma^2}{4\alpha}\Big) J_\nu\Big(\frac{\gamma\beta}{2\alpha}\Big) \tag{52}$$

The above equation can be evaluated to the following:

$$\langle \eta \rangle = \frac{8}{R^2 w_A^2}\Big|\int_0^R exp\Big(\Big(- \frac{2\pi^2\sigma^2}{\lambda^2 f^2} - \frac{1}{\omega_A^2}\Big) r^2\Big) J_0\Big(\frac{2\pi}{\lambda f} r_0 r\Big) r dr\Big|^2 \tag{53}$$

Normalizing the radial position as $\rho = r/R$ and substituting β:

$$\langle \eta \rangle = 8\beta^2\Big|\int_0^1 exp\Big(- \beta^2\Big(2\Big(\frac{\sigma}{\omega_B}\Big)^2 + 1\Big)\rho^2\Big) J_0\Big(2\frac{r_0}{\omega_B}\beta\rho\Big)\rho d\rho\Big|^2 \tag{54}$$

This integral cannot be analytically solved. However, Jing Ma et. all.[16] has solved this equation for the optimum β. The results are shown in Figure 18 and Figure 19.

Considering Figure 18, it is clear that the same rule applies to offsets from the lens and fiber misalignment with or without jitter as discussed in subsubsection 4.1.1 and subsubsection 4.1.2. The larger the offset the smaller the optimum

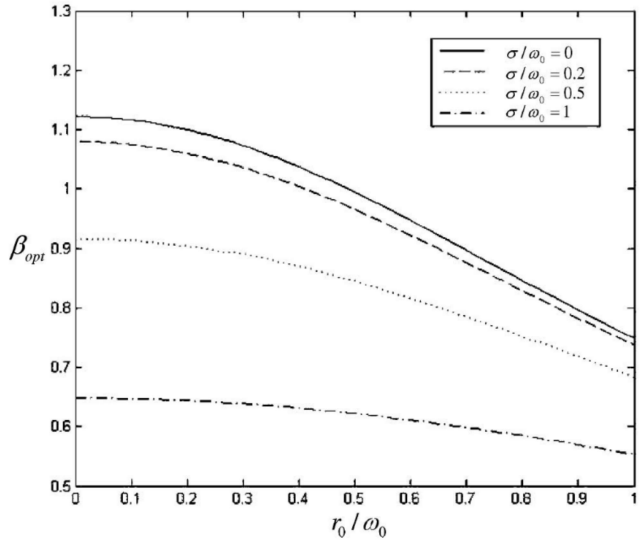

Figure 18: Optimum β (normalized aperture radius) for different normalized bias errors r_0/ω_B.

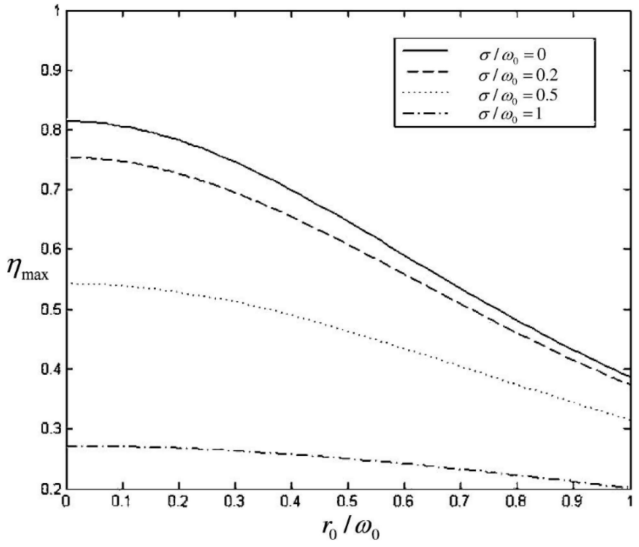

Figure 19: Optimized η (coupling efficiency) through use of optimized β (normalized aperture radius) for different normalized bias errors r_0/ω_B.

β, implying that the aperture is smaller and hence the spot on the fiber plane

is larger. The variation of β_{opt} is smaller for larger jitters, implying that the jitter is the dominant factor driving the spot size and not the bias error.

Figure 19 shows that the effect of offsets when a large jitter is present is smaller. The effect of jitter on the efficiency decreases the critical nature of the offset. This is due to the jitter being the dominant detriment to the coupling performance implying the spot size is driven by this aspect more then the offset.

The conclusion of the analysis of jitters and offsets is that these are an important factor in the fiber coupling efficiency. The overall system performance and link budget is hence dependent on the system being able to correct for this.

4.1.5 Mitigation Techniques for Pointing Offset and Jitter to Improve Fiber Coupling Performance

The previous subsubsections have discussed in detail as to the critical nature of jitter and offsets on the fiber coupling performance. There are some proposed methods to improve the performance of fiber coupling. These include both active and passive measures which allow for increasing the fiber aperture as well as correction of the offsets and jitters.

A passive measure proposed by Oswald Wallner, Peter J. Winzer and Walter R. Leeb[41] is the use of a GRIN-lenses (GRadient-INdex) as shown in Figure 20. GRIN-lenses are lenses which have a refraction index gradient that focuses the incoming light. The use of this lens magnifies/artificially increases the fiber mode radius. This has beneficial effects on the lateral offset and axis tolerances however comes at a cost of the angular offset tolerance and increased system side due to increased focal length.

The inclusion of a GRIN lens increases the workable fiber mode field radius by a factor $A = \omega_C/\omega_B$. The effects on the system can be seen in β and the focal length f:

$$f_C = Af \tag{55}$$

$$\begin{aligned} \beta &= \frac{\pi R\omega_c}{\lambda f_c} = \frac{\pi RA\omega}{\lambda A f_c} \\ &= \frac{\pi R\omega}{\lambda f} \end{aligned} \tag{56}$$

The system size is hence larger by a factor A while the optimal normalized aperture size has not changed. This implies that the spot size can be larger for the same performance. This is because the normalized lateral offset tolerance remains the same implying the total offset can be larger by a factor A. The axial offset is in fact increased by a factor A^2 due to it being inversely related to both the focal length and the mode field radius:

$$\Delta x' = \frac{\Delta x}{\omega_C} = \frac{\Delta x}{A\omega}, \quad \Delta z' = \Delta z \frac{R}{f_c \omega_C} = \Delta z \frac{R}{A^2 f \omega} \tag{57}$$

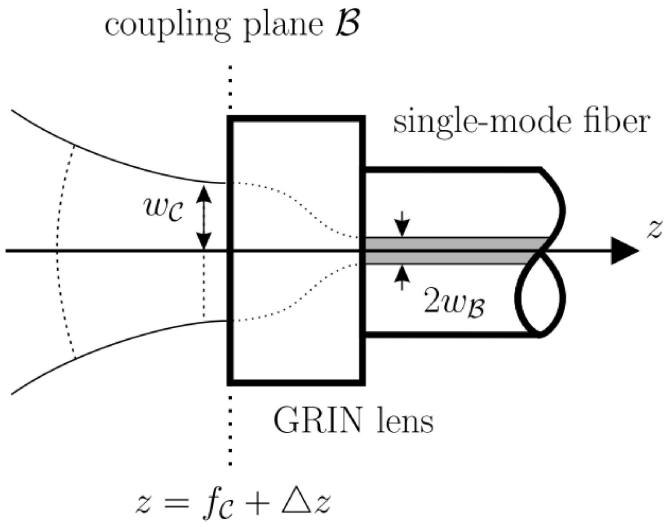

Figure 20: Illustration of fiber coupling using a GRIN lens. Figure is the work from Oswald Wallner, Peter J. Winzer and Walter R. Leeb[41], page 24, figure 6.

Note that the tolerance for the y-axis behaves in the same way as the x-axis. While the angular tolerance decreases by a factor A due to the focal length being increased with a factor A:

$$\Delta\Phi'_x = \Delta\Phi_x \frac{f_C}{R} = \Delta\Phi_x \frac{Af}{R} \tag{58}$$

Note that the angular offset for the y-axis behaves the same as the x-axis. The conclusions in subsubsection 4.1.1 note that the tolerance in the angular misalignment is not as critical as the lateral offset. Hence, the use of such GRIN-lens is justified. However, the stability of a mechanical system decreases with size as well as its SWaP friendliness. Hence, the incorporation of such lenses is not always beneficial. The use of this lens in combination with active correction of jitter and offset can be beneficial for both increasing coupling performance as well as maintaining SWaP attractiveness. Furthemore, the availability and use of so called "GRIN-lens fiber-pigtailed collimators" is very high and hence a COTS component can be procured easily to fit the system.

Yamaç Dikmelik and Frederic M. Davidson[10] propose a potential solution which does not suffer from increased focal lengths. The proposed solution is a coherent fiber array, which is in effect multiple fibers packed in a large circle, as depicted in. This has the advantage of increasing the aperture size, which in turn allows larger spots, offsets and jitter. At the same time, it allows for correction of the phase of each subaperture/fiber separately, implying higher

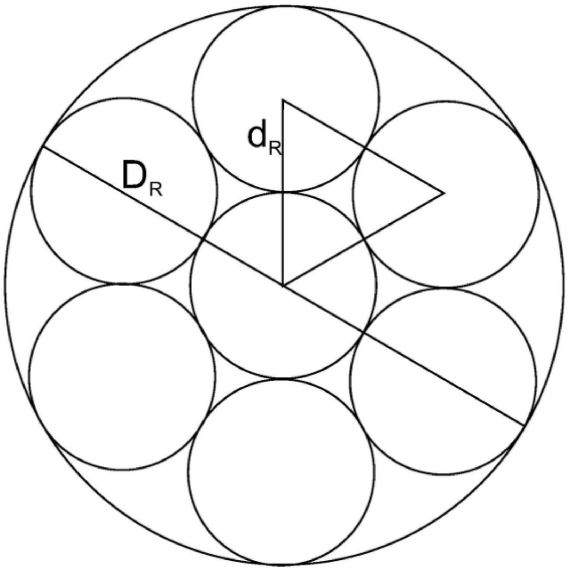

Figure 21: 7 fibers packed in the closest way as a hexagonal coherent fiber array with the larger circle being the new aperture diameter. Image taken from the work of Yamaç Dikmelik and Frederic M. Davidson[10] on page 4951, Fig. 6.

order adaptive optics can be performed in phase distortions below the aperture. Lastly, the sub-aperture phase distortions of 1/3 of the aperture are removed from each fiber implying that the quality of the light in the fiber is improved. This implies that stronger turbulence or jitter can be tolerated for the same performance while improving the requirements of an adaptive optics system or even removing it all together.

However, there are some drawbacks as well. For example, the space between the fibers are unused. This leads to an aperture area loss of 1/3 and hence available light intensity coupled into the fiber decreases by 1/3. Therefore, this solution would only be an improvement once the effects of jitter and offset decreases the coupling performance by at least 1/3, however likely more. Furthermore, there is additional complexity and SWaP costs of this design with the inclusion of a device which can correct the phases and coherently couple all the fibers. Lastly, the use of GRIN lenses for such a system is less COTS. The use of this solution is hence not necessarily advantageous.

Finally, the use of active optical correction or Adaptive Optics (AO) for jitter and offset is a very attractive option. There are a few ways to correct for jitter and offset. Turbulence mittigation in astronomy and ground stations for optical communications Deformable Mirrors (DMs) and Fast Steering Mirrors (FSMs) are able to correct for turbulence induced effects. For weak turbulence, FSMs

generate the most gain, while for stronger turbulence DMs are used as well. This is because strong turbulence causes large phase distortions in the wavefront and requires sub-aperture correction. Potentially, Reflective Modulators (RMs) could also correct phase as well as steer the beam. Lastly the use of Coherent Fiber Arrays (CFAs) can also help correct phase and pointing as well as generate multiple fiber apertures to couple into for a larger target, as discussed before.

Some problems arise when considering the multi-beam aspect of the system. This is because each beam has a separate target and the resulting beam from each target travels through a different part of the atmosphere. As a result, a separate FSM, DM, RM and/or CFA in combination with a wavefront sensor (WFS) would be required for each target, reducing its scale-ability. An array of FSMs could be replaced with a discrete DM/micro MEMS mirror array. However, to correct the wavefront for strong turbulence using a DM and WFS for each target would still meet the SWaP limits very quickly. This too can be said about the RMs and CFAs.

This problem can be solved by correcting and pre-correcting the signal on ground targets. This is discussed in more detail in later sections, however it relies on the principle that the ground station or target has subapperture wavefront correction capabilities. The principle uses the fact that light travels orders of magnitudes quicker then the changing air column and the signal up to the satellite and down form the satellite also travel through roughly the same air column. The correction of the incoming signal can hence be used to correct the outgoing signal at the same time. This removes the need for AO for subaperture wavefront correction in space. On top of this, the signals from other satellites in space will have no wavefront distortion from the atmosphere, implying that it is only a requirement for ground terminals.

Requiring ground stations to perform most wavefront corrections for atmospheric turbulence could be beneficial due to them having less SWaP limitations compared to satellites. However, some targets, such as airborne targets like UAV targets, can be negatively affected by this requirement.

4.1.6 Fiber Coupling Requirements for Multi-beam Optical Communication System in Space

To define if the system can sufficiently couple the signal into the fiber, it must meet the fiber coupling requirements. This subsubsection will discuss and distill these requirements. In order to allow design freedom, these requirements will be given in terms of normalized values where possible. The requirements will be given the designation of PS-FC-xxx, where PS stands for Pointing System and FC for Fiber Coupling.

The first, the angular misalignment will be considered. As has been discussed before in subsubsection 4.1.1, the fiber angular misalignment is not a critical parameter compared to the lateral misalignment. This is mainly because 0.2 rad or 11.2 deg for normalized angular misalignment of the fiber. Hence, if this parameter is sufficiently small, the effect of fiber misalignment can be ignored all together. From the analysis in subsubsection 4.1.1, the normalized angular

misalignment must be smaller then 0.1 for 95+% efficiency. With a safety factor of 2 the requirement shall be the following:

PS-FC-001: The normalized angular fiber misalignment, expressed as $\Delta\Phi' = \Delta\Phi f/R$, shall be less then 0.05.

During the production of the system or experimental setup, measuring systems are likely more then capable of meeting these requirements.

The axial misalignment is also not critical either as long as it is small compared to the focal length. Small in this case has to be defined. Oswald Wallner, Peter J. Winzer and Walter R. Leeb[41] claim that a normalized offset of 3 translates to a loss of 50%. If the axial normalized misalignment is less then 0.001 then the effect should be negligible. Hence, the requirement shall be:

PS-FC-002: The normalized axial misalignment, expressed as $\Delta z' = \Delta z R/(f\omega_B)$, shall be less then 0.001.

With laser rangers this can likely be achieved.

The major concern in the case of fiber coupling is the lateral offset. Taking an often used cut-off point of -3dB as considered signal lost. For this to be the case, for an optimum β this occurs at a normalized lateral offset of 0.35. Hence the requirement shall be:

PS-FC-003: The normalized lateral misalignment, expressed as $\Delta x' = \Delta x/\omega_B$, shall not be less then 0.35.

4.1.7 Conclusion on Fiber Coupling

Fiber coupling efficiency has significant effect on the signal power and hence data capacity of a link. The coupling of the signal into the fiber, which is common among optical receivers, is hence important to have the maximum efficiency possible. It is found that the geometry of the coupling system, pointing offset and jitter of the received beam are important factors. To reduce pointing offset, a number of passive and active adjustments to the systems can be performed to increase resilience to offsets and jitter. However, practicality and compatibility will have to be considered.

4.2 Optical Amplifiers

This section shall discuss optical amplifies and the effects of the space environment on their performance. In previous designs, a common design choice is the use of fiber optical amplifiers. Here, this will be mainly focused on as well. These have the advantage of having good efficiency as well as compact and light hardware which can be Commercial Of The Shelf (COTS).

Table 4: Literature overview on optical amplifiers and their performance in space.

Literature overview optical amplifiers			
Title	Date	Authors & Reference	Content Summary
Radiation-induced coloring of erbium-doped optical fibers	1993	Glen M. Williams, Martin A. Putnam, Charles G. Askins, Michael E. Gingerich, E. Joseph Friebele[43]	This paper discusses the effects of radiation on the coloring of Erbium-doped optical fibers. The paper explains some problems which occur when the fiber is exposed to radiation. namely, The coloring of the Erbium-doped fibers affects their performance. The parasitic darkening decreases the signal and pump intensities. Furthermore, ionized radiation can reduce the number of Erbium ions in the fiber decreasing its effectiveness. Lastly, the energy transition energies can be altered. The paper concludes that the parasitic loss is the dominant factor which affects performance of the fiber amplifier. This paper furthermore presents a simple model where the length of the fibers and the wavelength(s) of the light are used to find the overall amplification of a small signal. In this formula it is shown that 1480 nm is less affected by length and radiation then shorter 800 nm and 900 nm wavelengths. It was also found that the losses decreased again after a waiting period implying a recovery from radiation.

Literature overview optical amplifiers Continued			
Title	Date	Authors & Reference	Content Summary
A Model for the Prediction of EDFA Gain in a Space Radiation Environment	2004	Olivier Berne, Matthieu Caussanel, Olivier Gilard[2]	This paper describes and experiment where sample EDFA where radiated with Gamma rays. It is found that the gain decreases. A model is presented which can predict this degradation to an accuracy of 10% when corrected for temperature and darkening. The darkening was measured through a 1300 nm light source since this has low absorption by Er. The dosages used however are very large, much larger then expected in space. The smaller space level dosages are predicted to be less then 0.1 dB and hence EDFA are interesting for space applications. However, the model has not yet been tested for smaller dosages and longer exposure time. There was no mention of a waiting period between experiment and measurement, which has an effect as described by[43].
The Energy Efficiency of EDFA and Raman Fiber Amplifier	2016	Peng Wang[42]	This is a master thesis which analysis the energy performance of Erbium Doped Fiber Amplifiers (EDFA) and Distributed Raman Fiber Amplifiers (DRFA). The use cases for this analysis long distance fiber communication used for internet links. The analysis discussed the optimum use cases between the use of EDFA and DRFA in long distance communications. EDFA requires lower pump powers while DRFA has better Optical Signal to Noise Ratios (OSNR). It is found that under certain circumstances, namely fiber links beyond 2500 km using DP-QPSK, that DRFAs are more energy efficient. This is due to the Forward Error Correction (FEC) requiring less power thanks to a higher OSNR. However, under 2500 km EDFAs are more energy efficient due to their intrinsically lower pump powers.

Literature overview optical amplifiers Continued			
Title	Date	Authors & Reference	Content Summary
Qualification Testing of Fiber-Based laser Transmitters and On-Orbit Validation of a Commercial Laser System	2014	M. W. Wright, M. W. Wilkerson, R. R. Tang[46]	This paper shows the design of the laser system and the qualification there off for the OPALS payload. It describes the design and performance of the Commercial Of The Shelf (COTS) parts in the communication system. The OPALS system uses a MOPA (Master Oscillator Power Amplifier) fiber laser. It uses a semiconductor DFB (Distributed Feedback Laser) seed laser delivering the signal at the same rate as the oscillator. This is then amplified through a fiber amplifier made of 2 stages. The environmental requirements included being able to handle temperature variations from -10 to 65 C and 0 to 55 C while operational, vibration testing up to 7.53 g_{RMS} and a frequency range from 20 Hz to 2 kHz. It also pertained a life test of 3000 Hrs. "The OPALS experiment has demonstrated the robustness of low cost commercial technology for a laser transmitter designed for space borne free space optical communications. The laser was subjected to a nominal qualification test protocol compared to that required for a full space qualification program and has operated successfully on the ISS platform in LEO orbit for over 15 link opportunities of approximately 15 min each."
The NASA Optical Communication and Sensor Demonstration Program: An Update	2014	Siegfried W. Jason, Richard P. Welle [15]	The design illustrates both the ground and SC terminals. The chosen modulation is amplitude modulation. Initially a 975 nm wavelength was used but this was switched for a less power efficient 915 nm due to this being less temperature unstable. It uses a MOPA which is isolated and amplified again. The laser architecture is shown in Figure 9 and utilizes a MOPA architecture where the power amplifier uses a polarization maintaining (PM) Yb-doped fiber with a pump laser.

Literature overview optical amplifiers Continued			
Title	Date	Authors & Reference	Content Summary
Nanosatellite Optical Downlink Experiment: Design, Simulation, and Prototyping	2016	Clements Et. Al.[9]	A general overview document for NODE, which is more specific in design details compared to the presentation[25]. The transmitter is a fiber coupled laser diode MOPA. The fiber is placed in a racetrack to improve the quality of the beam. After each stage the light is sampled to measure the performance of that stage. This is done with the extinction fiber, after the extinction fiber and EDFA. The laser diode temperature is monitored as well, with an electric cooler in case of overheating. Light before and at the end of the extinction fiber allows for measuring the quality of the laser light and pollution (in the laser spectrum). It hence indicates the performance of the system.
Optimization of a laser satellite communication system with an optical preamplifier	2004	Anna Polishuk, Shlomi Arnon[26]	This paper discusses the optimal pre-amplification of the signal before it is received on the receiver. This pre-amplification is required for weak signals, in order to increase the performance of the photo detector. However, pre-amplification results in higher power usage and potentially larger amplifiers. Furthermore, the noise generated by the amplifier also increases, implying that the SNR of the signal is not improved. However, higher signal powers can compensate for jitter and hence an optimum can be found which can balance the required BER with the necessary amplification power. This paper has found a mathematical approach to finding this optimum based on an existing system. It concluded that this optimum exists, however changes significantly with higher RMS jitter. Furthermore, for higher jitters, the BER resulting from the jittering dominates the increased noise from the amplifier. Hence, the existence of an optimum tends to the minimal power/gain required to achieve a desired BER.

Literature overview optical amplifiers Continued			
Title	Date	Authors & Reference	Content Summary
A comprehensive study on EDFA characteristics: Temperature impact	2018	John A. Bebawi, Ishac Kandas, Mohamed A. El-Osairy, Moustafa H. Aly[1]	This paper analyses the impact of temperature on EDFA characteristics. The temperature was varied from -40 C to 80 C. The maximum gain decreased linearly with increasing temperature. This variation was on the order of 10 dB for an input pump of 1480 nm and pump powers greater then 60 mW.
End Literature overview optical amplifiers			

4.2.1 Environmental Considerations and Compatibility

The OPALS qualification tests did not include radiation testing, due to its short mission time. However the effects of radiation is important to consider. This is understandable, since the experiment was only to produce 15 links and each link was slated to have a duration of 15 minutes. However, it did show that these systems can withstand launch loads. The instrumentation was contained in a pressurized and temperature regulated container. Hence, the temperature effects cannot be seen in this experiment.

The radiation has a darkening effect on the fiber amplifiers[2]. The losses for this is expected to be 0.1 dB implying that the effect of darkening could be compensated for by increasing the amplifier power over time. However, this comes with SWaP cost and would compound amplifier noise problems, however these are small. A safety factor should be included which can compensate for this.

Temperature was shown to have large effects on the order of 10 dB by John A. Bebawi et all.[1], in a temperature range of -40 C to 80 C or 233 K to 353 K. This shows that the temperature would ideally be low, or the system should be designed to deliver enough power at the given temperature.

In conclusion, other then the temperature, there is little concern with the use of fiber amplifiers in space. It must however be designed for End Of Life (EOL) and operating temperature.

4.2.2 Performance of Laser Transmitters

Comparing EDFAs and DRFAs, it shows for short fiber distances EDFAs are more efficient due to their lower required pump powers up until 2500 km[42]. Note that this is under conditions experience by the optic fiber network used on Earth for internet. This is however not entirely comparable to a use case for a spacecraft. Inside a spacecraft the resulting power limitations are low and the efficiency requirements of the on board hardware is high. For error correction for ground communications to the satellite or FEC for a satellite relay this might not meet the 2500 km equivalent to fiber communications. Furthermore, for signal transport within the spacecraft, the length of the fiber used it would be

less then 2500 km. Hence, EDFAs are likely the fiber amplifier of choice instead of DRFAs. The error correction will take place at either ends of the link. Hence, intermediate error correction will not be done and hence not affect the power consumption, increasing the attractiveness of EDFA's.

Jason and Welle's [15] transmitter, illustrated in Figure 9, had an electrical input power of 50W and an output power of around 10W, which corresponds to 20% overal efficiency. The pump stage lasers are EO 48% at 1-2 W output (optical) and EO 47% efficient for 17.5 W output (optical) for the first and second amplifier stage respectively. This corresponds to roughly 40 W of the electric power consumption and is hence the majority of the power consumption of the transmitter. If roughly 20 W of optical power is produced and 10 W is emitted, then the optical train including the fiber amplifier is roughly 50% efficient. This is assuming that the MO contributes negligible amounts of power. The pump wavelength of 915 nm and an emission wavelength of 1064 nm would result in a $\frac{915}{1064} = 0.86$ theoretical efficiency. This is due to a 915 nm photon having a higher energy then a 1064 nm photon. This accounts for 3 W of power loss, implying that the resulting 7 W of losses are due to other optical train losses, or an optical train efficiency of roughly 60% relative to its optimal efficiency. These losses can be due to many reasons. These could be the coupling efficiencies in the pump signal combiner, losses in the pump diodes, losses during transmission in the fibers, etc... However, it can be concluded that a workable pump laser wavelength has to be selected as close to the transmission wavelength as possible for the highest efficiency. Hence, the choice between an EDFA and a YDFA can be made based on that. The choice of the pump laser also has to include consideration for the laser stability, as was the case for Siegfried W. Jason, Richard P. Welle [15].

The use of fiber amplifiers in previous spacecraft laser communication designs is evident that the technology TRL level is high enough. A common approach is to take a high performance MOPA which is low power and low efficiency and amplifying the signal using a higher power and higher efficiency fiber amplifier. It also allows for high design flexibility and COTS.

For increasing the receiver capabilities, a pre-detection amplifier can be used. This is investigated by Anna Polishuk, Shlomi Arnon[26]. The performance of the photo detector is related to the signal strength, hence amplification of a received signal can increase performance. Furthermore, fiber coupling requirements can be reduced, since the total power being coupled into the fiber is amplified. The draw back however is that the SNR does not improve due to the noise being amplified as well. It is found that for large jitters, the BER increase was dominated by jitter. Hence, the role of a pre-amplifier has to be investigated in conjunction with jitter and photo detector performance.

In conclusion, the performance and use of fiber amplifiers in space is advantageous for performance and efficiency for both the transmitter as a signal amplifier and the receiver as a pre-amplifier. There has also been a history of use, indicating a high TRL. The components can also be sourced commercially. However, the system still has to be carefully optimized for pump wavelength as well as BER performance in the pre-amplifiers.

4.2.3 Fiber Amplifier and MOPA Requirements

The temperature has effect on the performance of the system. Hence, the system must be designed handle the operating temperature:

RxTx-PA-001: The system shall be designed to deliver the required amplification at the highest expected temperature of operation.

Radiation has little effect on the performance, however it does have an effect. This should be included in the design of the system:

RxTx-PA-002: The power amplifiers shall be designed to meet the requirements at EOL radiation doses or at -0.5 dB which ever power output is lower.

The efficiency of the system should not be low in order to ensure lower operating temperature and improved SWaP:

RxTx-PA-003: Efficiency of the optical amplifiers shall not be below 40% from input electrical power to output optical power at the exit of the amplifier.

The use of a pre-amplifier is very useful when the jitter noise is dominant. However, it should be sized based on the existing jitter after correction.

RxTx-PA-004: Pre-amplifiers shall be included only if the jitter BER is dominant.

The total amount of power per link should not be substantially higher then for single beam terminals:

RxTx-PA-005: The optical power amplifiers shall not use more power then 60W per link.

4.3 Deformable Mirrors

A commonly used active optical machine is the Deformable Mirror (DM). DMs are often used to correct sub-aperture wavefront distortions for free-space optical communications through the atmosphere, implying they have a fast frame rates. It usually consistent of a MEMS array of micro-mirrors, in the case of discrete DMs, and an array of MEMS pistons under a continuous mirror sheet, in the case of continuous DMs. This implies that they are small, accurate and light. As

a result, for a pointing multiple beams, these can be a very promising alternative to larger and heavier FSM arrays.

This section shall examine some of the aspects of DMs and determine if it is fit for the application in multi-beam terminals. This will be done by considering their space environment compatibility, lateral pointing accuracy and lateral pointing travel capabilities. These will then be used to distill requirements and trade-off criteria for DMs in a multi-beam system.

Table 5: Literature on deformable mirrors interesting for free-space optical communication.

Literature Overview Existing Designs			
Title	Date	Authors & Reference	Content Summary
Wavefront control in space with MEMS deformable mirrors	2013	Kerri L. Cahoy, Anne D. Marinan, Benjamin Novak, Caitlin Kerr, Matthew Webber[7]	This paper mainly discusses the application of deformable mirrors for cube sat applications. This is used for the imaging of exoplanets. The use of DMs in this case is for wavefront correction, however this paper also specifies design requirements. The system was designed for a 3U cubesat. In this case, a BMC 6 x 6 (32 actuator) Mini deformable mirrors was chosen. This was chosen for its small size and compatibility with existing systems through USB. It also has a very quick update rate being in the multiple kHz (which is high for DMs).
Wavefront control in space with MEMS deformable mirrors for exoplanet direct imaging	2014	Kerri L. Cahoy, Anne D. Marinan, Benjamin Novak, Caitlin Kerr, Tam Nguyen, Matthew Webber, Grant Falkenburg, Andrew Barg[6]	More detailed version of [7], where the optical train is showed in more detail among others. Here optics is used to focus the beam onto the DM inorder to improve its effectiveness. The micromirror array was demonstrated successfully on the ground.

Literature Overview Existing Designs Continued			
Title	Date	Authors & Reference	Content Summary
MEMS micromirror characterization in space environments	2009	Byung-Wook Yoo, Jae-Hyoung Park, I.H. Park, Jik Lee, Minsoo Kim, Joo-Young Jin, Jin-A Jeon, Sug-Whan Kim, Yong-Kweon Kim[48]	This paper explains experiments related to space environment testing of a two-axis comb micromirror array. These space environment tests where shock, vibration, stiction (cold welding), electrostatic charging and out gassing as well as performance testing. During launch, the shocks and virbations did not detectable alter the micromirrors as the resonant frequency was never reached. Stiction is a risk for MEMS due to the high forces and close proximity. However, this was prevented by grounding a landing site and implementing a field-limiting shield from a dielectric. The mirrors showed no stiction even under humid conditions. It was found that this dielectric also prevented charged radiation from causing drift. Lastly, out gassing degraded the reflectively less then 2%. The performances where also similar as on Earth. It was found that the DM passed all criteria with the above changes made. However, other MEMS devices could still be strongly affected.
Unimorph deformable mirror for space telescopes: environmental testing	2016	Peter Rausch, Sven Verpoort, Ulrich Wittrock[28]	This paper reports on testing done on a unimorph/continuous DM for space telescopes. This experiment included vibration, vacuum and thermal testing. The mirror complied with all these tests. It was found that with the thermal testing between 100K and 300K that the Zernike amplitudes are different however still within requirements. It was also found that for this particular sized mirror one vibrational test required the mirror to be structurally re-enforcement.

Literature Overview Existing Designs Continued			
Title	Date	Authors & Reference	Content Summary
A review of micromirror arrays	2018	Yuanping Song, Robert M. Panas, Jonathan B. Hopkins[32]	This paper contains a detailed overview of a number of different DMs. The paper investigates many aspects of each DM including dimensions, nature of surface mirrors, tip, tilt, piston and actuation where applicable. There is also a theoretical approach to find the limits. Considering range of motion, DMs range between having next to no tip abilities to very large tip abilities. The paper compares 277 DMs of both discrete and continuous variants. More on the comparisons of this will be discussed later.
End Literature Overview Deformable Mirrors			

4.3.1 Space Environment Compatibility

The work by Byung-Wook Yoo, Jae-Hyoung Park, I.H. Park, Jik Lee, Minsoo Kim, Joo-Young Jin, Jin-A Jeon, Sug-Whan Kim, Yong-Kweon Kim[48] using a comb MEMS mirror and Peter Rausch, Sven Verpoort, Ulrich Wittrock[28] using a piezo electric system have demonstrated that these systems are compatible for space flight.

The launch loads and vibrations seem to be a hazard for systems of a particular size and resonant frequency. This is because localized stress during eigenmode vibration occurred due to the spiral arm design as shown in Rausch et. al.[28] and illustrated in Figure 22. This particular mirror has a spiral arm connection and once this was replaced by a stiffer design, the resilience to eigenmodes increased and the frequency at which these eigenmodes occurred increased making it less likely this will be met. The work by Yoo et. al. [48] also performed vibration tests on the comb micro-mirrors. Here, no problems where found and the mirrors performed without impact. Hence it can be concluded that DMs can withstand the vibrational loads associated with spaceflight.

An important environmental consideration is the tolerance of temperature variations. Rausch et. al.[28] found that their DMs where capable of surviving temperature variations from 100 K to 300 K. This, however, came at a cost of the actuation amplitude. In this case, the amplitudes for 200 K and 100 K were about half of the amplitude at 300 K. This is because piezos move less far when cold. Hence the use of piezos could come either with performance penalties or temperature requirements. There was also analysis on the increased deformation of the mirror during these tests, however during operation this can be compensated for by the piezo's them selves.

Yoo et. al[48] however did not present such extensive temperature ranges in their experiments. There tests included a temperature of 60 C during out

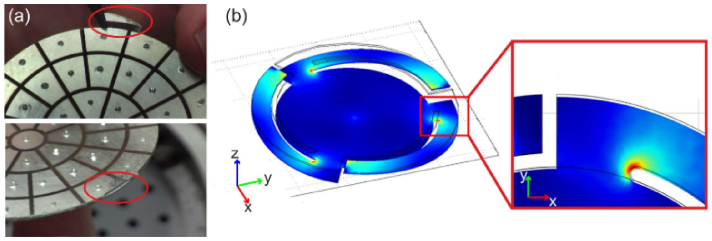

Figure 22: Illustration of stress concentrations and resulting fracture failure during vibration tests due to design. Image taken from the work of Peter Rausch, Sven Verpoort, Ulrich Wittrock[28], page 1539, Fig. 8. Given description: "(a) Fracture site of the spiral arm design after the random vibration test (DM-1). (b) Numerical calculation of the van-Mises stress inside the main mirror structure induced by the excitation of the first eigenmode."

gassing. This is used in out gassing tests for Russian micro-sats, however shed little light on the performance dependency on temperature. However, the use of a comb structure depends on the relative voltages between the plates, and as a result would have little performance dependencies. However, the changes in curvature would influence the performance. The size of these components however could imply that maintaining a constant temperature could be feasible.

Radiation and static charging is an important factor for the comb structure used in Yoo et. al[48], charged radiation can cause the micro-mirrors to actuate without command. Yoo et. al[48] indeed reported this effect. However it was found that with some shielding and the use of grounding pads that stiction was not observed anymore, even with very high humidity above 95%. Rausch et. al.[28] did not find significant effect of either γ or β radiation. This implies that minimal changes to DMs are required to make it radiation compatible with spaceflight.

In conclusion, DMs are compatible with the space environment, however do require consideration to be given to eigenmode effects on the structure and might require some radiation shielding. The thermal considerations could also play a role in piezo actuated DMs, mainly decreasing their strokes. Finally, the size of these systems can allow for thermal regulation to be implemented.

4.3.2 Pointing capabilities

Yuanping Song, Robert M. Panas, Jonathan B. Hopkins[32] have produced a very extensive survey of currently available MEMS mirrors. There are numerous aspects of their performances and compared and presented, and will hence give an overview of the capabilities of the modern DM.

Considering the design flexibility and FOV of the terminal, a large Field Of Reach (FOR) would be desirable. Considering the angular range of the considered DMs, the results are shown in Figure 23. It can be seen that a wide

verity of different DMs are capable of delivering a FOR greater then 1 deg at different pitches and accelerations. Hence, the design will likely not be limited by the DM capabilities.

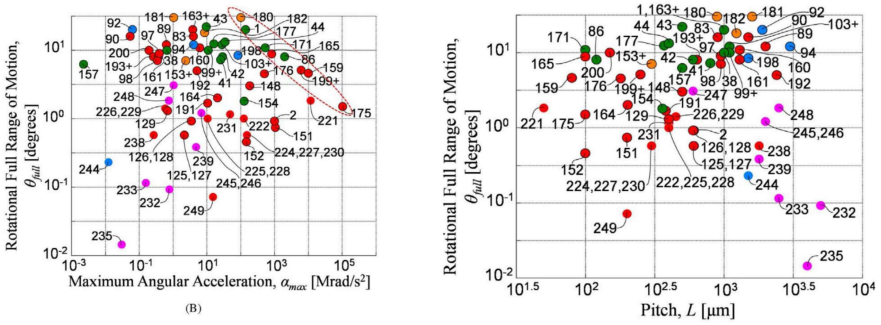

Figure 23: Different DMs and their full angular pointing capabilities. Right is depicted the rotational full range of motion plotted against the angular acceleration. This is indicates the speed by which the mirrors can be placed and their ability to correct for jitter. Left is depicted the rotational full range of motion against the pitch of the mirrors. This indicates the density placement of the mirrors which can be placed. These graphs are taken from the work of Yuanping Song, Robert M. Panas, Jonathan B. Hopkins[32], from page 746 Figure 16.

Ideally, a DM will have a large full range of motion while also being able to perform large angular accelerations. Hence, the DMs in the top right of the left graph in Figure 23. Furthermore, higher resolutions of micro-mirrors would be ideal as well. This would potentially allow for more beams to be steered more accurately and perhaps even sub-aperture wavefront correction.

Considering the pitch however could be misleading, since smaller DMs with the same resolution will have smaller pitch. Assuming that optics can change and focus the image onto smaller DMs, a consideration for the efficiency of the DM would be different fill factors. Lower fill factors subsequently cause signal loss and hence performance loss due to a smaller amount of the incident light being reflected. This however has also been investigated, and is illustrated in Figure 24. It too shows that a wide variety of different DMs are available.

Considering Figure 24, a mirror would ideally be in the top left corner. This would reduce some requirements from the optical system while at the same time having high fill factors and resolutions. It can be seen however that there is a clear separation between this area and the cataloged DMs. In fact, there is a trade-off to be had for the size of the mirror, fill factor and pitch. Moreover, the resolution seems not to vary beyond 10s of actuators across, meaning there resolution is limited to under 20x20 mirrors. This implies that if one DM was used to steer multiple beams, that the ability to correct for sub-aperture wavefront distortions decreases. This is a point of inflexibility and limitations for COTS DMs.

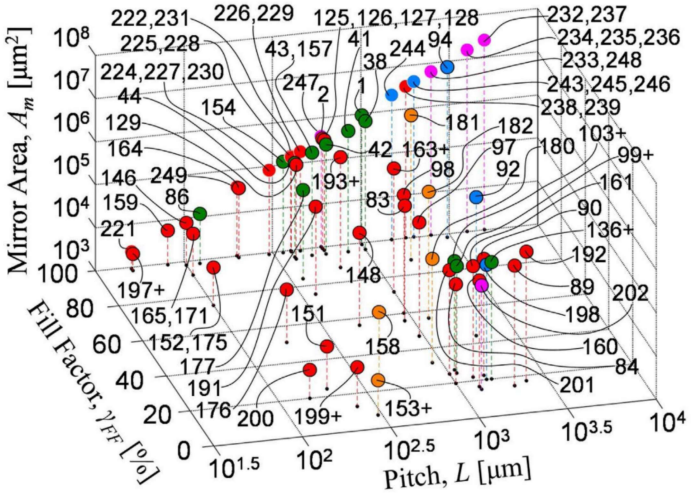

Figure 24: Different DMs and their pitch and fill factors. On the z axis is the mirror/array area while on the x axis is the pitch, the combination of which gives the resolution. The y axis indicates the fill factor, which in this application might reflect the efficiency of the mirror. This graph is taken from the work of Yuanping Song, Robert M. Panas, Jonathan B. Hopkins[32], from page 747 Figure 17 a.

When comparing both Figure 23 and Figure 24 it can be seen that not all DMs which perform well in the acceleration and FOR also do so in fill factor and resolution. There are however a few DMs which do have both a good pointing performance and fill factor.

In conclusion, there are a wide variety of different DMs to chose from. However, the current selection does not make it easy to find a large and high resolution DM with larger FOR and high angular acceleration. The DM must be carefully chosen based on the available DMs at the TUDelft. This could result in detrimental performance in the trade-off tables when compared to the other methods.

4.3.3 Requirements and Trade-off Criteria

For the use of DMs in the multi-beam terminal there are a number of requirements the system and DM must meet. These will be denoted as **SP-DM-xxx**, for Pointing System (PS) and Deformable Mirror (DM).

As discussed before, the use of continuous DMs makes beam pointing harder to do. Hence, hence a requirement for this must be made:

PS-DM-001: The deformable mirror shall be a discrete array of mirrors.

The space environment seems to be compatible with most DM designs and configurations in terms of radiation and vacuum. Hence, this will not be specified. However, a significant effect on performance was the temperature and structural considerations have to be made for the vibrational eigenmodes. For the temperature, the safe range is likely around 250 K to 320 K, when seeing the considered literature above. Hence, the temperature requirement is as follows:

PS-DM-002: The temperature range of the DM shall not go out side a range of 250 K to 320 K respectively.

The vibrational eigenmodes either should be designed for structurally or never reached. Hence the requirement can be as follows:

PS-DM-003: The DM shall be able to withstand launch amplitude vibration on its first 3 eigenmodes for 10 minutes without fracture or shall have its first eigenmode outside of the launch vibrational spectrum.

This is a requirement which will be given for all pointing mechanisms. Discrete DMs have space between the micro-mirrors. This results in signal loss and reflections into different directions. Hence, the DM should have a minimum fill percentage and should either point away from receivers or should not reflect any light in the area between the mirrors. Note, that this reflected light does not have to go to waste, and can in fact be used in measurement systems such as spot trackers and wavefront sensors.

For the fill factor, it is important that the signal losses are not larger. However, the use of this active optical device is to correct for jitter and offset. Hence, the losses should not exceed the gains. Hence, assuming an offset or jitter which reduces the efficiency by 20-30% the DM losses should not exceed this:

PS-DM-004: The fill factor shall not be lower then 80%.

The reflections in the space between the mirrors can be used. Hence, the requirement should not restrict the design. These reflections can be considered noise and hence a cut off of -3db is chosen:

PS-DM-005: The reflection of the light between the mirrors shall not induce noise by 3db.

Finally, to support 10 beams, the resolution should be high enough to ensure that each beam can be steered. However, if an individual beam can be steered with one mirror, because the mirror is large enough. It must hence ensure that a second beam at the Rayleigh criterion can be steered independently or have a resolution which is twice as high then the minimal required spatial resolution between targets in the FOV. The requirement is hence as follows:

PS-DM-006: The resolution/mirror size and pitch combination of the DM shall be twice as small as the required spatial separation/resolution of the FOV of the system or the Rayleigh criterion, which ever is bigger.

4.4 Fine and Fast Steering Mirrors

Fine and Fast Steering Mirrors (FSMs) are widely used in optical applications, including free-space optical communication. As the name suggests, the mirror can be used to fine and/or fast steer a beam to counter act jitter and to point to the beam into the right direction. These systems are also very fast, operating in 100's Hz and having pointing accuracy's on the order of milli to micro rad. Hence it is interesting to use multiple FSMs for multi-beaming applications. However, there are some challenges, namely with the space efficiency as well as with packing and weight, which makes this option less attractive.

Table 6: Literature on FSMs interesting for free-space optical communication.

Literature Overview Existing Designs			
Title	Date	Authors & Reference	Content Summary
Laser Communication with CubeSats	2018	Kerri Cahoy[4]	The FSM used for the NODE space terminal is the Mirrorcle MEMS FSM. This is a mirror bonded to an integrated circuit which contains the actuation. The mirror has an accuracy of +- 0.05 mrad. This mirror has a small form factor and interfaces with on board systems.
Design and Qualification of a Small, Customizable Fast Steering Mirror (FSM) for FSOC Stabilization and Scanning Applications	2018	N. Jacka, W. Walker, M. Roybal, J. McNally[14]	This paper analyzed the applications of FSMs in both free-space communications as well as and from there developed a custom FSM which can be used for scanning applications. This FSM is capable of 2.5 kHz closed-loop track bandwidth which less then 5 μrad accuracy and less then 15 nm surface finish. The FOR is smaller compared to the COTS mirrors, it ranges +-10 mrad. These, compared to the COTS components discussed later, are very high performances. This was achieved through the use of voice coils instead of MEMS or piezo actuators. The survival temperature range is -30 C to 50 C and operational temperature range is between -10 C and 50 C.

Literature Overview Existing Designs Continued			
Title	Date	Authors & Reference	Content Summary
Application of MEMS Accelerometers and Gyroscopes in Fast Steering Mirror Control Systems	2016	Jing Tian, Wenshu Yang, Zhenming Peng, Tao Tang, Zhijun Li[36]	This paper discusses the use of Fiber Optic Gyros (FOG) as a method of increasing the feedback loop speed of an FSM in conjunction with a CCD. The achieved response is faster and allowing for higher frame rates. The FSM can hence also be limited by the spot tracker. This is hence a reflection on both the spot tracker as well as the steering system.
Fine & Fast Steering Mirrors	2020	Cerdat Technologies[35]	This is a brochure from CERDAT Technologies. It serves as an overview of 12 COTS FSMs, their performances and limitations for different sized mirrors. It gives an indication of what is available. These include mirrors from 4x3 mm to 200x140 mm. From the brochure, it is clear that for larger mirrors, the housing which exceeds the mirror diameter is structural. Hence, if this was to be adjusted, the larger FSMs would have a better packing efficiency. The smaller FSMs have larger housings to accommodate the electronics, which decreases the packing efficiency.
Gimbal-Less Two-Axis Scanning MEMS Micromirrors Device Datasheet S5295	2016	Mirrorcle[20]	This is a mirror similar to the mirror referred to by Kerri Cahoy[4]. It operates at a frame rate of roughly 300-400 Hz however is recommended to operate at 200 Hz. The mirror is 3.6 mm in diameter and has a FOR of +- 5.7 degrees. This makes this type of mirror SWaP friendly and scalable. The chip and surrounding electronics implies that the mirror takes up more space then only its mirror, making the packing efficiency less efficient if the system was to focus the FOV onto a image plane.
End Literature Overview Fine and Fast Steering Mirrors			

4.4.1 Space Environment Compatibility

The FSM temperature ranges given in the brochure from CEDRAT Technologies are varied. These vary in the range of -50 C to 70 C for storage and about -10 C to 50 C for operation. This implies that thermal control has to be implemented, since temperature variations in space are larger. The temperature effects on different technologies likely also affects the performance, when con-

sidering differences such as piezo, coils, etc... This is true for radiation effects as well. Little literature on the radiation and other environment testing which specifically analysis these different technologies. However, the effects are likely similar as to those of DMs.

4.4.2 Pointing Performance

The use of FSMs are attractive for accurate and fast pointing. The effective frame rates of FSMs are in the 100's Hz and are commercially available. Here is a short discussion on the use and performance. From the above, the custom FSMs and/or with custom sensor setups seem to outperform COTS FSMs. This can be due to the feedback speed or the use of different technologies. However, this is not the case for all aspects.

However, the work by Jing Tian et all.[36], shows that there are limits to the frequency (which is also referred to as the frame rate in this work in keeping with the other pointing mechanisms). These are both the resonance as well as spot tracking and the feedback loop. Spot tracker can be a large limitation for higher bandwidth FSMs. Hence, there is a limitation to the advantages of high frame rate FSMs if the surrounding hardware is not capable of keeping up. If the frame rates of spot trackers are on the order of 100-300 Hz, the FSM loses its advantage.

The resonance frequency is effected by the size of the device/mirror and the structural aspects. Small mirrors, for example, have higher resonant frequencies then larger mirrors. The frequency by which the FSM can operate is therefore limited. However, smaller mirrors are more SWaP friendly and scalable. The result is hence that small mirrors would be a better design option.

The FOR performance of COTS FSMs ranges from +- 5 degrees to +- 0.05 degrees. This is likely the result of different actuator technologies used and mirror sizes. The selection of an FSM should hence not only include the speed, however also consider the FOR carefully.

COTS FSMs are often round and have a bigger footprints then the mirror it self. This strongly affects the ability of an array to reflect beams from a geographically conjugated focal plane into fibers. This is because of the empty space between the mirrors. The mirrors would hence have to be approximately square to improve the packing efficiency as well as a footprint not much larger then the mirrors.

In conclusion, FSMs have high frequency performance compared to the other pointing mechanisms considered. However, there are numerous drawbacks associated with surrounding hardware and footprint of FSMs.

4.4.3 Requirements

The coupling into different fibers from different parts of the aperture or to couple into geographically conjugated fibers is essential in multi-beaming terminals. The small FORs of some FSMs gives rise to a need to ensure that the pointing mechanism can do so. Increasing the FOR of the pointing mechanism also allows

for more optical design flexibility, since using optics to amplify the angles also results in amplification of the errors:

PS-CR-002: The FOR of the pointing mechanism, should it be used, shall be greater then 3 degrees.

FSMs can sometimes out pace the their feedback loop. Hence, the feedback loop must be fast enough to keep up with the FSM for pointing. However, this is also true for all pointing mechanisms.

PS-CR-003: The spot tracker shall have a frame rate higher then the pointing system.

The requirements for FSMs are hence similar to those of discrete DMs. The following are the adapted requirements from subsubsection 4.3.3:

PS-FSM-001: The temperature range of the FSM shall not go out side a range of 250 K to 320 K respectively.

PS-FSM-002: The FSM shall be able to withstand launch amplitude vibration on its first 3 eigenmodes for 10 minutes without fracture or shall have its first eigenmode outside of the launch vibrational spectrum.

PS-FSM-003: The fill factor shall not be lower then 80%.

PS-FSM-004: The reflection of the light between the mirrors shall not induce noise by 3db.

PS-FSM-005: The resolution/mirror size and pitch combination of the FSM shall be twice as small as the required spatial separation/resolution of the FOV of the system or the Rayleigh criterion, which ever is bigger.

4.5 Reflective Modulators

Reflective Modulators (RMs), also known as spatial modulators, are surfaces which can change the phase of the light incident on it. This subsequently allows for the phase to be changed such that the the beam can be steered. In this study, RMs are consistent of a liquid crystals in pixels which can change the phase of the light through an applied voltage. Hence, they might be referred to as Liquid Crystal Spatial Modulators (LCSLMs). This technology is interesting since the component does not require moving parts, light weight and is compact, hence it is SWaP friendly. Modern RMs have very high resolutions and frame rates comparable with HD high speed video and are sometimes HDMI compatible. This allows for sub-apperture phase correction and beam improvement/shaping.

Hence it has a quality improvement enhancement aspect which can be very attractive during the trade-off.

This section shall discuss the space environmental compatibility and pointing performance of RMs. After this a number of requirements and conclusions will be drawn which will be used for a trade-off later.

Table 7: Literature on reflective modulators interesting for free-space communication.

Literature Overview Existing Designs			
Title	Date	Authors & Reference	Content Summary
High precision beam steering using a liquid crystal spatial light modulator	2019	Qifeng Niu, Chunyang Wang[22]	This paper discusses the electrical models of an LCSLM (referred to here as an RM) and control methods by which the pointing accuracy of an optical beam was improved. There is a subsequent simulation and experiment where the theory is verified. The accuracy achieved in this case was 0.0098 Degrees at a wavelength of 532 nm. The paper illustrates that previous methods of controlling the RM previously resulting in pointing errors. This was improved upon by taking into account an improved electrical circuit and using iteration methods to achieve the point accuracy.
Spatial Light Modulators	2019	HOLOEYE[13]	This is a brochure for the Spatial Light Modulators (referred to here as RMs). It will serve as an example of a COTS RM. The brochure illustrates some of the COTS RMs and their performance parameters. It illustrates that the RM is controlled and behaves similar to a HD display and at similar frame rates. This is done through HDMI. Considering the color depth of HDMI can be 16 bits, it could allow for 65,536 different phases which would result in very accurate pointing. However, the exact resolution is unknown and is likely 8 bits, hence 256 different phases. The HD resolution can allow for ample sub-aperture wavefront correction and beam shaping.

Literature Overview Existing Designs Continued			
Title	Date	Authors & Reference	Content Summary
Steering and Shaping of Multiple Beams with a Spatial Light Modulator based Beamformer	2018	R. Bonjour, S. Welschen, J.F. Johansson, J. Leuthold[3]	This paper illustrates that it is possible to control and shape multiple beams independently and can even split these beams. The paper presents an experiment where the signal is switched between multiple channels/receivers and then split between 2 channels independently. It is found that the system was capable of accurately pointing and splitting the beams. In this case, this is done using an area of 50x50 pixels, hence a larger array would support multiple of these actions. This makes the system capable of doing this very versatile for pointing. The paper also mentions RMs to be used for high throughput space applications and is optimistic on it use for space applications.
Optical multi-beam forming method based on a liquid crystal optical phased array	2017	Feng Xiao, Lingjiang Kong[47]	This paper presents multiple control methods by which beams can be formed using the phased array characteristics of the RM. The phased array characteristics allows for the wavefront to be given any shape desired. The first method described is the sub-aperture method, which divides the RM into small segments and controls them independently. The second method also divides the aperture, however the whole aperture has each consecutive pixel dedicated to a different beam in a regular pattern (so the first for on beam, the second for an other, and then the third for the first beam again). This allows each beam to use a much larger aperture, however is harder to direct multiple unique beams. The control is done through the use of an itterative method which utilizes the Fourier transform.

Literature Overview Existing Designs Continued			
Title	Date	Authors & Reference	Content Summary
Radiation testing of liquid crystal optical devices for space laser communication	2009	Steven Lane, Jacob A. Brown, Meganb E. Tremer, Craig Uber, Elizabeth E. Gallagher, Steven R. Collins, Michael R. Benoit, William Miniscalco[18]	This paper discusses the effects of radiation on RMs to see if they are compatible with the space environment. The radiation tests performed where total dose of 70 krad (Si), prompt doses up to 6.5E8 rad (Si)/s for 20 ns and neutron dose of 1 MeV. The results showed that the phase achieved before and after the dose did not vary at small phases. At large phases, very minimal change in phase was found. However, changes where found in the achieved Strehl ratio, electrode resistance, switching time and dynamic range, depending on the radiation dose.
Preliminary space environment tests of nematic liquid crystals	1996	Alan Graham, Greg Kopp, C. Vargas-Aburto, R. Uribe [11]	This paper describes a series of experiments where RM analogs where subjected to a number of environmental tests, namely UV exposure, gamma radiation, ionizing radiation, vacuum and temperature tests. It was found that UV exposure was very detrimental. However the other experiments observed little to no effect. Note that the temperature was done by bringing the RM down to 150 K or up to 330 K and then returned to room temperature to be tested. The conclusion is that Liquid Crystal (LC) RMs are safe for use in space.
End Literature Overview Reflective Modulators			

4.5.1 Space Environment Compatibility

The work by Steven Lane et all.[18] has shown that RMs are capable of operating in the radiation environment. Steven Lane et all.[18] show that the radiation dose changes some aspects of RM performance.

The total dose radiation concluded that there was no significant change in the phase dynamics range, insertion loss, switching time, or Strehl. It did increase the electrode resistance, which might affect the electrical characteristics. Experiments with prompt exposure to radiation increased insertion loss and switching time while reducing Strehl. Neither phase dynamic range or electrode resistance have conclusive change. Neutron radiation increased the switching time and reduced Strehl, however did not affect the phase dynamic range, insertion loss or electrode resistance. A reduction in switching time implies a reduction in frame rate and hence ability to correct for jitter. The increase

however was on the order of 1-2 ms on a overall switching time on the order of 20-25 ms. The effect on the frame rates is low compared to the overall frame rate it self. The negative effect on the Strehl implies a worsting optical capabilities. However, this too was limited to less then 5%.

The effect of radiation on the RM seems to be small compared to its overall performance. Hence, the radiation compatablity with the radiation environment seems to be good. It is noted, however, that for all of these, that multiple experiments where done. During these, changes where detected which where non-negligible according to Steven Lane et all.[18]. This was relative to the requirements posed by their space mission. However, could still be relevant for the multi-beam terminal. Hence, the system bust be capable of adapting its output to compensate for loss of performance due to radiation. This requires a closed loop system or regular calibration.

Alan Graham et all. [11] also performed tests. Exposing a LC to 7000 $\mu W/cm^2$ for 24 hours of UV resulted in complete destruction of optical performance. Hence RMs should be shielded from UV. However, exposure to 500 times the yearly dose of gamma radiation seen in sun synchronous orbit, 3800 Rads, resulted in no damage. Hence, no shielding for this is required. Ionizing radiation of 32 MeV for 50 krad also did not result in evident damage. Lastly, temperatures between 150 K to 330 K and vacuum pressures did not damage the RM. However, the RM was always tested in room temperature. Hence, the performance at these temperatures is unknown, and likely a temperature regulation system is needed to ensure that the temperature stays within 270 K to 300 K.

Hence, the RMs are compatible with the space environment.

4.5.2 Pointing Capabilities

The pointing capabilities of an RM depends on the algorithm used and the resolution by which the phase of a pixel can be chosen together with the pixel resolution it self. The example COTS RM from Holoeye is available in the TUDelft facilities. It supports at least a 8 bit color depth at HD resolutions on the order of 1920x1080 pixels up to 4160x2464 pixels. It can do so at frame rates of 60 Hz to 180 Hz. However, if the technology from LCD screens can be used, 300 Hz and above can be achieved in future. The Greenwood frequency of the turbulence can hence not exceed these values. The sub-aperture wavefront correction will be an improvement over DMs because of the far superior resolutions.

Feng Xiao, Lingjiang Kong[47] have shown that the increased spatial resolution and phase depth increases the accuracy of the beam pointing and forming. Furthermore, the beam splitting and forming algorithms have been proven. It is shown that when iteration is applied, the quality increases. However, each update implies a frame is used implying that the effective frame rate drops. Hence, the quality of the beam will be lower with high frequency jitter. This implies a minimum Strehl ratio must be targeted proportional to the spot size and quality requirements for fiber coupling. The RMS error however falls by a

factor 10 by just a few iterations.

The work by R. Bonjour et all.[3] has shown that independent beam splitting and switching is possible. A schematic of this experiment is shown in Figure 25. The beams where successfully coupled into receiver fibers using collimators, indicating that RMs are accurate enough to do so. The speed by which the beams where split and switched between channel 1 and 4 was quick enough to not cause significant interference with the intermediate channels 2 and 3. This hence indicates that the system can be used for independent multi-beam steering, splitting and combining. This could be handy for signal handovers between receiver fibers.

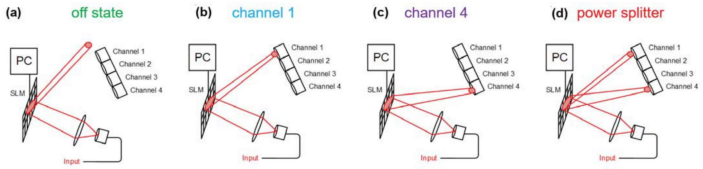

Figure 25: Demonstration of switching between channels and splitting beams. This was taken from the work of R. Bonjour, S. Welschen, J.F. Johansson, J. Leuthold[3], page 3 Fig. 4.

It can be found in the work by Qifeng Niu, Chunyang Wang[22] that the accuracy can be improved until 0.0098 degrees for their particular RM. This was achieved through an improved understanding of the LC layers and electrical modeling. The control of the RM will hence have to be either done by a dedicated controller from the supplier.

The use of an RM can meet the pointing requirements and is compatible with a optical communication terminal. Additional features such as the high resolutions, abilities to form beams for improved optical performance, split and combine beams, among others can increase the design flexibility, performance and features significantly. However, the pointing and beam forming might require iterations for improved performance, effectively decreasing the frame rates.

4.5.3 Requirements

The environmental concerns mainly concern the UV exposure and the operating temperatures. The UV exposure requirement should eliminate the UV exposure all together. Hence, the following was chosen:

PS-RM-001: The RM shall not be exposed to UV light.

The temperature should stay within the range of room temperature. Hence the following requirement is made:

PS-RM-002: The RM temperature when active shall not be outside the

temperature range of 270 K to 300 K.

The temperature range experienced during the entire mission should not exceed those tested and experienced in the literature:

PS-RM-003: The temperature range of the RM during the entire life shall not fall outside of 150 K to 330K.

The system performance will change over time due to radiation. Hence the control loop should be closed and use feedback for pointing to correct for this:

PS-RM-004: The system shall correct for RM drift over time using a closed loop control system.

The frame rates should not reduce its effective frame rate below that of the Greenwood frequency, or any jitter frequency, due to beam quality improvements:

PS-RM-005: The frame rate of the RM shall not fall below the jitter frequency due to beam quality improvements.

4.6 Piezo Actuator Arrays

Piezo Actuator Arrays (PAAs) are, as the name suggests, arrays of small piezo actuators in an array. For the application of PAAs a reflective layer on top of the arrays has to be applied. This results in the array becoming DM. However, it only has one vertical degree of freedom. Hence, 2 are required at minimum. However, the independent and very accurate actuation implies that fiber coupling can be done accurately. Furthermore, this technology is cheap and expandable, implying scalability.

Therefore there can be some confusion between DMs and PAAs. In this work, PAAs will specifically refer to single degree of freedom arrays of piezo actuators.

Table 8: Literature on piezo actuator arrays interesting for free-space optical communication.

Literature Overview Existing Designs			
Title	Date	Authors & Reference	Content Summary
Scalable stacked array piezoelectric deformable mirror for astronomy and laser processing applications	2014	Krystian L. Wlodarczyk, Emma Bryce, Noah Schwartz, Mel Strachan, David Hutson, Robert R.J. Maier, David Atkinson, Steven Beard, Tom Baillie, Phil Parr-Burman, Katherine Kirk, Duncan P. Hand[44]	This paper discusses the performance of a prototype stacked array piezoelectric deformable mirror. This is a continuous mirror, produced by applying a high reflective plate on top of actuators. The actuators are separated by electrodes of equal size, implying the actuator density is low. However, the mirror is continuous implying that for beam forming and sub-aperture correction is less penalized because of the mirror deformation. The mirror has 36 active elements in a 6x6 square configuration, with a size of 14x14 mm. The maximum actuator stroke in this paper is 2 μm which resulted in a 1.4 μm sag. The resulting hysteresis error was +- 200 nm.
Piezo Actuator Arrays	2020	NGK[21]	This is a website of NGK, who manufactures piezo arrays, among others. This particular product is a 9 cm^2 with 32x32 elements at 1 mm pitch. The displacement is on the order of 20 μm at 200 V. The response time is 0.1 ms which is very high, however there is no mention of speed of actuation, hence it will be assumed to be longer. The effective frame rate is hence not known, however it is lower then 10 kHz. Mirrors can be applied on each actuator at different angles. An illustration of its application as an array of mirrors is shown on the website, however also shown in Figure 26, where mirrors can be added on the PAA on a given angle to steer incoming light. However, they will likely not be at 45 degrees as shown, since the the travel is on the order of micrometers and the mirrors on that scale would be on the order of millimeters.

Literature Overview Existing Designs Continued			
Title	Date	Authors & Reference	Content Summary
Unimorph deformable mirror for space telescopes: environmental testing	2016	Peter Rausch, Sven Verpoort, Ulrich Wittrock[28]	This paper reports on testing done on a unimorph/continuous DM for space telescopes. This experiment included vibration, vacuum and thermal testing. The mirror complied with all these tests. It was found that with the thermal testing between 100K and 300K that the Zernike amplitudes are different however still within requirements. It was also found that for this particular sized mirror one vibrational test required the mirror to be structurally re-enforcement.
End Literature Overview Piezo Actuator Arrays			

4.6.1 Space Environment Compatibility

The technology is piezo, which is similar to the DMs previously discussed. The environmental effects on PAAs are hence likely similar as with piezo actuated DMs. Hence, this discussion can also be found under Table 5. Here it will be shortly summarized.

The the PAA must be able to with stand the vibrational loads during launch and operations. However the performance of the piezo actuated DMs after vibrational tests, once it is structurally fortified, did not perform different. Temperature wise, Rausch et. al.[28] found that their DMs where capable of surviving temperature variations from 100 K to 300 K. However, came at a cost of the actuation amplitude. In this case, the amplitudes for 200 K and 100 K were about half of the amplitude at 300 K. This is because piezos move less far when cold. Hence the use of piezos could come either with performance penalties or temperature requirements. The temperature effects are especially worrying, since an already small stroke is reduced even more. This implies that the PAA should be temperature regulated. There was also analysis on the increased deformation of the mirror during these tests, however during operation this can be (partially) compensated for by the piezo's them selves. Rausch et. al.[28] also did not find significant effect of either γ or β radiation. This implies that minimal changes to DMs are required to make it radiation compatible with spaceflight, and hence PAAs will likely also not have problems.

4.6.2 Pointing Performance

The pointing performance of a PAA with strokes on the order of micro-meters would require enhancement with other optics in the terminal to amplify the effects of the PAA. This places more critical requirements on the precision of the optics, making the construction harder and more expensive.

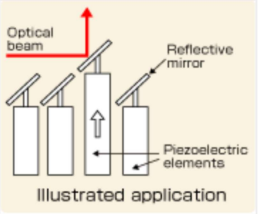

Figure 26: This is an illustration of an application of a PAA. The figure shows angles mirrors placed on each actuator which reflects beams of light at different heights. This image was taken from NGK[21].

If the PAA is to be made into a discrete DM mini-mirror array for beam steering, an approach seen in Figure 26 can be taken. However, the angles of the mirrors cannot be 45 due to the shadowing effect. The mirrors will be on the order of a square millimeter and hence the travel required for the PAA to raise at least one mirror out of the shadow of a mirror would be on the order of millimeters. If the travel is on the order of tens of micro-meters, the angle of the mirror must likely be smaller then a degree. This makes the effect of the travel less pronounced.

The PAA can potentially be used as a phased array/RM by shifting the phase of light reflected by changing the path length. However, RMs are better for these applications due to their high phase change resolutions and spatial resolutions in general, considering that the phase resolution would be on the order of 400 nm (twice 200 nm if the PAA used by Krystian L. Wlodarczyk et all.[44] is used). However, PAAs have advantages in terms of frame rates, if the frame rate is comparable to the response time, and those of the previously discussed RMs being on the order of 60 Hz. However, dedicated RMs might have higher frame rates, making this advantage also smaller.

In conclusion, the use PAAs have potential for wavefront corrections and crude and fast RMs substitutes in space. However, the use as a beam steering mechanism more challenging.

4.6.3 Requirements

The requirements for a PAA must include the effect of shadowing. This cannot be to high since it decreases space for other beams:

PS-PAA-001: Mirror shall be angles such that there is less then 10% shadow.

The rest of the requirements are comparable to discrete DMs:

PS-PAA-002: The mirror shall be discrete array of mirrors.

PS-PAA-003: The temperature range of the DM shall not go out side a range of 250 K to 320 K respectively.

PS-PAA-004: The PAA shall be able to withstand launch amplitude vibration on its first 3 eigenmodes for 10 minutes without fracture or shall have its first eigenmode outside of the launch vibrational spectrum.

PS-PAA-005: The fill factor shall not be lower then 80%.

PS-PAA-006: The reflection of the light between the mirrors shall not induce noise by 3dB.

PS-PAA-007: The resolution/mirror size and pitch combination of the PAA shall be twice as small as the required spatial separation/resolution of the FOV of the system or the Rayleigh criterion, which ever is bigger.

5 Link-budget

The multi-beaming terminal must communicate with multiple targets. The data rates achieved are dependent on multiple factors. This section shall discuss different aspects of the link budget and will produce requirements for it.

Table 9: Link budget associated literature.

Literature Overview Existing Designs			
Title	Date	Authors & Reference	Content Summary
Investigation on Multi-Beam Hybrid WDM for Free Space Optical Communication System	2016	S. Robinson, R. Pavithra[29]	This paper presents an investigation into multi-beam Hybrid Wavelength Division Multiplexing (HWDM). During this investigation, Coarse Wavelength Division Multiplexing (CWDM) and Dense Wavelength Division Multiplexing (DWDM) where used with steps of 10 nm and 0.8 nm steps respectively. The wavelengths considered where from 1510 nm to 1570 nm for CWDM and 1537.4 nm to 1543 nm for DWDM. There was also an EDFA incorporated on the receivers end to enhance the signal. DWDM has higher cross talk compared to CWDM due to smaller wavelength spacing, however is less affected by diffraction differences due to media differences. Each wavelength requires a separate laser beam and is then combined into a Wavelength Division Multiplexer (WDM) and transmitted. There is also a WDM de-multiplexing at the receiver. It is found that the bit error rate is superior for different link distances and receiver powers when CWDM DWDM.
Bandwidth specification for adaptive optics system	1977	Darryl P. Greenwood[12]	This is the original paper from Greenwood where the Greenwood frequency, which is the frequency by which the turbulence structures enter and leave the aperture. Its derivation comes from combining the Kolmogorov turbulence power spectrum with, which is a distribution of different turbulence structures and their frequency, and the expressions for the normalized Fried parameter. The Fried parameter indicates the coherence length over the aperture, and indicates the size of the sub-aperture wavefront distortions. The result is a frequency by which adaptive optics must correct for the wavefront distortions.

Literature Overview Existing Designs Continued			
Title	Date	Authors & Reference	Content Summary
Bandwidth considerations for tracking through turbulence	1994	Glenn A. Tyler[40]	This paper analyses the tip-tilt error and frequency of atmospheric turbulence. It uses the work from Greenwood[12], however analyses the frequencies for an FSM to tip-tilt correct optimally for the centriod and bright spot/RMS wavefront error. It is found that the wavefront correction in the tip-tilt requires a lower frequency then the sub-aperture corrections and hence reduces some of the required performances off of the pointing mechanisms.
An Atmospheric Turbulence Profile Model for Use in Army Wargaming Applications I	2006	David H. Tofsted, Sean G. O'Brien, Gail T. Vaucher[37]	This is a report where different turbulence altitude profiles are investigated. This profile produces a changing turbulence strength, $C_n^2(z)$, with altitude and allows for the derivation of the Greenwood and tip-tilt frequencies. The profiles where investigated for improvement of weapon system performances during wargaming. The main profile which will be used in this work is the Hufnagel-Valley profile and is given on page 4. This is often used for nighttime astronomical observation conditions. However, the paper notes that this is not a typical profile for other times of day or weather events. The paper goes on to improve this model for different situations, however these are out of the scope of this work.
Experimental Study and Modeling of Infrared Air Plasma Radiation	1995	Christophe O. Laux, Richard J. Gessman, Benoît Hilbert, Charles H. Kruger[19]	This paper accurately measured the spectral emissions of air and shows that 1550 nm +- 200 nm. However, likely the use of wavelengths lower and higher will have more atmospheric attenuation. The absorption spectrum graphs indicate between 80-90% transmission efficiency.
End Literature on Link Budget			

5.1 The Use of Multiplexing in a Multi-Beam Terminal

Multiplexing is a widely used method for increasing the data rates in long distance optical fibers. This is because multiple frequencies and modulation techniques are used to effectively increase the number of channels which can carry

data through the same media. This can increase the transmission rate by multiples of the capacity of one channel. This hence can also be applied for free-space optical communication, as shown by S. Robinson et all.[29].

The Wavelength Devision Multiplexing (WDM) used by Robinson et all.[29] shows that the BER of the signal for a given distance through the atmosphere and receiver power is lower for using multiple frequencies/wavelengths. The additional channels can also carry error correction bits. The methods used are CWDM and DWDM. There are a number of differences between these methods. CWDM has larger wavelength/frequency spacing, decreasing the amount of cross talk between channels compared to DWDM. However, the performance of DWDM is higher then CWDM, as seen in Figure 27 and Figure 28. Furthermore, these are not optimal for use with EDFAs as a result. Furthermore, the dispersion between the wavelengths are also lower for DWDM. This effect is also detrimental to the use of RMs. Hence, the likely candidate to be used in such a mutli-beam system would be DWDM.

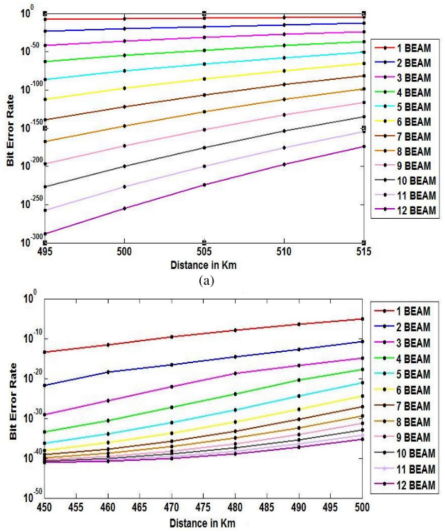

Figure 27: Illustration of the distance performance by CWDM (bottom) and DWDM (top). As can be seen, CWDM results are orders of magnitude higher BER for a given distance compared to DWDM. Furthermore, different frequencies have different effects on the BER. Taken from the work by Robinson et all.[29], page 25, Fig. 2.

The additional complexity and increased SWaP might result in a system which is to large and complex for this thesis. Hence, this will only be considered depending on the time and facilities. However, should be considered in the design in-case the feature is included later.

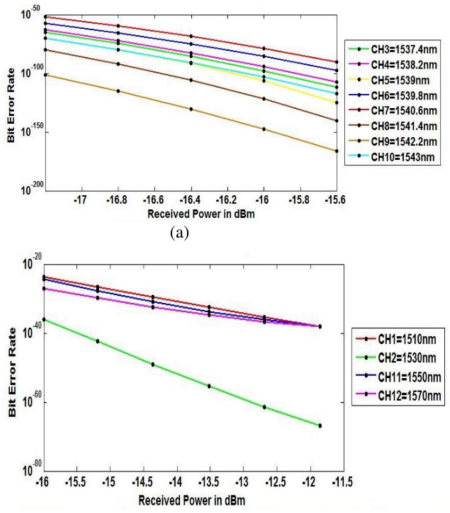

Figure 28: Illustration of performance of CWDM (bottom) and DWDM (top) at different receiver powers. As can be seen, CWDM results are orders of magnitude higher BER for a receiver power compared to DWDM. Furthermore, different frequencies have different effects on the BER, however, limited improvements after a certain frequency. Taken from the work by Robinson et all.[29], page 25, Fig. 3.

5.2 Wavelength Selection

The work by Christophe O. Laux[19] indicates that the absorption and emissions of the atmosphere are acceptable for wavelengths around 1550 nm. This is no coincidence one of the most used wavelengths in free-space optical communication and should be used in the terminal. This is coincidentally also a band where EDFA performance is high.

The transmission is assumed to be 80% from the data given considering Figure 29 and Figure 30. This will be used later when estimating the link budget of a link.

5.3 Link Budget Calculations

The capacity per link is an important characteristic and must be comparable to current link capacities to be competitive. Here a practical approach is taken, where each stage of the signal traveling from the terminal to the ground station receiver lumped in stages with efficiencies. The link budget is dependent on many aspects of the design of the terminal. However, the theoretical maximum

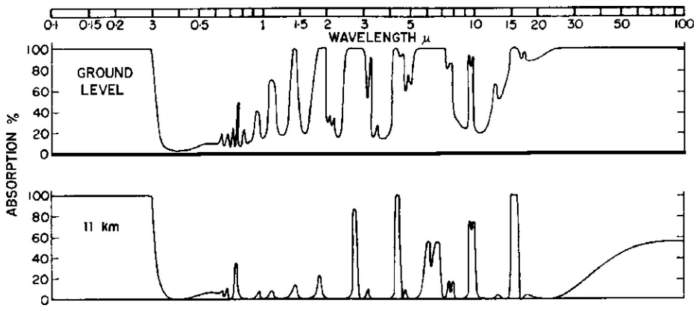

Figure 29: An illustration of the transmission efficiencies of the atmosphere. It can clearly be seen that the region surrounding 1550 nm has good transmission of roughly 80%. Taken from the work by Robinson et all.[29], page 2, Figure 1.

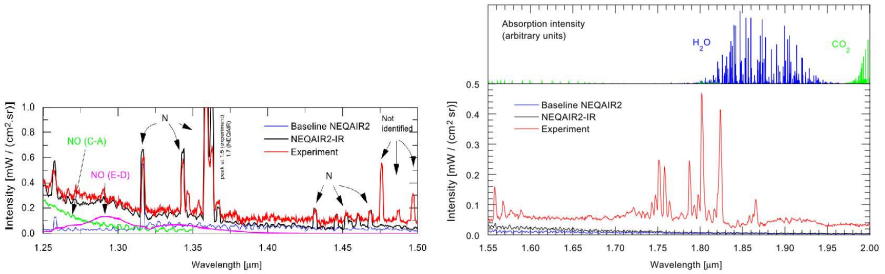

Figure 30: Illustration of the spectral emissions of the atmosphere. It can clearely be seen that the area surrounding 1550 nm has relatively little spectral lines, implying little interference from elements in the atmosphere. Taken from the work by Robinson et all.[29], page 7, Figure 9 and page 10, Figure 10.

link capacity is described by the Shannon–Hartley theorem:

$$C = Blog_2\left(1 + \frac{S}{N}\right) \tag{59}$$

Where C is the link capacity in bits per second (b/s or bps), B the bandwidth in Hz, S the signal power in W and N the noise power in W. This will serve as a guide to evaluating the link performance. This can only be done when considering signal power. Considering the down link from the satellite to the ground station, the signal is injected electrically into the terminal. The terminal has a efficiency when converting this to an optical signal and sending it through the telescope which includes the pointing system:

$$S_{out} = \eta_{T_x}\eta_T S_{in} \tag{60}$$

The telescope also has a pointing offset. It is assumed that the telescope creates an Airy beam, which has a disk size given by the Bessel function order 1 of the first kind. Its size and amplitude is for simplicity estimated conservatively with a sinc function:

$$L_T = \left(\frac{2J_1(\phi/\theta)}{\phi/\theta}\right)^2 = \left(\frac{sinc(\phi/\theta)}{\phi/\theta}\right)^2 \tag{61}$$

Where L_T is the pointing loss, the offset angle of the telescope is denoted by ϕ and the angle of the first zero is θ, given by the Airy disk equation $\theta = 1.22\lambda/D_T$ where D_T is the telescope diameter. The effect on the signal is as follows:

$$S_{out} = \eta_{T_x}\eta_T L_T S_{in} \tag{62}$$

The goal of the pointing system is to reduce ϕ as much as possible. After the telescope there is free-space loss, which is governed by the loss of intensity on the receiver en due to spread of the signal:

$$L_S = \frac{A_R}{A_S} = \frac{\pi\left(\frac{D_R}{2}\right)^2}{\pi\left(\frac{D_T(1+2Ztan(\theta))}{2}\right)^2} = \left(\frac{D_R}{D_T + 2Ztan(\theta)}\right)^2 \tag{63}$$

Where the area after free-space propagation is denoted by A_S, the receiver telescope area A_R, their respective diameters are given by D_R and D_S, given by the trigonometric equation given by the geometry in Figure 31 respectively. The distance of the propagation is denoted by Z and the spread of the beam is that of the Airy disk zero angle θ.

The pointing misalignment of the receiver telescope is also given by the following:

$$L_R = cos(\phi_R) \tag{64}$$

The signal in the mean time also propagates through the atmosphere, which also has an efficiency denoted by η_A. This gives the equation to be as follows:

$$S_{out} = \eta_{T_x}\eta_T L_T L_S \eta_A L_R S_{in} \tag{65}$$

The receiver, finally, also has an efficiency, η_R, and an amplification, A_R. This is leads to the signal power as follows:

$$S_{out} = \eta_{T_x}\eta_T L_T L_S \eta_A L_R \eta_R A_R S_{in} \tag{66}$$

Similarly, the noise figure is the same equation. However, at the stages of the transmitter propagation and receiver noise is added:

$$N_{out} = A_{RN}\eta_R(\eta_A(L_S L_T \eta_T \eta_{T_x} N_{Tx} + N_S) + N_R) \tag{67}$$

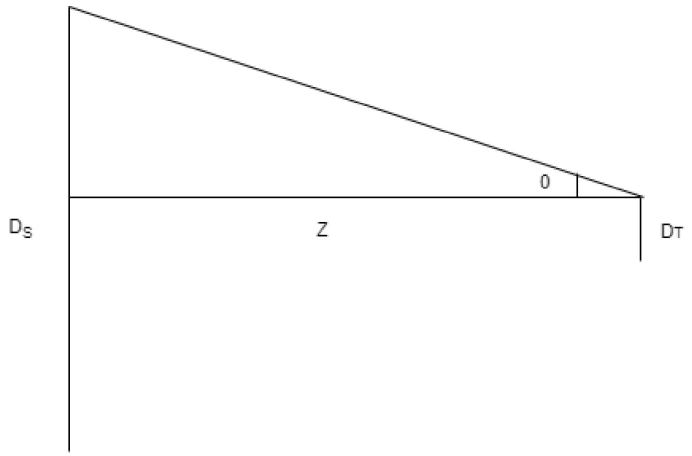

Figure 31: The geometry of free space propagation. The spreading angle is denoted by θ, the distance is denoted by Z, the transmitter diameter D_T and the diameter after propagation is D_S.

Where A_{RN} is the amplification factor of the noise, which due to the dynamics of an EDFA and photo diode, is different for the signal. The noise added by the transmitter is denoted by N_{T_x}, the noise added by space propagation is N_S and the noise by the receiver is N_R. These equations can reversed to go from the ground station to the multi-beam terminal in space.

Using Equation 66 and Equation 67, a few values can be inserted to understand the link capabilities, which can be found in Table 10. The transmitter efficiency was chosen based on the work by Siegfried W. Jason and Richard P. Welle[15], to be 20% as a guide line. The use of beam splitters and potential reflective losses, a telescope efficiency of 80% is assumed. The atmospheric attenuation was taken from subsection 5.2, and the receiver telescope losses where assumed the same as for the transmitter telescope losses. From the work of Kerri Cahoy et all.[7][6], the dimensions of the transmitter and receiver telescopes where taken, including their power consumption and pointing accuracy of the ground station. The wavelength was taken from subsection 5.2 and the pointing accuracy as a good impression from the pointing mechanisms in section 4. Lastly, the pre-amplifier amplification was taken to be 10 for the signal and 11 for the noise as a conservative estimate.

The result is 8.5E-6 W received signal S_{out} and 1.6E-2 W received noise N_{out}. If the laser transmitter has a bandwidth of 3 nm or 374.35 GHz, the bit rate according to Equation 59 would be 197.7 Mbps. This is within the ranges proposed in Figure 8 and hence the system will be competitive in delivering data rates per link compared with single beam systems. Should DWDM multiplexing be applied as suggested by Robinson et all.[29], then the signal to noise ratio would not change significantly with regards to each wavelength division. How-

Table 10: Values used in estimation of the link budget

Variable	Value	Unit
η_{T_x}	20%	-
η_T	80%	-
η_A	80%	-
η_R	80%	-
ϕ_T	15	μrad
L_T	81%	-
λ	1550	nm
θ	19	μrad
Z	10,000	km
D_T	0.1	m
D_R	0.3	m
L_S	2.05E-4%	-
ϕ_R	0.1	rad
L_R	99.5%	-
A_R	10	-
A_{RN}	11	-
S_{in}	5	W
N_{Tx}	0.1	W
N_S	-30	dBw
N_R	-30	dBw

ever, the bandwidth would scale proportionally with the number of channels. 6 channels would result in 1.2 Gbps, which is very attractive, however would also require 6 times more power.

Considering the results in the context of the losses, the most major loss is the free space loss. This can be improved through larger telescope apertures both on the ground as well as in space. This is because larger apertures on the ground capture more light, while at the same time a larger aperture in space decreases the beam spread and allows for a higher signal intensity on the ground. However, this comes with the associated losses in misalignment of the telescopes, since thinner beams require more precise steering. Furthermore, the losses in the transmitter are very large and also provide the largest share of the noise. This implies that this aspect of the design is very important to achieve high efficiency and low noise.

5.4 Adaptive Optics and Pointing System Requirements

When communicating through the atmosphere, the effects of turbulence have to be corrected for. Figure 32 shows different problems and solutions associated with propagation through turbulence. The multi-beam terminal must hence not only be able to geographically conjugate a fiber receiver with a target, however would also require to correct for tip-tilt errors due to misalignment, spacecraft

vibrations and atmospheric effects. In this work, only the tip-tilt correction will be considered for the terminal due to the facility and time limitations.

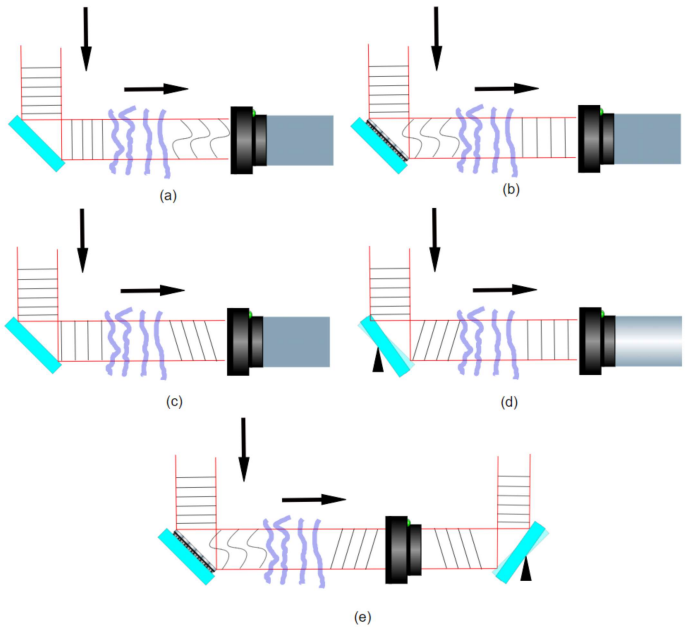

Figure 32: This is an illustration of different adaptive optics strategies. The beam is propagated from left to right and falls on some optical elements. It is then received on the right. (a) Illustrates the effect on the wavefront of atmospheric turbulence, where both tilt and sub-aperture wavefront distortions. When uncorrected, this will interfere when focused and decrease the intensity. (b) Can be viewed in both directions. When considering the beam traveling from right to left, the wavefront is distorted by the atmosphere and then a DM/RM/PAA/FSM array corrects the wavefront. However, this same wavefront correction can pre-distort the wavefront traveling from left to right. As a result the atmosphere corrects this wavefront to achieve the same effect. Although this is pre-distortion, it will be referred to as pre-correction as a more descriptive and intuitive term. (c) Shows a situation where the turbulence structures are larger then the aperture (when the Fried parameter is proportional to the aperture), and hence no significant sub-aperture wavefront distortion occurs and only tip-tilt. (d) Shows how this can be pre-corrected for by an FSM. However, the tip-tilt correction on the ground cannot correct for errors due to satellite vibration, misalignment and slight changes in the atmosphere during system reaction time. (e) Illustrates correction for this, where a tip-tilt correction FSM is illustrated however, for multiple beams DMs, RMs and PAAs can also be used.

To determine the requirements for the pointing mechanism, the speed of

change of the distortions has to be found. The frequency by which the Adaptive Optics (AO) system has to correct for turbulence is called the Greenwood frequency, first described by Greenwood[12]. This is derived probabilistic from the Kolmogorov spectrum associated with vortexes and turbulence structures:

$$f_G = 2.31\lambda^{-6/5}\left[sec(\zeta)\int_{z_0}^{40km} C_n^2(z)V(z)^{5/3}dz\right]^{3/5} \tag{68}$$

Where, ζ is the angle by which the light travels through the atmosphere, λ is the wavelength, C_n^2 is the turbulence strength, V is the wind velocity and z is the altitude. However, this includes the sub-aperture distortions. Glenn A. Tyler[40] derived expressions which quantifies the frequency required for tip-tilt:

$$f_{T_G} = 0.331D^{-1/6}\lambda^{-1}\left[\int C_n^2(z)V^2(z)dz\right]^{1/2} \tag{69}$$

$$f_{T_Z} = 0.368D^{-1/6}\lambda^{-1}\left[\int C_n^2(z)V^2(z)dz\right]^{1/2} \tag{70}$$

Where Equation 69 is the expression for spot centered tracking and Equation 70 is the tracking of the brightest part of the spot. It was concluded that the bright spot tracking resulted in the highest signal power, hence Equation 70 is used. The frequency is around 9 times smaller compared to the Greenwood frequency and hence decreases the requirements on the pointing system[40]. The turbulence profile was chosen to be the the Hufnagel-Valley profile, taken from David H. Tofsted et all.[37]. The an approximate wind profile was taken as presented in Fig. 2, page 365 in the work by Glenn A. Tyler[40]. This approximate profile is presented in Figure 33. The resulting turbulence profile is shown in Figure 34.

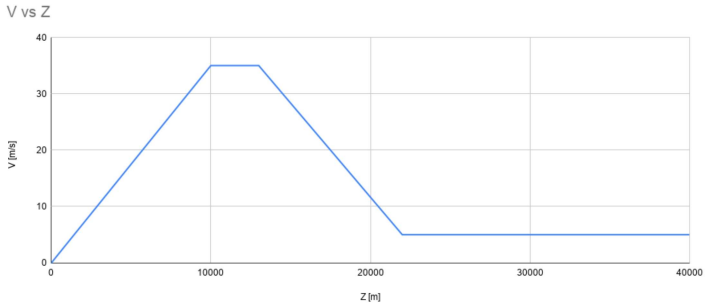

Figure 33: Assumed atmospheric velocity profile.

Equation 70 was numerically integrated. When the RMS wind speed between 5-20 km altitude was taken to be 21 m/s, or 75 km/hr, and a telescope diameter of 0.1 m was taken, this resulted in f_{T_Z} being 4.8 Hz. This is compared to a

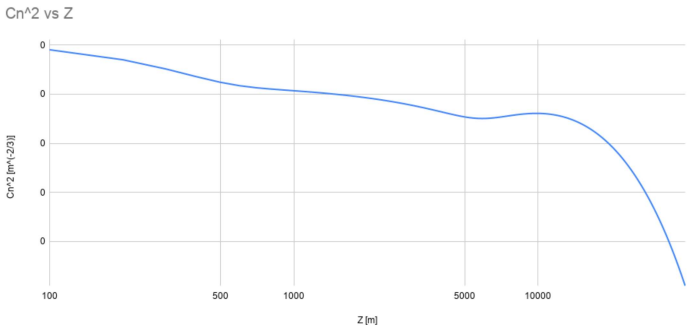

Figure 34: Resulting Hufnagel-Valley distribution of the velocity profile in Figure 33.

Greenwood frequency of 15.3 Hz. This is quite low, and when the wind speeds of the jet stream are taken into account, a velocity of 160 km/hr or 45 m/s is taken. This resulted in 9.7 Hz and 34 Hz respectively. This is significantly higher and hence there is great sensitivity to the weather. Furthermore, increasing the aperture diameter to 0.5 m and the wind speeds remain at 160 km/hr, this resulted in f_{T_Z} being reduced to 7.4 Hz. Note, that the Greenwood frequency remained the same at 34 Hz since it is not proportional to the aperture diameter. In this case, a safety factor of 4 is used, to ensure relatively high availability. This results in a tip-tilt of 40 Hz.

A satellite can vibrate at around 100 Hz for small amplitudes. This is thanks to the presence of reaction wheels and other components. Large amplitudes of 0.5 degrees due to wander and thermal snap can be around 10 Hz. Hence, the system also should be capable of handling this as well. These jitters and vibrations are in the same direction and equal for all the beams. Hence, this can be solved by a single accurate FSM and this should be considered for the terminal.

5.5 Link Budget Requirements

To ensure the performance of the link budget, there are a number of requirements which the terminal must adhere to. The first shall consider the wavelength selection as discussed in subsection 5.2:

GD-CR-020: The transmission wavelength of the terminal shall be 1550 nm +- 200 nm.

The use of WDM is very attractive, however, complex and expensive. Should this be used, the system must adhere to DWDM as discussed in subsection 5.1:

GD-CR-021: Wave Division Multiplexing (WDM) shall be done using DWDM.

The link budget should be competitive with other designs. The performance of each link seems to be able to do so in a mutli-beam system which can service both ground stations and LEO satellites as discussed in subsection 5.3. Furthermore, the competition with current satellites RF links must be met in order to be viable for networking and relay tasks:

GD-CR-022: The link budget according to the Shannon-Hartely theorem shall be greater then 40 Mbps.

And for competition with other optical links:

GD-NCR-003: The link budget according to the Shannon-Hartely theorem shall be greater then 100 Mbps.

The pointing system must have the ability to correct for turbulence effects when communicating with ground stations. This was analyzed in subsection 5.4:

PS-CR-004: The multi-beam steering/pointing system shall be able to operate at 40 Hz or higher.

The effects from spacecraft jitter and vibration must also be corrected for:

PS-CR-005: The pointing system shall be able to correct for tip-tilt errors of at least 1 mrad jitter in the entire aperture at at least 100 Hz.

This system must also be able to correct for pointing misalignements on the order of 0.5 degrees at 10 Hz:

PS-CR-006: The pointing system shall be able to correct for at least 8.7 mrad at at least 10 Hz.

6 Requirements Summary

Through the literature study, many requirements where proposed. These are summarized below.

6.1 (Multi-Beam) Terminal System Requirements

6.1.1 Critical General Design Requirements:

GD-CR-001: The terminal shall be designed to handle 10 targets.
GD-CR-002: The terminal shall be able to communicate with ground targets.
GD-CR-003: The terminal shall be able to communicate with LEO satellites.
GD-CR-004: The terminal shall have a FOV of 90 deg in total or the Earth + 1000 km either side (which ever comes first).
GD-CR-005: The terminal shall use COTS components.
GD-CR-006: The terminal shall be able to interface with the spacecraft through previously used Rx hardware.
GD-CR-007: The terminal shall weight no more then 10 kg.
GD-CR-008: The terminal shall not consume more then 500 W (50 W per link/beam).
GD-CR-009: The terminal shall not be larger then 1 m^3.
GD-CR-010: The terminal shall not exceed component thermal limits.
GD-CR-011: The terminal shall not exceed component structural limits.
GD-CR-012: The terminal shall be able to handle launch loads.
GD-CR-013: The terminal shall be able to handle the space environment in GEO.
GD-CR-014: The terminal shall be able to produce duplex communications with all targets.
GD-CR-015: The terminal shall be able to sustain a 10 second link without interruptions.
GD-CR-016: The terminal shall be able to communicate with at least 40 Mbps per link at its Shannon Limit for OOK modulation.
GD-CR-017: The terminal shall be able to withstand pointing towards the sun directly for 2 minutes.
GD-CR-018: The terminal shall not change its average center of mass during its life.
GD-CR-019: The transmission wavelength of the terminal shall be 1550nm +- 200 nm.
GD-CR-020: If Wave Division Multiplexing (WDM) is used, it shall be done using Dense Wavelength Division Multiplexing (DWDM).

6.1.2 Non-Critical General Design Requirements:

GD-NCR-001: The terminal shall preferably be capable of only increasing the number of steering and Rx-Tx components when scaled up to 20+ targets (scaling).
GD-NCR-002: The terminal design shall be capable of scaling to a multiple of 6 without increasing the projected mass by a multiple of 2. (Only rough estimation will suffice.)

GD-NCR-003: The link budget according to the Shannon-Hartely theorem shall be greater then 100 Mbps.

6.1.3 Transceiver Design Requirements

RxTx-PA-001: The system shall be designed to deliver the required amplification at the highest expected temperature of operation.
RxTx-PA-002: The power amplifiers shall be designed to meet the requirements at EOL radiation doses or at -0.5 dB which ever power output is lower.
RxTx-PA-003: Efficiency of the optical amplifiers shall not be below 40% from input electrical power to output optical power at the exit of the amplifier.
RxTx-PA-004: Pre-amplifiers shall be included only if the jitter BER is dominant.
RxTx-PA-005: The optical power amplifiers shall not use more power then 60W per link.

6.2 Pointing Sub-System Requirements

6.2.1 Critical Design Requirements:

PS-CR-001: All 10 targets shall share pointing components or arrays.
PS-CR-002: The FOR of the pointing mechanism, should it be used, shall be greater then 3 degrees.
PS-CR-003: The spot tracker shall have a frame rate higher then the pointing system.
PS-CR-004: The multi-beam steering/pointing system shall be able to operate at 40 Hz or higher.
PS-CR-005: The pointing system shall be able to correct for tip-tilt errors of at least 1 mrad jitter in the entire aperture at at least 100 Hz.
PS-CR-006: The pointing system shall be able to correct for at least 8.7 mrad at at least 10 Hz.

6.2.2 Non-Critical Design requirements

PS-NCR-001: The pointing component (DM, RM, FSM, etc...) shall preferably have the hardware capability to correct for higher order turbulence for each link independently should this be implemented.
PS-NCR-002: There shall be no duplicate hardware components in the design.

6.2.3 Fiber Coupling Requirements

PS-FC-001: The normalized angular fiber misalignment, expressed as $\Delta\Phi' = \Delta\Phi f/R$, shall be less then 0.05.

PS-FC-002: The normalized axial misalignment, expressed as $\Delta z' = \Delta z R/(f\omega_B)$, shall be less then 0.001.
PS-FC-003: The normalized lateral misalignment, expressed as $\Delta x' = \Delta x/\omega_B$, shall not be less then 0.35.
PS-FC-004: The pointing system shall be able to steer the brightest point in the spot at 100 Hz to stay within the coupling requirements.
PS-FC-005: Large perturbations of 0.5 deg/s at 10 Hz shall still be fiber coupled.
PS-FC-006: The pointing system shall be able to correct for first order jitter and turbulence (pointing errors) for each link independently.

6.2.4 Deformable Mirror Requirements

PS-DM-001: The deformable mirror shall be a discrete array of mirrors.
PS-DM-002: The temperature range of the DM shall not go out side a range of 250 K to 320 K respectively.
PS-DM-003: The DM shall be able to withstand launch amplitude vibration on its first 3 eigenmodes for 10 minutes without fracture or shall have its first eigenmode outside of the launch vibrational spectrum.
PS-DM-004: The fill factor shall not be lower then 80%.
PS-DM-005: The reflection of the light between the mirrors shall not induce noise by 3db.
PS-DM-006: The resolution/mirror size and pitch combination of the DM shall be twice as small as the required spatial separation/resolution of the FOV of the system or the Rayleigh criterion, which ever is bigger.

6.2.5 Fine and Fast Steering Mirror Array Requirements

PS-FSM-001: The temperature range of the FSM shall not go out side a range of 250 K to 320 K respectively.
PS-FSM-002: The FSM shall be able to withstand launch amplitude vibration on its first 3 eigenmodes for 10 minutes without fracture or shall have its first eigenmode outside of the launch vibrational spectrum.
PS-FSM-003: The fill factor shall not be lower then 80%.
PS-FSM-004: The reflection of the light between the mirrors shall not induce noise by 3db.
PS-FSM-005: The resolution/mirror size and pitch combination of the FSM shall be twice as small as the required spatial separation/resolution of the FOV of the system or the Rayleigh criterion, which ever is bigger.

6.2.6 Reflective Modulator Requirements

PS-RM-001: The RM shall not be exposed to UV light.

PS-RM-002: The RM temperature when active shall not be outside the temperature range of 270 K to 300 K.
PS-RM-003: The temperature range of the RM during the entire life shall not fall outside of 150 K to 330K.
PS-RM-004: The system shall correct for RM drift over time using a closed loop control system.
PS-RM-005: The frame rate of the RM shall not fall below the jitter frequency due to beam quality improvements.

6.2.7 Piezo Actuator Array Requirements

PS-PAA-001: Mirror shall be angles such that there is less then 10% shadow.
PS-PAA-002: The mirror shall be a discrete array of mirrors.
PS-PAA-003: The temperature range of the DM shall not go out side a range of 250 K to 320 K respectively.
PS-PAA-004: The PAA shall be able to withstand launch amplitude vibration on its first 3 eigenmodes for 10 minutes without fracture or shall have its first eigenmode outside of the launch vibrational spectrum.
PS-PAA-005: The fill factor shall not be lower then 80%.
PS-PAA-006: The reflection of the light between the mirrors shall not induce noise by 3dB.
PS-PAA-007: The resolution/mirror size and pitch combination of the PAA shall be twice as small as the required spatial separation/resolution of the FOV of the system or the Rayleigh criterion, which ever is bigger.

6.3 Pointing Sub-System Experiment Requirements

6.3.1 Critical Experiment Requirements:

EXP-CR-001: The pointing system design must be build able within the facility constraints:

(a) Half an optical bench.

(b) Components must be available or within time and financial budget.

EXP-CR-002: Experiment must be completed no later then 2 months before draft.

7 Pointing System Trade-off

The pointing mechanism on the basis of the requirements in section 6 can now be found. There is in fact a possibility that there will be 2 pointing mechanisms used. These are the multi-beam steering mechanism and the spacecraft jitter mitigation mechanism. The mechanisms considered in this case are the

Deformable Mirror (DM), Reflective Modulator (RM) (also referred to as spatial modulator), Fine and Fast Steering Mirror (FSM) and the Piezo Actuator Array (PAA).

The trade-off criteria will be designated a 1,0 and -1 for meets above required on its own, just meets required on its own and does not meet required on its own. Weights are given for each trade-off criteria. Weights will be given based on the ease, complexity, scalability and compactness of the design associated with the trade-off criteria.

First, the multi-beam steering mechanism will be trade-off'ed, this is shown in section 7. The winner of the trade-off is the RM with the DM as a close runner-up. The reason for the is the high optical efficiency and resolution, which give high flexibility and future ability to correct for sub-aperture wavefront distortions. However, the DM is more accurate and has, in general, a higher frame rate. Hence, there is great sensitivity between these. The FSM mainly lost due to its packing efficiency being lower, large array sizes and associated complex optical system to accommodate all this. However, its precision is very good and its frame rate is very high, which is why it is the strongest contender in the next trade-off. Lastly, the PAA, although very accurate, has significant drawbacks when it comes to accommodating diversely spaced multiple beams.

Table 11: Trade-off table for multi-beam steering systems.

	DM	RM	FSM	PAA	Weight
Pointing accuracy	1	0	1	1	1
Pointing FOR	1	1	1	-1	0.5
Resolution	0	1	-1	0	0.4
Frame rate	1	1	1	1	1
Precision optics dependent	1	1	-1	-1	1
Optical complexity	1	1	-1	-1	0.3
Mass	1	1	-1	1	0.3
Size	1	1	-1	1	1
Optical efficiency	0	1	-1	0	0.8
Environment effects	0	1	1	1	1
Total	5.1	6.3	-0.3	2.5	7.3

The steering system which will correct vibration and jitter of the spacecraft. The trade-off is shown in Table 7. Here, the FSM is the winner with the DM shortly followed after. The main advantage of the FSM is that it does not require adaptations for use in space compared to the DM. However, there is also an other benefit, namely that the whole aperture has to be corrected, making the FSM also more practical. The RM was mainly too slow and PAA quite complex to accommodate.

In conclusion. They system would likely use an RM for multi-beam steering and an FSM for aperture correction. However, for both of these a DM can be a substitute.

Table 12: Trade-off table for spacecraft jitter and vibration mitigation systems.

	DM	RM	FSM	PAA	Weight
Pointing accuracy	1	0	1	1	1
Frame rate	1	-1	1	1	1
Mass	1	1	1	1	1
Environment effects	0	1	1	1	0.5
Optical complexity	1	1	1	-1	1
Total	4	1.5	4.5	2.5	4.5

8 Reflection on Available Literature

Part I has shown and discussed many works about multiple topics. A few observations can be made over the prevalence of different papers and literature. The previous designs, discussed in section 2, for multi-beams mainly consist of patents on designs and concepts in early development phase. This can be seen in the content of the patents them selves, often consisting of abstract drawings of different processes and the variety of the different applications. Other patents include hardware design and terminal rendering. The most recent patents mainly focus on short distance communication between local networks and inter-building communications. These designs also mainly focus on the use of steering mirrors and FSMs for communication, implying SWaP unfriendly concepts for smaller satellites.

section 3 discussed previous endeavors into free-space communications in space and is mostly consistent of papers. These are all single beam terminal designs. It seems a lot of work is done on small satellites and demonstration missions and designs. The designs however are all relatively similar, namely the use of a MOPA with a fiber amplifier and subsequently a pointing system. The differences are more subtle, namely that the demonstration from NASA's OPALS implemented an artificial atmosphere, thermal control and adapters among others to the ISS. This understandably resulted in a very heavy and power inefficient design when compared to the cube-sat demonstrations. The data rates achieved are also in the range of 50-600 Mbps for link powers on the order of 0.2-6 W. The literature also shows that there is significant progress in this field and the systems are constantly improving. There is a large amount of available research literature is on single beam terminals compared to multi-beam terminals, which shows that there has been little done towards multi-beam design.

section 4 discusses different design aspects of the terminal and its optical train. There are many research and design papers on numerous topics on fiber coupling (the act of inserting the signal from free-space into an optic fiber), signal amplification and beam steering mechanisms. It is found that the spot size and misalignment's can be balanced with different magnitudes of jitter and offset can be balanced and optimized. This was the subject where literature was most easily found with the most theoretical approach. It is clear that there are

quite a number of requirements which are associated with efficient fiber coupling and can be considered driving for the pointing system design. The literature on the design of the MOPA's and the architectures for the transmitter has shown that a high performance master oscillator is power intensive and is hence use is made of efficient optical power amplifiers. For all the previous designs, this is done through fiber power amplifiers due to their high performance and optical properties. The combination with the wavelength used shows that the EDFA is most popular due to their efficiency at wavelengths around 1550 nm. These systems have also been used and qualified for space. The pointing mechanisms have a wide verity of options. For many of the technologies used, the performance and environmentally capabilities have been proven an is continuously being improved.

section 5 shows that there a few ways by which the link performance can be improved and enlarged. Wavelength multiplexing is particular attractive and often used in current internet fiber optic communication, especially DWDM. There are hence multiple channels at different wavelengths which can serve to communicate over links. This is not only used in fiber optics, however also for radio communications. This is hence also being considered for free-space communications. However, it does not seem that this concept is applied in space as much in optical communication. Additionally, interest in propagation of different wavelengths through the atmosphere is a topic which is shared with planetary sciences among other. Hence, data on the optimal wavelength is available and understood. Lastly, there is also a wide availability of analysis on the effects of atmospheric turbulence which also is a developing field. It cannot be ignored when communicating with ground stations and hence there is wide use of AO in free-space communication is used widely. The conditions simulated however showed that the spacecraft jitter could be more significant.

References

[1] John A. Bebawi, Ishac Kandas, Mohamed A. El-Osairy, and Moustafa H. Aly. A comprehensive study on EDFA characteristics: Temperature impact. *Applied Sciences (Switzerland)*, 8(9), 2018.

[2] Olivier Berné, Matthieu Caussanel, and Olivier Gilard. A model for the prediction of EDFA gain in a space radiation environment. *IEEE Photonics Technology Letters*, 16(10):2227–2229, 2004.

[3] R Bonjour, S Welschen, J F Johansson, and J Leuthold. Steering and Shaping of Multiple Beams with a Spatial Light Modulator based Beamformer. *2018 International Topical Meeting on Microwave Photonics (MWP)*, (1):1–4, 2018.

[4] K Cahoy. Laser Communication with CubeSats. Technical report, 2018.

[5] K. Cahoy, R. W. Kingsbury, T. Nguyen, and K. Riesing. Fast-steering solutions for cubesat-scale optical communications. page 169. SPIE-Intl Soc Optical Eng, nov 2017.

[6] Kerri L Cahoy, Anne D Marinan, Benjamin Novak, Caitlin Kerr, Tam Nguyen Thuc Nguyen, Matthew Webber, Grant Falkenburg, and Andrew Barg. Wavefront control in space with MEMS deformable mirrors for exoplanet direct imaging mirrors for exoplanet direct imaging. *SPIE*, 2014.

[7] Kerri L Cahoy, Anne D Marinan, Benjamin Novak, Matthew Webber, Kerri L Cahoy, Anne D Marinan, Benjamin Novak, and Caitlin Kerr. Wavefront control in space with MEMS deformable mirrors. *SPIE*, 861708(March 2013), 2013.

[8] Triebes S Capots L, Sigler R. Multi-channel wide-field laser communications method and apparatus.

[9] Emily Clements, Derek Barnes, Iñigo Portillo, Caleb Ziegler, Emily Clements, Raichelle Aniceto, Derek Barnes, David Caplan, James Clark, Iñigo Portillo, Christian Haughwout, Maxim Khatsenko, Ryan Kingsbury, Myron Lee, Rachel Morgan, Jonathan Twichell, Kathleen Riesing, Hyosang Yoon, Caleb Ziegler, and Kerri Cahoy. Nanosatellite optical downlink experiment : design , simulation , and prototyping. *SPIE*, 55(11), 2016.

[10] Yamaç Dikmelik and Frederic M Davidson. Fiber-Coupling Efficiency for Free-Space Optical Communication Through Atmospheric Turbulence. *Applied Optics*, 44(23), 2005.

[11] Alan Graham, Greg Kopp, Carlos Vargas-Aburto, and R. Uribe. Preliminary space environment tests of nematic liquid crystals. *Proceedings of SPIE - The International Society for Optical Engineering*, 2811(October 1996):46–50, 1996.

[12] Darryl P. Greenwood. Bandwidth specification for adaptive optics systems. *Lincoln Labratory*, (December):87–90, 1977.

[13] HOLOEYE. Spatial Light Modulators.

[14] N Jacka, W Walker, M Roybal, and J McNally. Design and Qualification of a Small, Customizable Fast Steering Mirror (FSM) for FSOC Stabilization and Scanning Applications. *SPIE*, 1052407(February 2018), 2018.

[15] Siegfried W. Janson and Richard P. Welle. The NASA Optical Communication and Sensor Demonstration Program: An Update. *AIAA/USU*, 2014.

[16] Ma Jing, Zhao Fang, Tan Liying, Yu Siyuan, and Han Qiqi. Plane wave coupling into single-mode fiber in the presence of random angular jitter. *Applied Optics*, 48(27):5184–5189, 2009.

[17] Ryan Kingsbury, Kathleen Riesing, and Kerri Cahoy. Design of a Free-Space Optical Communication Module for Small Satellites. *AIAA/USU*, 2014.

[18] Steven A. Lane, Jacob A. Brown, E. Tremer Megan, Craig Uber, Elizabeth E. Gallagher, Steven R. Collins, Michael R. Benoit, and William Miniscalco. Radiation testing of liquid crystal optical devices for space laser communication. *Society of Photo-Optical In- strumentation Engineers*, 48(November 2009):1–11, 2009.

[19] Christophe O. Laux, Richard J. Gessman, Benoit Hilbert, and Charles H. Kruger. EXPERIMENTAL STUDY AND MODELING OF INFRARED AIR PLASMA RADIATION. *American Institute of Aeronautics and Astronautics*, 1995.

[20] Mirrorcle. Gimbal-Less Two-Axis Scanning MEMS Micromirrors Device Datasheet S 5295, 2016.

[21] NGK. Piezo Actuator Arrays, 2020.

[22] Qifeng Niu and Chunyang Wang. High precision beam steering using a liquid crystal spatial light modulator. *Optical and Quantum Electronics*, 51(6):1–13, 2019.

[23] Bogdan V. Oaida, Matthew J. Abrahamson, Robert J. Witoff, Jessica N. Bowles Martinez, and Daniel A. Zayas. OPALS: An Optical Communications Technology Demonstration from the International Space Station. *IEEE*, 2013.

[24] D.G. O'Connel and Ken C. K. Cheung. MULTI-TARGET-TRACKING OPTICAL SENSOR-ARRAY TECHNOLOGY, 2009.

[25] Cadence Payne, Alexa Aguilar, Derek Barnes, Rodrigo Diez, Joseph Kusters, Peter Grenfell, Raichelle Aniceto, Chloe Sackier, Gregory Allan, and Kerri Cahoy. Integration and Testing of the Nanosatellite Optical Downlink Experiment. *AIAA/USU Conference on Small Satellites*, SSC18-XII-, 2018.

[26] Anna Polishuk and Shlomi Arnon. Optimization of a laser satellite communication system with an optical preamplifier. *Optical Society of America*, 21(7):1307–1315, 2004.

[27] Harry Presly and Michael O'Reilly. Agile Multi-Beam Free-Space Optical Communication Apparatus, 2003.

[28] Peter Rausch, Sven Verpoort, Ulrich Wittrock, J P Gardner, J C Mather, M Clampin, R Doyon, M A Greenhouse, H B Hammel, J B Hutchings, P Jakobsen, S J Lilly, K S Long, J I Lunine, J McCaughrean, M Mountain, J Nella, G H Rieke, M J Rieke, H-w Rix, E P Smith, G Sonneborn, M Stiavelli, H S Stockmann, R A Windhorst, G S Wright, L Gambicorti, F Lisi, A Riccardi, C Vettore, F Duo, A Guercia, D Gallieni, P Lazzarini, M Tintori, C Patauner, R Biasi, A Zuccaro Marchi, J Pereira, K Enya, H Kataza, P Bierden, R Rao, R Samuele, E Schmidtlin, M Shao, J K Wallace, S Chakrabarti, Di Gesu, X Gilbert, C Grezes-Besset, D Groeninck, M Hartung, H Krol, A Moreau, P Morin, H Pages, R Palomo, G Scharmer, D Soltau, and J-p Veran. Unimorph deformable mirror for space telescopes: environmental testing. *Publ. Astron. Soc. Pac*, 65(386):60–67, 2016.

[29] S Robinson and R Pavithra. Investigation on Multi-Beam Hybrid WDM for Free Space Optical Communication System. *International Journal of Photonics and Optical Technology*, (June 2016):24–28, 2016.

[30] Mathlouthi W Segura B. Multi-point free space optical communication system.

[31] Vladimir G. Sidorovich, Aleksei A. Leshev, Valery V Ragulsky, Mikhail A. Sadovnikov, Mikhail V. Vasiliev, and Vladimir P. Vasiliev. Free-Space Optical Communication System with Spatial Multiplexing, 2004.

[32] Yuanping Song, Robert M. Panas, and Jonathan B. Hopkins. A review of micromirror arrays. *Precision Engineering*, 51(August 2017):729–761, 2018.

[33] Robert A. Sprague and Donald R. Scifres. Multi-Beam Optical System Using Lens Array, 1984.

[34] Hideki Takenaka and Morio Toyoshima. Study on the Fiber Coupling Efficiency for Ground-to-Satellite Laser Communication Links. *SPIE*, (February 2010), 2010.

[35] Cedrat Technologies. Fine & Fast Steering Mirrors, 2020.

[36] Jing Tian, Wenshu Yang, Zhenming Peng, Tao Tang, and Zhijun Li. Application of MEMS Accelerometers and Gyroscopes in Fast Steering Mirror Control Systems. 2016.

[37] David H. Tofsted, Sean G. O'Brien, and Gail T. Vaucher. An Atmospheric Turbulence Profile Model for Use in Army Wargaming Applications I. Technical Report ARL-TR-3748, 2006.

[38] Morio Toyoshima. Maximum fiber coupling efficiency and optimum beam size in the presence of random angular jitter for free-space laser systems and their applications. *Optical Society of America*, 23(9):2246–2250, 2006.

[39] Capots L Treibes K, Enoch M. Multi-beam laser communications system and method.

[40] Glenn A. Tyler. Bandwidth considerations for tracking through turbulence. *Journal of the Optical Society of America*, 11(1):358–367, 1994.

[41] Oswald Wallner, Peter J. Winzer, and Walter R. Leeb. Alignment tolerances for plane-wave to single-mode fiber coupling and their mitigation by use of pigtailed collimators. *Applied Optics*, 41(4):637–644, 2002.

[42] Peng Wang. *The Energy Efficiency of EDFA and Raman Fiber Amplifier.* Master of engineering thesis, University of Melbourne, 2016.

[43] Glen M. Williams, Martin A. Putnam, Charles G. Askins, Michael E. Gingerich, and E. J. Friebele. Radiation-Induced Coloring of Erbium-Doped Optical Fibers. *Optical Materials Reliability and Testing: Benign and Adverse Environments*, 1791(February 1993):274–283, 1993.

[44] Krystian L Wlodarczyk, Emma Bryce, Noah Schwartz, Mel Strachan, David Hutson, Robert R J Maier, David Atkinson, Steven Beard, Tom Baillie, Phil Parr-burman, Katherine Kirk, Duncan P Hand, Krystian L Wlodarczyk, Emma Bryce, Noah Schwartz, Mel Strachan, David Hutson, Robert R J Maier, David Atkinson, Steven Beard, Tom Baillie, Phil Parr-burman, Katherine Kirk, and Duncan P Hand. Scalable stacked array piezoelectric deformable mirror for astronomy and laser processing applications and laser processing applications. 024502(12 February 2014), 2014.

[45] M. W. Wright, M. W. Wilkerson, and Ray R. Tang. Qualification testing of fiber-based laser transmitters and on-orbit validation of a commercial laser system. *SPIE*, 10563(ICSO October), 2014.

[46] M. W. Wright, M. W. Wilkerson, and Ray R. Tang. Qualification testing of fiber-based laser transmitters and on-orbit validation of a commercial laser system. *SPIE*, 10563(ICSO October), 2014.

[47] Feng Xiao and Lingjiang Kong. Optical multi-beam forming method based on a liquid crystal optical phased array. *Optical Society of America*, 56(36):9854–9861, 2017.

[48] Byung-wook Yoo, Jae-Hyoung Park, I H Park, Jik Lee, Minsoo Kim, Joo-young Jin, Jin-a Jeon, Sug-Whan Kim, and Yong-kweon Kim. MEMS micromirror characterization in space environments. *Optics Express*, 17(5):3370, 2009.